RIGA TECHNICAL UNIVERSITY

Andris Potrebko

THE MEASUREMENT OF THE MASS DIFFERENCE BETWEEN THE TOP QUARK AND ANTIQUARK AT 13 TEV PROTON-PROTON COLLISIONS USING CMS DETECTOR

Doctoral Thesis

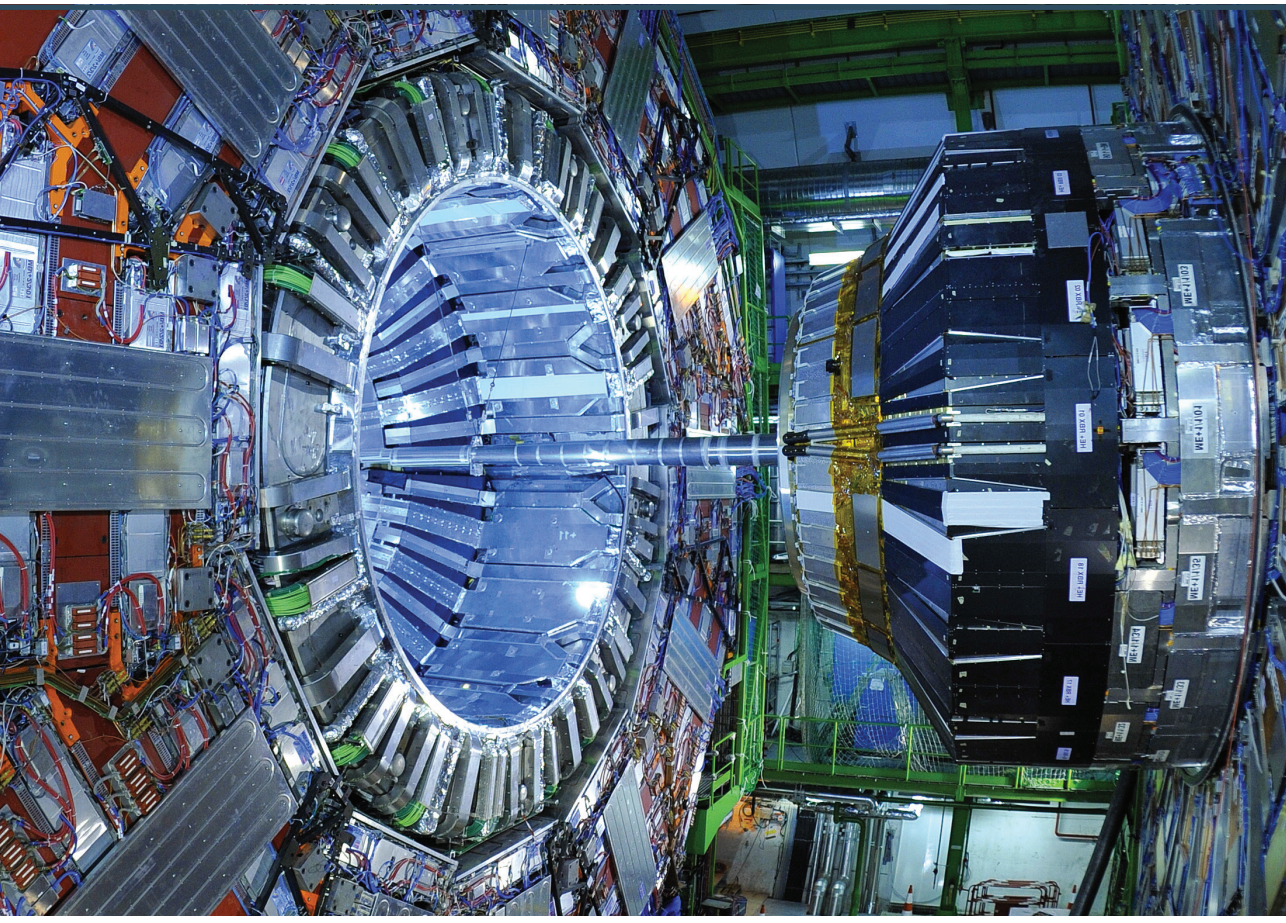

RTU Press
Riga 2025

RIGA TECHNICAL UNIVERSITY
Faculty of Natural Sciences and Technology
Institute of Particle Physics and Accelerator Technologies

Andris Potrebko
Doctoral Student of the Study Programme
"Particle Physics and Accelerator Technologies"

Measurement of the mass difference between the top quark and antiquark in 13 TeV proton-proton collisions using the CMS detector

Doctoral Thesis

Scientific supervisors:

Assoc. Professor Dr. phys.
KĀRLIS DREIMANIS

Dr. phys.
MARTIJN MULDERS (CERN)

Scientific advisor:
Associate Professor Dr. phys.
MARKUS SEIDEL

RTU Press
Riga 2025

Potrebko, A. Measurement of the Mass Difference between the Top Quark and Antiquark in 13 TeV Proton-Proton Collisions Using the CMS Detector. Doctoral Thesis. – Riga: RTU Press, 2025. – 168 p.

Published in accordance with the decision of RTU IPPAT attestation committee session of 29 January 2025, Minutes No. 1/2025.

The research was carried out within the framework and with financial support of the following projects:

- State Research Programme (SRP) "High-energy physics and accelerator technologies" VPP-IZM-CERN-2020/1-0002; VPP-IZM-CERN-2022/1-0001.

Cover picture from www.shutterstock.com.

DOCTORAL THESIS PROPOSED TO RIGA TECHNICAL UNIVERSITY FOR PROMOTION TO THE SCIENTIFIC DEGREE OF DOCTOR OF SCIENCE

To be granted the scientific degree of Doctor of Science (PhD), the present Doctoral Thesis has been submitted for defence at the open meeting of RTU Promotion Council on December 11, 2025 at 11.00 at the Faculty of Natural Sciences and Technology of Riga Technical University, Āzenes street 6, Conference Hall on the 11th Floor and Zoom online https://cern.zoom.us/j/69802317118?pwd=hkNGtWOXDjQCt95b8wuEoS3WWuRuNc.1.

OFFICIAL REVIEWERS

Professor Dr. phys. Mark Owen,
University of Glasgow, UK

Associate professor Dr. phys. Philip James Ilten,
University of Cincinnati, USA

Dr. phys. James Keaveney,
University of Cape Town, South Africa

DECLARATION OF ACADEMIC INTEGRITY

I hereby declare that the Doctoral Thesis submitted for review to Riga Technical University for promotion to the scientific degree of Doctor of Science (PhD) is my own. I confirm that this Doctoral Thesis has not been submitted to any other university for promotion to a scientific degree.

Andris Potrebko ...../signature/
Date .....

The Doctoral Thesis has been written in English. It consists of an Introduction, 6 chapters, Conclusions, 85 figures, 11 tables, and 7 appendices; the total number of pages is 168, not including appendices. The Bibliography contains 348 titles.

ABSTRACT

The Standard Model (SM) of particle physics has been remarkably successful in describing the fundamental forces and particles observed in experiments such as those at the Large Hadron Collider (LHC). However, it fails to explain several phenomena, including the matter-antimatter asymmetry of the universe, the nature of dark matter, and neutrino oscillations. The SM is built on a rich structure of symmetries, including the internal gauge symmetry $SU(3) \times SU(2) \times U(1)$, which governs the strong, weak, and electromagnetic interactions. Although strong and electromagnetic forces respect the parity (P), charge conjugation (C), and time reversal (T) symmetries, the weak force is known to violate C, P, T and the combined CP symmetry. Nevertheless, CPT symmetry has withstood all the experimental tests to date.

A discovery of even a slight CPT violation would fundamentally challenge our understanding of particle physics, requiring a significant revision of the SM. One of the key predictions of the CPT symmetry is the exact equality of particles and antiparticles. The top quark, as the heaviest known elementary particle, provides a unique opportunity to probe CPT symmetry at the highest available energy scales.

In this Thesis, the measurement of the mass difference between the top quark and antiquark Δm_t is presented using data collected by the CMS experiment at the LHC. The analysis is based on proton-proton collisions at a centre-of-mass energy of 13 TeV corresponding to an integrated luminosity of $137.63\,\mathrm{fb}^{-1}$. The measured value, $\Delta m_t = 139 \pm 67\,\mathrm{MeV}$, represents the most precise determination of Δm_t to date.

ANOTĀCIJA

Elementārdaļiņu standartmodelis (SM) apraksta līdz šim atklāto daļiņu īpašības, skaidrojot trīs no četrām fundamentālajām mijiedarbībām. SM veiksmīgi apraksta daļiņu fizikas eksperimentus, piemēram, tos, kas veikti, izmantojot Lielo hadronu paātrinātāju (LHC). Tomēr tas nespēj izskaidrot vairākas parādības, tostarp matērijas un antimatērijas asimetriju Visumā, tumšās matērijas dabu un neitrīno oscilācijas. SM ir balstīts bagātīgā simetriju struktūrā, tostarp $SU(3) \times SU(2) \times U(1)$, kas nosaka stipro, vājo un elektromagnētisko mijiedarbību. Lai gan stiprā un elektromagnētiskā mijiedarbība ir invariantas pret lādiņa saistīšanas, C, telpas inversijas, P, un laika inversijas, T, simetrijām, ir zināms, ka vājā mijiedarbība pārkāpj C, P, T, kā arī apvienoto CP simetriju. Neskatoties uz to, CPT simetrija līdz šim ir izturējusi visus eksperimentālos testus.

Pat neliela CPT simetrijas pārkāpuma atklāšana būtiski mainītu izpratni par daļiņu fiziku, prasot SM būtisku pārskatīšanu. Vienas no galvenajām CPT simetrijas sekām ir precīza daļiņu un antidaļiņu ekvivalence. Kā smagākā zināmā elementārdaļiņa virsotnes kvarks sniedz unikālu iespēju pārbaudīt CPT simetriju visaugstākajos pieejamajos enerģijas mērogos.

Šajā darbā tiek prezentēts virsotnes kvarka un antikvarka masas starpības Δm_t mērījums, izmantojot datus, kas iegūti *CMS* eksperimentā *LHC*. Analīze balstās protonu-protonu sadursmju datos ar 13 TeV masas centra enerģiju. Datu daudzums atbilst 137.63 fb^{-1} integrētajam mirdzumam. Iegūtais rezultāts $\Delta m_t = 139 \pm 67$ MeV ir līdz šim visprecīzākais šī SM raksturlieluma mērījums.

Contents

Acronyms

BDT boosted decision trees 76

BL Bowler-Lund 37, 158–160

BR branching ratio 152

BSM beyond the standard model 1, 26, 29, 36, 70

CERN European Organization for Nuclear Research 57

CHS charged hadron subtraction 73, 81, 86

CKM Cabbibo–Kabayashi–Maskawa 1, 18, 24

CL confidence limit 10, 32, 151

CMS Compact Muon Solenoid 3, 4, 8, 10, 35, 66

CR colour reconnection 39, 40, 43, 153

CS Catani-Seymour 32

CSC cathode strip chamber 63, 64

CTF combinatorial track finder 66

DIS deep inelastic scattering 32

DJR differential jet rate 87

DT drift tube 63, 64

DY Drell-Yan 32

ECAL electronic calorimeter 61, 67

EFT effective field theory 2, 26

ERD early resonance decays 154

EW electroweak 42

FKS Frixione-Kunszt-Signer 32

FPGA field-programmable gate array 65

FSR final-state radiation 33, 35, 40, 70, 132

GEM gas electron multipliers 64

GUT grand unification theory 29

HCAL hadronic calorimeter 59, 67

HEP high-energy physics 30, 40

HIC heavy-ion collisions 40

HL-LHC high-luminosity LHC 59

HLT high-level trigger 65

ID identifier 68, 76

IP interaction point 57

IR infrared 12, 28, 32

IRC infrared and collinear 68, 69

ISR initial-state radiation 33, 35, 70, 132

IT PU in-time pileup 73

JEC jet energy corrections 70, 73, 74, 83, 86, 90, 93, 129

JER jet energy resolution 74, 75, 129

JES jet energy scale 74, 166

LEP Large Electron–Positron Collider 39, 57

LHC Large Hadron Collider 1, 27, 57

LL leading logartihmic 35

LO leading order 12, 31, 36

MB minimum bias 39, 74

MC Monte Carlo 4, 28, 30, 34, 35, 40, 66

ME matrix element 11, 12, 32, 36, 37, 40

ML machine learning 43, 165

MPF missing transverse momentum projection fraction 74

MPI multi-parton interactions 38

MSSM minimally supersymmetric standard model 26

WM-DTM `WMassDeltaTopMass` 139, 142

WP working point 72, 76

1. INTRODUCTION

Since the discovery of the Higgs boson, the standard model of particle physics (SM) has been a consistent framework that describes the interactions of elementary particles, such as those produced at the Large Hadron Collider (LHC). So far no significant deviation from the theoretical predictions has been observed [1]–[3]. However, the SM is known to fail to account for the observed matter-antimatter asymmetry in the universe [4], describe phenomena such as neutrino oscillations [5], [6], dark matter [7], [8], and does not in a consistent way include the force of gravity [9], [10], motivating the search for extensions of the SM, called beyond the standard model (BSM) physics. The search for many theoretical ideas, such as supersymmetry (SUSY) [11], leptoquarks [12], axion-like particles [13], [14], has not been successful. Recently, the search for BSM physics has shifted towards precision tests of the SM, where increasingly precise measurements are compared with increasingly precise predictions.

The SM is a quantum field theory (QFT) which describes three out of four fundamental forces, electromagnetism, weak and strong interactions, but not gravity. The electromagnetic and strong interactions are symmetric under parity, P, charge conjugation, C, and time reversal, T, operations. In contrast, the weak force has been found to maximally violate P and partly the combined CP symmetry. However, it is predicted that the combination of the three discrete symmetries CPT will be completely preserved by any Lorentz-invariant and local quantum field theory, such as the SM [15]–[17]. Therefore, SM extensions violating CPT have to violate either locality or Lorentz invariance. It has been shown that using string theory, which is inherently non-local, it is possible to consistently implement CPT violating effects in the SM [18]. In addition, it has been shown that locality and Lorentz invariance violating effects can be added in the neutrino sector through a mechanism called ghost condensation [19], [20]. Nevertheless, based on the previous success of unexpected discoveries of C and CP violations, it is worthwhile to test CPT violation in the SM.

1.1. Previous tests of CPT symmetry

CPT symmetry predicts the equality of particles and their corresponding antiparticles. Tests of CPT symmetry include the measurements of mass, decay width, magnetic moments, production cross sections, and charges [21]. Currently the best constraint comes from neutral kaon K^0 and antikaon $\overline{K}^0$ measurements and is [22]

$$2\frac{|m_{K^0} - m_{\overline{K^0}}|}{(m_{K^0} + m_{\overline{K^0}})} < 6 \times 10^{-19}, \qquad 2\frac{|\Gamma_{K^0} - \Gamma_{\overline{K^0}}|}{(\Gamma_{K^0} + \Gamma_{\overline{K^0}})} < (8 \pm 8) \times 10^{-18}, \tag{1.1}$$

where m_{K^0} and Γ_{K^0} are kaon mass and decay width. Although the constraint is very significant, the result is obtained indirectly from the Cabbibo–Kabayashi–Maskawa (CKM)

mixing matrix parameters. This and other significant measurements of the particle-antiparticle mass asymmetry are shown in Fig. 1.1, comparing their precision and the scale at which the effect could take place. It shows that while the precision of the measurements at low scales of $\mathcal{O}(1\,\mathrm{GeV})$ is high, the region around the scale of the top quark mass is less explored. Recently, contributions have been made to assess the CPT violation systematically using the effective field theory (EFT) approach [23], which can assume a different sensitivity to the CPT violation for each quark generation. In addition to these searches, the Lorentz symmetry has been tested in the top-quark sector, and no deviation from the full symmetry has been found [24].

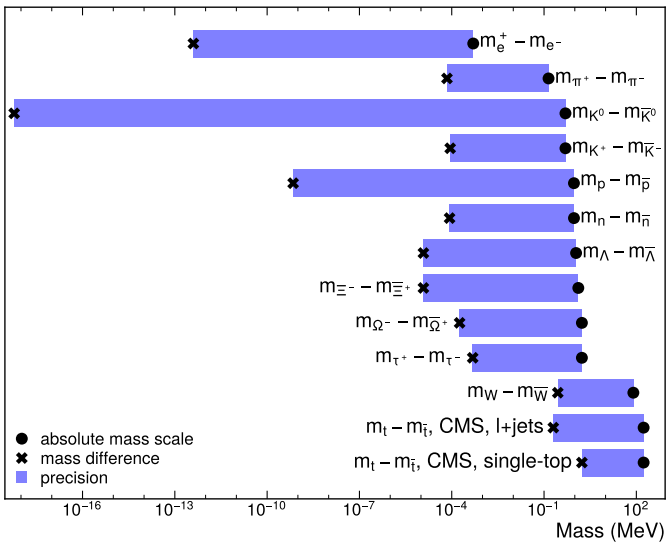

Fig. 1.1. The world best measurements of the mass difference between particles and antiparticles. The black markers represent the scale at which the measurement is made, i.e. the average mass of the particles. The crosses show the measured upper limit on the measured mass difference. The length of the bars corresponds to the precision of the measurement. Data from [21], [25]–[29] are used.

1.2. Previous measurements of top quark mass difference

The top quark, due to its short lifetime, decays weakly before hadronization. This allows direct measurements of its mass m_t, unlike for other quarks whose mass has to be deduced from hadron properties. Thus, it also allows for a precise measurement of the mass difference between the top quark and antiquark, $\Delta m_t = m_t - m_{\bar{t}}$. The current results of the measurements of Δm_t are shown in Fig. 1.2, where good consistency with the SM over all the measurements is seen. The most precise measurements of Δm_t are

performed in the top-quark pair process ($t\bar{t}$) in the lepton+jets decay channel, while a complementary measurement from single-top events provides a consistency check of the measurements. The different precision in the measurements is explained by different approaches to the measurement. In the measurements of the Compact Muon Solenoid (CMS) collaboration [30], [31] Δm_t was obtained from two separate datasets, for the top quark and the antiquark, only using the hadronically decaying top quark for the mass measurement and discarding the leptonically decaying top quark. On the other hand, in the other measurements, Δm_t was obtained for each event from both the hadronic and leptonic decays. The latter approach requires estimating the momentum of the lepton neutrino using the missing transverse momentum $p_{\mathrm{T}}^{\mathrm{miss}}$, which degrades the resolution of the measurement.

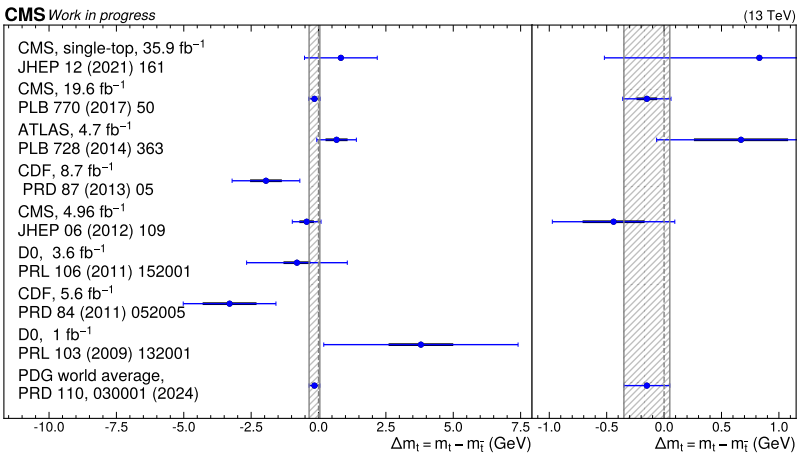

Fig. 1.2. The different measurements of the mass difference between the top quark and antiquark. The tick black bars show the systematic uncertainty, and the blue bars show the total uncertainty. The gray hatched bar shows the world average with the uncertainty obtained by the Particle Data Group (PDG) [21]. The right panel shows the zoomed in version of the left panel. The data from [21], [31]–[37] are shown.

1.3. Motivation for repeating the measurement in Run 2

The current world best measurement was performed by the CMS collaboration [30] using the data collected at the CMS Run 1 at the centre-of-mass energy $\sqrt{s} = 8\,\mathrm{TeV}$ with the integrated luminosity of $19.6\,\mathrm{fb}^{-1}$. The measurement was consistent with $\Delta m_t = 0$, but was statistically limited. Repeating the measurement using the CMS Run 2 dataset with a luminosity of $137.63\,\mathrm{fb}^{-1}$ offers a tenfold increase in the amount of $t\bar{t}$ events for analysis, and therefore, the statistical uncertainty could be reduced by a factor $\approx \sqrt{10} \approx$

3. In addition, an improved strategy for the quark vs. antiquark jet energy response uncertainty estimation provides a decrease in the systematic uncertainty.

This Thesis explains the various steps of the Δm_t analysis and provides the theoretical and experimental background necessary for it. The Thesis starts with Chapter 2, where the main theoretical concepts are introduced, giving great detail to symmetries in physics and the structure of the SM. Chapter 3 builds on that explaining how the Monte Carlo (MC) simulations for particle physics collisions are obtained. This section also mentions the author's study to obtain a CMS-ATLAS common MC $t\bar{t}$ dataset simulated using the SHERPA event generator. The results of this study are published in a CMS-ATLAS common note [38], [39]. While the dataset is not used for the current measurement, it will be important to understand and reduce the systematic uncertainties of further measurements, such as those due to different hadronization models.

The experimental system, including the collider and the CMS detector used to obtain the data used, is explained in Chapter 4, while the event reconstruction methods are described in Chapter 5. Expanding on that, the study of the author of this Thesis on jet flavour studies and jet energy reconstruction is shown in Chapter 6. The flavour-antiflavor uncertainties necessary for the Δm_t measurement are derived there as well as the flavour uncertainties necessary for the jet reconstruction in the CMS collaboration in general. The results shown in this section are described in an internal CMS note [40]. The measurement technique and results of Δm_t are described in Chapter 7. These results are published in an internal CMS note [41]. Finally, a short summary and outlook is provided in Chapter 8.

Aim of the Doctoral Thesis

To conduct the **most precise to date** measurement of Δm_t, performing the measurement using the full CMS Run 2 dataset selecting $t\bar{t}$ events in the lepton+jets decay channel.

Tasks of the Doctoral Thesis

1. Generate a $t\bar{t}$ dataset using the SHERPA event generator.

2. Obtain flavour-dependent jet energy corrections to correct the peak of the W boson mass in top-quark decays.

3. Obtain improved flavour-dependent jet energy scale uncertainties and quark-antiquark jet energy scale uncertainties comparing the flavour responses of the PYTHIA 8 and HERWIG 7 event generator programmes and thus estimating the uncertainty in the MC generators.

4. Obtain quark-antiquark jet energy scale uncertainties arising due to the disagreement of the simulated detector response with the CMS hadronic calorimeter test beam data.

5. Implement a profile likelihood fit for the Δm_t measurement. Add an estimation of all the relevant systematic uncertainties and evaluate their impact on Δm_t. Perform the fit, and analyse the result.

Thesis statements to be defended

1. The updated method for quark-antiquark jet energy uncertainty in CMS and the implementation of the profile-likelihood fit instead of the Ideogram method **reduces the systematic uncertainty of the Δm_t measurement by a factor of 3**.

2. The usage of the full CMS Run 2 dataset instead of the Run 1 dataset, **reduces the statistical uncertainty by a factor of 3**.

3. The disagreement of the simulated detector response with the CMS test beam data for charged pions **is the leading systematic uncertainty in the measurement**.

4. A $t\bar{t}$ dataset generated using the SHERPA event generator **describes the H_T distribution in data better ($\chi^2/n_{dof} = 0.42$)**than the currently used POWHEG +PYTHIA 8 dataset **($\chi^2/n_{dof} = 1.41$)**.

5. The flavour-dependent **jet energy uncertainty for gluons is reduced by 50 %** when using the CMS Run 2 simulation instead of Run 1.

Scientific novelty

1. This Thesis presents a novel approach for estimating the quark-antiquark jet energy scale uncertainties using the differences in event generators.

2. This Thesis shows the first estimation of the effect of the charged pion detector response mismodelling by the GEANT4 programme on the jet energy scale.

3. The Thesis introduces the first practically usable CMS-ATLAS common SHERPA $t\bar{t}$ dataset.

4. This Thesis presents the first measurement of Δm_t using the CMS Run 2 dataset and results in the world-leading measurement of this observable.

Practical significance

1. The refined flavour-dependent jet energy scale uncertainties developed in this Thesis will benefit the entire CMS collaboration, increasing the precision of key measurements, such as the measurements of the strong coupling constant, top-quark mass, and the cross-section measurements of top-quark pairs associated with additional jets. This will improve our ability to rigorously test the standard model, pushing the limits of current theoretical predictions and potentially revealing signs of new physics.

2. The new common CMS-ATLAS top-pair dataset generated with SHERPA enables a simplified ATLAS-CMS result comparison and validation, and can lead to an improved estimation of the jet flavour uncertainties.

3. A discovery of CPT symmetry violation would revolutionise our understanding of fundamental physics, challenging long-held assumptions and reshaping theoretical frameworks. Such breakthroughs not only expand scientific knowledge but historically have driven technological advancements of substantial practical significance, often in unforeseen ways, ranging from advancements in materials science to quantum computing and beyond.

Approbation of PhD Thesis in Scopus and Web of Science indexed articles

During the doctoral studies, the author of the Thesis co-authored 204 publications, most as a member of the CMS collaboration. Of these, 17 are the publications of the CMS Top Physics Analysis Group, where the author of this Thesis is an active member. Statistics was retrieved on 14.03.2025 from https://inspirehep.net/authors/1829953. The full list is added at the end of the Thesis.

Additionally, the study of the author of this Thesis is presented in the following 4 documents that are internally reviewed have been approved by the CMS collaboration to contain valuable information that will be included in further CMS publications.

[1] *CMS-ATLAS common note (Chapter 3 in the Thesis), public*
The ATLAS and CMS Collaborations, "Improved Common $t\bar{t}$ Monte-Carlo Settings for ATLAS and CMS", technical report CMS-NOTE-2023-004, CERN, Geneva, 2023 cds:2861366.

[2] *CMS internal note (Chapter 6 in the Thesis)*
Andris Potrebko, "Flavor dependent (L5) MC truth jet energy corrections and flavor uncertainties in Run 2", technical report, CERN, Geneva, 2024, CMS AN-23/074.

[3] *CMS internal note (Chapter 7 in the Thesis)*
Andris Potrebko et al., "Measurement of the Mass Difference between the Top Quark and Antiquark in $t\bar{t}$ Events with Lepton+jets Final States in 13 TeV Proton-Proton Collisions", technical report, CERN, Geneva, 2024, CMS AN-25/029.

[4] *Proceedings in the conference Moriond QCD'24 (sections in Chapter 2 in the Thesis)*
Andris Potrebko, "Review of the measurements of the strong coupling constant in CMS at 13 TeV. Contribution to the 2024 QCD session of the 58th Rencontres de Moriond". In: 58th Rencontres de Moriond on QCD and High Energy Interactions. June 2024. arXiv: 2406.01405.

Other publications on the topic that are not included in PhD Thesis

[1] **Andris Potrebko** and Inese Polaka, "Application of Gene Expression Programming in Improving the Event Selection of the Semi-leptonic Top Quark Pair Process". In: *2021 62nd International Scientific Conference on Information Technology and Management Science of Riga Technical University (ITMS)*. IEEE. 2021, pp. 1–6. DOI 10.1109/ITMS52826.2021.9615317.

Dissemination in international scientific conferences

[1] Andris Potrebko, "Flavor-dependent (L5) MC truth jet energy corrections and flavor uncertainties in Run 2". In: 3rd CERN Baltic Conference. Oct. 2023. URL: https://indico.cern.ch/event/1288731/contributions/5585483/.

[2] Andris Potrebko, "Flavor corrections". In: CMS JetMET workshop in Brussels. May 2023. URL: https://indico.cern.ch/event/1230157/contributions/5328141/.

[3] Andris Potrebko, "Common ttbar Monte-Carlo sample for CMS and ATLAS". In: 12th LHC students poster session. Nov. 2022. URL: https://indico.cern.ch/event/1204801/contributions/5136626/.

[4] Andris Potrebko, "Top pair process simulation and jet energy studies". In: 2nd CERN Baltic Conference. Oct. 2022. URL: https://indico.cern.ch/event/1147717/contributions/5082195/.

[5] Viesturs Veckalns and Andris Potrebko, "CMS Latvia Group activities in the CMS Top Physics Analysis Group". In: 1st CERN Baltic Conference. June 2021. URL: https://indico.cern.ch/event/970609/contributions/4415899.

2. THEORY: THE STANDARD MODEL OF PARTICLE PHYSICS AND THE TOP QUARK

2.1. Introduction

2.1.1. Basic structure of the standard model

In an experiment carried out in 1897 by J. J. Thomson, the first elementary particle, the electron, was discovered [42]. The last particle added to SM, the Higgs boson, was discovered in 2012 by the CMS and ATLAS collaborations [43], [44]. This finding was the final piece necessary to complete the SM. In this section, the author briefly introduces the structure of SM that was gradually assembled on the basis of several scientific breakthroughs between the two mentioned before.

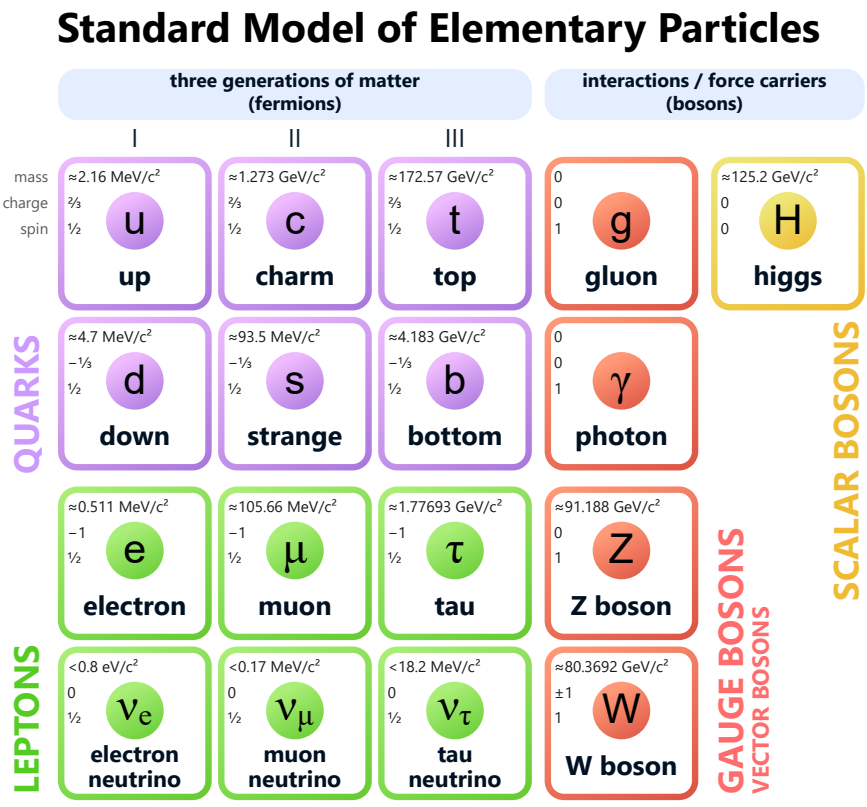

Fig. 2.1. The table of elementary particles constituting the SM.

The overview of currently discovered elementary particles is shown in Fig. 2.1. It consists of spin 1/2 particles, called fermions, spin 1 particles, gauge bosons, and the Higgs

boson. Fermions are subdivided into quarks and leptons, where leptons are further subdivided into charged leptons, electron e, muon μ, and tau τ, with electric charge $Q = -1$ and the corresponding neutrinos with $Q = 0$. In addition to interacting electromagnetically, leptons interact weakly. Quarks interact electromagnetically, weakly, and strongly. They have a subinteger Q, with up-type quarks (u, c, and t, or top quark) having $Q = 2/3$ and down-type quarks (d, s, and b) having $Q = -1/3$. Fermions are divided into three generations, where the second and third generations consist of successively heavier copies of the first-generation particles with the same quantum numbers.

Force is carried by gauge bosons: the electromagnetic force by photons γ, the weak nuclear force by heavy Z and W bosons, and the strong force by eight gluons g. The Higgs boson, H, is the boson corresponding to the Higgs field, which, through the Higgs mechanism, is responsible for the generation of the masses of elementary particles.

All the fermions mentioned above are known as matter particles. In the SM, each fermion has a corresponding antimatter counterpart (antiparticle) with the same properties as the matter particle, except for an opposite charge. Neutral bosons can be considered as their own antiparticles, while W^+ and W^- are the antiparticles of each other. A notable example of antimatter is the positron e^+, the antimatter partner of the electron e^-. Neutrinos ν and antineutrinos $\overline{\nu}$ have the same properties, but they participate in different interactions, as seen in W boson decays $W^+ \to e^+\nu$ and $W^- \to e^-\overline{\nu}$.

Quarks possess an additional quantum number, called colour, which is usually defined as red, blue, and green. Antiquarks have anticolour, i.e. antired, antiblue, and antigreen. Gluons come in eight different types, corresponding to all the possible non-singlet combinations of colour and anticolour. Confinement is an experimental fact that at low energies quarks bind into colour neutral hadrons before reaching the detector. This binding process is called hadronization. The colour-neutral bound states of quarks are called hadrons. Two typical types of hadrons are quark-antiquark bound states, called mesons, and three quark bound states, called baryons. An example of a baryon is the proton $p = uud$. Pions that can be charged, $\pi^+ = u\overline{d}$, $\pi^- = d\overline{u}$, or neutral, $\pi^0 = \frac{u\overline{u} \pm d\overline{d}}{\sqrt{2}}$ are examples of mesons. Additionally, tetraquarks [45] and pentaquarks [46] that are four- and five-quark bound states have recently been discovered.

The early 20th century revealed a remarkable observation – most of the physics governing our world satisfies a vast set of symmetries. Each symmetry is associated with a transformation that leaves the equations of motion unchanged. In this way, for each symmetry, a quantity that is not observable through physics experiments can be defined. Such quantities are effectively "hidden" by the invariance of the laws of physics and have no absolute meaning or relevance. For example, as a consequence of the space transformation, the absolute coordinate is meaningless and the start of the coordinate system can be chosen arbitrarily. In the SM of particle physics, the symmetries are embedded in the physics equations using the framework of quantum field theory (QFT). In QFT, for

each particle a separate field spanning the universe is introduced, where the particles are excitations of the field.

2.1.2. Success of the standard model

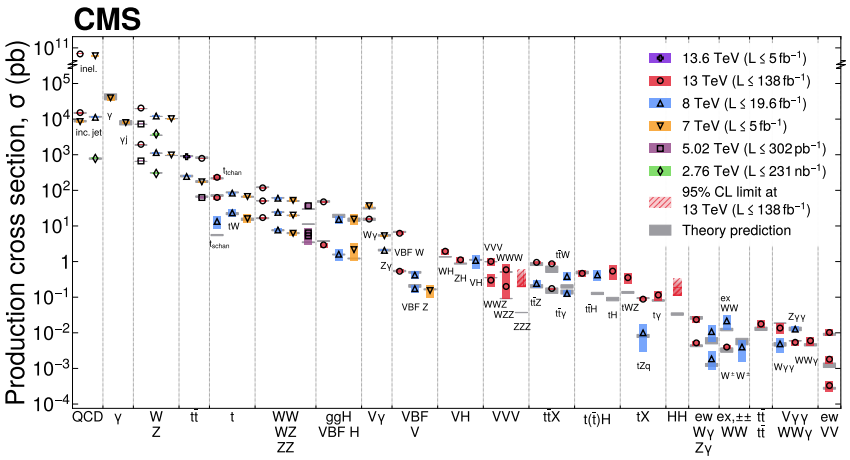

Fig. 2.2. The comparison of the predictions and the measured values of the cross sections of the SM processes [2]. The markers show the central values of the measurement for different collision centre of mass energy, the colourful error bands show the combined statistical and systematic uncertainty, while the gray bands show the uncertainties on the corresponding theory predictions. Dashed lines show the exclusion limits at the 95 % confidence limit (CL).

The SM has been successfully used to describe particle physics experiments. One remarkable achievement of the SM is the agreement between the measured and predicted cross sections of various processes. The cross section $\sigma_{pp\to B}$ corresponds to the probability for the initial state of two particles pp to interact, producing a given final state B. Fig. 2.2 shows the cross sections measured by the CMS collaboration compared with the theoretical predictions in absolute numbers, while more detailed comparisons with the data-to-simulation ratios can be seen in [2]. Note how the absolute cross sections of the processes span from $\mathcal{O}(10^{-3}\,\text{pb})$ for vector boson scattering, VV, where V is either Z or W boson, to $\mathcal{O}(10^{4}\,\text{pb})$ for γ production and to $\mathcal{O}(10^{10}\,\text{pb})$ for the total inelastic cross section of two protons. This shows both the great predictive power of the SM and the experimental capabilities to measure these processes. Remarkably, no significant deviation is seen in any of the processes.

In this section, the theoretical basis for the SM will be described, placing great emphasis on the symmetries embedded in it. We start in Section 2.2 by introducing the theoretical framework of QFT, and describing symmetries in Section 2.3. Building on the previous sections, in Section 2.4 we describe the Lagrangian of the SM. Finally, we

describe the top-quark physics in Section 2.5. The material covered is well described in standard textbooks, such as [47]–[49] and here the relevant parts to the Δm_t measurement are summarised. When additional sources are particularly beneficial, they are cited for each of the given sections.

2.2. Quantum field theory

A conventional way to represent a QFT is using the Lagrangian density formulation. Employing Lagrangians allows for a straightforward identification of the symmetries under which a particular theory remains invariant.

In classical mechanics, the Lagrangian principle evolves from the principle of least action, which requires that the equations of motion should minimise action, S, namely

$$\delta S \equiv \delta \int d^4x \mathcal{L} \stackrel{!}{=} 0. \tag{2.1}$$

Here, $\mathcal{L} = \mathcal{T} - \mathcal{V}$ is the Lagrangian density, where $\mathcal{T}$ and $\mathcal{V}$ are the kinetic and potential energy densities, respectively. The Lagrangian density further in this thesis is called simply the Lagrangian. The integral in Eq. (2.1) runs across the whole four-dimensional space-time and x^μ is a four-vector having components of space and time $x^\mu = (t\ x\ y\ z)^T = (t\ \vec{r})^T$ [1]. $\mathcal{L}$ in general is a function of the field, ϕ_r, and its derivatives $\mathcal{L} = \mathcal{L}(\phi_r(x), \partial_\mu \phi_r(x))$, where r is an index of Lorentz representation, e.g. spin components of a Dirac spinor. For scalar fields r omitted. From Eq. (2.1) the Euler-Lagrange equation (in the field form) can be derived, i.e.[2]

$$\frac{\partial \mathcal{L}}{\partial \phi_r} - \partial_\mu \frac{\partial \mathcal{L}}{\partial(\partial_\mu \phi_r)} = 0, \tag{2.2}$$

from which equations of motion of a classical system can be derived.

In the QFT, the fields are quantized and promoted to operators that create and annihilate quanta of the field. Particles are treated as excitations (quanta) of their corresponding fields. Physical observables, such as cross sections are computed from the scattering amplitude, called the matrix element (ME). The ME in bracket notation can be written as

$$\mathcal{M} = \langle f|T|i\rangle \equiv \langle f|S - 1|i\rangle, \tag{2.3}$$

where $|i\rangle$ and $|f\rangle$ are initial and final asymptotic states, i.e. eigenstates of the free Hamiltonian at $t \to -\infty$ and $t \to \infty$, respectively. The unitary operator S (the S-matrix or the scattering matrix) describes all the possible interactions in the evolution from $|i\rangle$ to $|f\rangle$, including also no interaction at all.

[1] In this thesis we use natural units, where the speed of light c=1 and the reduced Planck constant $\hbar = 1$.

[2] In the given section, unless stated otherwise, we use the Einstein summation convention where summation is implied over the free indices appearing twice in a single term.

As an example one can look at the ϕ^4 theory, which consists of the Klein-Gordon Lagrangian, which describes a scalar boson, and a quartic self-interaction. The Lagrangian of the ϕ^4 theory is

$$\mathcal{L} = \underbrace{\frac{1}{2}(\partial_\mu \phi)^2 - \frac{1}{2}m^2\phi^2}_{\text{kinetic term}} \quad \underbrace{-\frac{\lambda}{4!}\phi^4}_{\text{interaction term}} \quad , \tag{2.4}$$

where m is the mass of the scalar particle and λ is the coupling constant. The calculation of ME requires adding an infinite number of contributions, from each possible interaction history over all possible intermediate particle states. However, if $\lambda < 1$, the ME can be expanded perturbatively in powers of λ. At the leading order (LO) (tree level or Born level), the $2 \to 2$ scattering receives a single contribution from the contact interaction vertex, shown in Eq. (2.5) below. At the next-to-LO (NLO), quantum corrections arise from diagrams with two vertices connected by two internal propagators, forming loops:

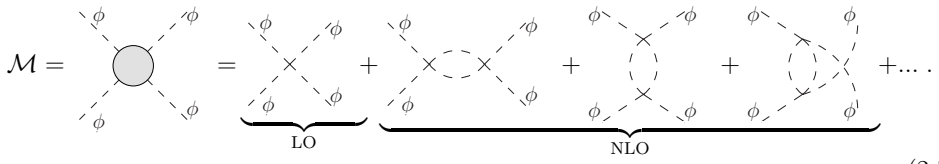

(2.5)

The diagrams in Eq. (2.5) are called Feynman diagrams and are pictorial representations of different contributions entering in the ME calculation. The time axis in the Feynman diagrams in this thesis flows from the left to the right.

Feynman rules allow to calculate the contribution of each of the Feynman diagram to the ME. The Feynman rules state:

1. Each vertex contributes a factor $(-i\lambda)$, corresponding to the interaction term in $\mathcal{L}$,
2. Add momentum k to each internal line. Due to the kinetic terms in $\mathcal{L}$, each internal line contributes a propagator

$$\int \frac{d^4k}{(2\pi)^4} \frac{i}{k^2 - m^2 + i\varepsilon}, \tag{2.6}$$

   where $\varepsilon > 0$ is an infinitesimal parameter.

Thus, adding an additional vertex to a Feynman diagram increases the order of the calculation.

A full NLO calculation must also include diagrams with additional legs, i.e. adding additional outgoing particles. These corrections, called real corrections contain infrared (IR) divergences due to integration over collinear and soft real emissions. On the other hand, the loop corrections, called virtual corrections, contain ultra violet (UV) divergences due to integration over the loop integrals. The KLN theorem [50], [51] states that these divergences cancel between the real and virtual corrections when combined at the same order. Dimensional regularisation is a method to subtract IR and UV divergences, by

converting four-dimensional integrals to $4-2\varepsilon$ dimensional integrals with ε again being a small parameter that at the end of calculation is required to $\varepsilon \to 0$. In this way, the poles can be isolated in terms of $1/\varepsilon^b$ and subtracted.

2.3. Symmetries

Transformations of ϕ that leave S in Eq. (2.1) and thus also the equations of motion unchanged are called symmetries. An overview of the symmetries present in the SM is provided in Table 2.1. The details will be discussed in this section. Symmetries are classified as continuous if they involve a smooth, continuous transformation of the system(to be discussed in Section 2.3.1), and discrete otherwise (to be discussed in Section 2.3.5). The internal symmetries that act only on fields and not on spacetime points will be discussed in Section 2.3.4.

2.3.1. Poincaré symmetry

Among the most important continuous symmetries is the Poincaré symmetry. It includes all the possible spacetime symmetries within the special relativity and includes invariance under rotation and under Lorentz boosts (both included in Lorentz symmetries) and invariance under translations. Poincaré symmetry is defined as a symmetry that preserves the spacetime interval $s^2 = x_\mu g^\mu_\nu x^\nu = \vec{x}^2 - t^2$, where g is the Minkowski metric. Sometimes also the discrete spacetime symmetries of parity P and time reversal T are included in the Lorentz symmetry as they also preserve s^2. However, neither P nor T can be obtained by a combination of the continuous (called proper orthochronous) Lorentz transformations $\mathbf{L}^\uparrow_+$, so a semidirect product of $\mathbf{L}^\uparrow_+$ with the discrete group $\{1, P, T, PT\}$ forms four disconnected subsets of the extended Lorentz symmetry.

2.3.2. Noether's theorem and groups

Noether's theorem [52] states that every continuous symmetry leads to a conservation law associated with a conserved quantity, called a conserved current j^μ. The generic infinitesimal transformation of ϕ can be written as $\delta\phi_r = \epsilon_s \Omega_{sr}(x)$, while the Lagrangian can change by a total derivative $\delta\mathcal{L} = -\epsilon_s \delta_\mu J^\mu_s(x)$. Expanding $\mathcal{L}$ one gets

$$\delta\mathcal{L} = \frac{\partial\mathcal{L}}{\partial\phi_r}(\delta\phi_r) + \frac{\delta\mathcal{L}}{\partial(\partial_\mu\phi_r)}\partial_\mu(\delta\phi_r) = \left[\frac{\partial\mathcal{L}}{\partial\phi_r} - \partial_\mu\frac{\partial\mathcal{L}}{\partial(\partial_\mu\phi_r)}\right]\delta\phi_r + \partial_\mu\left(\frac{\partial\mathcal{L}}{\partial(\partial_\mu\phi_r)}\delta\phi_r\right) \quad (2.7)$$

Noticing that the first term on the right hand side is vanishing due to Eq. (2.2), we can derive the conserved current as

$$\partial_\mu j^\mu = 0 \quad \text{with} \quad j^\mu = \frac{\delta\mathcal{L}}{\partial(\partial_\mu\phi_r)}\Omega_{sr} - J^\mu_s \quad (2.8)$$

Table 2.1

The symmetries of the SM showing the quantity that cannot be absolutely observed, the symmetry transformation that leaves the Lagrangian invariant and the conserved quantity due to Noether's theorem (for continuous symmetries) or the selection law (for discrete symmetries). Parity and time reversal are broken in weak interactions while the combined $SU_L(2)_L \times U_Y(1)$ is broken into $U_{\rm EM}(1)$ by the Higgs mechanism, just like $SU(N_f)$ is broken by different couplings of Higgs to each of the generations of the fermions

	Non-observable	Symmetry transformation	Conserved quantity
Poincaré	absolute space position	space translation $\vec{r} \to \vec{r} + \vec{\Delta}$	momentum $\vec{p}$
	absolute time	time translation $t \to t + \tau$	energy E
	absolute space direction	rotation $\vec{r} \to R \cdot \vec{r}$	angular momentum $\vec{L}$
	absolute velocity	Lorentz boost	centre of energy $\vec{K} = E\vec{r}_{cm} - t\vec{P}$ [3]
Discrete	absolute right or left	$\vec{r} \to -\vec{r}$	parity P
	absolute sign of electric charge Q	$Q \to -Q$	charge conjugation C
	absolute time direction	$t \to -t$	time reversal T
Internal	relative phase between states of different charge	$U(1)$ transformation $\psi \to e^{iQ\theta}\psi$	charge Q
	difference between coherent mixtures of a lepton and neutrino under weak interaction	$SU(2)$ transformation $\psi \to \psi' = \exp^{i\vec{\chi}(x)\cdot\vec{\sigma}/2}\,\psi$	weak isospin/ weak current
	absolute orientation in the colour space	$SU(3)$ transformation $\psi \to \psi' = \exp^{i\vec{\chi}(x)\cdot\vec{\lambda}/2}\,\psi$	total colour charge
	phase between the generations of fermions	$SU(N_f)$	the fermion generations

Examples of the conserved current is the energy-momentum tensor for the translation and time invariance. For Lorentz invariance, the three rotational degrees of freedom lead to conserved angular momentum, while the three boosts lead to the velocity of the centre of energy of the field being conserved, shown in Table 2.1.

To describe symmetries, a group concept is useful. A group is a set of elements with a bilinear operation between the elements of the set (multiplication) that satisfies

[3] Under Lorentz boosts, the conserved quantity corresponds to the components M^{0i} of the angular momentum tensor, which represent the generators of boosts. For a system of particles, this is equivalent to conservation of $\vec{K} = E\vec{r}_{cm} - t\vec{P}$, often called "centre-of-energy" vector. In the formula, $\vec{r}_{cm}$ is the location of the centre-of-mass and $\vec{P} = \sum_i \vec{p}_i$ is the total momentum of the system.

closure, associativity, the existence of an identity element, and the existence of an inverse element. Continuous symmetries can be described by Lie groups under multiplication, while discrete symmetries form finite groups. As an example, rotation, can be described by the $SO(3)$ group, i.e. a group of real 3×3 matrices O that are orthogonal ($O^{-1} = O^T$) and special (meaning that $\det(O) = 1$ with matrix multiplication as the group operation. $U(1)$ is a set of all complex numbers, $U = e^{i\alpha}$, with unit magnitude and multiplication, where U stands for unitary, $U \cdot U^\dagger = 1$. $SU(n)$ is a set of complex $n \times n$ matrices that are unitary and special with matrix multiplication. Lie groups are called Abelian if the product of the group elements is commutative $A \cdot B = B \cdot A$ and non-Abelian otherwise. In the SM, imposing the symmetries of $U(1)$, $SU(2)$ and $SU(3)$ in the QFT leads to electromagnetic, weak and strong interactions, respectively.

The elements of a Lie group can be written as generated by a Lie algebra $g = \exp\left[i \sum_j x_j T_j\right]$, where T_i are matrices, called generators of the Lie group, and x_i are real numbers. The generators satisfy the commutation relations $[T_i, T_j] = i \sum_k f_{ijk} T_k$, where f_{ijk} are the structure constants of the Lie group.

2.3.3. Lagrangian of the electromagnetic field

A classical electromagnetic field can be described using the Lagrangian density

$$\mathcal{L} = -\frac{1}{4} F_{\mu\nu} F^{\mu\nu} - J^\mu A_\mu, \tag{2.9}$$

where

$$F^{\mu\nu} = \partial^\mu A^\nu - \partial^\nu A^\mu \tag{2.10}$$

is a field strength tensor for a field with a four-potential $A^\mu = (V, \vec{A})$ and the four-current $J^\mu = (\rho, \vec{J})$. Using Eq. (2.2) and Eq. (2.9), the full set of Maxwell's equations

$$\partial_\mu F^{\mu\nu} = J^\nu \tag{2.11}$$

can be derived.

2.3.4. Internal symmetries

Internal symmetries are symmetries that act only on the fields but not on spacetime points. They act the same at each point of space. As an example, in the Dirac Lagrangian electromagnetic interaction is symmetric under the global $U(1)$ gauge transformation, representing the phase rotation, $\psi \to \psi' = e^{i\alpha}\psi$, i.e. the phases cancel out in $\mathcal{L}$ as

$$\mathcal{L} = i\bar{\phi}\gamma^\mu \partial_\mu \phi \to i\bar{\phi} e^{-i\alpha} \gamma^\mu \partial_\mu e^{i\alpha} \phi = i\bar{\phi}\gamma^\mu \partial_\mu \phi. \tag{2.12}$$

Note that unless stated otherwise in this thesis fermion fields are denoted ψ, while the scalar fields are ϕ.

Enforcing the Dirac Lagrangian to be invariant under the local gauge transformation $\psi \to e^{i\chi(x)}\psi$ requires an additional term to be added to the Lagrangian corresponding to a photon field A^μ transforming as $A^\mu \to A^\mu - \partial^\mu \chi(x)$. The form of the original Dirac Lagrangian can be restored only if the ordinary derivative is replaced with the so-called covariant derivative $D^\mu = \delta^\mu - iqA^\mu$, thus

$$\mathcal{L} = i\overline{\psi}\gamma^\mu \mathcal{D}_\mu \psi \equiv i\overline{\psi}\not{\mathcal{D}}\,\psi, \tag{2.13}$$

where in the second term the slashed notation is introduced.

Extending global symmetries to local symmetries for non-Abelian groups, such as $SU(n)$ implies a transformation of the form $\psi \to \psi' = \exp^{i\vec{\chi}(x)\cdot\vec{T}/2}\,\psi$, where, T^a are the $n^2 - 1$ generators of the $SU(n)$ group and $\vec{\chi}(x)$ is a vector of coefficients. Enforcing the symmetry, necessitates the introduction of $n^2 - 1$ gauge fields, A^a_μ with a denoting the index of the gauge field and a covariant derivative of the form

$$D_\mu = \partial_\mu - i\alpha \frac{T^a}{2} A^a_\mu, \tag{2.14}$$

where α is a coupling constant.

For the $SU(2)$ case of the weak interaction, T^a corresponds to the three Pauli matrices, σ^i, so that

$$D_\mu = \partial_\mu - i\alpha_2 \frac{\sigma^i}{2} W^i_\mu = \partial_\mu - i\alpha_2 \frac{1}{2} \begin{pmatrix} W^3_\mu & W^1_\mu - iW^2_\mu \\ W^1_\mu + iW^2_\mu & -W^3_\mu \end{pmatrix}, \tag{2.15}$$

where W^i_μ are the three gauge fields of $SU(2)$ and α_2 is the weak coupling constant. Similarly, in the QCD case with $SU(3)$ this leads to the introduction of the eight gluon fields, G_μ, corresponding to the eight gluon types, and T^i correspond to the Gell-Mann matrices, λ^a_{ij}.

For a non-Abelian gauge theory, the field-strength tensor in Eq. (2.10) has to be changed to

$$F^a_{\mu\nu} = \partial_\mu A^a_\nu - \partial_\nu A^a_\mu + \alpha f^{abc} A^b_\mu A^c_\nu. \tag{2.10′}$$

2.3.5. Discrete symmetries

The discrete symmetries in the SM are depicted in Fig. 2.3. As mentioned, two discrete spacetime symmetries P and T transform the spacetime as $(t, \vec{x}) \to (t, -\vec{x})$ and as $(t, \vec{x}) \to (-t, \vec{x})$, respectively. Assuming rotational symmetry in the SM, two of the three dimensions in the P transformation can be rotated to the initial position, such that P is analogous to the mirror reflection around one of the axes. Another, non-spacetime discrete symmetry, charge conjugation (C), is of great importance in the SM, under which particles and antiparticles are interchanged by conjugating all internal quantum numbers,

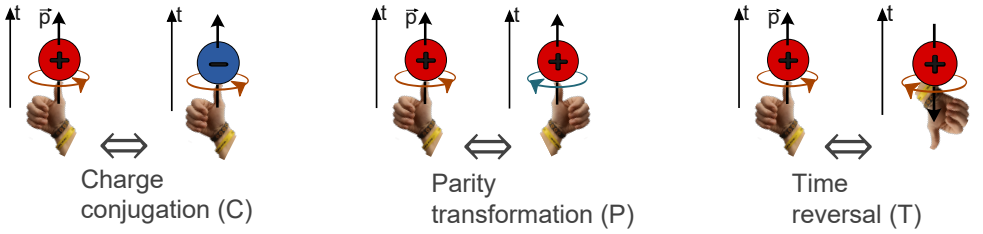

Fig. 2.3. Graphical depictions of the C, P, and T symmetries.

like for the electromagnetic charge, $Q \to -Q$. Although any relativistic field theory must be invariant under $L_+^\uparrow$, it can be violated under C, P or T.

Experimentally, no deviation from the exact C, P, and T symmetries are found in the gravitational, electromagnetic and strong interactions. However, the weak force maximally violates P, as first discovered in the experiment carried out by Chien-Shiung Wu measuring the beta decays of the cobalt-60 nuclei [53]. This unexpected discovery led to a consequence that only left-handed particles and only right-handed antiparticles interact with the weak force. In other words, the weak interaction discriminates between the interaction and its mirror image. Since these early discoveries of P violation in atomic decays, it has also been observed in different atomic systems [54] and proposed to be detectable also in molecular systems [55].

After the discovery that P is not a fundamental symmetry of nature, it was assumed instead that simultaneously applying the C and P symmetries would restore complete symmetry in nature. However, as first seen in neutral kaon, $K^0 = d\bar{s}$ and $\overline{K}^0 = \bar{d}s$, decays, the combined CP symmetry is also violated in certain weak decays. Both K^0 and $\overline{K}^0$ are typically produced by the strong interaction. Their decay, on the contrary, takes place weakly. It was discovered that K^0 and $\overline{K}^0$ called the strong eigenstates are not equal to the weak (or mass) eigenstates, $K_{L,S}$[4]. Instead, $K_{L,S}$ are in a superposition of the strong eigenstates as $K_{L,S} = \frac{(1+\varepsilon)K^0 \pm (1-\varepsilon)\overline{K^0}}{\sqrt{2(1+\varepsilon^2)}}$, where ε is a small complex parameter describing the strength of the CP violation.

Applying the CP transformation on $K_{L,S}$ in the case of $\varepsilon = 0$ gives

$$CP(K_{L,S}) = \frac{1}{\sqrt{2}}(CP(K^0) \pm CP(\overline{K^0})) = \frac{1}{\sqrt{2}}(\overline{K}^0 \pm K^0) = \mp K_{L,S}. \tag{2.16}$$

Thus, $K_{L,S}$ exactly coincide with the pure CP-even and CP-odd eigenstates. In such a case, the CP-even K_S would only decay into CP-even final states such as $\pi^0\pi^0$ or $\pi^+\pi^-$, while the CP-odd K_L would only decay into the CP-odd $\pi^0\pi^0\pi^0$. However, in 1964, oscillations between K_S and K_L were discovered, where K_L would oscillate to K_S and decay into two pions $\pi^+\pi^-$ [56]. Thus, it turns out that the weak eigenstates of neutral kaons are no longer exact CP eigenstates, but mixtures containing a small amount of

[4]The subscripts in $K_{L,S}$ denote the long- and short-lived kaons, differing in their decay times.

opposite CP components determined by the parameter ϵ. This result was confirmed in the asymmetry of K_L decays to $\pi^- l^+ \nu_l$ and $\pi^+ l^- \overline{\nu_l}$. The absolute value $|\varepsilon|$ can be measured as $|\varepsilon| = \left(2 \cdot \left|\frac{A(K_L^0 \to \pi^+\pi^-)}{A(K_S^0 \to \pi^+\pi^-)}\right| + \left|\frac{A(K_L^0 \to 2\pi^0)}{A(K_S^0 \to 2\pi^0)}\right|\right)/3$, where $A(a \to b)$ is the amplitude for state a to decay into b. The experiments show a very small CP-violation effect $|\varepsilon| \approx (2.228 \pm 0.011) \times 10^{-3}$ [57], therefore, unlike the maximally violated P symmetry, the CP symmetry remains largely conserved, with only a small deviation.

The discoveries above indicate the so-called indirect discovery of the CP violation because of its observation in the mixing of neutral kaons and not in their decays. The discovery of the CP violation in the decays of neutral kaons was later discovered [58], [59] and its strength is characterised by $\mathbf{Re}(\varepsilon'/\varepsilon) = (1.66 \pm 0.23) \times 10^{-3}$. Since the initial experiments, CP-violation has been also confirmed in B [60] and D [61] meson decays[5].

CP violation can be shown to be only possible in the SM with at least three flavour generations N_f. This comes from the fact that the CP-violation requires a complex phase in the matrix describing the strength of the flavour-changing weak interactions, mediated by the W boson, also called the Cabbibo–Kabayashi–Maskawa (CKM) matrix. The CKM matrix is a unitary complex matrix that can have $N_f^2 - (2 \cdot N_f - 1)$ degrees of freedom. For $N_f = 2$, there is only one free parameter, while for $N_f = 3$ there are four, where one has to be a complex phase. The CKM matrix describes the mixing of the mass eigenstates q and the electroweak eigenstates q' of the quark generations:

$$\begin{pmatrix} d' \\ s' \\ b' \end{pmatrix} = \begin{pmatrix} V_{ud} & V_{us} & V_{ub} \\ V_{cd} & V_{cs} & V_{cb} \\ V_{td} & V_{ts} & V_{tb} \end{pmatrix} \cdot \begin{pmatrix} d' \\ s' \\ b' \end{pmatrix}, \tag{2.17}$$

with the currently best know values being

$$\begin{pmatrix} |V_{ud}| & |V_{us}| & |V_{ub}| \\ |V_{cd}| & |V_{cs}| & |V_{cb}| \\ |V_{td}| & |V_{ts}| & |V_{tb}| \end{pmatrix} = \begin{pmatrix} 0.97435 \pm 0.00016 & 0.22501 \pm 0.00068 & 0.003732^{+0.000090}_{-0.00008} \\ 0.22487 \pm 0.00068 & 0.97349 \pm 0.00016 & 0.04183^{+0.00079}_{-0.00069} \\ 0.00858^{+0.00019}_{-0.00017} & 0.04111^{+0.00077}_{-0.00068} & 0.999118^{+0.000029}_{-0.000034} \end{pmatrix}, \tag{2.18}$$

as obtained by the global fit performed in [21]. Not, that the sub-diagonal elements are small compared to the diagonal elements with $|V_{ub}| \ll |V_{cb}| \ll |V_{us}|$. Due to the unitarity of the CKM matrix, $\sum_i V_{ij} V_{ik}^* = \delta_{jk}$ and $\sum_j V_{ij} V_{kj}^* = \delta_{ik}$. Each vanishing contribution of these can be represented by a triangle in a complex place. The area of this triangle is equal to half the Jarlskog invariant J, which can be defined by $\mathrm{Im}[V_{ij} V_{kl} V_{il}^* V_{kl}^*] = J \sum_{m,n} \varepsilon_{ikm} \varepsilon_{jln}$, where ε_{ijk} is a totally antisymmetric tensor and there is no Einstein summation over identical indices. J is another quantity to represent the strength of the CP violation with $J = 0$ corresponding to the case of no CP violation in the SM.

[5] B mesons consist of a b quark and another non-b quark, e.g. $B^0 = d\bar{b}$. D mesons are mesons that contain a c quark and either u, d or s quark, such as $D^0 = c\bar{u}$.

The observed universe consists predominately of matter, whereas the early universe is expected to be charge-neutral and consist of an equal amount of matter and antimatter. This is called the matter-antimatter asymmetry problem. The Kolmogorov's criteria include CP violation as one of the necessary conditions for the matter-antimatter asymmetry in the universe. However, according to the current estimates, the observed CP violation is too weak to explain the observed matter-antimatter imbalance [4].

CP violation is theoretically allowed also in quantum chromodynamics (QCD) by introducing an additional term, called the vacuum angle, which contains an arbitrary coefficient $0 < \theta < 2\pi$. No discovery of the CP violation in the QCD sector indicates $\theta = 0$, which constitutes a fine-tuning problem called the Strong CP problem. The Strong CP problem can be explained by an introduction of a new anomalous symmetry that is broken at low energies and leads to the introduction of a Goldstone boson called axion [62], [63]. Until now, no discovery of axions or more general axion-like particles has been observed [13], [14].

2.3.6. CPT violation in the standard model

It turns out that no physical Lagrangian appearing in nature, contains terms that couple $\phi(\vec{x}, t)$ to $\phi(\vec{y}, t)$ with $\vec{x} \neq \vec{y}$, a principle called locality. In other words, this property tells that an object can only be influenced by its immediate surroundings. As an example, Coulomb's law was first thought to be non-local and an interaction of two charges was described by an instantaneous force proportional to the inverse distance between the particles squared. However, later it was discovered that the interaction is carried out by a mediating particle, a photon, which interacts with each of the charges locally.

The CPT theorem states that any local Lorentz invariant QFT must be invariant under the CPT transformation [15]–[17]. Therefore, CP violation also implies T violation. An intuitive analogy of this is that particles can distinguish not only the interaction from its mirror image but also the direction in time. The CPT theorem implies that antiparticles (obtained by the CP transformation) behave like particles moving back in time. Thus, it also implies that observables like masses should be equal for particles and antiparticles.

Despite strong limits on CPT violation, as mentioned in Chapter 1, the violation can be introduced by violating locality [18] or Lorentz symmetry [19], [20], [64]. However, both must be violated only weakly to ensure agreement with current SM measurements.

2.4. The standard model of particle physics

2.4.1. The Lagrangian of the standard model

The Lagrangian of the SM consists of all the terms that are invariant under the Poincaré symmetry and the local $\mathrm{SU}(3)_c \times \mathrm{SU}(2)_L \times \mathrm{U}(1)_Y$ gauge symmetry, where the

subscript c represents that the $SU(3)$ symmetry is in the colour space, L represents that the $SU(2)$ symmetry is over the left-handed fermions and Y represents the $U(1)$ symmetry with a charge called hypercharge, Y_W, which can differ from particle to particle. All these symmetries were summarized in Table 2.1. The Lagrangian can be divided up in several terms [47], [48]:

$$\mathcal{L}_{SM} = \mathcal{L}_G + \mathcal{L}_F + \mathcal{L}_H + \mathcal{L}_Y, \tag{2.19}$$

where $\mathcal{L}_G$, $\mathcal{L}_F$, $\mathcal{L}_H$ and $\mathcal{L}_Y$ are the gauge field kinetic energy term, Dirac kinetic energy and interactions with gauge fields, Higgs field and interactions with the weak gauge bosons and Yukawa term giving masses to the fermions, respectively. These are described in the following chapters. The kinetic energy term is

$$\mathcal{L}_G = -\frac{1}{4}B_{\mu\nu}B^{\mu\nu} - \frac{1}{2}\mathrm{tr}[W_{\mu\nu}W^{\mu\nu}] - \frac{1}{2}\mathrm{tr}[G_{\mu\nu}G^{\mu\nu}], \tag{2.20}$$

which is an extension of the electromagnetic Lagrangian in Eq. (2.9), where $B_{\mu\nu}$, $W_{\mu\nu}$, and $G_{\mu\nu}$ are the field strength tensors for $U(1)$, $SU(2)$, and $SU(3)$, respectively. This term describes the propagation of the gauge fields and their self-interactions.

2.4.2. Electroweak theory

To represent the fact that only left-handed fermions interact weakly, one defines a left-handed lepton $SU(2)$ doublet as

$$L = \begin{pmatrix} \nu_e \\ e^- \end{pmatrix}_L \tag{2.21}$$

and a right-handed singlet e_R. A rotation in $SU(2)$, physically corresponding to the radiation of a W boson, performs a replacement $\nu_e \leftrightarrow e^-$ in the doublet. The singlet on the contrary is invariant under $SU(2)$ and therefore does not interact with W. The same is done for quarks, where the left-handed quark doublet is $Q_L = (u,\ d)^T$ and the right-handed singlets are u_R and u_L. The same notation applies for the other generations, with uppercase symbols used for $SU(2)$ doublets and lowercase symbols for singlets.

Quarks are triplets in the $SU(3)$ space, i.e. vectors consisting of three components. This represents the invariance under the rotation in the colour space, e.g. simultaneously changing all the colours as red↔blue↔green. Eight different gluon types correspond to the eight generators of the $SU(3)$ group. The rest of the particles are singlets in $SU(3)$ space.

The second term in Eq. (2.19) is responsible for the kinetic energy and interactions of the fermions with the gauge fields. It can be written as a Dirac equation, Eq. (2.13), but expanding the covariant derivative in Eq. (2.15) to correspond to $SU(3)_c \times SU(2)_L \times U(1)_Y$,

so that

$$\mathcal{L}_F = \sum_{\psi} \overline{\psi}\gamma^{\mu}\left(i\partial_{\mu} - \alpha_1 \frac{1}{2} Y_W B_{\mu} - \alpha_2 \frac{1}{2}\sigma^i W_{\mu}^i - i\alpha_{\rm s}\frac{\lambda^a}{2} G_{\mu}^a\right)\psi, \tag{2.22}$$

where the term in the bracket is the covariant derivative and α_1, α_2 and $\alpha_{\rm s}$ are the electromagnetic (fine-structure), weak, and strong coupling constants, respectively. The sum goes over the fermions $\psi = L, e_R, Q_L, u_r, d_r$. Note that in Eq. (2.22), G_{μ}^a acting on lepton fields vanishes, representing the fact that leptons do not interact with gluons. Similarly, W_{μ}^a vanishes acting on right-handed singlets.

The fields B_{μ} and W_{μ}^i do not correspond to the physical photon and the weak bosons, but instead are called hypercharge field and weak isospin, symmetric under $U(1)$ and $SU(2)$, respectively. The introduction of these two new fields leads to a unified description of the electromagnetic and weak interactions relying on works of Glashow [65], Salam [66], Weinberg [67], and t'Hooft [68].

After the symmetry breaking, the initially massless bosons B_{μ} and W_{μ}^a mix into a massless photon and three massive gauge bosons. The mixing of B and W^3 leads to a photon field, A_{μ} and a charge-neutral boson field, Z^0 as

$$\begin{pmatrix} A \\ Z^0 \end{pmatrix} = \begin{pmatrix} \cos\theta_W & \sin\theta_W \\ -\sin\theta_W & \cos\theta_W \end{pmatrix} \begin{pmatrix} B \\ W^3 \end{pmatrix}, \tag{2.23}$$

where θ_W is the weak mixing or the Weinberg angle. The fermion specific electric charge, Q, can be identified as the mixture of Y_W and the third component of the weak isospin, T_3 in the following way

$$Q = T_3 + Y_W/2. \tag{2.24}$$

The W_1 and W_2 bosons produce charged bosons $W^{\pm}$ as

$$W^{\pm} = \frac{1}{\sqrt{2}}(W_1 \mp iW_2). \tag{2.25}$$

Due to the spontaneous symmetry breaking mechanism, the Z^0 and $W^{\pm}$ boson obtain masses, while A remains massless.

2.4.3. The Higgs mechanism

The mass term of the form $-m\overline{\psi}\psi$ is not allowed in the SM because it is not gauge invariant, since the left- and right-handed fermions transform differently under $SU(2)$. In addition, the electroweak theory defined in Section 2.4.2 does not produce masses of the known gauge bosons.

This issue is resolved by employing the Englert–Brout–Higgs–Guralnik–Hagen–Kibble mechanism (Higgs mechanism) and the spontaneous symmetry breaking [69]–[71]. The

boson masses are added by introducing a Higgs potential term

$$\mathcal{L}_H = |D_\mu \phi|^2 - V(\phi), \tag{2.26}$$

where

$$\phi = 1/\sqrt{2} \begin{pmatrix} \phi^+ \\ \phi^0 \end{pmatrix}, \tag{2.27}$$

is a complex scalar Higgs field under $SU(2)$ and

$$V(\phi) = \mu^2 \phi^\dagger \phi - \lambda (\phi^\dagger \phi)^2 \tag{2.28}$$

is the Higgs potential with $\mu > 0$ being the Higgs boson mass and $\lambda > 0$ an arbitrary coefficient.

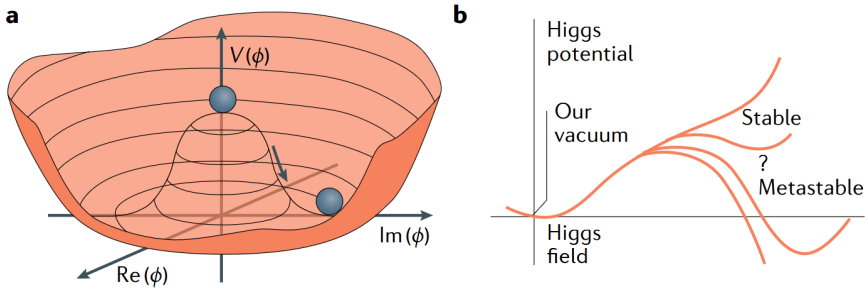

Fig. 2.4. The Higgs potential in a complex singlet case showing a potential minimum after the spontaneous symmetry breaking (left). Loop corrections can introduce an additional minimum to the Higgs potential, creating a potential sign change (right). Image source: [72].

The so-called "Mexican hat" shape of V in a simplified case of a complex singlet with two degrees of freedom is drawn in Fig. 2.4. A rotation symmetry by a phase $e^{i\alpha}$ is seen. With $\mu > 0$ and $\lambda > 0$, the potential has a minimum for non-zero field values. Since ϕ in general is a complex doublet, it has four degrees of freedom and thus the potential has four dimensions. The physical Higgs doublet field is four dimensional and can be imagined as an extension of this potential into four dimensions. Despite being invariant under $SU(2)$ the non-zero minimum requires for the ground state to take an arbitrary minimum. Thus the ground state is not symmetric under $SU(2)$, while V itself it.

Such a concept, when $\mathcal{L}$ is symmetric under a specific symmetry but not the ground state of the system, is called the spontaneous symmetry breaking. This is in contrast to adding an explicit symmetry-breaking term to $\mathcal{L}$. According to current estimates, the symmetry breaking took place in the early universe, when the average temperature of the universe was around 160 GeV [73].

After the spontaneous symmetry breaking the Higgs field can be written with only one arbitrary parameter as

$$\phi = 1/\sqrt{2} \begin{pmatrix} 0 \\ \nu \end{pmatrix}, \tag{2.29}$$

where ν is a non-vanishing vacuum expectation value and has units of mass. Goldstone's theorem states that whenever a spontaneous symmetry breaking occurs, one massless, spin-zero particle, Goldstone boson, per broken degree of freedom appears in the spectrum of possible excitations. In the case of the Higgs mechanism, for the three degrees of freedom that are broken, one separate Goldstone boson appears. Due to the local gauge invariance, three fields can always be removed or absorbed by applying the gauge variation $\phi \rightarrow \phi' = e^{\sigma^i/2 \cdot W^i}\phi$. These Goldstone bosons turn out to be absorbed in three of the initially massless bosons and provide the massless gauge bosons with mass. In other words, the degree of freedom of the Goldstone boson becomes a longitudinal component of the gauge bosons, which requires that the gauge bosons acquire mass.

The explicit mass terms in the Lagrangian can be seen if Eq. (2.29) the SM covariant derivative is inserted in Eq. (2.26). The acquired $W^{\pm}$ boson mass is $m_W = \nu\alpha_2/2$, the Z boson mass is $m_Z = 1/2\nu\sqrt{\alpha_1 + \alpha_2}$, and the photon mass is $m_\gamma = 0$. Although ν is a free parameter in the SM and thus needs to be measured, there is a fixed relation between the boson masses, $m_W/m_Z = \cos\theta_W$.

2.4.4. Fermion masses

The $\mathcal{L}_H$ term in Eq. (2.26) is responsible for the generation of the gauge boson masses but not the fermion masses. The Yukawa term

$$\mathcal{L}_Y = \overline{L}_i(y_e)_{ij}(e_R)_j\phi + \overline{U}_i(y_u)_{ij}(u_R)_j\phi_c + \overline{D}_i(y_d)_{ij}(d_R)_j\phi + h.c \tag{2.30}$$

generates the fermion masses, where y_e, y_u and y_d are 3×3 diagonal matrices, containing the couplings between generation i and j, $\phi_c = -i\sigma\phi^*$ and $h.c$ represents the complex conjugate to the term to the left of it. Expanding ϕ around the minimum as

$$\phi = 1/\sqrt{2} \begin{pmatrix} 0 \\ \nu + H(x) \end{pmatrix}, \tag{2.31}$$

inserting in Eq. (2.30) and expanding again gives terms like

$$(y_e)_{11}\nu/\sqrt{2}\overline{e}e + (y_e)_{11}/\sqrt{2}\overline{e}eH \equiv m_e\overline{e}e + \frac{m_e}{\nu}\overline{e}eH, \tag{2.32}$$

where the first term corresponds to the electron mass and the second term corresponds to the particle interaction with the Higgs particle, H. Thus, the interaction with H is proportional to the particle mass, scaled by ν. Particles not interacting with H, obtain no

mass. Moreover, inserting Eq. (2.31) in Eq. (2.26) provides terms for Higgs interactions with Gauge bosons and Higgs self-interactions.

The discovery of neutrino oscillation has revealed that neutrinos also have a nonzero mass [5], [6]. However, their masses are too small for the current experimental capabilities to detect. Neutrino masses are not accounted for in the SM. Theoretical models capable of including the neutrino masses include light Dirac neutrinos, light Majorana neutrinos (a Majorana particle is a fermion that is its own antiparticle) and the Seesaw mechanism. An analogue matrix to the CKM matrix exists to account for the neutrino mixing, called the Pontecorvo–Maki–Nakagawa–Sakata (PMNS) matrix. Neutrino oscillations enable CP violation also in the lepton sector, not only in the quark sector.

2.4.5. Allowed interaction vertices in the standard model

Expanding Eq. (2.22) yields kinetic terms describing the propagation of fermions and interaction terms. The kinetic terms consist of fields and their derivatives, and interaction terms consist of three or four different fields. An example of interaction term is the charged current

$$\frac{\alpha_2}{2}(\overline{\nu}\gamma^\mu e W_\mu^+ + \overline{e}\gamma^\mu \nu W_\mu^-) \quad \rightarrow \quad \text{ 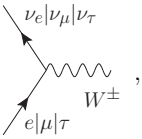 } \quad , \tag{2.33}$$

which connects $W^\pm$, charged lepton, and a corresponding ν.

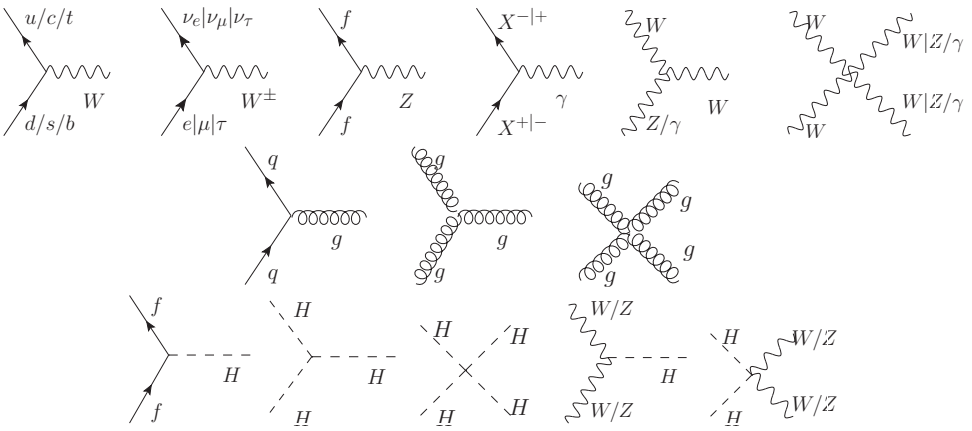

Fig. 2.5. The allowed interaction vertices of SM. The top row shows the vertices of the electroweak interaction. The middle row shows the strong interaction. The bottom row contains vertices of the interactions with Higgs. Here, f represents any fermion, and X represents any charged particle. In diagrams with multiple particle labels separated by '/', each particle can be chosen independently of the others, while for particle sets separated by '|', choices must be made consistently across the particle sets. For example, in the four-boson vertex, the valid diagrams are $WWWW$, $WWZZ$, $WW\gamma\gamma$, and $WWZ\gamma$.

The list of vertices allowed in the SM is shown in Fig. 2.5. Note that each vertex fulfils charge conservation as well as is required to conserve colour, spin, and angular momentum. The only particles that connect fermions of different generations are the W bosons. Fermions with the arrows in the opposite direction in time are interpreted as antifermions.

2.4.6. Renormalization and running coupling

Particles, like electrons, are surrounded by fields that constantly create and annihilate virtual particles. When an electron is probed by a scattering photon, the measured α_1 is screened by the virtual particle pairs around the electron arranged as dipoles. When the energy of the probe increases, the effect of screening decreases and thus α_s also increases. In the Feynman diagram picture, this equates to adding additional loops to the diagram propagators.

The integrals over the momenta in the loops contain divergences. Since actual couplings can be measured and are finite, these divergences must be removed, which is done by introducing an UV cutoff. This introduces the dependence of the coupling on the energy scale, i.e. the so-called running of the coupling. For α_1 the dependence on the energy scale, Q at one-loop level (NLO) is as

$$\alpha_1(Q) = \frac{\alpha_1(\mu_R^2)}{(1 - N\frac{\alpha_1(\mu_R^2)}{3\pi^2}\ln\frac{Q^2}{\mu_R^2})}, \tag{2.34}$$

with

$$N = n_l + 3\left(\frac{2}{3}\right)^2 n_u + 3\left(\frac{1}{3}\right)^2 n_d, \tag{2.35}$$

where μ_R is the renormalization scale, i.e. the scale at which the coupling is measured, while n_l, n_u, and n_d are the number of leptons, up-type, and down-type quarks with mass lower than Q.

For α_s the dependence is as follows

$$\alpha_\mathrm{s}(Q) = \frac{\alpha_\mathrm{s}(\mu_R^2)}{(1 + \frac{\alpha_\mathrm{s}(\mu_R^2)}{3\pi^2}(\frac{11}{3}C_A - \frac{4}{3}T_R n_f)\ln\frac{Q^2}{\mu_R^2})}, \tag{2.36}$$

where n_f is the number of fermions with masses lower than Q, $C_A = \sum_a t^a t^a = 3$, and $T_R = Tr[t^a t^b] = 1/2$. In general, $C_A = N_c$ and $C_F = \frac{N_c^2-1}{2N_c}$, where $N_c = 3$ is the number of colours, represent the Casimir operators of the fundamental (corresponding to quarks) and adjoint (corresponding to gluons) representation of $SU(3)$, respectively. Their meaning can be interpreted as the absolute value of the gluon and quark "colour charges".

It can be seen that α_1 increases with Q. The energy scale at which the magnitude of α_1 diverges is called the Landau pole. For α_s, the behaviour is the opposite. At large Q α_s becomes small, enabling asymptotic freedom, where quarks and gluons (collectively called

partons) at large energies behave like free particles, while at low Q due to large value of α_s and due to linear increase of the potential between colour charged particles, quarks are confined in colour neutral hadrons. The process in which free partons from high-energy collision turn into hadrons is called hadronization. At low energies α_s increases and perturbation theory breaks down. The scale $\Lambda \approx \mathcal{O}(100\,\mathrm{MeV})$ at which α_s diverges is called confinement scale. For α_2, the behaviour is similar to α_1. Some BSM theories such as minimally supersymmetric standard model (MSSM)[74] can predict the unification of the three coupling constants, i.e. that at large energy they converge at the same value.

This treatment of the infinities is called renormalisation and introduces a dependence on μ_R^2. Physical quantities should be independent of the choice of μ_R^2. This introduces a renormalization group equation

$$(-\frac{\partial}{\partial t} + \beta(\alpha_s)\frac{\partial}{\partial \alpha_s})R = 0, \tag{2.37}$$

with $\beta(\alpha_s) = \mu_R^2 \partial\alpha_s/\partial\mu_R^2$ and $t = \ln(Q^2/\mu^2)$. Conventionally, the value of α_s is presented at the scale m_Z^2, while the value of α_1 is presented at the scale of 0, where $\alpha_1(0) = \frac{1}{137}$.

Most theories that have nondimensional couplings can be renormalised. All forces in the SM are renormalizable, whereas gravity is not renormalizable. QFTs that are non-renormalizable can also be useful in physics, and common examples of those include the Fermi interaction of the weak decay, chiral field theory and the SM EFTs. The method for subtracting the divergences is not unique and depends on the renormalisation scheme. The scheme used in this section is the modified minimal subtraction ($\overline{\mathrm{MS}}$, pronounced "MS bar") scheme. In the next section, other schemes will be mentioned.

2.5. Top quark physics

The top quark is the heaviest particle in the SM. Due to the large mass of the mediators of the weak interaction compared to the massless gluons and due to $\alpha_s > \alpha_2$, strong interactions are usually preferred in the SM over the weak interactions. Hadronization starts to take place at distances similar to the proton size $R \sim R_p \sim 1\,\mathrm{GeV}^{-1} \sim 1\,\mathrm{fm}$, where after the last equality sign the value is converted to SI units [75]. This is of the same order as $1/\Lambda$. At distances $R \lesssim 1\,\mathrm{GeV}^{-1}$ the quarks behave as free particles, radiating quarks and gluons in a similar way to the quantum electrodynamics (QED) bremsstrahlung radiation for electrons. In contrast, the lifetime of the weak decay $t \to Wq$ depends on the quark mass as $\tau_Q \sim R_p(m_W/m_t)^3$ and due to the large mass of the top quark with $m_W/m_t \sim 1/2$, the weak decay becomes dominant. Due to the small non-orthogonal CKM matrix elements for the top quark, the decays to other than b quarks are suppressed, and thus the top quark almost always decays through $t \to Wb$. Although a two-top-quark state, called toponium, is expected to exist, it has not been discovered so far. In a similar way, the short decay time of the top quark ensures that other properties of

the top quark can be measured, such as entanglement [76]–[78] and charge asymmetry [79] in $t\bar{t}$ events.

Besides the properties above, the top quark mass m_t is important due to its entry in the higher-order corrections for the Higgs self-coupling, which for certain values of m_t and a Higgs boson mass m_H can cause a second minimum in the Higgs potential and thus make the universe unstable or metastable [80], [81]. The different cases of the stability of the Higgs potential are shown in Fig. 2.4. The currently measured values of m_t and m_H lie in the range where the universe is metastable. Another importance for the top is that the higher-order corrections in the SM require a relation between m_t, m_H, and m_W, which has been tested to be fulfilled within the standard deviations of the measured values [82]–[84].

At the LHC and in pp and e^+e^- colliders in general, the top quark is mostly generated in top quark-antiquark pairs $t\bar{t}$ as this way it does involve weak interaction in the top production unlike the single top production. An example of a Feynman diagram for the $t\bar{t}$ process is shown in Fig. 2.6, where the red lines show the hard process and the orange lines show the decays of the top quark. The dominant $t\bar{t}$ production process is the gluon-gluon fusion $gg \to t\bar{t}$, although it can also be produced by other means, such as quark-antiquark annihilation. After the top decay, the W boson can undergo a leptonic $W \to l\nu$ or hadronic decay $W \to qq'$, where the quarks hadronize and produce a collimated spray of particles, called jets.

The $t\bar{t}$ events are classified according to the decays of each of the W bosons, into all-hadronic, lepton+jets and dilepton decay channels, if, respectively, both, one or none of the W bosons decay hadronically. The typical decay channel used in precision measurements is the lepton+jets channel. The signature of this channel, namely, the presence of one high-energetic (hard) charged lepton, large missing transverse momentum, $p_{\mathrm{T}}^{\mathrm{miss}}$[6], and at least four jets, out of which two can be further identified as bottom jets (b tagged), ensures good event purity (number of signal events over the total number of events). On the other hand, good precision in the measurement can be achieved using the hadronically decaying top quark.

2.5.1. Renormalization and the top quark mass definition

The weak decay of the top quark enables precise measurements of m_t from its decay products, unlike for other quarks, where the mass has to be inferred from the hadron properties by methods like lattice QCD or chiral perturbation theory. In this thesis, the top quark mass and the mass difference between the top quark and antiquark are obtained by comparison of kinematic distributions in the data and simulation, where the latter is obtained using different top-quark mass parameters. Thus, the experimental result

[6]The missing transverse momentum vector $\vec{p}_{\mathrm{T}}^{\mathrm{miss}}$ is defined as the projection onto the plane perpendicular to the beam axis of the negative vector sum of the momenta of all reconstructed the objects in an event. Its magnitude is referred to as $p_{\mathrm{T}}^{\mathrm{miss}}$.

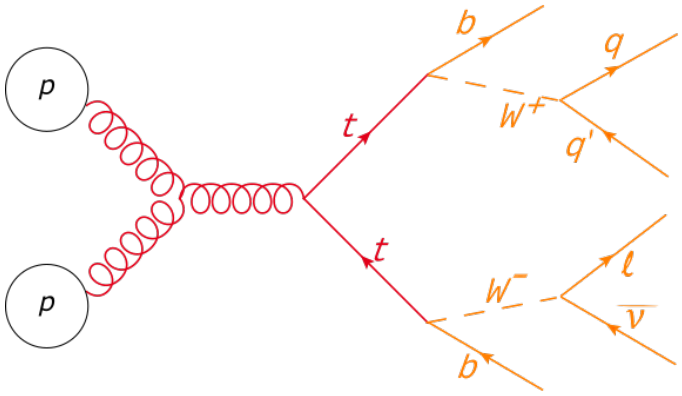

Fig. 2.6. An example of a Feynman diagram showing a top quark pair production with the gluon fusion and the lepton+jets decay channel.

corresponds to the optimal top-quark mass parameter used in simulation that describes the data best, and is often called "MC mass". By m_t we denote the top quark MC mass and correspondingly the top mass difference as obtained from two MC masses $\Delta m_t = m_t - m_{\bar{t}}$. It is theoretically debated how m_t corresponds to a theoretically well-defined mass scheme. A comprehensive explanation of this issue is provided, for instance, in [21], [85], [86], and here we merely present a concise summary of the essential points.

Fermion masses enter the SM Lagrangian through coupling with the Higgs boson in Eq. (2.30). However, due to loop contributions in the fermion propagator such as

$$\frac{i}{p^2 - m^2} = \longrightarrow \rightarrow \longrightarrow + \;\; \overset{\sim}{\longrightarrow} \;\; + \;\; \overset{\sim}{\longrightarrow}\overset{\sim}{\longrightarrow} \;\; + \ldots \equiv \frac{i}{p^2 - (m_t^p)^2} \tag{2.38}$$

the so-called "bare" mass becomes infinite and requires renormalisation. The divergences arising from the loop contributions can be fully absorbed by redefining the top-quark mass. For leptons, typically the mass is redefined to correspond to the pole of the propagator, as is done behind the last equality sign in Eq. (2.38). This is referred to as the pole mass m_t^p, and the renormalisation scheme used is called the on-shell scheme. Unlike the $\overline{\text{MS}}$ renormalisation scheme which in Section 2.4.5 caused the coupling constant to run, m_t^p remains constant across different energy scales.

Since quarks do not exist as free particles at long distances, applying this scheme for quarks requires IR QCD corrections that are $\mathcal{O}(\Lambda)$. These corrections, called renormalons, are not easily calculable. Thus, for quarks, typically the $\overline{\text{MS}}$ scheme is used, where the top quark obtains a scale dependence $\overline{m} = \overline{m}(\mu)$. The scale dependence of $\overline{m}(\mu)$ is described by the same renormalisation group equation as in Eq. (2.37). Typically, the mass is self-consistently evaluated on the scale of the mass itself $\overline{m}(\overline{m})$. The difference between m_t^p and $\overline{m}_t$ has been calculated using the perturbative QCD up to N^4LO to be $\mathcal{O}(10)\,\text{GeV}$ at the scale of $m_t = 170\,\text{GeV}$ [87].

It is argued that in the direct approaches, i.e. measuring m_t from kinematic reconstruction, m_t contains corrections of the unknown size corresponding to missing higher than LO terms in the parton shower simulation and non-perturbative corrections of undetermined size, and thus the correspondence of m_t to any theoretically well-defined renormalisation scheme is unknown. Other renormalisation schemes, such as the MSR scheme, have been shown to approach m_t at low scales [88]–[90]. In addition, the difference between m_t and m_t^p has been calculated to be 350 MeV to 600 MeV using different event generators. This shift is close to the limits of the current precision measurements, e.g. 330 MeV uncertainty in [91] and 370 MeV in [92].

Alternative experimental approaches include using $t\bar{t}$ cross-section measurements [93], $t\bar{t}$ events involving an additional jet ($t\bar{t}$ + jet) [94], and $t\bar{t}$ events with Lorentz-boosted top quarks, where the top quark is reconstructed as a single large-radius jet [95], which are sensitive to m_t^{pole} as they involve calculation available beyond the LO. However, currently these measurements suffer from uncertainties that are greater than 1 GeV and thus significantly larger than in direct measurements.

Irrespective of the chosen mass definition, the impact of the absent perturbative and non-perturbative corrections is expected to be equivalent for both the top quark and the top antiquark, largely leading to cancellation in Δm_t. Consequently, the measurement of Δm_t in this thesis is performed using the direct method, as it has the largest sensitivity to the observable top-quark mass difference regardless of the specific interpretation of the top quark mass.

2.6. Summary

We have thus shown how imposing symmetries in Table 2.1 in the QFT leads to the SM. It is not a priori known why these are the exact symmetries that describe the world we see and if the strategy of looking for more symmetries in physics will continue giving clues to physicists how to describe the BSM physics. Theories like supersymmetry SUSY and grand unification theory (GUT) seem to continuously fail the test of modern experimental particle physics. Still, the remarkable success of the SM and its description by the gauge symmetries seems to hold firm, as shown by, e.g. Fig. 2.2 and consistency checks such as the electroweak fit.

3. MONTE CARLO SIMULATION

To test our understanding of the SM, experimental results are compared with numerical ones, typically obtained using MC techniques. As the experimental precision improves, the numerical precision must also be improved to achieve sufficient sensitivity for detecting any deviations from the SM or signals of New Physics. This drives the continuous development of high-energy physics (HEP) event generators.

In general, the objective of MC generators is to predict an expectation value of an observable, O. Typically, this is a count of events that are observed in a given detector acceptance. Mathematically, it is equivalent to evaluating an integral

$$\langle O \rangle = \int d\phi_n \frac{d\sigma_{A,B\to n}}{d\phi_n} O(\phi_n), \tag{3.1}$$

where the integral runs over, ϕ_n, the phase space of n final-state particles, $\frac{d\sigma_{A,B\to n}}{d\phi_n}$ is the differential cross section for initial state particles A and B to produce final state n, and $O(\phi_n)$ is the value of the observable at the given phase space point.

Due to the large number of final-state particles in HEP events, the integral in Eq. (3.1) becomes highly dimensional. In such high-dimension cases, the MC sampling techniques become more advantageous than other numerical techniques for estimating integrals. This advantage arises because the uncertainty in MC methods scales with the number of sample points, n, as $\Delta_{MC} \approx n^{-1/2}$, which is independent of the number of dimensions. In contrast, other typical sampling methods exhibit worse scaling with the number of dimensions such as, for instance, the trapezoidal method having $\Delta_{trapez} \approx n^{-2/d}$.

To estimate Eq. (3.1) by MC generators, the task is to efficiently sample the phase space $d\phi_n$ and to evaluate $\frac{d\sigma}{d\phi_n}$. In general, $\frac{d\sigma}{d\phi_n}$ is challenging to calculate as it involves both perturbative and non-perturbative physics at different scales and a large number of particles. However, the process can be factorised into regimes with scales larger than the confinement scale $\Lambda \approx 100\,\text{MeV}$, which can be perturbatively calculated, and regimes with scales lower than Λ, where α_s is large and particles interact non-perturbatively. These regimes are linked by evolutionary processes that can be calculated from perturbative QCD. In the following, Sections 3.1 to 3.5 provide an overview of different stages of MC event generation. The general principles are summarised from reviews in [96]–[99], while to describe the current challenges in MC generators, we refer to [100]. Subsequently, we introduce some particular event generators, paying greater attention to the SHERPA event generator [101]. Finally, Section 3.7 presents the work of the generation and validation of a common CMS-ATLAS $t\bar{t}$ sample generated using SHERPA conducted by the author of this Thesis.

3.1. Factorisation and hard process generation

Protons, being hadrons, are composite particles with a complicated time-dependent structure where virtual partons are constantly being emitted and absorbed. However, since momentum transfer in hard interactions is large $Q \gg \Lambda$, these interactions occur on time scales much shorter than those of soft interactions, i.e. $1/Q \ll 1/\Lambda$. In this picture, partons inside protons can be viewed as "frozen" on the time scales of the hard interactions. Consequently, the cross section for $p_1 p_2 \to n$ can be factorised as follows

$$d\sigma_{p_1,p_2\to n} = \sum_{a,b} \int_0^1 dx_a dx_b \int f_a^{p_1}(x_a,\mu_F) f_b^{p_2}(x_b,\mu_F) d\hat{\sigma}_{ab\to n}(\mu_F,\mu_R), \tag{3.2}$$

where $d\hat{\sigma}_{ab\to n}(\mu_F,\mu_R)$ is the parton level cross section for the process where the partons a and b in the protons produce the final state n and f_a^p is the parton distribution function (PDF), which depends on the momentum fraction of a with respect to p, denoted by x and on the factorisation scale, μ_F. In this way, the new (non-physical) scale μ_F separates the hard parton-parton collision from the soft processes. Exactly as with the renormalisation scale μ_R introduced in Section 2.5.1, μ_F is introduced to absorb the soft and collinear divergences. The physical cross section should not depend on the choice of μ_F and μ_R. This is the so-called renormalisation group invariance. However, since event generators evaluate observables up to a limited perturbative order, the scale choice does impact the result. Scale variations can help estimate the uncertainty caused by the missing higher-order corrections. Scale variations are usually performed in the so-called 7-point variation scheme where each μ_F and μ_R are independently varied by factors of 2 and 1/2, except for the case when both μ_F and μ_R are varied in the opposite direction. The choice of μ_R and μ_F is usually provided by theorists for a specific process, but for an example of the s-channel resonance of mass M, a suitable choice is $M^2 = \mu_R^2 = \mu_F^2$.

PDFs at LO of α_s describe the probability that a given parton carries a momentum fraction of the proton between x and $x + dx$. At all orders of α_s, PDFs are described by sets of rules, including a rule that the sum of a PDF over all flavours and over all x has to equal the total beam momentum, that is, $\sum_a \int_0^1 dx\ x\ f_a^p(x,\mu_F) = 1$, and sum rules, $\int_0^1 dx\,(f_a^p(x,\mu)F) - \bar{f}_a^p(x,\mu_F)) = n_a$, where for protons $n_a = 1$ (2) for down (up) and 0 for the rest of the quarks. Since PDFs implicitly hide the soft physics inside them, they cannot be calculated from the first principles but are fitted from data at some scale. Nevertheless, the energy scale dependence of the PDFs is calculable in perturbation theory using the so-called DGLAP evolution [102]–[104].

Due to different sets of data available for the PDF fits, as well as different statistical frameworks (and different parameterisations) and theoretical inputs (NLO or NNLO DGLAP evolution [105], α_s value used, heavy-quark scheme used [106]), several different PDF fits are available carried out by different groups. A set of the PDFs for each flavour and the corresponding uncertainties is called a PDF set. For accessing and storing the

common PDF sets, a framework called LHAPDF is commonly used [107]. Some of the commonly used PDF sets in the LHC experiments in Run 2 include `NNPDF3.1`, using NNLO at α_s for data and theoretical input [106], [108], `CT14` at NNLO [109], `MMHT2014` at NNLO (68 %CL) [110] and `PDF4LHC15` at NNLO [106]. The uncertainties are estimated by varying independent sets of parameters (eigenvectors) found by diagonalisation of the Hessian matrix so that $\chi^2 s$ of the fit would increase corresponding to 68 % CL (90 % CL in the case of CT14).

The hard process cross section in Eq. (3.2) can be computed from the absolute square of the ME, $|\mathcal{M}|^2$, expressed as

$$d\hat{\sigma}_{ab\to n} = \frac{1}{2\hat{s}}|\mathcal{M}_{ab\to n}|^2 d\phi_n, \tag{3.3}$$

where $\hat{s} = (p_a + p_b)^2$ is the centre of mass energy squared. Eq. (3.3) is calculated at fixed orders of α_s. Imagine that one wants to obtain the cross section for the final state F that can be a $t\bar{t}$ pair or an n-jet event, for example. To obtain higher order corrections, one has to add terms with additional final-state partons (legs) leading to jets, and with additional loops, so schematically it is expressed as

$$d\hat{\sigma}_F = \sum_{k=0}^{\text{legs}} d\Phi_{F+k} \left| \sum_{l=0}^{\text{loops}} \mathcal{M}_{F+k}^{(l)} \right|^2 . \tag{3.4}$$

To obtain a full N^nLO calculation for the final state F, it is necessary to sum up all the contribution with $k + l \leq n$. As mentioned in Section 2.4.5, IR and UV divergances from real and virtual corrections should cancel each other due to the KLN theorem. However, the exact procedure for achieving this cancellation is not unique. Common examples include Catani-Seymour (CS) dipole subtraction [111], [112] used, e.g. in the CS-shower in SHERPA and the DIRE [113]–[115] and HERWIG 7 [116] showers, antennae formalisms [117] in VINCIA [118], Frixione-Kunszt-Signer (FKS) subtraction [119] in POWHEG [120], [121] and MC@NLO [122].

While adding an additional loop and an additional leg helps to reach the NLO accuracy for the F production, the $F+1$ production that has been added to the calculation still only has LO accuracy. To reach the NLO accuracy for the $F+1$ production, it requires the 2-jet diagram and the 1-loop + 1-jet diagram. This also requires phase-space cuts, since the divergences of the two soft jets will not be removed. Another common confusion among experimental particle physicists is that the one-loop contribution in Eq. (3.4) is a mixed term $2\text{Re}\left|\mathcal{M}_0^{(1)}\mathcal{M}_0^{(0)*}\right|$, not the one-loop ME squared $\left|\mathcal{M}_0^{(1)}\right|^2$. The latter contributes to the NNLO coefficient. The LO, diagram calculations have since long been automated. Some of the hard process generators have also automated the NLO calculation to be discussed further in Section 3.3.

Although factorisation is proven only for simple processes like deep inelastic scattering (DIS) or Drell-Yan (DY), it is assumed to work in all hadronic collisions. Moreover, further

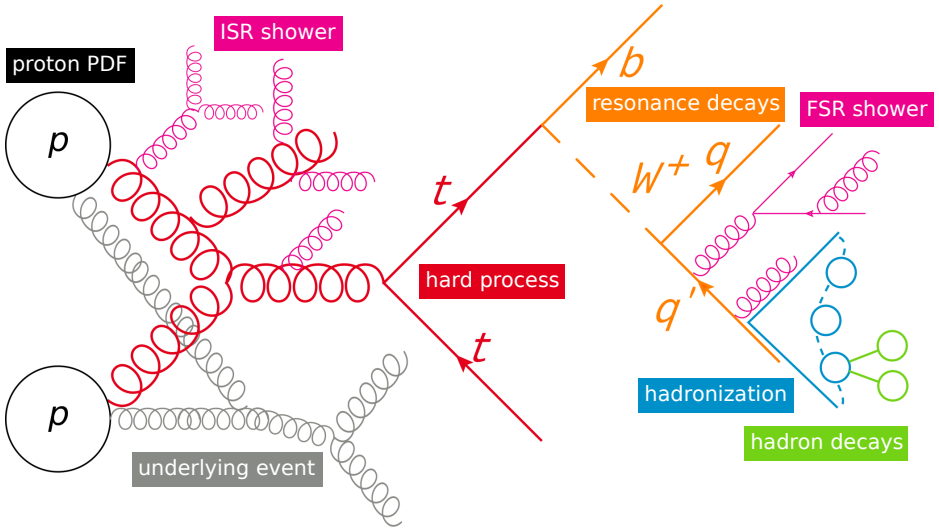

Fig. 3.1. A schematic depiction of the several steps required for a generation of a top quark pair event. ISR and FSR stand for initial-state radiation and final-state radiation, respectively [123].

evolution of the hard partons created in hadron collisions to stable partons is also assumed to factorise, like

$$\begin{aligned} \mathrm{d}P(\text{partons} \to \text{hadrons}) = \; & \mathrm{d}P(\text{resonance decays}) && [\Gamma > \Lambda] \\ & \times \mathrm{d}P(\text{parton showers}) && [\text{TeV} \to \Lambda] \\ & \times \mathrm{d}P(\text{hadronization}) && [\sim \Lambda] \\ & \times \mathrm{d}P(\text{hadronic decays}) && [\mathcal{O}(\text{MeV})]. \end{aligned}$$

Resonance decays occur if the heavy object, such as the top quark, has $\Gamma > \Lambda$, where Γ is the decay width of the heavy object. The transition takes place at the scale Λ. To illustrate all the steps of the event generation up to the level of stable particles that sequentially enter the detector simulation, the diagram $t\bar{t}$ shown in Fig. 2.6 should be schematically appended to what is shown in Fig. 3.1. In this section, the hard process generation and proton PDFs were already explained. In the following sections, we describe parton showers, hadronization, underlying event (UE), and hadronic decays.

3.2. Parton showers

The use of fixed-order calculations allows for the computation of cross sections for processes with up to a few hard partons. However, real events contain jets with a large number of soft particles, highly exceeding the capabilities of the current fixed-order generators. Calculating these requires the resummation of perturbative corrections of all orders

of α_s. This resummation is usually approximated by an iterative algorithm called parton showers. Assuming a cross section for some hard process producing several partons with a flavour (gluon, quark or antiquark) i is σ_0, the cross section for this process to be accompanied by a parton j with momentum fraction z is given by

$$d\sigma \approx \sum_{\text{partons},i} \frac{\alpha_s}{2\pi} \frac{d\theta^2}{\theta^2} dz P_{ji}(z,\phi) d\phi, \tag{3.5}$$

where θ is the opening angle between the partons i and j and $P_{ji}(z,\phi)$ are the Altarelli-Parisi splitting functions

$$\begin{aligned} Pqq(z) &= C_F \frac{1+z^2}{1-z}, & Pgg(z) &= C_A \frac{z^4+1+(1-z)^4}{z(1-z)}, \\ Pgq(z) &= C_F \frac{1+(1-z)^2}{z}, & Pqg(z) &= T_R(z^2+(1-z)^2). \end{aligned} \tag{3.6}$$

Two types of divergences appear visible in Eq. (3.5) and Eq. (3.6), a collinear divergence, where $\theta \to 0$ and a soft divergence, where $z \to 0$ or $z \to 1$. These divergences are usually dealt with by introducing a cutoff Q_0 and instead of Eq. (3.5), describing the probability for a splitting to occur, looking at the probability to have no branchings from the starting scale Q until some scale q. This probability is described by the Sudakov form factor

$$\Delta_i(Q^2,q^2) = \exp\left\{ -\int_{q^2}^{Q^2} \frac{dk^2}{k^2} \frac{\alpha_s}{2\pi} \int_{\frac{Q^2}{k^2}}^{\frac{1-Q^2}{k^2}} dz\, P_{ji}(z) \right\}. \tag{3.7}$$

Practically, in parton showers an MC chain is implemented, where a random number between 0 and 1 is drawn and Eq. (3.7) is solved for q^2. If q^2 is above Q_0^2 a branching is generated at the scale q^2 and the chain is continued from the new scale q^2. Otherwise, if $Q_0^2 > q^2$, the chain is stopped.

In the above example, the evolution parameter is taken as the virtuality of the parton, q^2. However, several different approaches are possible. In the angular-ordered or coherence-improved showers, the evolution parameter is chosen to be the angle between the initial and the radiated parton. This approach is based on QCD coherence. For instance, consider a process $q \to g_1 q \to g_1 q g_2$. The amplitude for such a process is the sum of amplitudes where the new g_2 is attached to each of the two partons. However, if the radiation is of a wider angle than the angle between g_1 and q, g_2 cannot distinguish the two partons and effectively "sees" the two partons as one object, i.e. it behaves like a coherent pair. The explicit calculation shows that the two amplitudes interfere destructively, leaving only a contribution that is equal to the gluon being radiated from the initial quark. Conversely, if the radiation is of a narrow angle, the interference is negligible, and the total cross section can be calculated as a sum of individual radiation cross sections. A prominent example of a coherence-improved parton shower is the one inherent to HERWIG 7 event generator (see also Section 3.5.2).

In another approach to parton showers, the ordering variable is the parton p_T and the partons are emitted from a colour dipole that stretches between a colour-anticolour pair. The dipole shower allows for the energy conservation at each splitting, unlike the coherent showers where the energy conservation needs to be restored by reshuffling the momenta of the partons when the parton shower algorithm is done. The dipole approach is used in the SHERPA, VINCIA parton showers, while PYTHIA 8 [124], [125] utilises a hybrid shower, combining collinear splitting kernels with dipole kinematics.

The parton shower described above is the so-called final-state radiation (FSR) added on the final-state coloured particles exiting the hard process and resonance decays. However, the initial-state partons and proton remnants also radiate, creating initial-state radiation (ISR). Running the parton showers on the initial-state partons is inefficient because most of the resulting partons have low momenta and do not participate in the hard process. Thus, a so-called backward evolution is performed on the initial states of the hard process: one generates the probability distribution that the parton at the given evolution scale and momentum fraction has come from another parton at lower evolution scale and a higher momentum fraction.

Typically, parton shower uncertainties are estimated by varying the value of α_s for μ_R and μ_F using the prescription in [126]. However, since only leading logartihmic (LL) showers are available, these variations are not guaranteed to cover the difference to the true data [127], [128]. Parton showers in a broad picture resum terms like $\alpha_s^n \sum_{i=1}^{n+1} c_i L^i$, where L is a large logarithm of a ratio of two disparate scales, c_i is a process-dependent coefficient and n is the perturbative order. Most standard dipole showers used in general-purpose MC generators resum terms proportional to $\alpha_s^n L^{n+1}$ corresponding to LL accuracy, while next-to-LL (NLL) prediction by adding terms, like $\alpha_s^n L^n$ (called single-logarithmic terms) also becomes relevant for scales of corresponding to the W and H boson [129], [130].

Recently, progress has been made in obtaining NLL- and even NNLL-precise showers [129], [130], but these are currently only available for specific, mostly colourless initial and final states in processes like vector-boson fusion and for global event-shape observables. Angular-ordered showers provide full-colour NLL accuracy for global observables, but care must be taken when reinterpreting the ordering variable [131], [132]. Currently, a typical way of estimating parton shower uncertainty is by comparing predictions of a dipole and angular-ordered showers like PYTHIA 8 and HERWIG 7, respectively[7], where large discrepancies between generator predictions translate into large uncertainties. This method is used, for instance, in Section 6.4.4 in obtaining the flavour uncertainty in CMS.

Dipole showers usually also act in the large-N_c limit, discarding the interference between different colour states that are suppressed by $1/N_c^2$. in the large-N_c limit, the colour state structure of the shower is usually expressed in the so-called colour-flow basis, where

[7] PYTHIA 8 and HERWIG 7 comparison also presents a comparison of the hadronization models and the UE.

one connects the partons in the Feynman diagram in all the possible colour combinations and assigns two colours to gluons.

It should be noted that both coherent and dipole showers are approximations, and the picture in which partons are emitted in chains is not what happens at the fundamental level. Instead, an interference of all possible amplitudes must be summed. Still, it is rather surprising that such perturbative calculations can be described by subsequent splittings modelled classically. Another remark is that the starting condition of the parton shower is not Lorentz invariant, nor are terms such as the initial- and final-state showers. However, it is shown that the final result of the shower is always Lorentz invariant [133].

3.3. Matching and merging

Fixed-order calculations provide the best description of well separated high-p_T jets while parton showers excel at generating a large number of soft jets. These two regimes must be merged to avoid the double counting of terms and to provide the correct cross sections for processes. Matching is the procedure where a fixed-order (usually LO or NLO) process for F+0 jets that has been supplemented with a parton shower is combined with a fixed-order F+1 jet, also supplemented with a parton shower. Some of the most common methods for NLO matching are MC@NLO and POWHEG, which are based on the subtraction method. These methods usually lead to events with negative weights, reducing the statistical efficiency of the generator. The main issue with negatively-weighted events is the requirement to run the computationally intensive detector simulation on a larger number of events if the events with negative weights are present. For MC@NLO, the number of negative weights is around 10 %. The POWHEG method was created to mitigate the issue of negative weights, although for some processes events with negative weights may still be present. While MC@NLO [122] is automated to work with any SM and BSM process for which the user can write a so-called UFO file [134], POWHEG method has only been implemented for a limited number of (mostly SM) processes.

Other methods for reducing the number of negative weights exist. An example is the MC@NLO-Δ method [135]. This method allows folding, that is, averaging many triplets of variables associated with a radiated particle at a given phase-space point. This increases the computational complexity, but brings about a several-fold decrease in the number of negative weights. Nevertheless, at the moment of writing this Thesis, MC@NLO-Δ has not been widely adopted. A KrkNLO method exists with no negative weights, however it has been rarely used and exists only for a few processes [136]. In addition, moving to NNLO brings further sources of negative weights which need to be considered.

Merging is a method allowing to shower and merge MEs with a different number of hard jets in a way that the number of jets does not overlap in the phase space. Thus, it enables the generation of multi-jet events with a high number of jets generated by the ME. Merging usually involves defining a merging scale above which all the radiation is

generated by the corresponding ME, while below the scale the radiation is generated by the parton shower. Methods of merging include CKKW [137], MLM [138] and CKKW-L [139] (for LO merging), where parton shower histories are constructed recursively. Since NLO ME changes the inclusive cross section of the merged calculation, NLO merging is more complicated, but methods like FxFx [140], UMEPS [141] and UN2LOPS [142] exist. Alternatively, the VINCIA parton shower allows to interatively include ME corrections.

3.4. Hadronization and underlying event

After the parton evolution down to the scale of $Q_0 \approx 1\,\text{GeV}$, hadronization begins, leading to confinement of partons into colour-neutral hadrons. Two typical classes of methods for hadronization are the Lund string [143], [144] and the cluster models [145], [146]. The difference between the two is that the former transitions into hadrons directly by breaking of strings (which is a classical interpretation of the potential energy flux created by the partons separating apart from each other), while the latter first groups partons into cluster objects and performs the gluon splittings, followed by the decays of the clusters.

When two quarks move further apart, a colour flux tube is stretched between them. In the Lund string model, this tube is assumed to be uniform along its length and thus the potential between the quarks is rising linearly, $V(r) = \kappa$, where $\kappa \approx 1\text{GeV/fm}$ is known from hadron spectroscopy. As the separation distance between quarks, r, increases, $V(r)$ stored in the string also increases until it reaches a point where it is sufficient to create a new pair of quarks and the string may break. Gluons that at leading colour ($N_C \to \infty$) can be seen as having two colour indices, are placed as kinks in the string with two colour lines attached to it. A closed gluon string is also possible with, e.g. ggg.

It turns out that there is no natural ordering in which the string breakage happens, so in practice the string algorithm goes iteratively from the ends up to the centre. The probability of string breakage taking place is governed by the fragmentation function $f(z) \sim \frac{1}{z}(1-z)^a \exp\left(-\frac{bm_\perp^2}{z}\right)$, where z is the fraction of the remaining lightcone momentum that the new hadron takes, $m_\perp$ is the transverse mass of the hadron, and a and b are free parameters [147]. For heavy quarks with mass m_Q, such as bottom and charm, the fragmentation function has to be modified to so-called Bowler-Lund (BL) function [148]

$$f(z) \sim \frac{1}{z^{a+bm_Q^w}}(1-z)^a \exp\left(-\frac{bm_\perp^2}{z}\right). \tag{3.8}$$

An additional Peterson parameterisation is often used as a systematic variation for b-jet fragmentation [149].

The method described above can only account for the creation of mesons. To generate baryons, antidiquark-diquark pairs in triplet-antitriplet representations are created when the string breaks, where a diquark is a two-quark state in a triplet or antitriplet representation. The most popular implementation of the string model is the one in PYTHIA 8.

The cluster model is based on the preconfinement property of the parton showers. Preconfinement is a property that in the evolution of the shower, partons and gluons become organised in lumps or colour clusters and the masses of these lumps are distributed independently of the starting scale of the shower Q being dependent only on the cut-off scale Q_0. Such clusters can then decay into colour-neutral hadrons without any need of large reshuffling of the momenta of the partons. In the cluster algorithm, the initial step is to enforce the splitting $g \to q\bar{q}$. Each colour line of the decayed quark or antiquark is connected to its anticolour partner. These partners are connected to form colour singlets. Since these partners are often close in the phase space, the created colour singlets are usually low mass. Further, the clusters undergo quasi-two-body decays, where their flavour, kinematics, and spins are taken into account. The production of heavy-flavour hadrons is highly suppressed by the limited cluster masses.

Such a cluster model contains no free parameters except for Q_0. Two widely used cluster hadronization models are implemented in HERWIG 7 and SHERPA, differing slightly in the treatment of large and small mass clusters. In particular, dealing with heavy clusters requires running a string-like initial stage, where these clusters would decay into lighter clusters.

The benefit of the string model over the cluster model is that it is collinear and infrared safe. The string model also in general has more accurate predictions at the cost of having a larger number of tunable parameters. The cluster models, on the other hand, have fewer tunable parameters. Despite their good descriptive power, neither model can describe collective phenomena, similar to those in heavy-ion collisions. Complicated events like these might also occur in dense proton-proton collisions, for example, through the spatial overlap of several strings or clusters.

A surprising fact is that both models turn out to have a non-violent nature, i.e. no large reshuffling of the momenta of coloured partons is required to create the confinement. However, both models rely on a number of tunable parameters and assumptions. There exist first-principles calculations of non-perturbative processes, where one example is lattice-QCD [150], [151]. However, they demand huge computational resources and are presently able to adequately compute only time-independent processes, such as the hadron masses and their form factors.

In the above, it was assumed that only one hard parton from each hadron interacts with each other. However, after the colliding partons are removed, the remnants of the hadrons continue to interact with each other, and there are other typically soft quark and gluon interactions in the hadron-hadron collision, referred as multi-parton interactions (MPI). This should not be confused with the so-called pileup (PU), which is a background coming from simultaneous collisions of additional hadrons in the same hadron beams, not those undergoing the hard interaction. MPI is usually described by models derived from the one originally proposed by Sjöstrand [100], [152], [153]. In rare cases, the momentum transfer of the secondary interaction can exceed 10 GeV, which is at the scale of interest

in LHC events. Double and even triple-parton scatterings have recently been observed and several additional searches have been proposed [154], [155].

Minimum bias (MB) events refer to events selected in a way that minimises selection bias, providing a "general" hadron-hadron event. In the experimental context, MB is obtained using a specific MB trigger that requires minimal conditions to be met, such as a small amount of energy in the detector or the detection of at least one particle. This thereby ensures that a wide and representative range of events is included. with typically low thresholds. MB consists mostly of soft-QCD but can rarely contain some hard process. In theoretical contexts, MB describes soft-QCD subprocesses within a given model. MB samples are used to describe PU and obtaining MB events is important for UE studies.

UE is the activity in the jets that is not associated with the hard-parton interaction. It consists of the beam remnants and MPI production in the event and is of constant $p_T/(d\phi \cdot d\eta)$, where ϕ and η are the azimuthal angle and the pseudorapidity of the jet[8], respectively. The UE is found to rise steeply with the centre-of-mass energy and for dijet events at $\sqrt{s} = 13\,\text{TeV}$ with the leading jet $p_\text{T} = 20\,\text{GeV}$ is found to be $p_T/(d\phi \cdot d\eta) \approx 1.5\,\text{GeV}$ in the region transverse to the main dijet activity [156]–[158]. An interesting effect, the called jet pedestal effect [159], [160], causes an access of the UE activity at events with high-p_T jets beyond that expected from MB events after subtracting PU. It is found to be caused by the dependence of the UE on the impact parameter, where events with high-p_T jets are biased towards having a smaller impact parameter [152].

Each event generator comes with a set of free parameters that are theoretically unknown and have to be obtained from the available data. Some parameters such as α_s are common to all the event generators, while others, such as the h_damp parameter specifying the dampening of the first emission in POWHEG and thus regulating the ME to parton shower merging, are specific to some event generators. PYTHIA 8 comes with the default Monash hadronization and UE tune obtained from the Large Electron–Positron Collider (LEP), e^+e^-, LHC, super proton synchrotron (SPS) and Tevatron data [161], while CMS and ATLAS have obtained tunes using newer LHC data. The most commonly used PYTHIA 8 tunes are CP5 [162] and A14 [163] tunes at CMS and ATLAS, respectively. If no custom tune is available, it is recommended to rely on the default values provided by the generator experts.

At the Tevatron, it was found that the average p_T of the particles, $\langle p_T \rangle$, was increasing with respect to the number of charged particles per event, N_{ch}, while expected to be constant [164], [165]. This was later confirmed at the LHC [156], [166]. To explain this and other discrepancies, colour reconnection (CR) is introduced, where colour fields before hadronization are rearranged, thereby altering the resulting hadronization pattern. The explanation of this is the string overlap, interference and gluon exchange that make the colour flow not straight-forward. Several models for CR exist, but the most common is

[8]Pseudorapidity is defined as $\eta = -\ln[\tan\left(\frac{\theta}{2}\right)]$, where θ is the angle between the particle three-momentum and the positive direction of the beam pipe.

by introducing the string length $\lambda \approx \ln\left(1 + \frac{(p_i+p_j}{C}\right)$, where C is a constant, the so-called QCD inspired model [167]. Given initial colour-connected pairs of partons (i,j) and (k,l), the pairs are reshuffled into (i,l) and (k,j) if $\Delta\lambda = \lambda_{ij} + \lambda_{kj} - \lambda_{il} - \lambda_{kl} < 0$ is fulfilled. Thus, CR can be imagined to minimise the length of the string. Shorter strings produce fewer hard hadrons, thus explaining the $\langle p_T \rangle (N_{ch})$ discrepancy.

3.5. Description of some commonly used MC generators

As discussed in the previous sections, generating HEP events is an intricate task with different shower and hadronization options. There are significant challenges such as the matching of NLO or NNLO fixed-order calculations to parton showers without adding events with negative weights. Additionally, there are challenges in obtaining better fixed-order precision in both QCD and QED fixed-order calculations or by adding more final-state particles, as well as improving parton shower precision. This explains the plethora of different event generators available. In this section, we discuss the most commonly used event generators in HEP, with a particular focus on the generators used for the modelling of top-quark events.

3.5.1. PYTHIA 8 and VINCIA

PYTHIA 8 [124], [125] is a general-purpose MC event generator, which means that it allows to generate the entire chain of event generation from ME up to the parton showers and hadronization, and to obtain stable final-state particles. It contains physics models for heavy-ion collisions (HIC) and γ-beams. The hallmark of PYTHIA 8 is its p_T-ordered parton shower and an implementation of the Lund string model for hadronization. Thus PYTHIA 8 has become the standard tool in CMS for HEP event generation. Nevertheless, the precision of PYTHIA 8 is only LO, so it is often used in conjunction with other ME generators that are matched or merged to the parton shower. For this, typically POWHEG (e.g. for $t\bar{t}$ modelling) or MC@NLO are used. Originally written in FORTRAN 77, PYTHIA underwent a major rewrite to C++ when introducing PYTHIA 8.100. The version used in CMS for Run 2 production is v.8.240.

A plugin exists to replace the default parton shower with an alternative p_T-ordered shower, VINCIA [118]. VINCIA is a dipole-antenna based parton shower which incorporates both collinear (DGLAP) and soft (eikonal) limits of QCD ME at LO. This is unlike the default PYTHIA 8 dipole shower which is only DGLAP-based. This treatment allows for the coherence of FSR to resonances (like t-b antenna) and permits to correctly estimate the recoils of the final-state radiation. In addition, the work is ongoing to add the initial-final and final-final recoils. In addition, as relevant for $t\bar{t}$ modelling, VINCIA implements new ways resonances (like t or W) are treated [168]. In PYTHIA 8, resonance decays are treated sequentially with the parton shower, i.e. the resonances are treated as stable until the showering of the born process finishes and then each of the resonances is showered

one by one. Since $\Gamma(t) \approx 1\,\text{GeV}$, due to finite width effects, this kind of treatment violates strong ordering. It can happen with resonances with high virtualities when the assigned mass of the resonance is different from the pole mass, and it can emit low-frequency radiation that normally would not be allowed. To properly treat this issue, VINCIA implements the interleaved approach in which the resonance decays are inserted into the overall event evolution. Another benefit of VINCIA, however, not included in the recent PYTHIA v8.3 [169], is that it allows one to estimate several uncertainties in the parton shower as weights.

The PYTHIA 8 collaboration is foreseeing work on NLO parton showers, resonance-aware matching, and NLO subtraction. With the merging scheme in [170], it was already possible to merge up to 9 hard jets in vector boson production events matched using the so-called VINCIA shower sectors. In addition to VINCIA, there is also another dipole shower interfaced to PYTHIA 8 called DIRE [113]–[115] that is also available in SHERPA.

3.5.2. HERWIG 7

HERWIG 7 [116], [171] is another general-purpose event generator that implements the cluster fragmentation model and is often used as an alternative to PYTHIA 8 for uncertainty estimates. It consists of a hard process generator that can generate any SM process at the NLO in QCD matched to Proton Synchrotron (PS) using both MC@NLO-like (subtractive) and POWHEG-like (multiplicative) schemes. The matchbox tool within HERWIG 7 allows for interfacing HERWIG 7 to a wide range of ME generators [172]. While its predecessor HERWIG ++ [173] only contained angular-ordered shower, HERWIG 7 also contains a p_T-ordered shower. Like PYTHIA 8, HERWIG 7 collaboration also has been working on improving the shower accuracy.

3.5.3. SHERPA

SHERPA [101] stands out as a highly modular general-purpose event generator written in C++ with interfaces to many external libraries or separate modules. It supports a wide range of ME generators, including BLACKHAT [174], MADLOOP [122], MCFM [175], OPENLOOPS [176], RECOLA [177], [178] alongside its own built-in ME generators AMEGIC [179] and COMIX [180], [181]. For parton showers, it allows users to switch between the Catani-Seymour dipole shower (CS-shower) [182] and a new reimplementation of a hybrid dipole-parton shower algorithm called DIRE [113], [183]. Both of the showers allow for QED photon emissions for some processes. For NLO matching SHERPA uses a variant of the MC@NLO method, while for some processes it uses the UN2LOPS method. SHERPA excels in merging MEs with large jet multiplicities. For instance, it can simulate h+jets production with up to 3 jets at NLO QCD and 5 jets at LO, while $t\bar{t}$ can be generated with up to one jet at NLO and 4 jets at LO. At the moment of writing this Thesis, other generators that can produce $t\bar{t}$ events with a large number of events

are MadGraph [122] with the MLM scheme [184] and MadGraph5_aMC@NLO [122] with the FxFx scheme [140] which can do up to 3 jets at LO and up to 2 jets at NLO respectively. For this reason, to calculate the large jet multiplicity events, the ATLAS collaboration often benefits from using SHERPA, whereas at CMS FxFx is preferred currently.

For any SM process, SHERPA allows for an automated subtraction of infrared divergences to achieve the NLO accuracy in QCD and an approximate NLO accuracy in electroweak (EW). The EW corrections appear as weights, facilitating the user to easily see their effect on the result. Although having its own cluster-based Ahadic fragmentation model, a very beneficial option in SHERPA is an interface to load PYTHIA 6 [9] libraries for string hadronization and hadron decays. This switch can be exploited to determine the hadronization uncertainty. For a precise description of heavy flavour generation (e.g. processes involving b quark), SHERPA has implemented a FONLL-like merging. This scheme merges in a consistent way the 5-flavour-scheme (5FS), where quarks are massless, and the 4-flavour-scheme (4FS), where b quarks are massive [185].

In methods like POWHEG or MC@NLO, it is common to store the list of particles produced by the fixed-order generator (LHE particles) in a common file format, LHE file, before it enters as input in the parton shower. Due to the high modularity within SHERPA and its several built-in modules, there is no need to split event generation into LHE files and then supply them to a shower; this process is integrated within SHERPA. The philosophy of SHERPA is to keep the event record as physical as possible and not include non-physical intermediate parton shower particles. SHERPA has been known for its CPU-consuming event generation. Nevertheless, recent efforts have led to around $\mathcal{O}(10)$ improvement of the computation speed at some event generation stages [100].

3.5.4. Current developments in top quark event generation

As mentioned in Section 2.5, the dominant process of the top production at the LHC is $t\bar{t}$, while the single top production is also observed. In many practical processes, the narrow-width approximation works well, i.e. it can be assumed that there is no interference between different physics processes. However, at NLO $t\bar{t}$ has a significant interference with the tW single top process. Methods like diagram subtraction and diagram removal exist to approximately compensate the interfering terms, but both show differences in some top decay observables. Using the new POWHEG bb4l tool [186] instead of the typically used hvq process within the POWHEG-Box-v2 programme [120], [121], enables the calculation of the full $t\bar{t}$ + single top correctly at NLO. However, bb4l is still being validated within CMS.

It is only partly true when it is said that the top quark does not hadronize. Just below the so-called threshold region of $2m_t \sim 375\,\text{GeV}$ a thus far unobserved bound state of top quark and antiquark called toponium is expected to be formed. The toponium contribu-

[9] Since SHERPA 3 it can also load PYTHIA 8 string model.

tion is significant in several measurements involving the $t\bar{t}$ two lepton decay channel, in particular measuring the $t\bar{t}$ spin correlations [187] or $t\bar{t}$ entanglement [77], [188]. There are known models for calculating only the pseudoscalar colour-singlet resonance contribution of the toponium [189], while the colour-octet contribution is still missing a usable theoretical model [190].

Further precision studies of m_t require moving up from NLO precision in α_s to NNLO. A potentially good tool for doing that is MiNNLO$_{PS}$ which allows for merging POWHEG simulation to a NNLO+parton shower generation of $t\bar{t}$ events [191], [192]. In addition, there are other potentially good options not mentioned in this section like GENEVA [193], [194].

A recent issue in the PYTHIA 8 event generator is regarding the options for the recoil of the $t \to Wb \to Wbg$ system, i.e. which particle to use as a recoiler for the radiation of g to preserve the conservation of momentum. The theoretically best approach where the recoil is created with respect to the top quark is not available in PYTHIA 8. The default option in the m_t measurements in CMS Run 1 was to use "recoilToColoured = on" option in PYTHIA 8. This option makes the radiation recoil from b, while in CMS Run 2, the default option "recoilToColoured = off" recoiled it from W. However, neither option is precise. PYTHIA 8 contains a new option that adds a correction to the recoil to W to match it more to the recoil to t. The effect on m_t appears to be 250 MeV, which is a significant contribution compared to the uncertainty of m_t ($\mathcal{O}(0.1 - 1\,\text{GeV})$) [195]. As explained in Section 3.5.1, a better option would be to use the VINCIA shower which includes these effects properly. However, for Run 2 measurements it was not yet possible.

3.5.5. Prospects in MC generators

To further improve MC generators, the community has to develop in several areas [100]. A frequent request from the experimental community is about optimizing computational speed. One direction seeing some momentum is using machine learning (ML) frameworks to improve the efficiency of unweighting [196], [197]. Additional improvement can be obtained by porting software modules to GPUs.

Conventionally, some of the variations for the MC samples are available to be computed on-the-fly, i.e. as alternative weights for each event without repeating the whole generation process. These include, e.g. parton shower scale variations [126] and, more recently, fragmentation weights [198]. However, for many physics parameters, including parton shower starting scale, CR schemes or the h_{damp} parameter in POWHEG this is not available. New weights are being implemented, for example, the merging scale in SHERPA [100]. As an alternative, SHERPA offers an option to store all coefficients in the HEPMC event format that offers arbitrary scale and PDF variations. To avoid the need to run the expensive detector simulation on the same samples but with a different choice of some parameter (e.g. h_{damp}), a neural network weight can be learnt [199], [200]. The weight

is obtained before the detector simulation but applied afterward. In this way, it is only necessary to run the detector simulation once.

The bottlenecks encountered during event generation vary among different generators. For fixed-order MC generators, such as MadGraph5_aMC@NLO, challenges may arise with NLO real emissions and with the accurate handling of the SU(3) colour algebra [201]. The latter difficulty comes due to the non-orthogonal and overcomplete character of trace or colour-flow bases used. A potential way to speed up this process is the adaptation of an orthogonal basis set using SU(N) group invariants [202], [203].

3.6. CMS detector simulation

The chain of physics event generation described in Sections 3.1 to 3.4 ends with stable final-state particles. In the CMS definition, these represent particles that are long-lived enough to reach the first parts of the tracker, i.e. their proper lifetime, τ, is such that $c\tau > 1$ cm. To be able to compare the MC data with the reconstructed collision data on the same footing, MC data have to go through the detector simulation and the same reconstruction that is performed on the real data. The summary of the steps performed on MC and collision data is shown in Fig. 3.2. Event generation does not always have to start from the general-purpose event generator or ME generator but can also start from a particle gun where single particles of specific energies are shot to the detector. Within the framework of the CMS software (cmssw), the output from each event generator is converted to the GEN data format stored in root [204] files. The SIM step goes through substeps of simulating the particle interactions with the Geant4 programme [205]–[207]. Then, the conversion of the simulated hits to the digital signal in the detector is done and the trigger simulation is performed. To store reconstructed events in CMS, custom data formats are used based on root trees. These include AOD (Analysis Object Data), MiniAOD and NanoAOD.

3.6.1. Data unfolding and RIVET tool

When comparing different MC generator versions, the computationally expensive SIM and RECO steps can be avoided if the collision data are unfolded to the particle level, that is, to stable final-state hadrons [209]. Unfolding uses an MC sample that has gone through the full reconstruction step. On this sample, a statistical model is fitted that learns to undo the smearing of the distributions performed by the detector, and this statistical model is applied to the reconstructed collision data, bringing them to the particle level. Comparing particle-level data with particle-level MC has the benefit that many different physics models can be compared without the need to run the full simulation chain. In addition, the unfolded data are detector-independent, and since they do not require specific knowledge about the experimental setup, they can be used by theorists or phenomenologists to compare several different MC models even long after the measurement itself is performed.

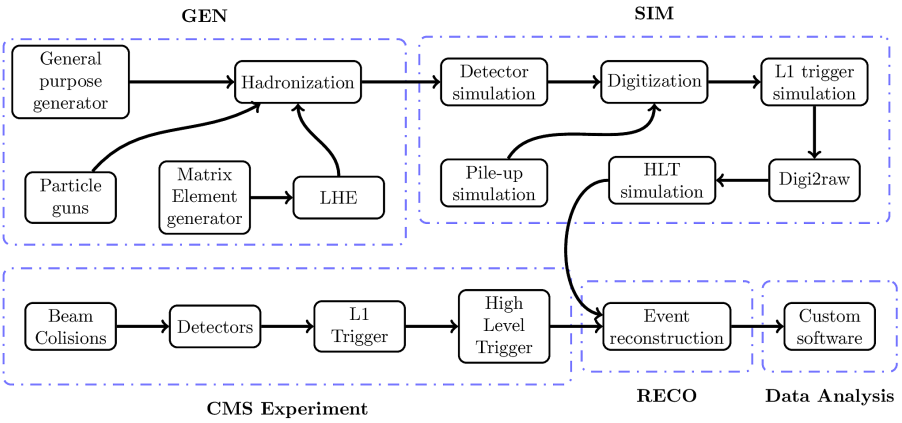

Fig. 3.2. Steps of the event simulation and event reconstruction within the CMSSW framework and their representative names [208].

RIVET is a tool that allows one to easily perform cuts and create distributions on particle-level data [210]. It stores many analyses (routines) that have been performed by CMS, ATLAS, and other experiments and allows to compare different MC results with the unfolded data. All analyses within CMS are recommended to create RIVET routines. However, for the top quark vs antiquark mass measurement, no unfolding is planned as the physics distributions are similar to the ones in the typical $t\bar{t}$ differential cross section measurements. The only exception is the $m_t/m_{\bar{t}}$ ratio.

3.7. A common SHERPA top-pair Monte-Carlo sample for ATLAS and CMS

The standard MC samples for $t\bar{t}$ production in both CMS and ATLAS collaborations use POWHEG-Box-v2 implementation of the hvq process interfaced with PYTHIA 8. For the latter, the parton shower, hadronization, and UE are tuned by each of the experiments, as discussed in Section 3.4. Some settings, including the α_s value, are different among the nominal ATLAS and CMS samples and lead to differences in the predictions. An effort within the LHC Top Working Group (LHCTopWG) [211] was dedicated to agreeing on common MC settings for both POWHEG+PYTHIA 8 and SHERPA. These settings are to be used in ATLAS+CMS combinations[10] and for comparison of measurements performed with slightly different event cuts, especially if one of the experiments sees a result that is not seen in the other.

The POWHEG+PYTHIA 8 MC sample is beneficial as it offers a small number of negative weights and the generation of $t\bar{t}$ at NLO in α_s. However, as discussed in Section 3.5.3, a

[10] In the recent LHC top mass combination [91], for example, it was necessary to assume 50 % correlation between the MC samples of CMS and ATLAS.

SHERPA $t\bar{t}$ MC can be a better choice because it allows one to switch between the Lund hadronization and cluster-based AHADIC model. Additionally, it allows the generation of a high multiplicity of hard jets and has implemented EW corrections as weights. Before the study described in this Thesis, there had been no centrally generated $t\bar{t}$ SHERPA sample in CMS available for hadronization studies and experimental measurements. In contrast, ATLAS had already produced a SHERPA $t\bar{t}$ sample. The ATLAS settings were deemed a suitable starting option for the common CMS-ATLAS SHERPA sample. The aim of the author of this Thesis was to generate a SHERPA sample within the CMSSW framework and validate that the sample produced is the same as the sample produced using the same settings within the ATLAS software, called ATHENA. In addition, the sample was also validated with respect to the unfolded data measured by ATLAS and CMS experiments at $\sqrt{s} = 13$ TeV during Run 2 of the LHC. A comparison was also made with respect to the POWHEG+PYTHIA 8 setup. Although it is possible to run a standalone SHERPA installation within CMSSW, interfacing it to the CMSSW framework has the benefit that further steps of the event simulation can be easily and consistently run as described in Section 3.6.

This section explains the results of the CMS-ATLAS MC $t\bar{t}$ sample project to which the author of this Thesis was the main contributor from the CMS side, i.e. the CMS-ATLAS common SHERPA sample. The results have been published by the ATLAS and CMS experiments in a common note [38], [39]. First, we show the settings, which were used for the common sample, after which we compare the obtained CMS and ATLAS SHERPA samples with each other and with the CMS and ATLAS unfolded data, as well as with the common POWHEG+PYTHIA 8 sample.

3.7.1. The common CMS-ATLAS SHERPA settings

For the SHERPA Common Settings, it was agreed to use the settings of an existing ATLAS sample produced with SHERPA v2.2.11. The main settings are summarised in Table 3.1 while a more detailed set of settings is shown in Table 3.2. Notably, the $m_t = 172.5\,\text{GeV}$, $m_W = 80.399\,\text{GeV}$ and $\alpha_s(m_Z) = 0.118$ were chosen, which are equal to the settings of the common POWHEG+PYTHIA 8. Note that the table uses the PDG MC particle numbering scheme (PDG id) to characterise the SM particles [212]. W boson width and other parameters characterising SM particles are taken as the world averages [57]. Note that for the bottom quark the given value is the pole mass, not the mass in the $\overline{\text{MS}}$ scheme. The PDF set used is `NNPDF30` [213]. The calculation is performed for up to one additional jet at NLO, and up to four additional jets in LO.

For `CSS_EVOLUTION_SCHEME` and `CSS_SCALE_SCHEME` the default values of 30 and 20 were chosen. The `CSS_EVOLUTION_SCHEME` parameter switches the ordering scheme of the default SHERPA CS parton shower. The options range from choosing the p_T ordered showers and the modified p_T ordered showers. Both can include or exclude parton masses. Since v.2.2.11, the new default option, `CSS_EVOLUTION_SCHEME=30`, corresponds to using

the p_T ordered shower while taking into account parton masses only for the $g \to gg$ splitting. `CSS_SCALE_SCHEME` specifies the way the CS shower finds the scale at which α_s for the shower splittings is evaluated. The default option up to SHERPA v.2.2.11 corresponded to α_s being evaluated at p_T of the splitting for the parton splittings and for the gluons at the virtuality of the gluon. `CSS_SCALE_SCHEME=20` performs the same scheme but for gluon splitting into a soft t-channel gluon evaluates α_s at the p_T of the gluon.

Table 3.1

Main proposed SHERPA Common Settings for $t\bar{t}$ production

Setting name	Setting description	Common SHERPA v1
	SHERPA version	v2.2.11
`MASS[6]`	top-quark mass [GeV]	`172.5`
`HDH_WIDTH`	top-quark width [GeV]	`1.32`
`QCUT`	CKKW merging cut [GeV]	`30`
`MASS[24]`	W boson mass [GeV]	`80.399`
`WIDTH[24]`	W boson width [GeV]	`2.085`
`MASS[5]`	b-quark mass [GeV]	`4.8`
`PDF`	PDF set to be used for proton beams	`NNPDF30_nnlo`
`USE_PDF_ALPHAS`	Whether to use the α_s evolution provided in LHAPDF	`1`
`AlphaS`	Value of α_s	`0.118`
`CSS_EVOLUTION_SCHEME`	Choice of evolution variable in the shower	`30`, modified p_T order incl. m_{parton} for $g \to qq$
`CSS_SCALE_SCHEME`	The choice of the scale at which α_s is evaluated	`20`
`MePS@NLO`	Multijet merging configuration	`0,1j@NLO + 2,3,4j@LO`

The additional parameters for the event generation are placed in Table 3.2. Among others, it specifies the options for the OpenLoops NLO ME generator used and the options for the tree ME generators. The typical 7-point μ_R and μ_F variations are used and the NLO EW corrections are evaluated as weights.

3.7.2. SHERPA sample validation

It was found impossible to implement the same random number scheme in ATHENA and CMSSW, thus the comparison needed to be made within the statistical uncertainties of each sample. For the CMS SHERPA sample, 95 million events, 40 million events and 20 million events were generated in $t\bar{t}$ dilepton, lepton+jets and all hadronic channels, respectively. The dilepton channel was made large to ensure small enough statistical uncertainties for the $\Delta\phi^{e\mu}$ measurement. This was compared to an ATLAS sample with 20 million, 40 million, and 20 million events in each of the decay channels.

The validation was run using two Rivet routines: `MC_TTBAR` (`ONELEP`) and `MC_FSPARTICLES`. The former is particularly used for comparing $t\bar{t}$ predictions and selects events with exactly one lepton (electron or muon) in the final state with $p_T > 30\,\text{GeV}$ and $|\eta| < 4.2$. Further, events are required to have $p_{\text{T}}^{miss} > 30\,\text{GeV}$. From all the final-state particles with $|\eta| < 4.2$, jets are clustered using the anti-kT algorithm with

Table 3.2

Additional proposed SHERPA Common Settings for $t\bar{t}$ production

Setting name	Setting description	Common SHERPA v1
EW_SCHEME	The set of SM EW parameters used	3
GF	Fermi constant	1.166397e-5
SHERPA_LDADD	Adding a user defined library	SherpaFusing
USERHOOK	Enabling of a user defined plug-in	Fusing_Fragmentation
FUSING_FRAGMENTATION_STORE_AS_WEIGHT	Choice between setting event weights or rejecting events	1
CORE_SCALE	Tag to define the core scale	QCD
EXCLUSIVE_CLUSTER_MODE	Tag for exclusive cluster mode	1
NLO_SUBTRACTION_SCHEME	Choice of modifying the splitting kernels	2
MAX_PROPER_LIFETIME	Maximum proper lifetime (in mm)	10.0
OVERWEIGHT_THRESHOLD	Maximum overweight taken into account	10
CSS_REWEIGHT	Whether to perform parton shower on-the-fly reweighting	1
REWEIGHT_SPLITTING_PDF_SCALES	Whether to perform PDF scale on-the-fly reweighting	1
REWEIGHT_SPLITTING_ALPHAS_SCALES	Whether to perform α_s scale on-the-fly reweighting	1
CSS_REWEIGHT_SCALE_CUTOFF	Tag to disable shower variations for emissions	5
HEPMC_INCLUDE_ME_ONLY_VARIATIONS	Tag for including only ME variation in the HEPMC output	1
SCALE_VARIATIONS	Renormalisation and factorisation scale variations	0.25,0.25 0.25,1. 1.,0.25 1.,1. 1.,4. 4.,1. 4.,4.
HDH_WIDTH[6,24,5]	$t \to W^+ b$ partial width [GeV]	1.32
HDH_WIDTH[24,2,-1]	$W^+ \to u\bar{d}$ partial width [GeV] (same for all quarks)	0.7041
HDH_WIDTH[24,12,-11]	$W^+ \to \nu_e \bar{e}$ partial width [GeV] (same for all leptons)	0.2256
OL_PREFIX	OpenLoops ME generator release	openloops/2.0.0
OL_PARAMETERS	Parameter specifications for OpenLoops ME generator	ew_scheme=2 ew_renorm_scheme = 1
PDF_LIBRARY	PDF interfaces to load	LHAPDFSherpa
PDF_SET	PDF set for hadronic bunch particles	NNPDF30_nnlo_as_0118_hessian
FSF:	Tag to set the factorization scale factor	1
RSF:	Tag to set the renormalization scale factor	1.
QSF:	Tag to set the resummation scale factor	1
SCALES	Tag to set a process-specific scale	STRICT_METS{FSF*MU_F2}{RSF*MU_R2}{QSF*MU_Q2}
NLO_QCD_Mode	Tag to setup QCD NLO processes	3 {LJET}
CKKW	Tag to setup multijet merging	sqr(QCUT/E_CMS)
ME_Generator	Tag to specifiy the tree ME generator	Amegic {LJET}
RS_ME_Generator	Tag to specifiy the real-subtracted ME generator of an MC@NLO process	Comix {LJET}
Loop_Generator	Tag to specifiy the loop ME generator	LOOPGEN
Associated_Contributions	Tag to specify the associated contributions	EW|LO1|LO2|LO3 {LJET}
ASSOCIATED_CONTRIBUTIONS_VARIATIONS	Associated NLO EW and sub-leading order contributions to be included as weights	EW EW|LO1 EW|LO1|LO2 EW|LO1|LO2|LO3
Order	Tag to fix the coupling order	(*,0)
EVENT_GENERATION_MODE	Tag for setting the mode of using weights	PartiallyUnweighted
Enhance_Function	Tag to set an enhance function	VAR{pow(max(sqrt(H_T2)-PPerp(p[2])-PPerp(p[3]),(PPerp(p[2])+PPerp(p[3]))/2)/30.0,2)} {3,4,5,6}

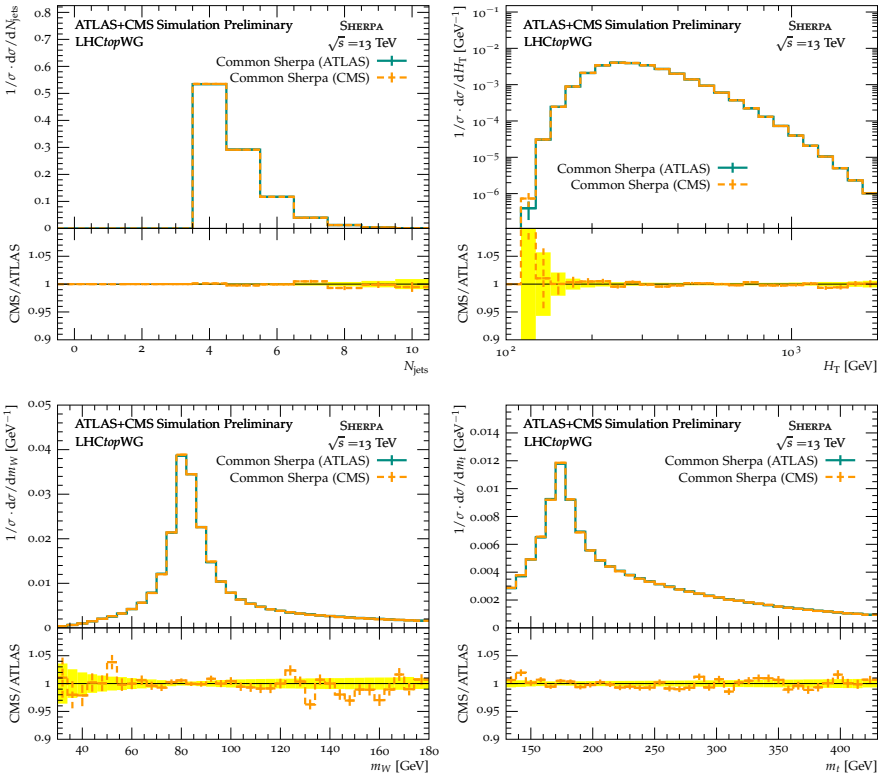

Fig. 3.3. Comparison of events produced with the common SHERPA settings within ATLAS (cyan) and CMS (orange) frameworks. The results shown are obtained using the RIVET routine `MC_TTBAR (ONELEP)`. The number of jets (top left), the scalar sum of the jet transverse momentum (top right), W boson candidate mass (bottom left) and hadronically decaying top mass (bottom right) distributions are shown. Plots published in [38], [39].

$R = 0.6$. Afterwards, a jet-lepton cleaning is performed, that is, the jets that are within ΔR of 0.3 from the lepton are removed to exclude the jets caused by the prompt leptons. Then events with at least four jets with $p_{\mathrm{T}} > 30\,\mathrm{GeV}$ and $|\eta| < 4.0$ are selected, out of which at least two are required to stem from the hadronization of a b quark. A candidate for the hadronically decaying W boson is found from the combination of two light jets that gives the W mass closest to 80.4 GeV. Then, the hadronically decaying top quark is constructed with all possible W boson and b jet combinations as there is no option to distinguish from which of the top quarks a bottom jet originated. Fig. 3.3 shows four observables from the analysis: the number of jets, N_{jets}, the sum of the transverse momentum scalar of all jets, H_T, the mass of the hadronically decaying W, m_W, and the mass of the hadronically decaying top quark, m_t. The uncertainty bars show only the statistical uncertainty to facilitate the evaluation of the compatibility between the two samples. Good agreement within the statistical uncertainties is seen in all four observables.

The other RIVET routine used, `MC_FSPARTICLES`, shows characteristic distributions for all final-state particles with $|\eta| < 5.0$ and $p_T > 500$ MeV. This routine is suitable for validation of the parton shower that produces most of these multiplicities of particles. Fig. 3.4 shows the comparison between energy, E, η, the number of particles per event, N, and N_{ch}. All these distributions show good agreement within the statistical uncertainties, except for N_{ch}, where a slight slope is visible, predicting that CMS SHERPA produces a slightly smaller number of charged particles than the ATLAS sample. A less prominent slope can be seen in the distribution of N as well. A similar trend was also observed in the POWHEG+PYTHIA 8 sample [38], [39], leading to a conclusion that it could be an unknown issue of the CMS and ATLAS frameworks. One possible reason for this could be that the CMS framework loses momentum precision of soft particles when storing them in the data files, e.g. because of the different floating-point precision. In addition, MC generators usually generate the interaction vertex at the same coordinate for all the events, which is afterwards smeared by the reconstruction frameworks to match that seen in the data. It was not possible to verify if this is done in the ATHENA framework at this stage or afterwards. The difference is only seen for the softest particles and is not seen to impact any of the relevant distributions.

3.7.3. Comparison of the common SHERPA sample with the common POWHEG+PYTHIA 8 sample and with the ATLAS and CMS data

In this section, we show the comparison of the common SHERPA sample with the POWHEG+PYTHIA 8 sample generated using the common ATLAS-CMS settings as well as the ones generated using the default ATLAS and CMS settings of each generator. The CMS version of the sample is used for comparison, but both versions are almost identical. The comparison relies on RIVET routines containing ATLAS and CMS data obtained at $\sqrt{s} = 13\,\mathrm{TeV}$ unfolded to the particle level.

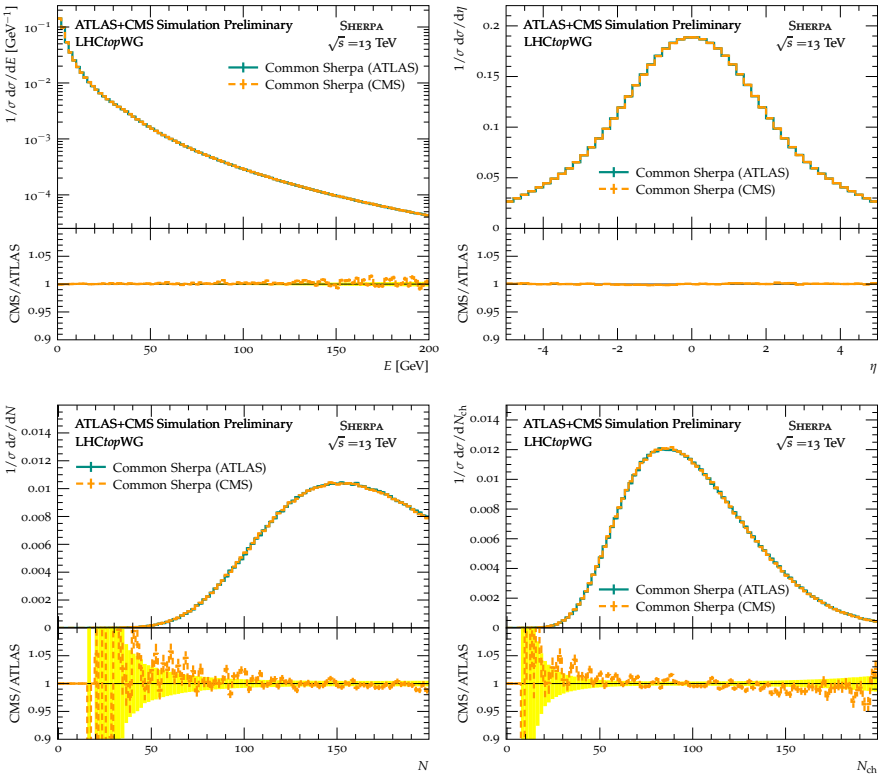

Fig. 3.4. Comparison of events produced with the common SHERPA settings within ATLAS (cyan) and CMS (orange) frameworks. The results shown are obtained using the RIVET routine `MC_FSPARTICLES`: the energy of all the final-state particles with $|\eta| < 5.0$ and $p_T > 500$ MeV (top left), η (top right), the total number of particles per event, N, and the number of charged particles per event, N_{ch} is shown. Plots published in [38], [39]

The first ATLAS analysis shown is the single- and double-differential cross section measurement of the kinematic properties of top quark in the boosted lepton+jets channel [214]. The analysis selects events with exactly one dressed lepton (electron or muon) with $|\eta| < 2.5$ and $p_T > 27\,\text{GeV}$. At least two anti-kT jets with $R = 0.4$, $p_t > 25\,\text{GeV}$ and $|\eta| < 2.5$ (AK4 jets) are required to be in the event, out of which one has to be ghost-matched to a b-hadron. AK4 jets are reclustered into large-R jets (R=1.0), which are trimmed by removing subjets with p_T less than 5 % of the large-R jets p_T. Large-R jets are required to have $|\eta| < 2$ and $p_T > 200\,\text{GeV}$. A large-R jet is classified as hadronic if its mass falls within $120 < m < 220\,\text{GeV}$ and the distance between the lepton and the jet fulfills $|\Delta\phi(l, \text{jet}_{R=1.0})| > 1.0$. The leptonic top is selected using the leading (small-R) b-tagged jet with $\Delta R(l, \text{b-jet}) < 2.0$ and $\Delta R(\text{jet}_{R=1.0}, \text{b-jet}) > 1.5$. If no b-tagged jet fulfils these requirements than the leading p_T jet is used. Further, the events are required to have $p_{\text{T}}^{\text{miss}} > 20\,\text{GeV}$ and $p_{\text{T}}^{\text{miss}} + m_T^W > 60\,\text{GeV}$. Fig. 3.5 top left shows the p_T of the hadronically decaying top quark and Fig. 3.6 top left shows the p_T of the $t\bar{t}$ system.

The second ATLAS analysis shown is the differential cross section measurement in the boosted all-hadronic channel [215]. The events are required to have at least two large-R jets with $p_{\text{T}} > 350\,\text{GeV}$ (out of which at least one with $p_{\text{T}} > 500\,\text{GeV}$), $|\eta| < 2.0$ and jet masses $m = 172.5 \pm 50\,\text{GeV}$ and two AK4 jets with $p_{\text{T}} > 25\,\text{GeV}$ and $|\eta| < 2.5$. Events are required to have no dressed leptons with $p_{\text{T}} > 25\,\text{GeV}$ and $|\eta| < 2.5$. Fig. 3.5 top right shows the leading top quark p_{T} distribution, while Fig. 3.6 top right shows the p_T of the $t\bar{t}$ system in these events. Fig. 3.5 top left shows the p_T of the hadronically decaying top quark and Fig. 3.6 top left shows the p_T of the $t\bar{t}$ system.

The third analysis shown is from CMS, which shows the double-differential cross section in the resolved l+jets channel [216]. Events with exactly one dressed lepton with $p_{\text{T}} > 30\,\text{GeV}$ and $|\eta| < 2.4$ and at least four AK4 jets with $p_{\text{T}} > 20\,\text{GeV}$ and $\eta| < 2.4$ are selected. Two jets must be b tagged. Fig. 3.5 bottom shows the p_{T} of the hadronically and leptonically decaying top quarks and Fig. 3.6 bottom shows the p_T of the $t\bar{t}$ system in these events.

Fig. 3.5 shows the comparison of the hadronic top and the leading top p_T distribution in different $t\bar{t}$ decay channels. For all of these, the SHERPA sample provides a just as good or better description than all the POWHEG+PYTHIA 8 samples, especially in the CMS analysis, where the prediction agrees well with the data unlike the POWHEG+PYTHIA 8 samples which predict a harder top quark than in the data: a known issue in many NLO generators [217]. Fig. 3.6 shows the p_T distributions of the $t\bar{t}$ system in different $t\bar{t}$ decay channels. Similarly to the top p_T distributions, all the POWHEG+PYTHIA 8 samples show a slope compared to the CMS and ATLAS data. The slope is not clearly visible only in the boosted all-hadronic channel compared to the ATLAS data. Nevertheless, this distribution has the largest statistical uncertainties. On the other hand, the SHERPA sample shows good agreement with the data, except for the boosted all-hadronic channel,

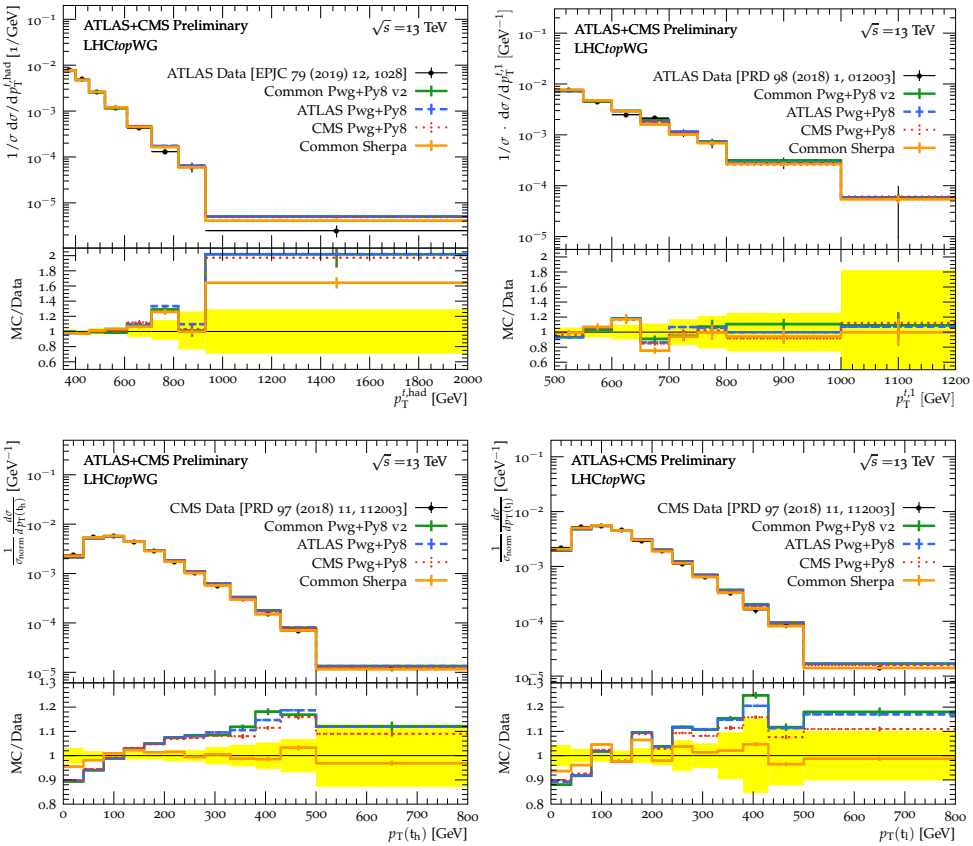

Fig. 3.5. Comparison of the CMS-ATLAS common MC SHERPA settings with the common and default ATLAS and CMS POWHEG+PYTHIA 8 settings. On the top row, hadronically decaying top quark p_T distribution in the lepton+jets boosted channel (left), and the leading top p_T in the all-hadronic boosted channel (right), compared to ATLAS data. The bottom row shows the hadronically decaying top p_T in the lepton+jets resolved channel and the leading top p_T in the dilepton channel compared to CMS data. Plots published in [38], [39].

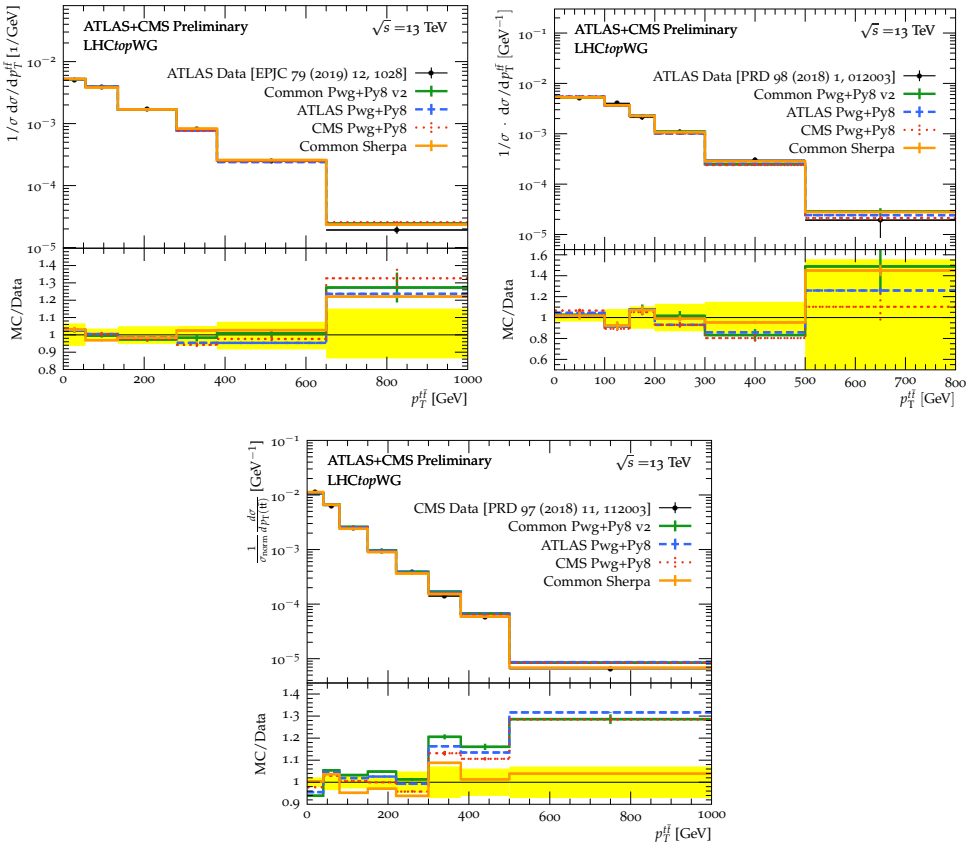

Fig. 3.6. Comparison of the CMS-ATLAS common MC SHERPA settings with the common and default ATLAS and CMS POWHEG+PYTHIA 8 settings. A distribution of p_{T} of the $t\bar{t}$ system in the boosted lepton+jets channel (top left), boosted all-hadronic channel (top right) compared to the ATLAS data and in resolved lepton+jets channel (bottom) compared to CMS data is shown. Plots published in [38], [39].

where the predictions are similar to that of POWHEG+PYTHIA 8 and fail to describe the data at large $m_T^{t\bar{t}}$.

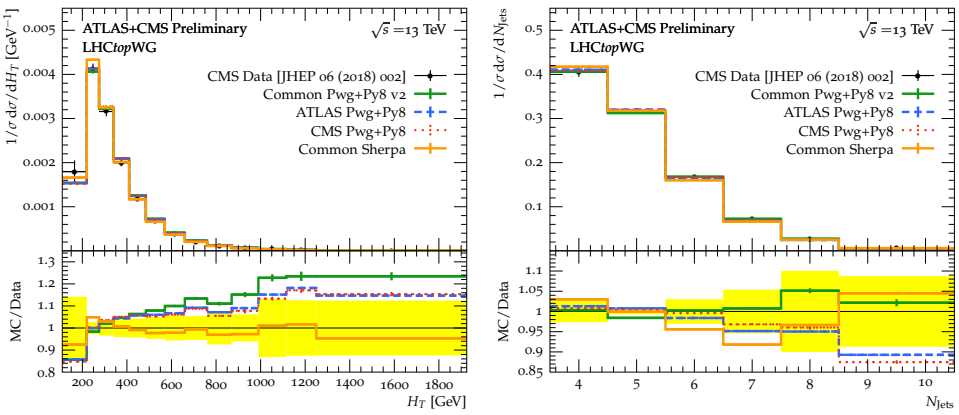

Fig. 3.7. Comparison of the CMS-ATLAS common MC SHERPA settings with the common and default ATLAS and CMS POWHEG+PYTHIA 8 settings. The distribution of the sum of the jet transverse momentum scalar (left) and the number of jets (right) is shown compared to the CMS data. Plots published in [38], [39].

The final analysis shown is the CMS analysis of differential cross section in the resolved l+jets channel and contains the cross section distribution with respect to different kinematic distributions as the above analysis, including H_{T} and N_{jets} [218]. Events are required to have one dressed lepton with $p_{\mathrm{T}} > 26\,\mathrm{GeV}$ and $|\eta| < 2.4$. The events are required to have at least for jets with $p_{\mathrm{T}} > 30\,\mathrm{GeV}$ and $|\eta| < 2.4$, of which two should be ghost-matched to a b hadron. Fig. 3.7 shows distributions of H_{T} and N_{jets} from this analysis compared to CMS data. It is visible that SHERPA tends to produce a smaller number of jets that are also less hard while POWHEG+PYTHIA 8 tends to produce a larger number of jets that are harder. This presents a common trade-off in tuning these two observables in NLO generators. Due to the conservation of total momentum, it is complicated to tune both the H_T and N_{jets} distributions. While SHERPA improves the agreement with the data for H_T, the agreement for N_{jets} becomes slightly worse than for POWHEG+PYTHIA 8.

3.8. Summary

In this section, an introduction to the MC event generation for HEP was presented. In addition, the author's contribution in generating a common CMS-ATLAS SHERPA $t\bar{t}$ MC sample and the first CMS SHERPA $t\bar{t}$ sample was presented. The SHERPA sample was found to provide an alternative to the commonly used POWHEG+PYTHIA 8 sample, giving better agreement with the unfolded data for distributions such as top and jet p_T, while being slightly worse on others like N_{jet} distributions. It is encouraged by the LHCTopWG to add the predictions of the common SHERPA sample to unfolded distributions of all $t\bar{t}$

analyses in CMS and ATLAS to simplify their comparison between experiments and result combinations.

A potential way to continue this project is to repeat the generation of the common sample after incorporating a new cluster hadronization model tune in SHERPA [219]. The tune has been made using e^+e^- data for the two showers available and is set by default since SHERPA 2.2.14 now incorporated in CMSSW. Validated SHERPA settings in CMS enable additional studies of the effect of the hadronization model on jets, for example, by performing studies of the jet energy scale as done by ATLAS [220]. Such studies would be an important next step of the study presented later in Chapter 6.

4. EXPERIMENTAL SETUP: THE LHC AND THE CMS DETECTOR

4.1. The Large Hadron Collider

The Large Hadron Collider (LHC) is the worlds largest particle accelerator capable of accelerating two counter-rotating proton beams to a maximum energy of 7 TeV each and lead ions up to 2.8 TeV [221], [222]. The map of the LHC, and the smaller super proton synchrotron (SPS), tunnel is shown in Fig. 4.1 (left). The LHC was installed in the tunnel formerly built for the Large Electron–Positron Collider (LEP) located at a depth between 45 m and 170 m below ground [223]. The tunnel is 26.7 km long and crosses the French-Swiss border at four points.

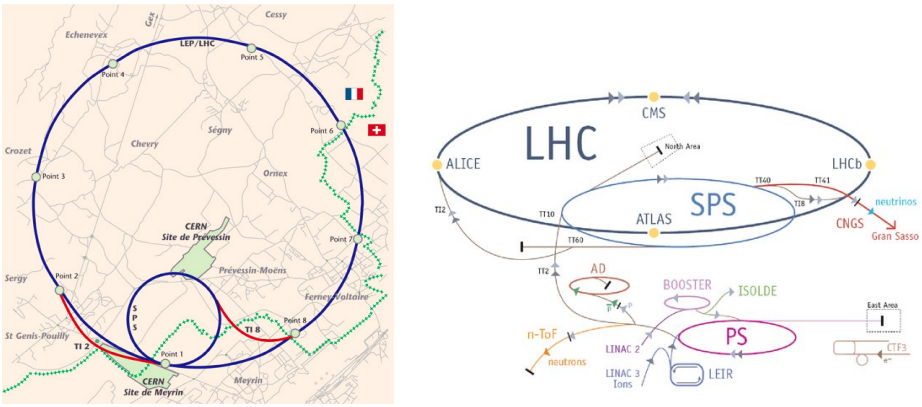

Fig. 4.1. Left: A map of the LHC and SPS tunnels (in blue) in Geneva together with the transfer lines (red) [224]. The border between France and Switzerland is marked with the green dotted line. The centres of the eight straight sections with access to the accelerator and where the inner and outer beampipes are interchanged are marked by grey points. Right: A scheme of the European Organization for Nuclear Research (CERN) accelerator complex and the main experiments at CERN benefiting from it [225].

The proton acceleration consists of several stages with particles from one accelerator being injected into another and accelerated further. The full CERN accelerator complex is shown in Fig. 4.1 (right) along with the experiments benefiting from the pre-accelerators of the LHC. Protons are sourced from a duoplasmatron device, which ionises the hydrogen gas available in bottles and creates a beam of protons with the energy $E_{\text{beam}} = 90\,\text{keV}$ [226]. The injection chain then continues in a linear accelerator, LINAC 2 [227], the Proton Synchrotron Booster (PSB), the PS, and the SPS, providing beams with E_{beam} of 50 MeV, 1.4 GeV, 25 GeV and 450 GeV, respectively.

The LHC is not a perfect circle but consists of eight 2.45-km-long arcs comprising superconducting dipole magnets responsible for bending the beam, and eight 545-m-long straight sections. Four of the straight sections are dedicated to the interaction points (IPs)

for the four large LHC experiments: ALICE [228], [229], ATLAS [230], CMS [231], and LHCb [232], [233]. At the IPs, the beams are focused in a way that the they overlap and the collisions are possible. One of the straight sections not used for collisions is the beam dump, two are for beam quality monitoring, and one contains eight superconducting radio frequency (SRF) cavities responsible for accelerating the beams [222]. Each SRF cavity maintains an accelerating field of 2 MV, in this way adding up to 16 MV RF acceleration potential per revolution. The operational frequency of SRF cavities is $f_{\mathrm{RF}} = 400.789\,\mathrm{MHz}$ at the proton energy of 450 GeV, which, due to the slight increase of the proton velocity,[11] reaches 400.800 MHz at 7 TeV. Such operational frequency allows for $h = \frac{f_{\mathrm{RF}}}{f_{\mathrm{rev}}} = 3564$ bunches of particles to be stored in the accelerator, called buckets, where $f_{\mathrm{rev}} \approx 11.25\,\mathrm{kHz}$ is the revolution frequency of the proton bunches. The number h is called the harmonic number, and its value for historical reasons is borrowed from LEP [223]. Nevertheless, not all of the buckets are filled with proton bunches. There are typically 2808 bunches per beam.

The LHC superconducting dipole magnets are made of NbTi Rutherford cable and are operated at a temperature of 1.9 K. In addition to the dipole magnets, quadrupole magnets are used to keep the beam focused while higher pole magnets are used to correct for imperfections in the magnetic field. At the IPs the beams can be confined to the transverse size of 10 µm.

Two of the main accelerator parameters determining its performance for particle physics experiments are the centre-of-mass energy of the collisions, $\sqrt{s}$, and the integrated luminosity $\int dt\mathcal{L}$ that the accelerator is able to produce, where $\mathcal{L}$ is the instantaneous luminosity. For collisions of two identical beams, $\sqrt{s}(\mathrm{protons}) = 2 \cdot E_{\mathrm{beam}}$, but due to the composite nature of protons, $\sqrt{s}(\mathrm{partons}) < \sqrt{s}(\mathrm{protons})$, which makes it a probabilistic number for individual collisions. $\mathcal{L}$ in collider experiments is determined by the number of bunches in the storage ring, n, number of particles in each bunch, k, the cross section of the interaction area, A, luminosity reduction factor, R, and f_{rev} [234]

$$\mathcal{L} = f_{\mathrm{rev}} n k^2 / A \cdot R. \tag{4.1}$$

Here, R accounts for the reduction of luminosity due to the crossing angle of the colliding beams and the so-called hourglass effect. The latter describes the increase in the beta function $\beta(s)$ with increasing distance s from the IP. $\beta(s)$ is related to the transverse beam size and assuming a Gaussian beam distribution is expressed as

$$\beta(s) = \frac{\sigma^2(s)}{\varepsilon}, \tag{4.2}$$

[11] At 450 GeV $(1-\beta) \approx 2.5 \cdot 10^{-6}$ while at 7 TeV $(1-\beta) \approx 1.0 \cdot 10^{-8}$.

where ε is beam the emittance and $\sigma(s)$ is the width of the Gaussian shape of the beam. The interaction area A can be expressed as

$$A = \frac{4\pi\beta^*\varepsilon_n}{\gamma},$$

where β^* is the beta function in the IP of the beam and γ is the relativistic gamma factor.

The total number of collisions can be calculated as

$$N = \sigma \int dt\mathcal{L}, \tag{4.3}$$

where σ is the cross section of the process. The design (nominal) centre-of-mass energy of the LHC is 14 TeV and the design luminosity at the IPs in the ATLAS and CMS experiments is $1 \times 10^{34}\,\mathrm{cm^2\,s^{-1}}$ [222], which was reached during Run 2 and exceeded during Run 3. The machine was optimised to deliver a larger luminosity than initially expected. After Run 3, a major upgrade of the LHC accelerator is planned, called the high-luminosity LHC (HL-LHC), which will increase instantaneous luminosity by a factor of five [235]. For detector and accelerator safety reasons, it was decided to run at a reduced centre-of-mass energy of $\sqrt{s} = 13\,\mathrm{TeV}$ and $\sqrt{s} = 13.6\,\mathrm{TeV}$ during Run 2 and Run 3, respectively.

4.2. The Compact Muon Solenoid

CMS is a hermetic multipurpose experiment [231]. Here, hermetic indicates that the detector covers an extensive phase space, as the CMS hadronic calorimeter (HCAL) reaches up to $|\eta| < 5.2$. Originally designed to discover the Higgs boson and understand its properties, CMS is well suited to carry out a variety of precision physics measurements, as well as searches for new physics. CMS has a cylindrical shape, is azimuthally symmetric, 21 m long, and 15 m in diameter. A sector of a slice in the transverse direction of the CMS detector is shown in Fig. 4.2, together with example trajectories of particles traversing it. It illustrates the layered structure of CMS with the first layers responsible for particle tracking, followed by the electromagnetic and hadronic calorimeter layers, then a magnet, and finally the muon chambers dedicated to muon tracking. In the following, Sections 4.2.1-4.2.4 contain descriptions of the central CMS subdetectors.

CMS uses a right-handed coordinate system as shown in Fig. 4.3, where the z-axis points in the direction of the counterclockwise beam, the x-axis points to the centre of the LHC, and the y-axis points vertically upwards. In addition, cylindrical coordinates (r, ϕ, z) and spherical coordinates (r, θ, ϕ) are often used, where the r-coordinate represents the radial distance from the z-axis. The ϕ-coordinate represents the azimuthal angle around the beam axis. The θ-coordinate represents the polar angle from the beam axis but is often replaced by η.

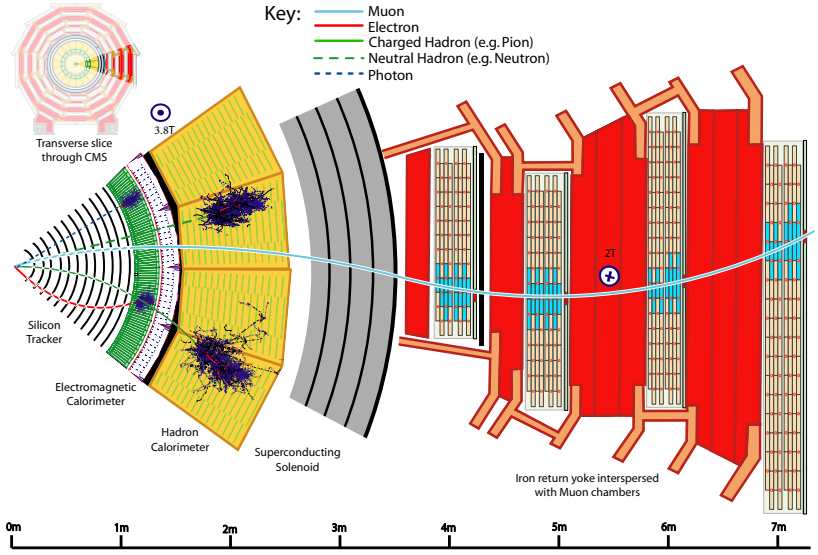

Fig. 4.2. A sector of a cross section of the CMS detector along the x-y plane (i.e. taken perpendicularly to the beamline) [236].

The detector is divided into the barrel, endcap, and forward regions, with barrel and endcap detectors inside the CMS magnet shown in Fig. 4.4. The barrel region contains cylindrical subdetectors and covers up to $|\eta| < 1.3$. The endcap region covers the sides of the CMS cylinder and is divided into a region with the CMS tracking detector (tracker) coverage, $1.566 < |\eta| < 2.5$, and with no tracker coverage, $2.5 < |\eta| < 3$. This leaves a transition region of $1.3 < |\eta| < 1.566$ with a larger material budget due to the cabling and limited detector coverage. The forward region with the forward HCAL has $3 < |\eta| < 5.191$.

4.2.1. The superconducting solenoid

One of the distinguishing features of the CMS experiment is its superconducting solenoidal magnet[12] [239]. The magnet is able to generate a 3.8 T magnetic field inside its core[13] and a 2 T field in the opposite direction outside its core. Together with CMS detailed vertexing capabilities, this allows measurements of p_{T} of particles passing through with a precision of up to 1 % for particles up to $p_{\mathrm{T}} = 200\,\mathrm{GeV}$. At higher p_{T} the calorimetric information can be used to reliably measure particle energies.

The magnet is made out of NbTi Rutherford cable and an iron yoke, extending the magnetic field up to around 14 m in diameter, far outside the magnet itself, which is

[12]The ATLAS experiment has toroidal magnets and a smaller solenoid. LHCb has a dipole magnet. ALICE has a solenoid, but only reaching 0.5 T magnetic field and not superconducting.

[13]The magnet was designed to reach a 4 T magnetic field, but for magnet safety and stability reasons it was decided to keep it at a slightly lower magnetic field.

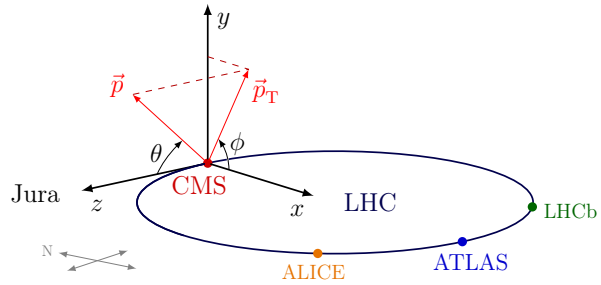

Fig. 4.3. The coordinate system used in CMS [237].

around 6 m in diameter. The iron yoke in the barrel region is made out of three iron layers, alternating with the muon chambers outside the magnet. Additional iron yoke disks are placed at the endcaps.

4.2.2. Silicon tracker

The subdetector closest to the beamline is the silicon tracker, made of fine-grained layers of pixel and strip sensor layers [240], [241]. The pixel layer is the closest to the beamline consisting of 150 µm × 150 µm pixels.

During the so-called Phase-1 upgrade between 2016 and 2017 data collection, the pixel detector underwent a major upgrade, shown in Fig. 4.5, where instead of three pixel layers in the barrel, four were installed. In addition, the distance to the beamline was decreased from 44 mm to 29 mm. Finally, the number of layers in the forward direction was increased. This marks a significant difference in the experimental conditions between 2016 and the rest of Run 2 data taking.

The strip subdetector, encompassing the pixel layers, is comprised of 300 µm thick silicon strips extending radially up to 1.20 m from the beamline. The resolution of these strips is significantly higher in one dimension compared to the other. Consequently, to enhance spatial precision, the various layers are arranged at slight angles relative to each other, thereby acquiring more detailed information about traversing particles.

4.2.3. Electromagnetic and hadronic calorimeter

The electronic calorimeter (ECAL) [242] following the tracker layer is designed to measure energies of electrons and photons and absorb them, whereas the HCAL is designed to measure energies of hadrons [243]. ECAL is constructed of $PbWO_4$ crystals with a size at the front face of 22 mm × 22 mm. This corresponds to $\Delta\phi \times \Delta\eta = 0.0175 \times 0.0175$ in the barrel. Between the barrel and the endcap ECAL and the tracker, a thin layer of ECAL preshower is installed. It had an initial purpose of helping to distinguish prompt photons from π^0 decays and, in general, to help identify electrons and photons. However,

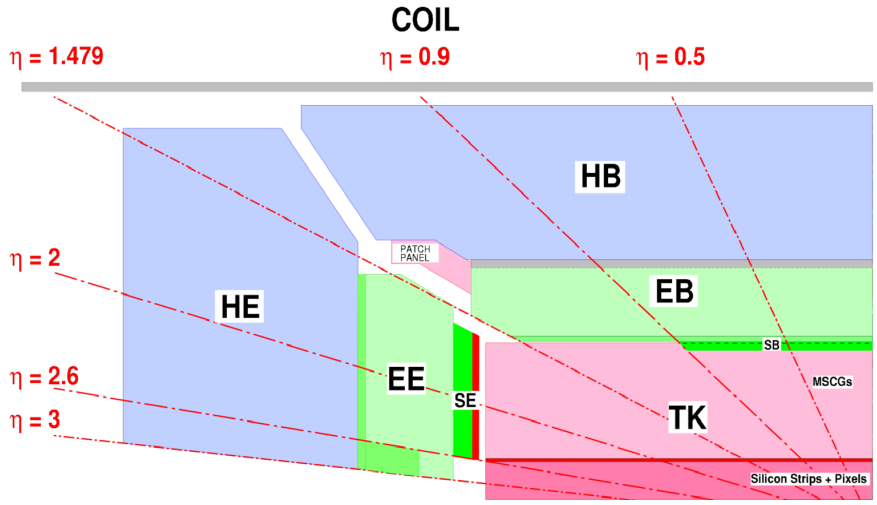

Fig. 4.4. The cross section of the CMS detector along the R-z plane, showing the subdetectors housed within the magnet coil. Only one quatre of the cross section is depicted, with opposite sections in R and z being its mirror images. Muon chambers and the forward HCAL are outside the image. TK=tracker, HB/HE=barrel/endcap HCAL, EB/EE=barrel/endcap ECAL, SB/SE=barrel/endcap preshower [238].

due to the parasitic signal from the large amount of π^0 in CMS, it was not used, and the energy absorbed in it is added to the closest associated ECAL cluster [236].

The rapidity gap between the barrel and the endcap ECAL is smaller than that for the tracker and spans $1.4442 < |\eta| < 1.566$. Commonly, electrons and photons falling in this region are removed from the measurements in CMS [244]. $PbWO_4$ as the detector material was chosen due to several properties, such as its small radiation length (0.89 cm compared to, e.g. CeF_3 which has 1.68 cm) allowing the compact design of CMS with the calorimeters placed before the magnet, and short light decay time (15 ns compared to, e.g. 25 ns CeF_3).

The barrel and endcap HCAL (HB and HE) is made of copper absorber plates, interleaved with plastic scintillators, and with one steel plate at each end [243], [245], [246]. The face size of the HCAL scintillator corresponds to $\Delta\phi \times \Delta\phi = 0.087 \times 0.087$, so 5×5 ECAL towers fit into one HCAL tower. Despite not being as finely segmented as ECAL, HCAL is very hermetic. The forward HCAL (HF, not shown in Fig. 4.4) located 6 m downstream of HE outside the magnet reaches $|\eta| < 5.2$. Unlike HB and HE, HF employs steel absorbers interspersed with quartz fibres.

4.2.4. The muon detectors

Muon tracks are measured using large gas ionisation detectors of three different designs [248], [249]. Their positions in CMS are shown in Fig. 4.6. It is not attempted to

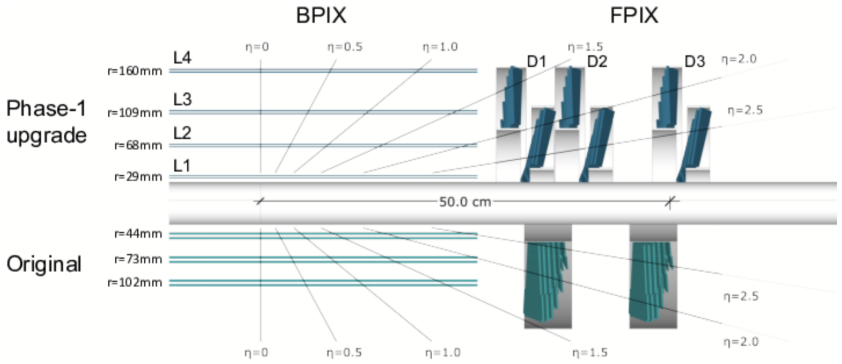

Fig. 4.5. The comparison of the barrel (BPIX) and forward (FPIX) pixel layers before (bottom) and after (top) the Phase-1 upgrade [240].

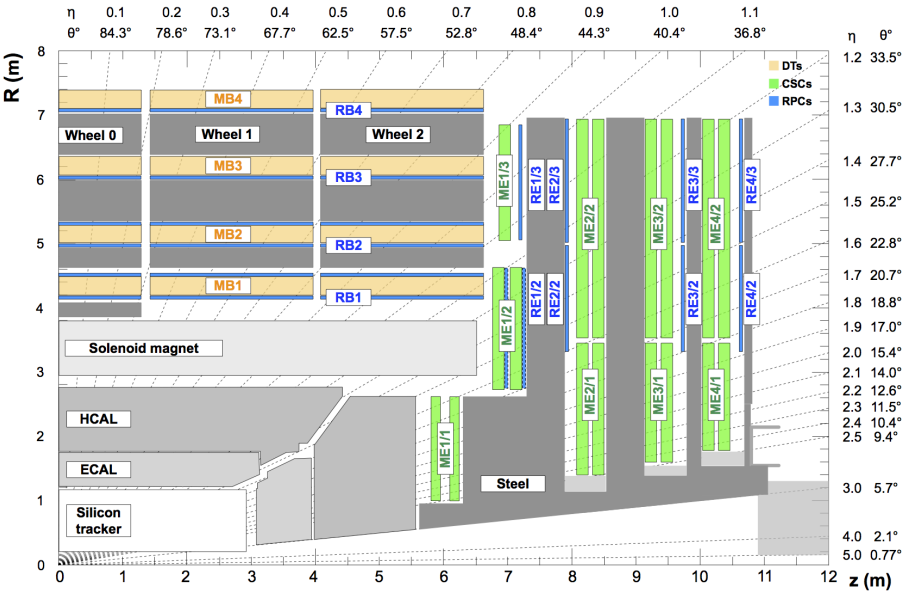

Fig. 4.6. Cross section of the CMS detector along the R-z plane showing explicitly the locations of muon detectors in CMS [247]. One quarter of the cross section is shown while the other sections are its mirror images. Drift tubes (DTs) are marked with MB, cathode strip chambers (CSCs) are marked with ME. Resistive plate chambers (RPCs) are located both in barrel and endcaps, marked with RB and RE, respectively.

stop the muons, but rather to identify them and measure their p_{T}. In the barrel region where muon and background rates are not as large (only the hardest muons emerge in the barrel region), the simplest drift tube (DT) technology was chosen. This technology is also suitable because DTs can easily be placed in cylindrical formations to keep the shape of the barrel CMS. The drift time for each DT reaches around 400 ns [248], which is the duration needed for the ionised electrons, collected by the particle traversing the gas, to migrate to the wires in the DT. This time is relatively long compared to other muon chamber technologies, and particularly in contrast with ECAL response times, where $PbWO_4$ decay time is $\mathcal{O}(10\,\mathrm{ns})$ [242]. The spatial resolution achievable with DT is around 250 µm.

At the endcap regions, where the particle rates are larger and the magnetic field is non-uniform, the cathode strip chamber (CSC) technology was chosen. CSCs can be segmented more finely, allowing one to increase the track resolution, and are reliably working in a non-uniform magnetic field. Instead of having one wire per tube, CSCs employ a two-dimensional readout system with cathode strips and anode wires, which allows for higher-precision tracking in high-magnetic-field regions.

The two aforementioned technologies can provide an excellent offline muon reconstruction efficiency of $96 - 99\,\%$ in most of the rapidity regions. For the purpose of selecting good events to store (triggering, see Section 4.3), the resistive plate chamber (RPC) technology was installed in addition to the other two technologies. RPCs are very fast with excellent time resolution.

As part of the Phase-2 upgrade (occurring between Run 3 and HL-LHC), a novel supplementary array of muon chambers, designated as gas electron multipliers (GEM) [250], is planned to be installed. A set of GEM detectors intended for testing purposes have already been installed in CMS during the long shutdown between the Run 2 and Run 3. GEMs are to be added at the very forward regions, where the largest radiation doses are present. The large radiation harness of gas electron multipliers (GEM) ensures a longer operational lifetime of the subdetector. GEM consists of three layers, each with a 50 µm thick metal-coated polymer foil with a high density of tiny holes. This innovative design allows for efficient ionised electron multiplication, leading to improved signal amplification and detection efficiency.

Note that CMS does not have special subdetectors tailored for hadron identification such as the Ring Imaging Cherenkov Detectors in LHCb [251]. Nevertheless, the use of novel machine learning techniques or special b parking datasets (see Section 4.3 on b parking), enables CMS analysers to perform flavour physics, such as measuring CP violation in B hadron decays [252] or D^0 meson decays [253].

4.3. Trigger

With collision events in CMS taking place with a rate of 40 MHz and one event at RECO level taking around 1 MB of memory, rates of about 40 TB/s for storage are created

— impossible for modern data storage capacities. The trigger system lowers this event rate by selecting events with possible interesting physics signatures [254]. For example, these can be events with high-p_{T} isolated leptons or photons or a large H_T. The trigger system consists of two levels. The level one (L1) trigger is hadrware-based and built using reprogrammable field-programmable gate arrays (FPGAs) and lowers the rate of events to 100 kHz. The L1 trigger selects events with possibly interesting objects such as muons, electrons, photons, missing transverse momentum, p_T^{miss}, or jets. The latency of the L1 trigger is around 4 µs. The software-based high-level trigger (HLT) reduces the event rate further to 1 kHz. HLT selection is organised into HLT paths, where each path is a sequence of reconstruction steps of increasing complexity and selections based on them. HLT often shares the framework with the offline reconstruction. The average HLT processing time is around 100 ms.

Some trigger paths still produce higher rates than the electronics are able to transmit and store. The rates of these trigger paths are prescaled, namely, reduced by only selecting every n-th event. The number n is called a prescale. A novelty in CMS in comparison to other large LHC experiments is the storage of specialised data processing streams, called data scouting and data parking [255]. In data scouting, only HLT objects are being stored instead of the full event information. This enables the collection of a substantially larger amount of data. During data parking, raw, unreconstructed detector data are stored on tape and reconstructed only later during the shutdowns of the LHC. One benefit of such data is the access to large amounts of low-p_{T} objects necessary for data calibration[14].

4.4. Summary

Thus, the meaning behind the words in the acronym CMS, "Compact Muon Solenoid" has become clear. CMS is a layered detector made out of dense calorimeters with short radiation lengths and interaction lengths fit between a huge and strong superconducting solenoid and a fine-grained tracker. This explains the words "compact" and "solenoid". The compactness can also be viewed by comparing how large the mass of material, i.e. 14 000 t is squeezed within the 15 m in diameter and 21 m long detector, while its other larger counterpart, ATLAS, weighs 7000 t within a 25 m in diameter and 46 m long detector. "Muons" describe the excellent muon tracking capabilities of CMS. It is truly remarkable how such a large machine, by a collaboration of thousands of physicists, has been successfully put to work and is able to deliver excellent results to be applied in precision analyses. Part of this success is a detailed reconstruction and bias removal procedure conducted in event reconstruction, as described further.

[14] Such calibrations are of particular interest for measurements where a heavy object, such as a Higgs or a new BSM particle, decays into two, where one is on-shell and the other is off-shell, and can be low p_{T}.

5. EVENT RECONSTRUCTION IN CMS

After a signal is detected, the information about the event, in terms of hits and absorbed energy, has to be transformed into information in terms of physics objects, their momenta, trajectories, and other information. This is done in the event reconstruction. Among other things, the tracks of individual particles have to be obtained from hits in the tracker and the muon detectors. The CMS tracking algorithms are explained in Section 5.1. The properties of CMS allow an implementation of a global physics object reconstruction algorithm by combining information in several of the subdetectors. This algorithm, called particle flow (PF), is described in Section 5.2. The multitude of particles emerging from perturbative QCD have to be clustered into simpler objects, called jets, as is commonly done by the methods shown in Section 5.3. In addition, jets have to be classified according to their origin in the MC calculations, as shown in Section 5.4, and in the data, as shown in Section 5.5. The reconstructed physics objects also contain bias due to, for example, uncompensated detector effects that have to be corrected for in jet energy corrections for jets and corrections and efficiency scale factors (SFs) for leptons. These methods are explained in Section 5.6 and Section 5.7.

5.1. Reconstruction of tracks and vertices

The average amount of simultaneous proton-proton collisions in CMS in 2018 reached 32, while for the whole Run 2 it was 29 [256]. This creates a large amount of tracks deposited in the CMS tracker at every bunch crossing. The tracking algorithm uses information from the pixel and strip tracker (here, also called inner tracker) and muon detectors (also called outer tracker) to reconstruct these tracks with the highest possible efficiency while also keeping the fraction of fake tracks low [257]. The latter might be formed from a wrong combination of hits or by falsely combining the noise exceeding the defined thresholds with other tracker hits.

The tracking algorithm applies an adaptation of a combinatorial Kalman filter [258], called combinatorial track finder (CTF), which is performed iteratively [257]. In the first iteration only the tracks that are easiest to find are sought, for example, the highest-p_{T} tracks. Afterward, lower-p_{T} tracks and tracks not originating in the beamspot are searched for. In each iteration, seeds are generated using only 2 or 3 hits. Then the Kalman filter extrapolates the seed trajectories to the subsequent layers by finding additional hits that match best to the given track. This takes into account the effect of multiple Coulomb scattering, which causes abrupt changes of direction in the tracks. After each iteration, the hits combined in the tracks are removed. After all tracks are reconstructed, the primary vertices (PVs) are reconstructed by extrapolating the tracks and fitting the position of the track origin. The PV with the highest track p_{T} pointing to it is chosen as the leading PV. The tracking efficiency is greater than 99 % for isolated muons and around 80-99 % for

electrons and pions. The fake rates are 5 % (15 %) in the barrel (endcap and transition) regions.

5.2. The particle flow algorithm

Classically for older detectors and in ATLAS until Run 2, to reconstruct jets, only the calorimeter information was used without trying to distinguish separate tracks. Similarly, other particles, like isolated photons, electrons, and muons were reconstructed using only information from the CMS ECAL and muon detectors, respectively. The coarseness of the CMS HCAL required improvements in jet reconstruction. The sufficient granularity of the CMS tracker and the superb tracking capabilities enables a global event description explained in this section.

The PF algorithm combines the information from all the subdetectors to reconstruct physics objects [236]. The algorithm starts with reconstructing PF elements, i.e. raw objects from the individual subdetectors that are later linked and combined. Tracks are obtained as explained in Section 5.1. Electrons travelling through the tracker are radiating a large amount of bremsstrahlung, so they are reconstructed in superclusters, captured in a small η window and a large ϕ window [259]. Muons are reconstructed from the muon chambers and can be supplemented with the information from the inner tracker [247], [260].

ECAL and HCAL clusters are formed by selecting seeds that have deposits greater than the neighbouring cells and their corresponding energy threshold. The neighbouring cells passing a threshold are then agglomerated around the seeds. The centres of the energy deposits within the clusters are then searched using an iterative fit assuming a Gaussian energy deposit around the interacting particle. In this way, the particle interaction position can be found even within an ECAL or HCAL cell. The PF hadron calibration corrects the threshold and non-linear detector response. The ECAL clusters are calibrated using a photon particle gun simulation and compared to data using π^0, which, entering the tracker, decay into two photons.

Afterwards, ECAL and HCAL are calibrated for their hadron response using particle gun simulation of charged pions. This is performed in two steps, where the energy-dependent and η dependent calibrations are performed. This is performed separately for hadrons that leave deposits in only HCAL and in HCAL and ECAL.

The final PF elements obtained are linked to their most proximate neighbours, producing PF blocks. Then, the PF candidates, like muons, electrons, photons, charged, and neutral hadrons, are identified sequentially using a detailed algorithm. Here, we simply identify the most relevant parts of the algorithm. Identified PF candidates are removed from the PF blocks before proceeding to the next reconstruction step. First, isolated muons are obtained by combining tracker, muon chamber, and HCAL deposits. For non-isolated muons, the selection is more complicated and requires passing compatibility tests

like those of a tight muon identifier (ID) or requiring that the corresponding calorimeter deposits are compatible with the muon hypothesis. Electrons are reconstructed on the basis of information from the inner tracker and calorimeters. Isolated photon candidates are seeded from ECAL clusters with $p_{\mathrm{T}} > 10\,\mathrm{GeV}$ and no tracks associated with them. Photons entering the tracker can undergo photon conversion $\gamma \to e^+e^-$, so tracks tangentially pointing to the clusters are also included in the photons. In cases where the photon emitted by the electron undergoes photon conversion, the photon can be recovered and associated with the parent electron, which avoids double counting of the track p_{T}.

ECAL and HCAL (ECAL-only) clusters that do not have tracks pointing to them are identified as neutral hadrons (non-isolated photons); otherwise, they are identified as charged hadrons. Outside the tracker acceptance, all the HCAL+ECAL deposits are identified as neutral hadrons, while ECAL-only clusters are identified as photons. Checks are made to see the compatibility of the track momenta with the calorimetric deposit. If the deposit is larger than expected from the given track momenta, a new photon or neutral hadron is created. If the calorimetric sum is smaller than the sum of the track momenta by more than three standard deviations, a relaxed search for muons is performed.

5.3. Jet clustering and calibration

The colour confinement and large logarithms appearing for the matrix elements of soft and collinear emissions of quarks and gluons cause the creation of a large multiplicity of hadrons[15] collimated in narrow cones as depicted in Fig. 5.1. Precise treatment of such large multiplicities of particles is complicated both theoretically (e.g. due to limited order calculations in coupling constants and parton shower approximation) and experimentally (e.g. due to computational power required to track the large number of particles and the limited detector resolution). This complexity can be efficiently reduced by combining the particles into jets originating from an initial colour-charged particle.

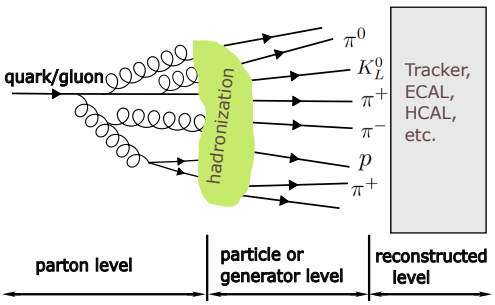

Fig. 5.1. Schematic picture of a jet. MC generators allow to distinguish jets clustered from different types of objects. Parton level denotes jets clustered from partons. Particle-level jets are clustered from stable hadrons. Reconstructed jets are obtained by clustering reconstructed objects like energy deposits in the calorimeters or PF candidates.

Jet clustering algorithms assign final-state particles to jets. A consistent jet clustering algorithm is required to be infrared and collinear (IRC) safe, where an IRC

[15] This includes also other particles, like leptons arising from the decays of unstable hadrons.

observable O is defined to remain unchanged in the event of infinitely soft radiation ($O(X; p_1, ..., p_n, p_{n+1} \to 0) \to O(X; p_1, ..., p_n)$) and in the event of a collinear splitting ($O(X; p_1, ..., p_n || p_{n+1}) \to O(X; p_1, ..., p_n + p_{n+1})$). This condition ensures the cancellation of real and virtual divergences in higher order calculations as well as securing robustness towards detector uncertainties on the experimental side.

Examples of non-IRC safe observables are iterative cone clustering algorithms that start with the hardest objects in the event and iteratively search for cones around them that would form jets [261]. Such algorithms are not collinear safe, as the hardest particle in the event can change by a collinear splitting.

In the last decade, the most popular jet clustering algorithms are sequential or "cluster" algorithms, that iteratively add particles together based on a distance measure, d_{ij} [262], [263]. For three of the most widely used ones, d_{ij} can be expressed as

$$d_{ij} = \min\left(p_{T,i}^{2p}, p_{T,j}^{2p}\right) \frac{\Delta R_{ij}^2}{R^2}, \qquad d_{iB} = p_{T,i}^{2p}, \tag{5.1}$$

where R is the jet radius parameter and $\Delta R_{i,j}$ is the distance between particles i and j. The parameter p determines the algorithm class. The algorithm runs sequentially, finding the particles with the smallest d_{ij}, combining them into one, and repeating the process again. If for the particle the distance measure is smaller than the threshold, $d_{ij} > d_{iB}$, then it defines a jet. With $p = 1$, the so-called k_T or Durham algorithm can be seen as undoing the parton shower as it starts with the softest and closest particles and combines them into larger ones. The most common one is the $k = -1$ or anti-k_T algorithm, preferred due to delivering conically symmetric jets, which are simpler to experimentally correct for UE, out-of-cone radiation and PU. Using $k = 0$, the Cambridge-Aachen algorithm is defined, which is often used for jet substructure measurements [264], [265] because it is more stable to the so-called grooming techniques, i.e. cleaning the jets from contamination from soft radiation [266]. As depicted in Fig. 5.1, jet clustering can be run on various objects, including partons for parton-level jets, hadrons for particle-level jets, and calorimeter deposits or PF candidates for experimental reconstructed jets.

5.4. Parton- and hadron-level jet flavour assignment

The definition of a generator-level jet flavour is an intricate task and several possible algorithms exist for assigning a flavour to a jet [267]–[269]. An ideal jet flavour algorithm must adhere to certain principles. Firstly, such an algorithm would be collinear and infrared safe, e.g. the flavour of a jet should not change if a collinear splitting $q \to qg$ occurs with the gluon taking a larger energy fraction than the quark. Secondly, a well-constructed jet flavour definition would not classify jets that originate from gluon splittings $g \to q\bar{q}$ in the same category as jets originating from prompt quarks. This distinction is crucial, as the prompt heavy-flavour jets may arise from decays of heavy

resonances (e.g. W boson or a new BSM particle) offering insight into potential new-physics phenomena [270]. The quarks from a colour singlet state are colour-connected with each other, while the quarks from a gluon, a colour octet, would remain colour-connected to the beam or other particles [271]. Moreover, the Lorentz scalar quantities, like the number of charged particles inside the jet and the invariant mass of the two jets coming from decays of heavy resonances, exhibit more uniform behaviour, whereas for gluon-split jets these quantities are more spread out. Thirdly, a good jet flavour algorithm would ideally not use the event record of the parton shower which is an ill-defined and non-physical concept due to interference effects and due to gauge non-invariance of the different channels. Some event generators such as SHERPA go as far as not to allow the user to access any intermediate objects, so several typical MC truth jet assigning algorithms are impossible with SHERPA.

In Run 1, two distinct jet flavour definitions were employed in CMS, the *physics definition* and the *algorithmic definition*. Both definitions use particle-level jet matching to partons with a ΔR usually taken as 1/2 of the jet radius parameter, but the selection of appropriate partons differs. For the *physics definition*, only the prompt partons are selected, i.e. partons originating directly from the hard process[16]. The jets originating from the ISR or FSR in this case are most often left unmatched. In this definition, jets originating from a LO $t\bar{t}$ process would never include gluon jets. In contrast, the *algorithmic definition*, utilises *algorithmic partons* that denote final-state partons that do not have daughter partons, i.e. partons after the shower but before hadronization. However, this does not treat quarks from gluon splitting as gluon jets and neither is it collinear safe.

For CMS Run 2, these two definitions were replaced with the *parton flavour* and *hadron flavour*. To determine the jet flavour both methods rely on repeating the jet clustering including so-called ghosts to the list of particles where ghosts are non-physical partons or hadrons that have their four-momenta rescaled by a very small number (usually 10^{-18}) [272]. The *parton flavour* uses the physics definition of partons as ghosts, i.e. all the partons in the event history from the hard process up to the partons before hadronization. The jet is assigned to be a b jet (c jet) if there is a b parton (c parton and no b parton) clustered inside this jet. Otherwise, the jet adapts the flavour of the hardest parton clustered inside. For the anti-k_{T} algorithm, the ghosts are the very last constituents to be added to the jets and are assigned to their closest jet, but unlike the ΔR matching, each parton can be assigned to only one jet. Since b and c flavours take precedence over all flavours even if the p_T of the original b or c parton is tiny, the b or c jets coming from gluon splitting are incorrectly assigned as b or c jets. For the impact of including and excluding gluon splitting within the heavy-quark jet sample in the measurement of jet energy correctionss (JECs), see Section 6.5.

[16] In PYTHIA these partons have a status code 23 and for other MC generators, status code 3.

For the *hadron flavour*, ghost hadrons are clustered into the jets. The jet is assigned the b jet flavour (c jet flavour) if there is at least one b hadron (c hadron and no b hadron) clustered within, and otherwise it is assigned a light flavour. Thus, the hadron flavour cannot distinguish among the light flavours and gluons, making it less suitable for flavour uncertainties, yet still valuable for data-driven heavy-flavour jet tagging.

Other jet flavour algorithms try to fully discard the usage of the event history and base the training of unsupervised learning models only on well-defined jet substructure information. A step further in this new paradigm shift is the idea of "jet topics", where the notion of individual jet flavours is discarded altogether. Instead, each jet is assigned a probability of how much it is gluon- or quark-like [268], [273]. These probabilities allow for the distribution of quarks and gluons to be determined without direct jet flavour assignment. These approaches have already been tested in experimental data [274]–[276]. However, these definitions should still be generalised and tested for differentiating light quarks from heavy-flavour quarks. Finally, treating leptons separately is another option helping to intrinsically clean the jets from leptons and understand the reasons for unmatched jets in the parton flavour definition.

The flavour content differs in different physics samples. Examples of the flavour content of different physics samples are shown in Section 6.3.1.

5.5. Identification of jets originating from *b* quarks at the detector level

A distinguishing feature of $t\bar{t}$ decays is the presence of two b jets. In $t\bar{t}$ and other LHC measurements, like searches for new physics, it is beneficial to discriminate b jets from other jets. For this reason, several types of b jet discriminants or identifiers (b taggers) have been developed [277]. With some lower success, c jet taggers have also been created. Since there is no hadron identification in CMS, these taggers have to rely on other b hadron and b jet properties.

Both b and c hadrons produce secondary vertex (SV). For the b quark, it is due to the fact that it is the lightest quark in the quark (b, t) doublet and due to the small non-orthogonal element of the CKM matrix $|V_{cb}| \approx 0.04 \approx |V_{us}|/5$ (see Eq. (2.18)). This ensures that the b hadron lifetime is large ($\tau(B^0) \approx 1.5\,\text{ps}$, $\tau(B^+) \approx 1.6\,\text{ps}$) compared to the c hadron lifetimes ($\tau(D^\pm) \approx 1.0\,\text{ps}$, $\tau(D^0) \approx 0.4\,\text{ps}$), but not enough to be considered stable as, e.g. s hadrons ($\tau(K^\pm) = 12\,\text{ns}$) [21]. The lifetime of c hadrons is shorter than for b hadrons because their CKM matrix element for decay to s is not suppressed and m_c is large. In general, b hadrons travel around $\mathcal{O}(1 - 10\ \text{mm})$, creating a distinct SV. In Section 6.4.5, we investigate the modelling differences of b hadrons with lifetimes large enough to reach the CMS tracker and those that do not reach it.

Most b hadron decays are well described by the *spectator model* where the decay of the hadron is modelled by the b quark decay without including the other quark [21], [278], [279].

There can be either hadronic (2/3 of the times) or semileptonic (1/3 of the times) b hadron decays[17]. The transition $b \to u$ is suppressed with respect to the decay $b \to c$, which, in turn, can decay leptonically again. In this way, the neutrino proportion in the decay products of b hadrons is usually larger than for other quarks, distorting the relation between the quark energy and the measured hadron energy. In addition, b or c quarks have a larger mass and a harder fragmentation, which helps to distinguish b and c hadrons from other hadrons.

In Run 2, the typically used b tagging algorithm is DeepCSV, besides the older CSVv2 tagger. Both of them output a discriminant value of $0 < x < 1$, where a higher value corresponds to a higher probability of the jet stemming from a b quark. A specific threshold in the discriminator value is called a b tag working point (WP). Three WPs are created, "loose" (L), "medium" (M), and "tight" (T), which correspond to misidentification probability of 10 %, 1 % and 0.1 %, respectively. A tighter WP decreases both the b jet efficiency and the b jet misidentification efficiency. The newer Particle Net algorithm, not yet used in Run 2, can perform jet flavour discrimination, jet energy calibration, and other tasks at the same time [281], [282]. Instead of relying on typical convolutional neural networks, Particle Net relies on graph neural networks to represent particles in a jet as an unordered set of constituents.

The input distributions used for training the taggers have some data-to-MC disagreements, thus the efficiency of b tagging is different for data and MC. This is corrected for using per jet SF, such that, $SF_f = \varepsilon_f^{\text{data}}(p_T, \eta)/\varepsilon_f^{\text{MC}}(p_T, \eta)$, applied to MC as a weight to the events, where $\varepsilon_f^{\text{data/MC}}$ is the efficiency of the flavour f in the data or MC. Consequently, no bin migration occurs and the number of b tagged jets in the event stays the same before and after applying the weights. SFs are obtained from dijet events enriched in muons (methods such as RelPt or LifeTime [277], [283]) and $t\bar{t}$ events in the dilepton decay channel (kinematic method, tag-and-probe method [277]). For example, in the kinematic method, a discriminant is built using only the kinematic properties of the $t\bar{t}$ dilepton channel, such as the top mass. SFs are obtained by comparing the total number of b jets, tagged and not tagged, obtained from the data, with the number of b expected to get tagged or not tagged, obtained from the MC. Thus, without knowing the truth information of the jet, the data-to-MC SF can be obtained using the total number of jets tagged. In a similar way, SFs are also obtained for not-tagged jets.

5.6. Jet Energy Corrections

Ideally, jets would have a one-to-one correspondence with the initial hard parton generated in the ME. However, the parton showers and hadronization cause jets to deviate from the initial partons. In addition, PU particles from several different PVs can overlap, creating jets hard enough to pass the selection criteria, called PU jets. Thus, instead

[17] In principle also fully leptonic decays are possible but not detected so far [280].

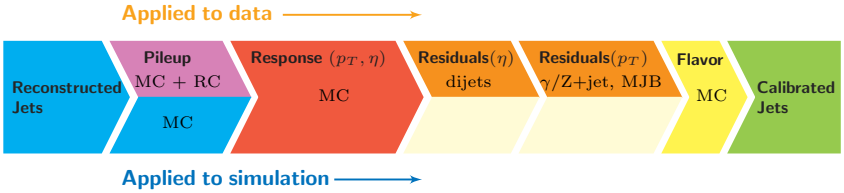

Fig. 5.2. JEC scheme in CMS Runs 1 and 2 [284]. Flavour MCs are optional but used in the Δm_t analysis. The top shows the corrections applied to data, and the bottom shows the corrections applied to MC.

of matching the detector-level jets to partons, they are usually corrected to particle-level jets. This removes effects like the losses in the detector, e.g. due to dead material and the detector non-compensation, PU, out-of-cone radiation escaping the jet, and UE contaminating the jet cone. Since different jet algorithms produce different jet shapes, the idea of a jet itself is ambiguous. However, as long as the same IRC definition is used for particle-level and detector-level jets, a theoretically well-described comparison of experimental and theoretical results can be achieved. In CMS, the scheme to correct jets in Run 2 is shown in Fig. 5.2. It is factorised in several steps, each responsible for removing the corresponding effects. In the following, these steps will be explained in order.

The additional energy that the jet acquires due to PU particles flying into the jet area is called the offset. Pileup can be characterised by the median energy density, ρ, the number of good PVs, N_{PV}, and the average number of PU interactions, μ. The latter is obtained from the measurement of the instantaneous luminosity once per luminosity section, which is about 23.3 s long. Usually, $N_{PV} < \mu$ because not all PVs get reconstructed. Given the 25 ns bunch spacing, not all of the signal gets fully captured in HCAL and ECAL, leading to PU contributions from the collisions immediately preceding and following the collision of interest [246]. This contribution is called out-of-time pileup (OOT PU), contrasting with in-time pileup (IT PU) from the same collision event.

The charged hadron subtraction (CHS) method is applied to eliminate IT PU from charged particles. Here, all tracks pointing at PVs except for the leading PV are removed from the jets. The remaining neutral and OOT PU is removed using the hybrid jet area method. In this method, the jet energy is corrected for by a factor that depends on ρ, η, p_T, and the jet area, A. Here ρ is a per-event variable and the rest are per-jet variables. The correction factor is obtained from simulated events composed uniquely of jets produced through QCD, referred to as QCD multijet events. It is calculated by comparing the jet p_T in the same event with and without including PU in the event. Jets are matched to each other requiring $\Delta R < 0.2$, which assumes that jet directions are not affected significantly by adding PU. The matching is at least 80 % (98 %) effective for jets with p_T =10 GeV (p_T =30 GeV). The missing unmatched jets are mostly created by PU jets These jets are often removed using a PUJetID discriminator [256]. The remaining

data-to-MC JECs are obtained using the random cone (RC) method on MB data. These corrections are applied to data to match the MC.

It should be noted that in Run 3, a different approach is employed to remove the neutral PU. It is done using the pileup per particle identification (PUPPI) algorithm, where a weight to each neutral particle is assigned based on the vicinity of the particle [256], [285]. This weight, used to differentiate the neutral particle from the leading and subleading PVs, is derived from a multivariate fit.

After the PU offset is removed, further steps correct for the detector losses. These are first obtained in MC simulations (MC-truth corrections), after which the residual variation is obtained from data-driven techniques. In the MC-truth corrections the reconstructed-level p_{T} ($p_{T,\mathrm{reco}}$) after offset removal is corrected to match exactly the particle-level p_{T} ($p_{T,\mathrm{ptcl}}$). Since $p_{T,\mathrm{reco}}$ is smeared by detector effects, the jet energy response $R = \frac{p_{T,\mathrm{reco}}}{p_{T,\mathrm{ptcl}}}$ is a distribution similar to the one shown in Fig. 5.3. MC-truth corrections thus shift the JES, namely the mean (or median) of this distribution, to 1. The corrections are obtained in bins of η and as functions of $\langle p_{T,\mathrm{reco}} \rangle$, where $\langle p_{T,\mathrm{reco}} \rangle$ is the average $p_{T,\mathrm{reco}}$ in the given bins of $p_{T,\mathrm{ptcl}}$ and η. The particle-level objects used in the clustering are all the particles with proper lifetimes so that $c\tau > 10\,\mathrm{mm}$. Neutral pions π^0 are not considered stable, but instead the photons created in their decays in the detector are considered for the particle-level jets. It should also be noted that in CMS neutrinos are not included in the particle-level jets.

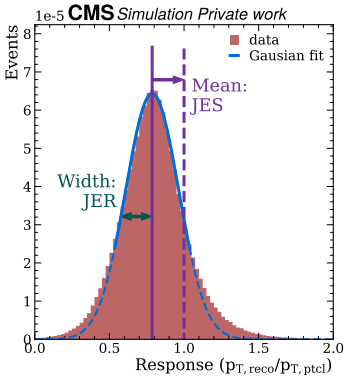

Fig. 5.3. Jet energy response distribution showing its mean, jet energy scale (JES), and the width, jet energy resolution (JER).

The terms relative (L2) and absolute (L3) correspond to η-dependent and p_{T}-dependent corrections, respectively. The MC-truth corrections used to be obtained separately as p_{T}-dependent and η-dependent corrections, but now both corrections are obtained in one step. The residual η-dependent and p_{T}-dependent corrections remove the remaining small ($\mathcal{O}(1\,\%)$) data to MC differences in the jets. Both exploit the principle that the p_{T} of all objects in the event should balance out. η-dependent residual corrections are obtained using either the p_{T} balance or the missing transverse momentum projection fraction (MPF) method using QCD dijet events, i.e. events with two jets of almost the same p_{T} going in the opposite directions. There, a jet (at $|\eta| < 5.2$) energy scale is corrected relative to the reference jet sample with $|\eta| < 1.3$. In this way, the JES of the jets in all η is matched to the jets at $|\eta| < 1.3$.

p_{T}-dependent residual corrections are obtained using Z+jet and γ+jet events and balance the jet with respect to a precisely measured object, Z or γ, respectively. For very

hard jets with $p_{\mathrm{T}} > 800\,\mathrm{GeV}$, they are constrained using QCD multijet events, where a jet is balanced by a recoil system of two or more jets. First, an absolute factor for the correction is obtained using the $\mathrm{Z}(\rightarrow \mu\mu)$+jet events. Subsequently, the p_{T} dependence is corrected using a global fit of all the aforementioned processes. The function used for the p_{T} dependence in the global fit is linear

$$a + b(f_{\mathrm{HCAL}}(p_{\mathrm{T}}) - f_{\mathrm{HCAL}}(p_{T,\mathrm{ref}})), \tag{5.2}$$

where $p_{T,\mathrm{ref}}$ is the chosen reference p_{T} with respect to which the response is corrected and f_{HCAL} is a shift of the PF jet energy at the given p_{T} that is caused by a constant shift of HCAL $\pi^{\pm}$ response (see, also Fig. 6.27). At $p_{T,\mathrm{ref}}$, the uncertainty of the global fit is the lowest.

Detector effects do not only shift the JES, but also smear the jet energy response distribution itself in the data. The JER, i.e. the width of the distribution, in MC needs to be smeared to match the distribution in the data. Usually, one of two different approaches is used to achieve this. In the scaling method $p_{T,\mathrm{reco}}$ is shifted, according to

$$p_{T,\mathrm{reco}} \rightarrow p_{T,\mathrm{reco}} + (s_{\mathrm{JER}} - 1)(p_{T,\mathrm{reco}} - p_{T,\mathrm{ptcl}}), \tag{5.3}$$

where s_{JER} is a data/MC scale factor obtained from dijet and γ+jet events. Although simple, the scaling method only smears jets that have a match to a particle-level jet, i.e. missing some low p_{T} or PU jets. In the stochastic method, JER is smeared using a normally distributed random variable, $p_{T,\mathrm{reco}} \rightarrow p_{T,\mathrm{reco}} \cdot c_{\mathrm{JER}}$, where

$$c_{\mathrm{JER}} = \mathcal{N}\left(1, \sigma_{\mathrm{JER}}\sqrt{\max(0, s^2_{\mathrm{JET}} - 1)}\right). \tag{5.4}$$

Here, $\mathcal{N}(\mu, \sigma)$ represents a normally distributed number with a mean μ and a standard deviation σ. In Eq. (5.4), the max function represents the fact that the stochastic method is only able to increase JER. However, it is rarely the case that the JER in the data is better than the one in MC. In CMS, it is recommended to use a hybrid approach where the scaling method is used when a match for a jet is available, and the stochastic method is used otherwise.

After all the mandatory CMS JECs described above, optional flavour-dependent JEC (flavour corrections, L5 corrections) obtained from the MC can be applied. These take into account the fact that different flavour jets have different fragmentation patterns and behave in the detector differently. In addition, flavour uncertainties account for the mismodelling of each individual jet flavour. These uncertainties are mandatory in CMS for all analyses that use jets. The flavour corrections and flavour uncertainties will be discussed in Chapter 6. All the steps mentioned above come with a separate set of uncertainties.

Some calorimeter regions produce anomalously high or low jet rates or responses. For these regions either separate sets of JEC can be derived or these regions can be removed altogether using jet veto maps. In the Δm_t measurement the latter approach is taken.

5.7. Lepton energy corrections, identification, and data to MC scale factors

Similarly, as explained for jets in Section 5.6, the reconstructed muon, electron and photon energy values contain a bias and the width of $E_{\text{reco}}/E_{\text{gen}}$ is usually narrower in MC than in the data [286]. Superclusters in the ECAL forming electrons and photons obtain a bias due to possible shower leakage outside of the supercluster or in the intermodule gaps and dead crystals. Electron energy corrections are derived in two stages. The first stage uses MC events with two electrons and two photons. Boosted decision treess (BDTs) are used to improve the scale and resolution of E_{reco}. The inputs used for the BDT algorithm include the energy and position of the supercluster, the number of saturated crystals, and other supercluster parameters. The second stage corrects the residual small data to simulation differences using $\text{Z} \to ee$ events.

For muons, the p_{T} is determined by the track curvature and thus impacted by detector misalignment, the uncertainties in the CMS magnetic field distribution, as well as a limited precision of the reconstructions software. Muon p_{T} corrections are obtained from $\text{Z}/\gamma^* \to \mu\mu$ events using a method developed by a Rochester group, commonly referred to as Rochester corrections [287]. For muons no additional SF to match the resolutions in data and MC are necessary as the resolution in data is very good.

The relative isolation helps to distinguish prompt leptons, i.e. originating in hard processes, from leptons originating in hadron decays. In CMS the relative PF isolation I_{rel} is typically calculated as

$$I_{\text{rel}} = \frac{\sum_{CH} p_T^{CH} + \max\left(0, \sum_H p_T^{NH} + \sum_\gamma p_T^\gamma - 0.5 \sum_{PU} p_T^{PU}\right)}{p_T^l} \tag{5.5}$$

where the sums run over all particles within $\Delta R < 0.4$ of the lepton, and indices CH, NH, γ, and PU correspond to the charged hadrons, neutral hadrons, photons and pilup particles, while p_{T}^l is the lepton p_{T}. The value describes the amount of additional activity around the lepton, so an isolated lepton should have a lower value of I_{rel}.

For electrons and muons, IDs are used to clear the set of reconstructed leptons from fake leptons and only keep the leptons with sufficient reconstruction quality. The electron ID used in CMS is typically based on a tuned set of selection criteria. Several WPs are made based on the requirements for the given lepton: tight, medium, loose, and veto. Tighter WPs are attempting to achieve a better separation of prompt leptons, from leptons originating in hadron decays. The ID criteria consist of one set for $|\eta| < 1.479$ and one set

for $|\eta| > 1.479$ as described in [288]. The requirements include a p_{T} dependent relative isolation requirements (e.g. for the tight WP, $I_{\mathrm{rel}} < 0.0287 + 0.506 p_{\mathrm{T}}$ for $\eta < 1.479$ and $I_{\mathrm{rel}} < 0.0445 + 0.963 p_{\mathrm{T}}$ for $\eta > 1.479$). Further requirements include a selection criterion on hadronic and electron calorimeter deposit ratio, number of missed inner hits and others.

Muon identification is built from optimised selection criteria where tight selection attempts to select a highly pure set of prompt muons, but with $2-3\,\%$ inefficiency. Loose WP selects muons with a high efficiency and a small number of fake muons, but also includes muons from quark decays. Selection criteria are based on variables such as the fraction of valid hits in the inner tracker and the χ^2 value of an algorithm that matches the standalone muon track to the tracker muon track.

Efficiencies to reconstruct leptons are also different in data and MC. For muons these efficiencies are factorised in three steps:

$$\varepsilon_{\mathrm{ID|TRK}} \cdot \varepsilon_{\mathrm{Iso|ID}} \cdot \varepsilon_{\mathrm{Trigger|Iso}}, \tag{5.6}$$

where, e.g. $\varepsilon_{\mathrm{ID|TRK}}$ represents the efficiency (probability) that an initial tracker muon will pass the identification criteria. Similarly with the other two ε terms. Data-to-MC SF factors are obtained using the tag-and-probe method using $\mathrm{Z} \to \mu\mu$ events [289], [290]. In CMS they are available in a single file, where each SF can be easily found.

For electrons isolation criterion is already included in the identification criteria and there is no need to separate it, thus the factorization is as follows

$$\varepsilon_{\mathrm{Reconstruction}} \cdot \varepsilon_{\mathrm{ID+Iso|TRK}} \cdot \varepsilon_{\mathrm{Trigger|ID+Iso}}. \tag{5.7}$$

The appropriate data to MC SFs for each of the terms in Eq. (5.7) are derived from $\mathrm{Z} \to ee$ events and have to be applied.

6. FLAVOUR-DEPENDENT JET ENERGY CORRECTIONS AND QUARK-ANTIQUARK RESPONSE ASYMMETRY

6.1. Introduction

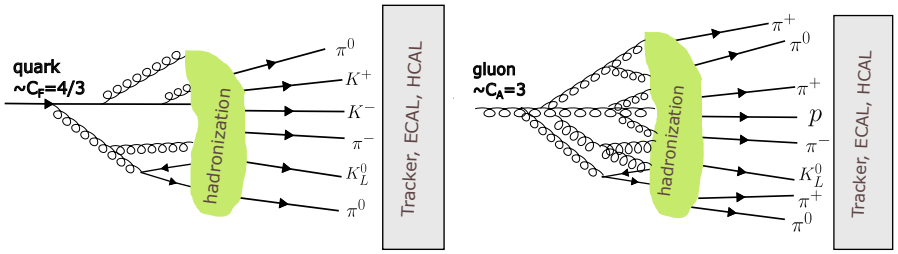

Fig. 6.1. Schematic picture of the differences between a quark jet (left) and a gluon jet (right). Gluon jets have a larger particle multiplicity and a wider jet radius. The hadron content between the jets also differs, for example, jets initiated by strange quarks have a higher probability of producing kaons (strange hadrons).

As described in Section 5.6, jets clustered from particle-level constituents and from reconstructed particles differ. In CMS, these effects are typically accounted for using JEC obtained from the QCD dataset dominated by gluon jets. Nonetheless, the response varies depending on the flavour of the jet due to differences in jet fragmentation [291]. Response-varying effects include hadron content differences [220], the momentum spectrum of the constituent hadrons, and the shape of the jet [276]. The differences in jet flavour are schematically depicted in Fig. 6.1. For instance, light quark jets (u, d) tend to exhibit the highest energy response, while gluon jets present a comparatively lower response. This is due to the larger gluon Casimir colour factor leading to gluons fragmenting into a greater number of softer particles, with a wider spread in the detector. This can also cause the deposits in some of the calorimeter cells to fall below the detector thresholds and thus reduce the energy response. Moreover, the potential mismodelling of the jet fragmentation across different flavours leads to flavour uncertainty. Although residual JEC corrects for possible mismodelling through data-driven approaches, the flavour uncertainties become pertinent when the flavour composition of the sample differs from the composition of the Z+jet and γ+jet samples at the reference point value of $p_{\mathrm{T}} = 208\,\mathrm{GeV}$ and $\eta = 0$ used for the global fit.

The necessity for flavour-dependent JEC (flavour corrections) is to facilitate the estimation of the flavour uncertainties and to bring into agreement the gluon-jet-dominated dijet and quark-jet-dominated Z+jet samples used to derive the L2 and L3 corrections. In addition, analyses relying on b jet identification, such as the top quark mass measurement, would benefit from the correction of the b jet to light quark jet response. Such a correction is applied in the Δm_t measurement as described in Section 7.2.1. On the contrary, the flavour uncertainty is necessary for all the analyses using jets in CMS. The uncertainty

associated with b jets has emerged as the dominant uncertainty in some analyses, such as the top-quark mass measurement [92], while the gluon jet uncertainty is one of the leading in measurements of α_s [292]–[295] or cross-section measurements of the $t\bar{t}$ + jet process [296].

Flavour corrections are usually derived using MC-truth methods as an extension of the inclusive JEC derivation procedure described in Section 5.6. The difference is that for flavour corrections the sample of jets is split according to the jet flavour. Data-driven techniques have also been attempted that involve, e.g. extensions of the residual Z+jet and γ+jet analyses where the jet is required to be b tagged [297], [298]. The Z+b response has been found to be consistent with the Z+jet response within the systematic uncertainty and thus shows to require no correction for b jets. Yet the systematic uncertainty, typically around 1 %, remains larger than that of MC-driven analyses. Other promising data-driven alternatives include dijet balancing techniques, which rely on quark/gluon discrimination using graph neural networks [299], [300]. Although these initial studies produced estimates for flavour-dependent JES from data in good agreement with simulations from the PYTHIA 8 Monte Carlo (MC) event generator, they revealed discrepancies when compared to the HERWIG 7 MC event generator and require further consistency checks. As a result, data-driven methods have so far primarily served only as a validation of the MC-driven results.

The previous CMS flavour corrections were obtained using a QCD dijet sample generated by PYTHIA 6 (Z2* tune), while the flavour uncertainties were obtained from the differences against a HERWIG++ (EE3 tune) dijet sample [284]. Additionally, a private set of corrections using HERWIG++ and PYTHIA 8 was derived with early Run 2 samples [301]. In this study, we repeat the work using PYTHIA 8 (CP5 tune) for the flavour corrections and a comparison to HERWIG 7 (CH3 tune [302]) for determining the flavour uncertainties. Instead of only using the dijet sample, we do simultaneous fits of the QCD dijet, DY (or Z+jets), and $t\bar{t}$ samples, in addition to a fit of the $t\bar{t}$ sample individually. Alternative MC-truth methods for the estimation of jet flavour uncertainties exist, for example, by splitting the flavour uncertainty into three components: hadronization, shower and UE+shower as done by ATLAS [303]. These rely on the interface of the SHERPA event generator to use the PYTHIA Lund string model instead of the default AHADIC++ clustering model. In this study, however, we continue the approach previously used in CMS, estimating the flavour uncertainty through differences between HERWIG (angular-ordered shower + cluster hadronization) and PYTHIA (p_T-ordered dipole shower + Lund string hadronization).

This section contains a description of the experimental studies performed by the author of this Thesis. It begins with a description of the samples utilised in this analysis and the criteria for event and jet selection as outlined in Section 6.2. Then, the methodology and the results of the flavour corrections are covered in Section 6.3 followed by the methodology and results of the flavour uncertainties in Section 6.4. Moving forward,

Section 6.5 provides an analysis of jets resulting from gluon splittings and prompt quarks to explain differences in the responses across various physics samples. Subsequently, Section 6.6 addresses uncertainties for flavour vs antiflavour jets, employing similar principles used for flavour uncertainties. These uncertainties are crucial for the Δm_t measurement discussed in Chapter 7, which is the main focus of the author's Thesis. Lastly, the findings and conclusions are summarised in Section 6.7.

6.2. Technical details

6.2.1. Monte Carlo samples

Here, we summarise the MC samples utilised for the derivation of the flavour corrections and flavour uncertainties in this analysis, while the full dataset names as available in the CMS Data Aggregation System are listed in appendix A. The *flavour corrections* are obtained from a simultaneous fit of three distinct physical processes, QCD dijet, $t\bar{t}$ and Z+jets production, as well as from individual fits of $t\bar{t}$ and QCD. The corrections are obtained for both PYTHIA 8 and HERWIG 7 showered samples. The *flavour uncertainties* are obtained from a simultaneous fit of the PYTHIA 8 and HERWIG 7 differences of the same three physical processes. This is in contrast to the Run 1 flavour uncertainties, where only the QCD sample was used [284]. Including the $t\bar{t}$ process enhances the data with more events featuring b quark jets. The Z+jets process is added because it is used in the residual data/simulation JEC CMS. PYTHIA 8 is used with the CP5 UE tune while HERWIG 7 is used with the CH3 tune.

The QCD samples are generated at NLO in QCD. They have the hard process generated with the MADGRAPH 5_aMC@NLO v2.6.1 program [122] and are matched to a parton shower using the MLM matching prescription with the merging cut at $q_{\text{cut}} = 14\,\text{GeV}$. In addition, a QCD sample generated with a standalone PYTHIA 8 at LO is used only for flavour corrections. The jet p_{T} spectrum of QCD events is intrinsically steeply decreasing, as shown in Fig. 6.2. To ensure a sufficient number of events with jets at large p_{T}, separate datasets for different H_{T} intervals starting from $H_{\text{T}} = 50\,\text{GeV}$ were generated with MADGRAPH and merged according to the cross sections of each dataset. The standalone PYTHIA 8 dataset, on the other hand, is intentionally generated with an almost flat jet p_{T} spectrum as shown in Fig. 6.2 but the events can be weighted to ensure a physical jet p_{T} spectrum.

It can be seen in Fig. 6.2 that except for the low p_{T} bins affected by missing contributions from the $H_{\text{T}} < 50\,\text{GeV}$ samples, the weighted PYTHIA 8 sample has a reasonable agreement with the MADGRAPH samples. For flavour corrections the unweighted PYTHIA 8 sample was used. Although the p_{T} spectrum can bias the jet energy response, no differences were found in the jet energy responses in the relevant p_{T} range between the weighted and unweighted samples, if selecting only the three leading generated jets.

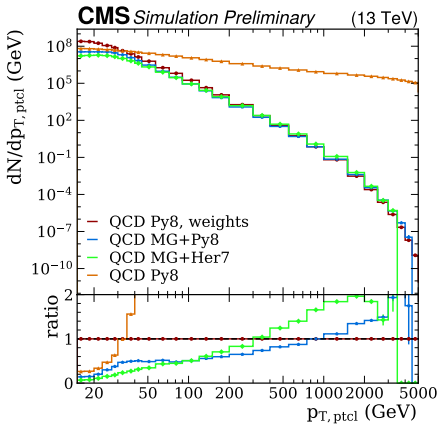

Fig. 6.2. Comparison of the p_T spectra of the QCD samples generated with MADGRAPH+PYTHIA 8, MADGRAPH+HERWIG 7, as well as the weighted and unweighted QCD samples generated with PYTHIA 8.

The $t\bar{t}$ samples are at NLO and have the hard process generated using the hvq programme that is part of POWHEG-Box v2. The Z+jets samples are generated at NLO with MADGRAPH 5_aMC@NLO and matched to a parton shower using MLM matching. All the samples are run through a detailed CMS detector simulation based on GEANT4 [205] to describe the interaction of the final-state particles with the detector.

6.2.2. Event and jet selection

For the Z+jets sample, the selection matches the event selection for the residual JEC analysis performed with the Z+jets sample. For the $t\bar{t}$ and QCD samples, the selection is adapted to have the same event and lepton selection criteria (cuts) as for the Z+jets sample, but a different number of reconstructed leptons is selected and no Z boson window is required. In addition, to improve the agreement between the busy $t\bar{t}$ topology with the other samples, a jet non-overlap cut was added. Comparisons with Run 1 results were made without the non-overlap cut and the impact of the cut on the jet responses is investigated in Section 6.3.5. Specifically, the selection is:

- Select events with at least 1 well-reconstructed PV and require that the leading vertex satisfies $|z| < 24$ cm and $\rho < 2$ cm, where z is the distance from the PV to the beam spot along the beam axis and ρ is the radial distance from the PV to the beam spot.

- Select charged hadron subtraction (CHS) jets clustered via the anti-k_T algorithm with the jet radius $R = 0.4$ (AK4) that have a matched particle level jet within $\Delta R < 0.2$. No cut on the z distance of the jet to the generated vertex from the PV is applied as it was only implemented in JEC starting with Run 3.

- Select leptons:
  - Electrons are required to have $p_T > 25$ GeV, $|\eta| < 2.4$ and pass the tight cut-based ID. No additional isolation requirement is applied as isolation is already included in the cut-based ID.
  - Muons are required to have $p_T > 20$ GeV, $|\eta| < 2.3$, pass the tight cut-based ID and pass the tight PF isolation working point.
- Events with exactly 2 reconstructed electrons or 2 reconstructed muons are selected for the Z+jets sample. For the $t\bar{t}$ and QCD samples, events, where the number of reconstructed leptons matches the number of generated prompt (coming from the hard process) leptons, are selected. This helps to automatically catch the cases of all three $t\bar{t}$ decay channels (which can have 0, 1 or 2 generated leptons) and QCD (with 0 generated leptons).
- For the Z+jets sample, the invariant mass of the two leptons is required to be within 20 GeV of the Z boson mass, $|m_{ll} - m_{Z,pdg}| < 20\,\text{GeV}$, and the sum of the transverse momenta of the two leptons should be $p_{T,l_1} + p_{T,l_2} = p_{T,Z} > 15\,\text{GeV}$.
- The jets are further required to have the tight lepton veto jet id [18].
- Since the tight lepton veto jet id does not clean all the leptons from the jet collection, the jets are required to have $\Delta R > 0.4$ from any of the selected leptons.
- The matched particle level jets are required to have $p_T > 15\,\text{GeV}$.
- The events are required to fulfil $\alpha = \frac{p_{T,\text{2nd jet}}}{p_{T,Z}} < 1$ for Z+jets sample. No stronger α cut is imposed as it creates a bias for events with a large PU contribution.
- Select the three (two) leading generated jets for the QCD (Z+jets) sample.
- Jets are required to be separated by at least $\Delta R = 0.8$ from each other (non-overlap cut).

In addition, to remove soft parton shower jets, a back-to-back condition, $\Delta\phi < 2.7$, was tested. In the dijet case, $\Delta\phi = \Delta\phi(j_1, j_2)$ and in the Z+jets case $\Delta\phi = \Delta\phi(Z, j_1)$ were used, where j_1 and j_2 are the hardest jets in the event. However, as shown in Fig. 6.3, the cut removes almost 2/3 of the Z+jets events. Since the tight lepton cut was already harsh on removing events, this additional cut makes the sample almost unusable for any fits. While for the dijet sample, the cut removes a less significant amount of events and the agreement among the datasets was seen to improve slightly, it was deemed more important to keep the cuts consistent among the datasets.

[18] Tight lepton veto id cleans jets that are originating as leptons. Since all the final-state particles enter the jet clustering also leptons get clustered inside them.

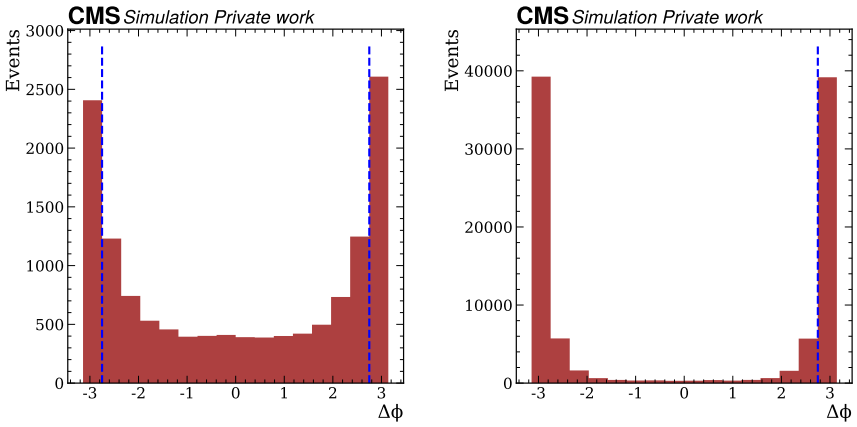

Fig. 6.3. The distribution of $\Delta\phi = \phi_{j_{1,ptcl}} - \phi_{Z,ptcl}$ in the Z+jet sample (left) and the distribution of the $\Delta\phi = \phi_{j_{1,ptcl}} - \phi_{j_{2,ptcl}}$ in QCD dijet events (right). The dashed line shows the back-to-back condition $\Delta\phi > 2.7$ applied on the MC data.

6.2.3. The binning strategy

The determination of JEC was performed using the standard p_T binning used in the CMS jet energy resolution and correction (JERC) group taking the lowest p_T bin to be 15.0 GeV: {15.0, 17.0, 20.0, 23.0, 27.0, 30.0, 35.0, 40.0, 45.0, 57.0, 72.0, 90.0, 120.0, 150.0, 200.0, 300.0, 400.0, 550.0, 750.0, 1000.0, 1500.0, 2000.0, 2500.0, 3000.0, 3500.0, 4000.0, 4500.0, 5000.0, 10000}.

Since the flavour corrections are $\mathcal{O}(10)$ smaller than the L2L3 corrections and the samples are split into flavours of smaller flavour fractions, the standard η binning was changed to {0.000, 0.261, 0.522, 0.783, 1.044, 1.305, 1.566, 1.740, 1.930, 2.043, 2.172, 2.500, 2.964, 5.191}, with the inverse for the negative η bins. To improve statistical precision, the positive and negative η bins were merged as no significant difference was found between the two sides. Some comparisons use an even coarser η binning in HCAL sections: {0., 1.305, 2.5, 3.139, 5.191}.

The events are split into flavours of b, c, s, u, d, g, and *unmatched* flavours according to the parton flavour.

6.3. Flavour Corrections

6.3.1. Flavour fractions

The flavour content using the parton flavour definition is shown in Fig. 6.4 for different QCD, Z+jet and $t\bar{t}$ samples showered with HERWIG 7 and PYTHIA 8. One can observe how the three different physics processes complement each other by providing data for different flavour jets in different p_T regions. In particular, $t\bar{t}$ provides a large amount

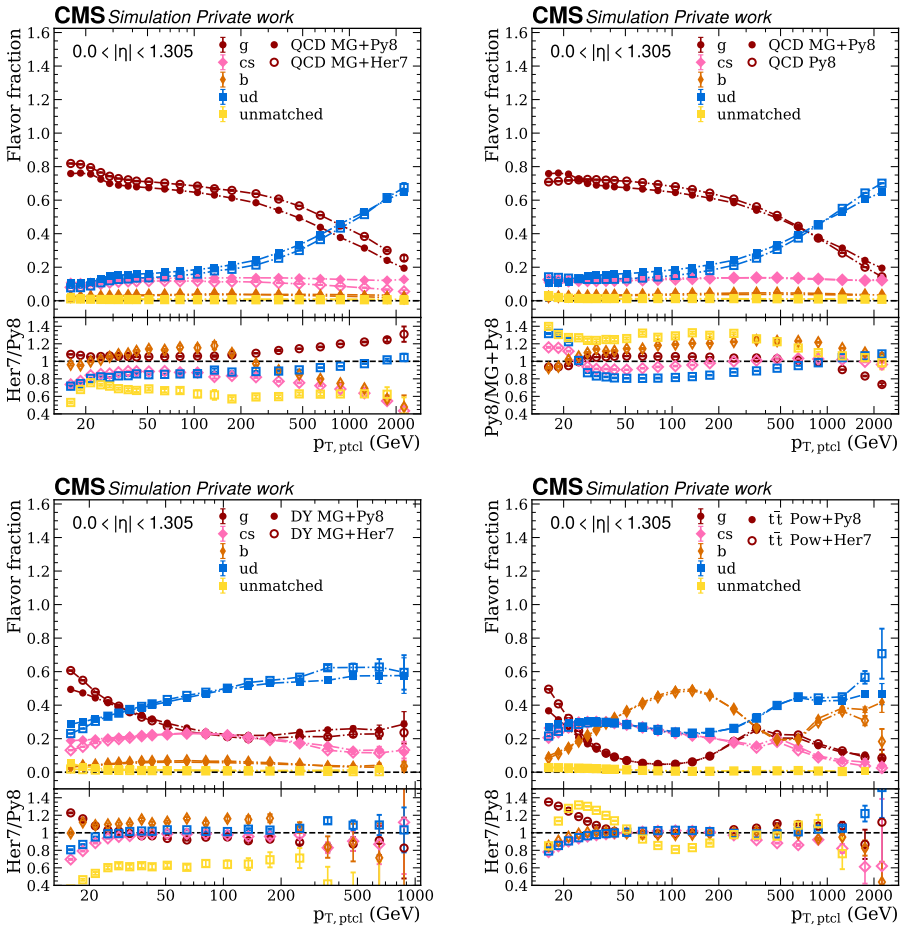

Fig. 6.4. Jet flavour fractions for QCD (top), Z+jet (bottom left) and $t\bar{t}$ (bottom right) samples. Shown are both flavour fractions of the sample showered with HERWIG 7 (open markers) and PYTHIA 8 (filled markers), as well as the sample generated with standalone PYTHIA 8.

of data necessary to improve the b jet flavour uncertainty fits with respect to Run 1. Similarly, the Z+jet sample provides large statistics for light-flavour jets at low p_T while the sample runs out of data at $p_T > 500\,\text{GeV}$, unlike the QCD dataset.

For determining the flavour corrections and flavour uncertainties in Run 1, the physics definition was used. The unmatched jets in this definition, mostly arising from ISR and FSR, were added to the gluon flavour. For the parton flavour in Run 2, jets only stay unmatched if there is no ghost parton clustered inside, which can be caused by a lepton accidentally passing the lepton cleaning or because of unremoved PU. The fraction of unmatched jets is significantly lower for the parton flavour definition than with the physics

definition (compare, e.g. with [284]) and is lower than 1 % for jets with $p_{\mathrm{T}} > 30\,\mathrm{GeV}$. For this reason, the unmatched jets were discarded in this study.

In Fig. 6.4 one can notice a second peak for the b jets in the $t\bar{t}$ dataset above $p_{\mathrm{T}} = 700\,\mathrm{GeV}$. This corresponds to the region where the top quarks become boosted (for $p_{\mathrm{T}} > 400\,\mathrm{GeV}$) and its decay products, a b jet and two light jets, merge into one jet. In the jet assignment, the b jets would take precedence and such jets would be assigned as b jets. Thus, many of the boosted b jets would be contaminated with light jets. Note also that the u+d fractions become larger than c+s fractions above $p_{T,\mathrm{ptcl}} > 150\,\mathrm{GeV}$, where the valence quark PDF starts to dominate.

6.3.2. Response distributions

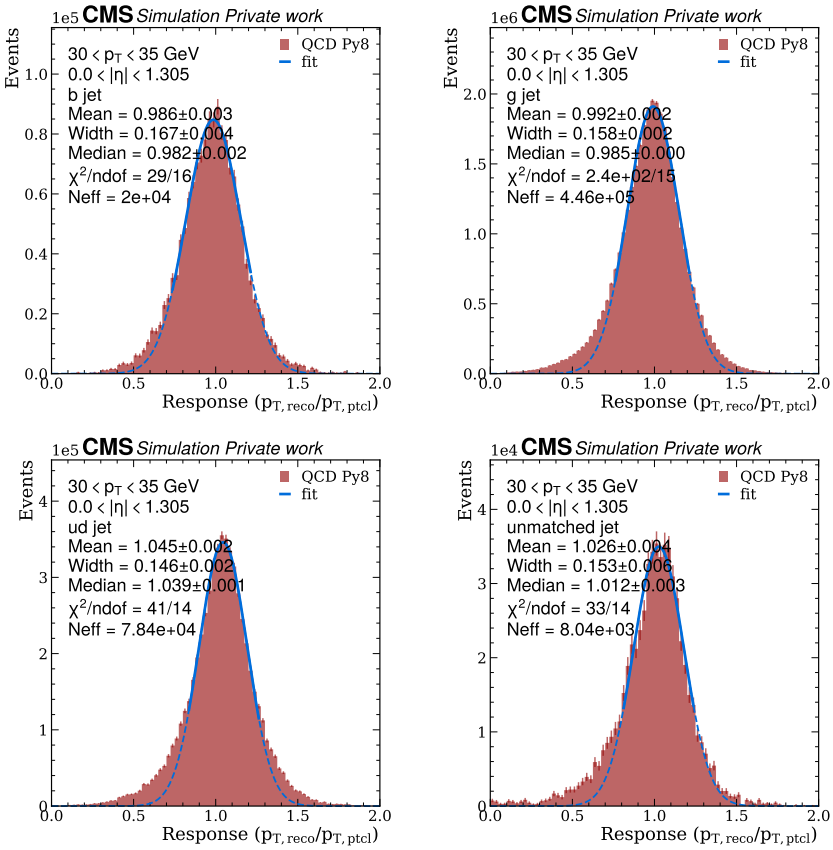

Fig. 6.5. Jet response distributions in the $30 < p_{T,\mathrm{ptcl}} < 35\,\mathrm{GeV}$ and $0 < |\eta| < 1.305$ for four different jet flavours for the QCD sample, generated using PYTHIA 8. The median and its uncertainty are shown as well as the results of the Gaussian fit and N_{eff} in the bin. The fit result is shown by the solid blue curve within the fit limits and by the dashed blue curve ouside its limits.

The jet energy response is obtained using $R = \frac{p_{T,\text{reco}}}{p_{T,\text{ptcl}}}$, where $p_{T,\text{reco}}$ is the p_T of the reconstructed jet and $p_{T,\text{ptcl}}$ is the p_T of the particle-level jet. The response distributions for different jet flavours in the $20 < p_{T,\text{ptcl}} < 23\,\text{GeV}$ and $0 < |\eta| < 1.305$ bin for the QCD sample generated using PYTHIA 8 are shown in Fig. 6.5. For further calculations, the median of the distribution is used, as in the MC truth analyses it was found to give a better closure at low p_T and to be more stable than the fitted mean [304]. The standard deviation of the median is obtained assuming that the distribution is Gaussian, that is, $\sigma = 1.253 \cdot \text{RMS}/\sqrt{N_\text{eff}}$, where RMS is the root-mean-squared of the distribution and N_eff is the effective number of entries in the distribution. If $N_\text{eff} < 50$ in the given p_T and $|\eta|$ bin, the bin is discarded from further calculation. The median and its uncertainty are shown in the figure. The Gaussian fit is performed three times, the first time in the entire response range, while the second and third fits are performed in the range $\{\mu - 1.5\sigma; \mu + 1.5\sigma\}$ of the previous fit results, where μ (σ) is the fitted mean (width) value. The fitted mean, its width, and the χ^2 value of the last Gaussian fit are shown as well for comparison.

The response distributions are in general well represented by a Gaussian distribution, while sometimes having a slightly larger tail at low responses, especially seen for the unmatched jets. This tail can be removed by adding a cut on the z distance from the generated vertex to the primary vertex, as is done for the Run 3 PUPPI jet MC truth studies. For the CHS jets, where the JEC chain also includes L1 corrections to account for PU, such a cut is not necessary.

6.3.3. Median responses of the QCD PYTHIA 8 sample for the sample inclusive in jet flavour

All the standard JECs are applied to jets before performing the studies. Nevertheless, when obtaining JEC on the sample inclusive in jet flavour, some non-closure is observed as displayed in Fig. 6.6. The closure plot is obtained using the QCD sample generated using PYTHIA 8 and without the jet non-overlap cut, i.e. the same sample used to derive all the applied JEC corrections and the same cuts. At $p_{T,\text{ptcl}} > 100\,\text{GeV}$, the closure is consistent with what was derived for the MC truth corrections [304]. The median response at $0.0 < |\eta| < 1.305$ does not deviate from 1 by more than one per-mille. However, at low $p_{T,\text{ptcl}}$ in the same $|\eta|$ bin, the closure deviates by around 0.5 % more than what was seen in the MC truth analysis. The non-closure could be caused by the differences in the analysis frameworks but is not expected to affect the flavour corrections and uncertainties. For all further studies, the median values of the jet response in each $|\eta|$ and $p_{T,ptcl}$ bin are divided by the inclusive median jet response values of the PYTHIA 8 QCD sample to compensate for the non-closure. In other words, the responses for each jet flavour are obtained with respect to the inclusive PYTHIA 8 QCD sample. The results for the normalised inclusive flavour (*all*) are also derived and saved in the correction files.

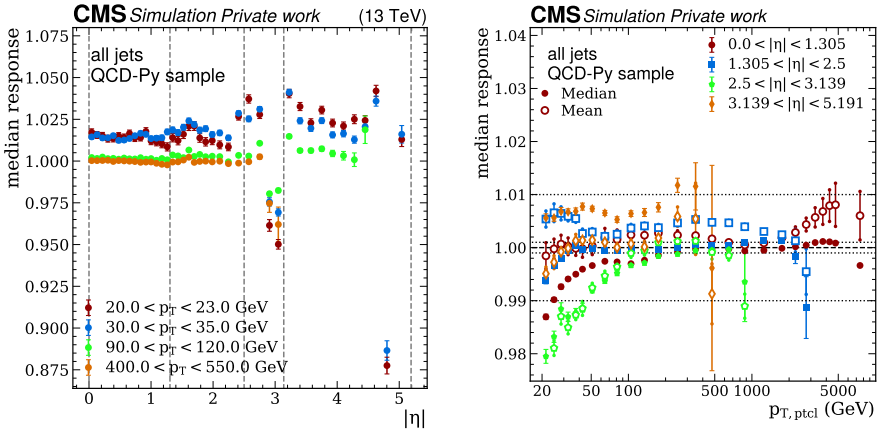

Fig. 6.6. Median (full markers) and mean (open markers) response vs jet $|\eta|$ in different $p_{T,ptcl}$ bins (left) and response vs $p_{T,ptcl}$ in different jet $|\eta|$ bins (right) for the sample inclusive in jet flavours after applying the L1-L3 corrections. The responses are obtained on the QCD sample generated using PYTHIA 8.

6.3.4. Comparison of the median responses between the top-pair, Z+jet and QCD data sets

In this section, the agreement between the median responses for all four samples showered with PYTHIA 8 is examined. Jets are selected using the criteria presented in Section 6.2.2, including the jet non-overlap cut. Fig. 6.7 shows the median jet response vs $p_{T,ptcl}$. All responses are normalised to the response of the inclusive jet flavour of the QCD dataset generated using PYTHIA 8. See, e.g. how the response for the inclusive "all" sample for the QCD PYTHIA 8 dataset falls exactly on 1.00. The results are shown for six different jet flavours in the most central $|\eta|$ bin. For the samples showered with HERWIG 7, the comparison is shown in appendix B. Significant disagreement was found for the two QCD samples at $p_{T,\text{reco}} < 50\,\text{GeV}$. This disagreement is likely caused by QCD datasets starting at $p_T = 15\,\text{GeV}$ (in the PYTHIA 8 sample) or minimum $H_\text{T} = 50\,\text{GeV}$ (in the MADGRAPH+PYTHIA 8 sample), limiting the phase space and biasing the responses towards lower values.

The MADGRAPH+PYTHIA 8 disagreement can also be explained by a non-ideal matching of the hard process and the shower (inappropriate q_cut and/or matching scale, q_match). Fig. 6.8 shows the differential jet rate (DJR) for the $2 \to 3$ and for the $3 \to 4$ transition. DJR measures the scale at which the transition between n jets to $n+1$ jets takes place [305]. The distribution shows cases where there are 2, 3 or 4 initial hard partons generated by the hard process. Jets can be created by either the matrix element generator (above q_match) or by the parton shower (below q_match). For a well-matched sample, the DJR distribution is expected to be smooth in the transition region. However, it is seen that 2 jets do not transition well into the 3 jets, and a sharp discontinuity is observed.

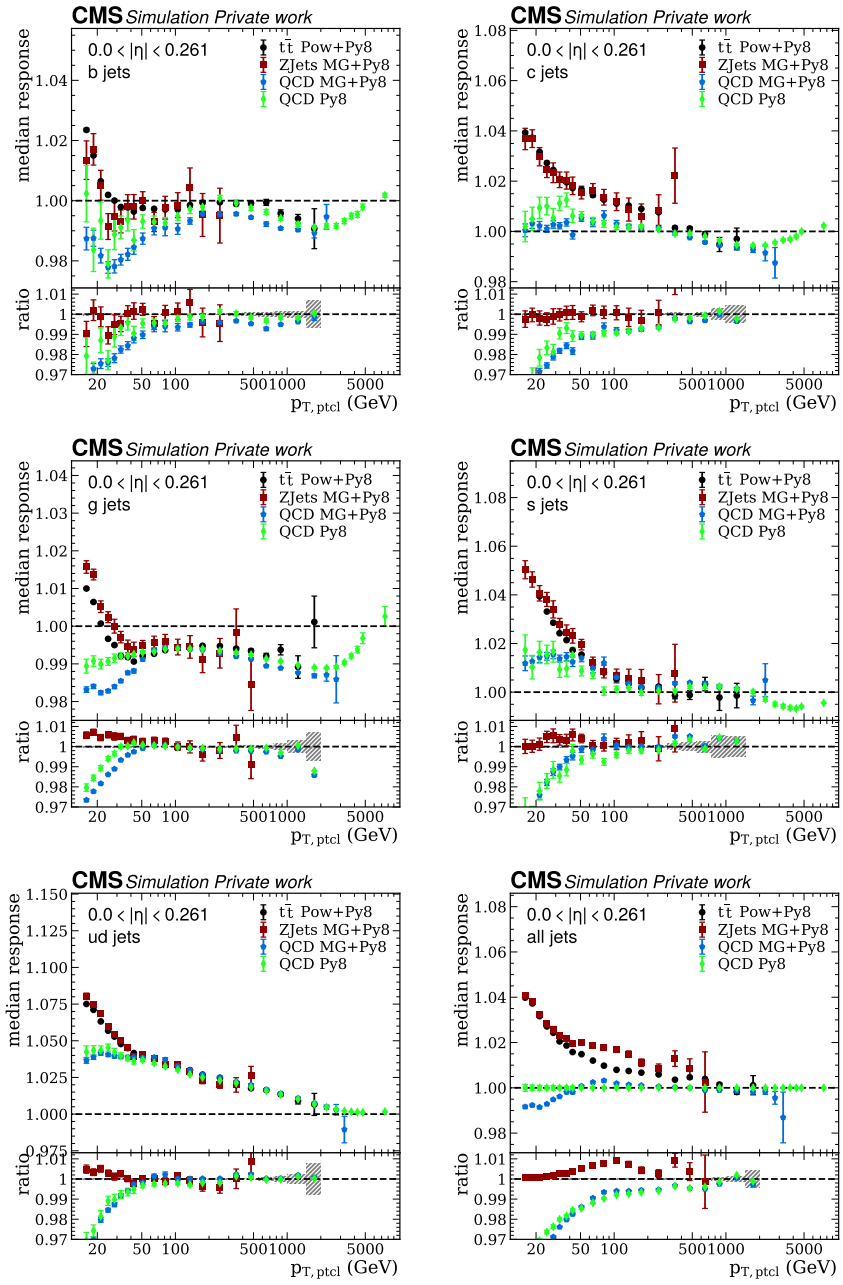

Fig. 6.7. Comparison of the median of the jet energy response for four MC physics samples. Results are shown in the $0 < |\eta| < 0.261$ bin for six different jet flavours.

This can explain the disagreement between the two QCD datasets even at large $p_{T,\text{reco}}$ values.

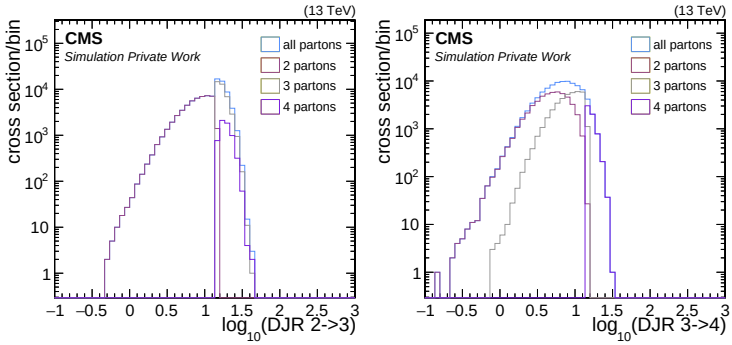

Fig. 6.8. Differential jet rate for the $2 \to 3$ (left) and $3 \to 4$ (right) transition for the QCD sample generated using MadGraph+pythia 8. The x-axis is the $\log(Q)$, where Q is the jet virtuality.

As seen in Fig. 6.7, the $t\bar{t}$ and Z+jet samples agree within 1 %, but outside of the statistical uncertainties. The largest disagreement is for the g and b jets below a $p_{T,\text{ptcl}}$ of 50 GeV. The agreement between these two datasets and the QCD pythia 8 dataset becomes good for $p_{T,\text{ptcl}} > 50\,\text{GeV}$. A sharp transition can be observed for the c correction in the QCD MadGraph+pythia 8 dataset. Below $p_{T,\text{ptcl}} \approx 300\,\text{GeV}$ the MadGraph+pythia 8 QCD dataset highly disagrees with the rest, while above that the datasets start to agree.

While the cuts on the events and jets try to ensure that the selected jets are consistent between the three physics processes, there are still intrinsic differences between them. For instance, b jets coming from a $t\bar{t}$ process are mostly in the range of $50\,\text{GeV} < p_{T,\text{ptcl}} < 300\,\text{GeV}$, seen also in the flavour fractions Fig. 6.4, and would have a larger overlap with the light jets coming from the same top quark. On the other hand, b jets that come from the QCD process have a constantly falling distribution over p_T. In Section 6.3.5 the same comparison after repeating the computation with the non-overlap cut removed is shown. It can be seen that the cut improves the agreement between the datasets. Thus, the cut was added to the general JEC cut scheme. In addition, response distributions from a custom colour flip $t\bar{t}$ sample were compared to a normal $t\bar{t}$ sample. In the colour flip sample, the colour connections between the W bosons and top quarks are artificially swapped with colour connections with the beam causing more radiation to be added between the W bosons and the beam instead of between the W boson and the top quark. However, this study did not find a definite explanation for the differences between the physics samples.

6.3.5. Impact of the jet non-overlap cut

This section illustrates the agreement between the datasets presented in the previous section, without applying the jet non-overlap cut. The results are depicted in Fig. 6.9. Compared to in Fig. 6.7, the agreement between the Z+jet and $t\bar{t}$ datasets deteriorates,

in particular the agreement for g jets, which increases from 0.5 % to 1 %. The same is seen for low-$p_{T,\text{ptcl}}$ ud and s jets. The QCD dataset tends to deviate less from the rest compared to the case without the non-overlap cut. However, the overall disagreement at low p_T remains just like the disagreement in c jets. Since the ud flavour was used in the next sections to correct for the QCD low-p_T bias, the agreement in ud quarks was favoured, thus the non-overlap cut was kept in the JEC workflow.

6.3.6. Fits of the median responses

This section shows the methods for fitting the p_T-dependence of the JEC. First, the procedure to obtain the fits on individual datasets is shown. Afterwards, the method of simultaneous fits over all three samples is explained. As was shown above, the jet energy response from jets of different physics samples shows some disagreements, so the combined fit is not always optimal. The final flavour corrections are made available for the QCD PYTHIA 8 dataset, $t\bar{t}$ POWHEG+PYTHIA 8 dataset, and from the simultaneous fit.

For the individual samples

To obtain the correction factors, the inverse of the median responses are fit as a function of $p_{T,\text{reco}} \equiv \langle p_{T,\text{reco}} \rangle$ for each $|\eta|$ bin. We obtain $p_{T,\text{reco}}$ as the mean of the reconstructed jet p_T in the given $p_{T,ptcl}$ and $|\eta|$ bin. The fits are performed with third- and fourth-order log-polynomials. In some cases, where the low-p_T behaviour has a sudden drop, an additional term, $a \cdot (\log_{10}(x))^b$, was added. For all three fit functions the corresponding χ^2 values are calculated. If the quantile of the χ^2 value for the third-order log-polynomial is larger than 0.842 (one-sided two-σ value), i.e. when the third-order log-polynomial describes the given points well, it is kept. Otherwise, the fitting function having the smallest cumulative distribution function for the given χ^2 values and the degrees of freedom is taken. The response points have highly variable uncertainties across the $p_{T,\text{ptcl}}$ range in the given $|\eta|$ bin. This is because the N_eff highly differs for different $p_{T,\text{ptcl}}$ values. To prevent overfitting points with small uncertainties, the minimal relative uncertainty of the points is set to $0.05 \cdot (\max(y) - \min(y))$, where y are the median response values in the given plot. The lower limit of the fit is $17.5\,\text{GeV} < p_{T,\text{reco}}$ and all the points having $N_\text{eff} \geq 50$ when extracting the median response are used. To prevent the polynomial fits from deviating too much due to large statistical uncertainties at large $p_{T,\text{reco}}$, the highest end of the fit is truncated at the closest static point, i.e. where the derivative of the curve is zero, but not earlier than 3 points from the end. Outside the fit range, the correction is extrapolated as a constant.

Fig. 6.10 shows the examples of the fits for six different jet flavours in the most central $0 < \eta < 0.261$ bin for the QCD sample generated using PYTHIA 8.

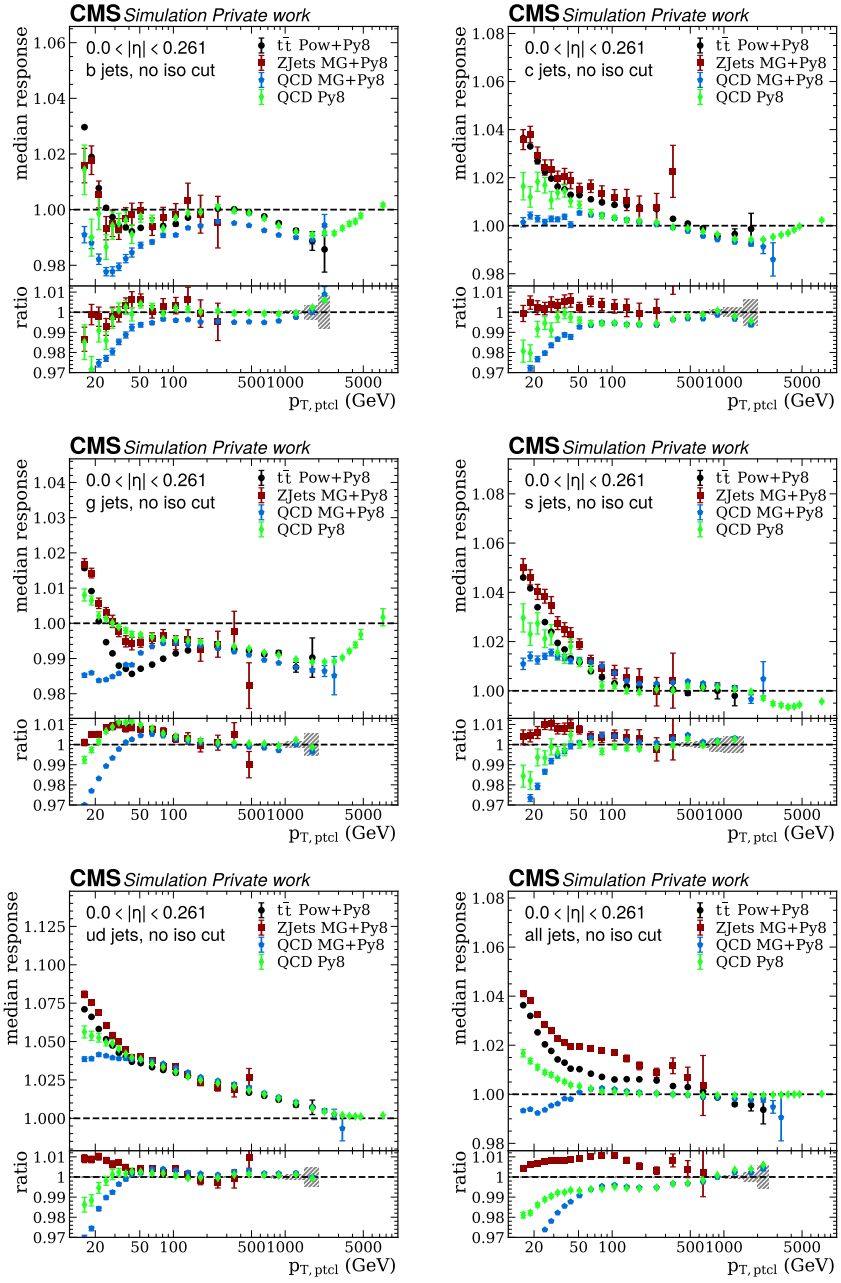

Fig. 6.9. Same as Fig. 6.7 but for the samples before applying the jet non-overlap cut.

In addition, the 6- and 9-parameter functions used for MC truth analyses in CMS of the type

$$f_1(p_{T,\mathrm{reco}}) = p_0 + \frac{p_1}{log_{10}^2(p_{T,\mathrm{reco}} + p_2)} + p_3 e^{-p_4\left(log_{10}(p_{T,\mathrm{reco}} - p_5)\right)^2} \tag{6.1}$$

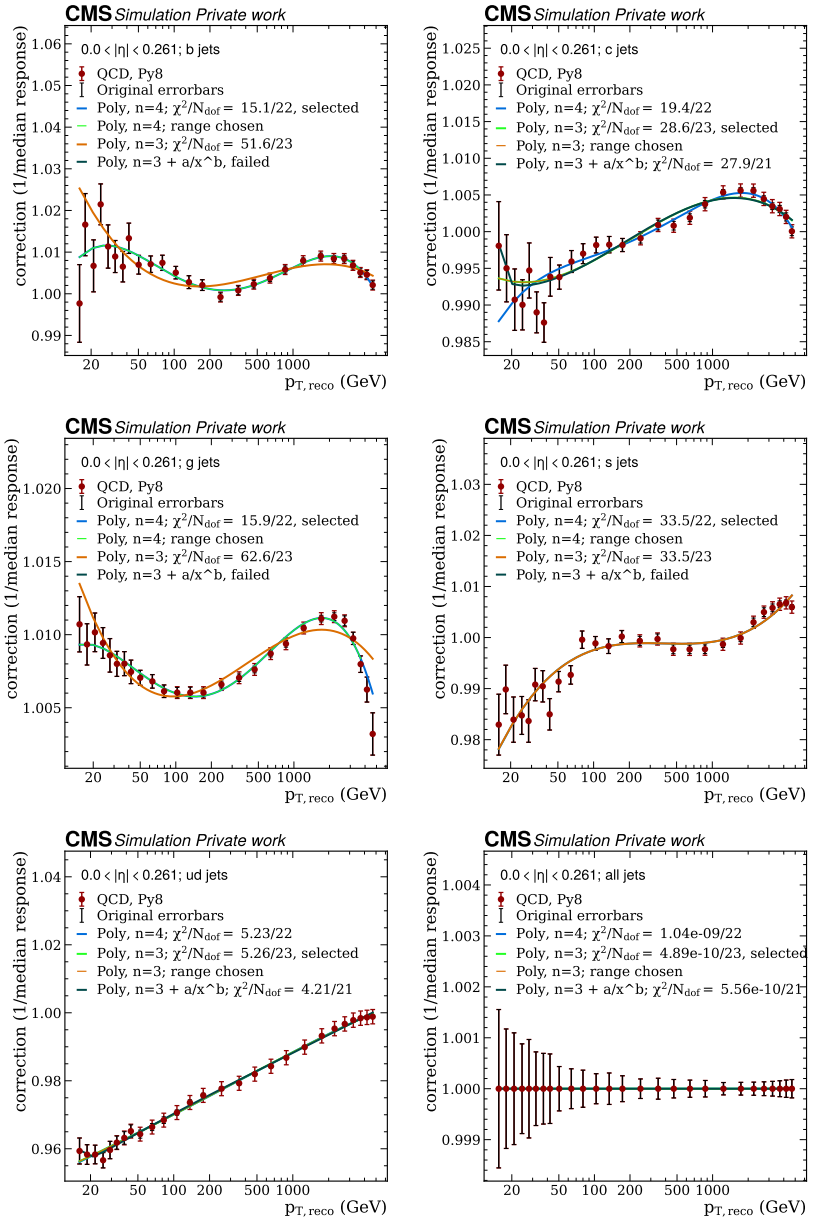

Fig. 6.10. The fits of the median correction vs $p_{T,\text{reco}}$ in the $0 < |\eta| < 0.261$ bin for the different jet flavours. The results are shown for the QCD sample generated using PYTHIA 8. The plots show the error bars before and after the application of the minimal relative uncertainty (black error bars vs the red error bars). The fit results of the three fitting functions are shown, and the one selected for the corrections is indicated in the legend.

and

$$f_2(p_{T,\text{reco}}) = f_1(p_{T,\text{reco}}) + p_6 e^{-p_7\left(log_{10}(p_{T,\text{reco}}-p_8)\right)^2} \tag{6.2}$$

were tested as well. Nevertheless, since the form of the corrections is different from the MC truth absolute corrections, these fit functions were found to fail to converge for most of the cases and were highly dependent on the initial conditions. This issue was also seen in the previous flavour correction fit attempts [301].

Simultaneous fit of all three datasets

Despite the differences between the physics datasets seen in Section 6.3.4, an attempt was made to derive universal flavour corrections to be applied independently of the dataset. The standalone PYTHIA 8 QCD dataset was used together with the $t\bar{t}$ and Z+jet, while the MADGRAPH 5_aMC@NLO+PYTHIA 8 QCD dataset was excluded. The JEC fits were carried out in two stages.

First, to correct for the bias created by the minimum jet p_T in the QCD dataset, a fit was performed for the *ud* flavour but removing the QCD points with $p_{T,\text{reco}} < 60\,\text{GeV}$. As shown in Fig. 6.11 (bottom left), the agreement between the different datasets and the fit of the n=4 polynomial is good when removing the biased QCD points. This is supported by the value of $\chi^2/N_{dof} = 69/49$, showing a good fit quality.

After the first fit, the QCD responses for the rest of the flavours were corrected in the whole $p_{T,\text{ptcl}}$ range by the difference between the values and the fit in the *ud* flavour. After that, the fits were repeated for the rest of the flavours, and the results in the $0.0 < |\eta| < 0.261$ bin are seen in the remaining panels in Fig. 6.11. In contrast to the individual fits, only log-polynomials with n=3 and n=4 were used, where n=4 was used if the quantile of the χ^2 value for the n=3 log-polynomial was smaller than 0.842. To protect against cases where one dataset with the largest number of events in the simulation is dominating the fit, in the given $p_{T,\text{reco}}$ bin, the smallest uncertainty was inflated to match the second-smallest uncertainty. The effect of this is seen, for example, for the *b* flavour, where the error bars of the $t\bar{t}$ data points in the range $20\,\text{GeV} < p_{T,\text{reco}} < 350\,\text{GeV}$ are inflated to match the QCD uncertainties, while in the range of $p_{T,\text{reco}} > 500\,\text{GeV}$ the uncertainties are inflated for the QCD data points.

The fit of the *b* flavour demonstrates how the simultaneous fit takes advantage of the distinct flavour compositions inherent in each data set. The $t\bar{t}$ sample is rich with events with *b* jets in the range up to $p_{T,\text{reco}} = 350\,\text{GeV}$ while QCD takes over above that, where the jets from the top quark stop being produced. The simultaneous fit is thus able to cover a broader range of $p_{T,\text{reco}}$ than a fit of each individual dataset.

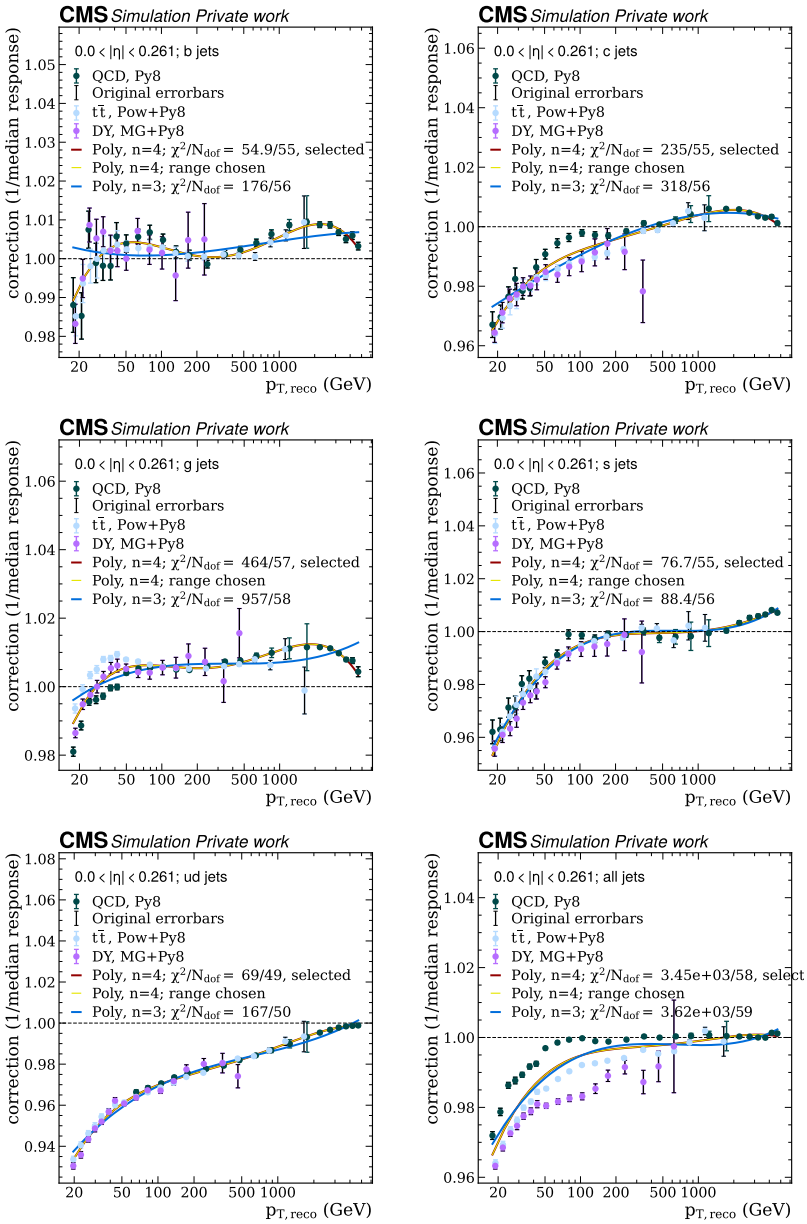

Fig. 6.11. The simultaneous fit of the jet energy correction vs $p_{T,\text{reco}}$ of the three physics processes showered using PYTHIA 8. The fit is shown in the $0 < |\eta| < 0.261$ bin for the different jet flavours. The plots show the error bars before the application of the minimal relative uncertainty (black error bars) and after (colourful error bars). The fit results of the two fitting functions are shown, and the one selected for the corrections is indicated in the legend.

6.3.7. Comparison of the flavour-dependent jet energy corrections with Run 1 corrections and previous private Run 2 corrections

The corrections derived using the PYTHIA 8 QCD sample as described in Section 6.3.6 (Summer20) were compared to the corrections used in Run 1 (Winter14) obtained from the QCD sample generated using PYTHIA 6 with the Z2* tune [284]. In addition, an earlier set of corrections using an independent framework was derived in Ref. [301] on the QCD dataset generated using PYTHIA 8 (Autumn18). These corrections rely on an older CMS MC campaign, which contains earlier versions of JEC that were less fine-tuned than in the UL campaign. For this comparison, the Summer20 corrections are derived in the same $|\eta|$ binning as the Autumn18 corrections. The Winter14 fits were derived in a coarser binning corresponding to HCAL sections.

The Autumn18 samples were derived as flavour-dependent L2L3Rel corrections, that is, without applying the inclusive L2L3Rel corrections on the samples used. To make a meaningful comparison, the Autumn18 fits were normalised by the inclusive corrections. In this way, corrections with respect to the inclusive "all" correction are obtained similarly to the approach used for the Summer20 fits to ensure the closure of the L2L3 Residual corrections.

Fig. 6.12 compares the new Summer20 with the Autumn18 and Winter14 fit results of the JEC factor defined as the inverse median response. The results are shown in the most central $|\eta|$ bin. The legend displays the corresponding $|\eta|$ bin used for the Winter14 fit. It shows a reasonable agreement between the Summer20 and Autumn18 fits. The Winter14 corrections show a significant disagreement with the other two fits. The main reason for this is the intrinsic differences between PYTHIA 6 with the Z2* tune and PYTHIA 8 with the CP5 tune, such as UE parameters and the α_s value in the parton shower. Moreover, the number of events for the PYTHIA 6 sample used for the Winter14 fits (around 10 million events) was significantly smaller than in the PYTHIA 8 QCD dataset (around 20 million events). This is also seen by the larger statistical fluctuations in the Winter14 fits. In addition, the Winter14 fits were derived on jets clustered with $R = 0.5$ instead of $R = 0.4$ and using different binning in $|\eta|$ than the Summer20 fits. Finally, the Winter14 fits used the physics definition for the jet flavour while in Summer20 and Autumn18, the parton flavour was used. Despite the differences between the PYTHIA 6 and PYTHIA 8 flavour corrections, they show the same global trends. Namely, b and g jets have a lower response, generally $R < 1$, while light jets have a larger response with $R > 1$. In addition, as will be shown in Section 6.4.4, the PYTHIA 8 to HERWIG 7 differences will be consistent with the PYTHIA 6 to HERWIG ++ differences. As a consequence, the flavour uncertainties will not change as significantly with respect to the Run 1 flavour uncertainties.

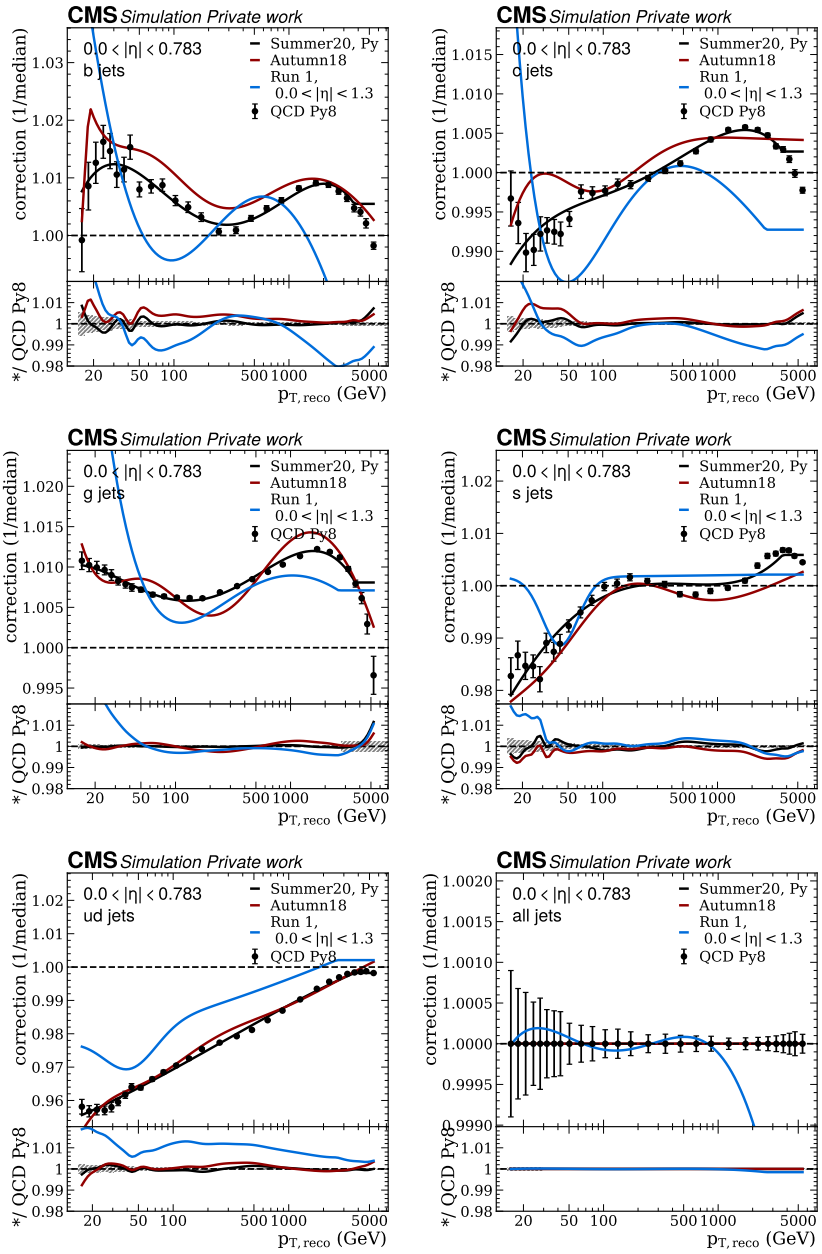

Fig. 6.12. Inverse median of the jet energy response in the $0 < |\eta| < 0.783$ bin for six different jet flavours for the QCD sample, generated using PYTHIA 8 (black markers). The fits of the QCD sample are shown (Summer20, black curve) together with the Autumn18 (early Run 2, red curve) and Winter14 (Run 1, blue curve) corrections.

6.4. Flavour uncertainties

6.4.1. Method for obtaining the uncertainties

The flavour uncertainties for a specific jet flavour, f, were estimated by comparing the response differences between HERWIG 7 and PYTHIA 8,

$$\hat{R}_f(p_{\mathrm{T}}, \eta) = R_{f,\mathrm{Her}}(p_{\mathrm{T}}, \eta) - R_{f,\mathrm{Py}}(p_{\mathrm{T}}, \eta), \tag{6.3}$$

where $R_{f,\mathrm{sample}}$ are the responses for flavour f obtained as the inverse of the JEC fits as described in Section 6.3.6. In addition, the response differences are normalised to match the effect of the global fit as explained in Section 6.4.4. The flavour uncertainties were obtained from the $t\bar{t}$ and QCD datasets individually and from the simultaneous JEC fit of all three physics processes. In Fig. 6.13 we show the HERWIG 7 and PYTHIA 8 comparison for the jet energy responses in the $t\bar{t}$ sample. The inverse of the JEC fits are shown as curves. One can see that light flavours need the highest JEC and gluon jets need the lowest, and the rest of the flavours are in-between the two. The ordering is consistent with what was seen in the Run 1 analysis [284]. However, at low $p_{T,\mathrm{reco}}$ for the HERWIG 7 sample the g jet response becomes larger than the b jet response. The $t\bar{t}$ flavour uncertainty, as formally derived in the following sections, is proportional to the difference between the solid curve and the dot-dashed curve before it is normalised for the global fit.

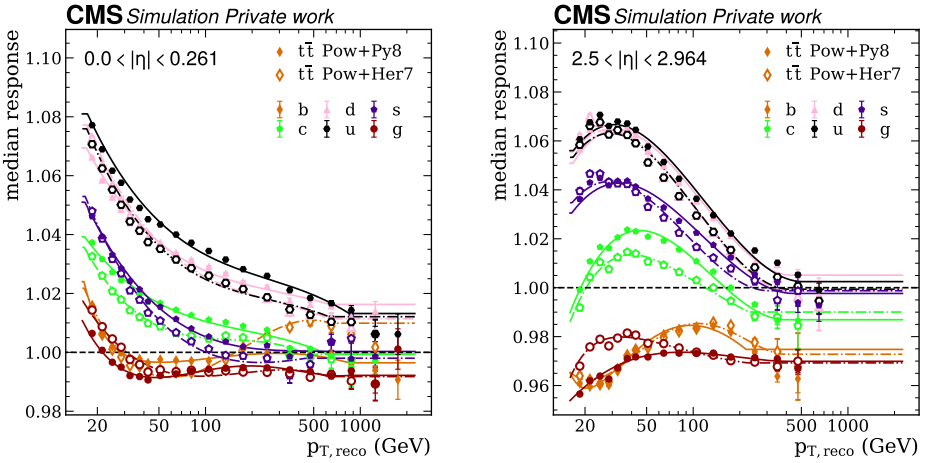

Fig. 6.13. Comparison of the median jet energy response predicted by PYTHIA 8 (closed markers) and HERWIG 7 (open markers) showers for different jet flavours. The inverse of the JEC fits are shown as curves. Results are shown for two different η regions..

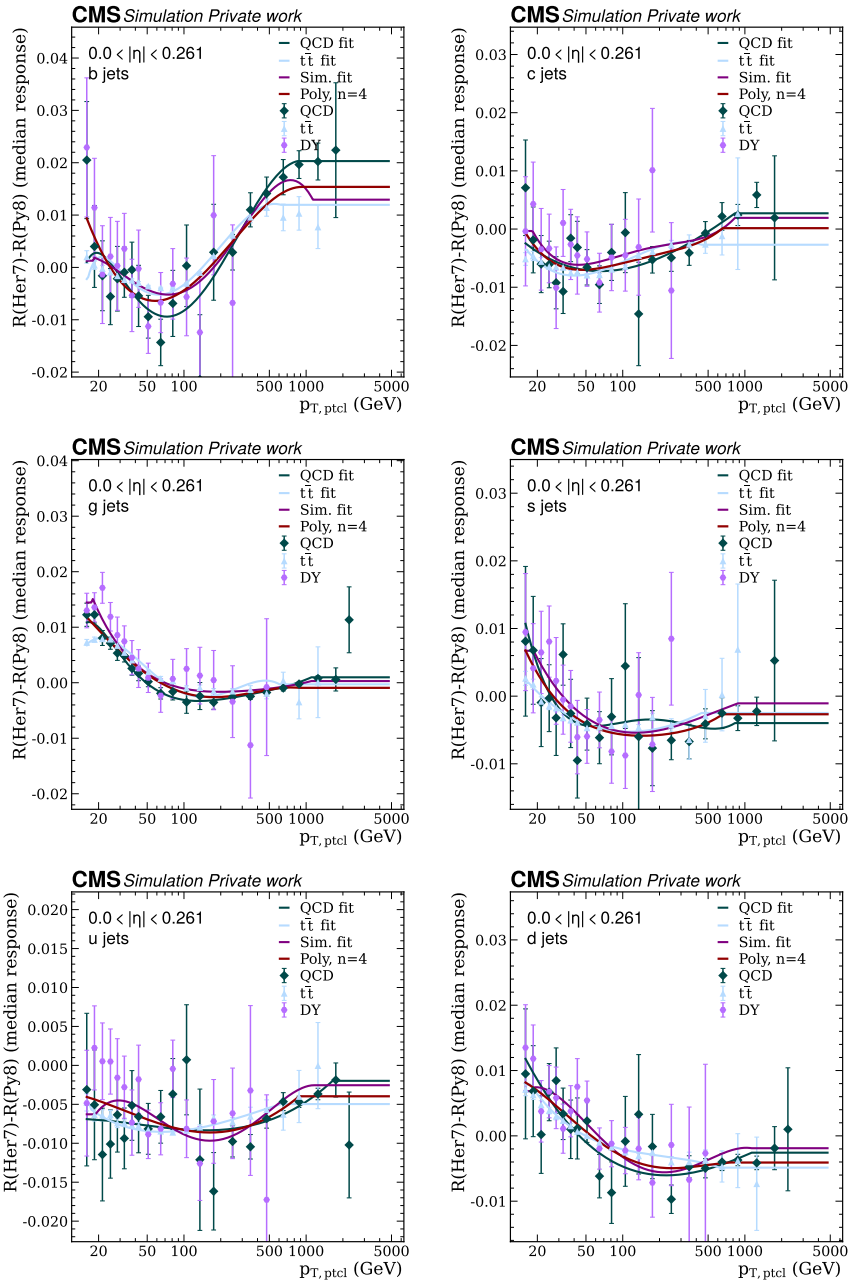

Fig. 6.14. The median response HERWIG 7 to PYTHIA 8 differences for the QCD, $t\bar{t}$, Z+jet samples. The curves show the fits of the individual QCD and $t\bar{t}$ samples as well as the result of the simultaneous fit of all three samples using a forth-order log polynomial.

6.4.2. The response differences predicted by HERWIG 7 and PYTHIA 8

Fig. 6.14 shows $R_{\mathrm{Her}} - R_{\mathrm{Py}}$ for the three physics processes used in the analysis. Fits for the QCD and $t\bar{t}$ as well as the simultaneous fit of the corrections are obtained by subtracting the PYTHIA 8 JEC fit from the HERWIG 7 JEC fits obtained as described in Section 6.3.6. A fit of all three samples with an n=4 log-polynomial is also shown. To avoid overfitting the high-p_{T} ends, the smallest error bar for the given $p_{T,\mathrm{ptcl}}$ is increased to match the second smallest in the bin as it was done for the fits in Section 6.3.6. Note again the difference between the two simultaneous fits. What we call here the simultaneous correction fit (Sim. fit in the legend) is obtained by subtracting PYTHIA 8 and HERWIG 7 simultaneous correction fits, while the uncertainty simultaneous fit (Poly, n=4) is obtained from fitting the given points. It is seen that the dependence of $R_{\mathrm{Her}} - R_{\mathrm{Py}}$ on the physics dataset is smaller than for the individual R_{Her} and R_{Py} (compare with Fig. 6.7 and Fig. B.1). Especially, the bias of the QCD datasets cancels out when subtracting the two showers. Slight differences between the datasets remain at low $p_{T,\mathrm{ptcl}}$, especially for gluons. However, the disagreements are much smaller than what was seen without the jet non-overlap cut.

The two simultaneous fits in general follow in-between the two individual sample fits. Note that the $t\bar{t}$-only fit is the most stable because the dataset has the smallest statistical uncertainties in most of the relevant $p_{T,\mathrm{pctl}}$ range and, unlike in the simultaneous fit, the uncertainty was not artificially increased. However, the results obtained from the simultaneous fits of the corrections and of the direct ratio differ from the $t\bar{t}$-only fit by only up to 0.2 %. In this analysis, preference is given to the simultaneous fit as in this way also the other datasets are taken into account.

6.4.3. Remixing to the flavour content of the other samples

As was seen in the lower right plots of Fig. 6.7 and Fig. B.1, the response for the sample inclusive in jet flavours is fully closed only for the QCD PYTHIA 8 dataset since the L2/L3 MC-truth uncertainties were derived on it. Since the other samples have different flavour mixes and each flavour has different responses, the inclusive response for them is deviating from unity. Flavour corrections are supposed to bring this response to unity regardless of the sample composition in jet flavours, and flavour uncertainties estimate the uncertainty due to this correction procedure.

A good test to verify the compatibility of the flavour corrections obtained from the different physics samples is to plot the remixed inclusive uncertainty

$$\hat{R}_{\mathrm{mix}}(p_{\mathrm{T}}, \eta) = \sum_{f} \left(R_{f,\mathrm{Her}}(p_{\mathrm{T}}, \eta) \cdot F_{f,\mathrm{Her}}(p_{\mathrm{T}}, \eta) - R_{f,\mathrm{Py}}(p_{\mathrm{T}}, \eta) \cdot F_{f,\mathrm{Py}}(p_{\mathrm{T}}, \eta) \right), \tag{6.4}$$

where, $F_{f,\mathrm{sample}}$ is the f flavour fraction in the given sample and is obtained as a spline over p_{T} using the data shown in Section 6.3.1. The sum in Eq. (6.4) runs over each flavour

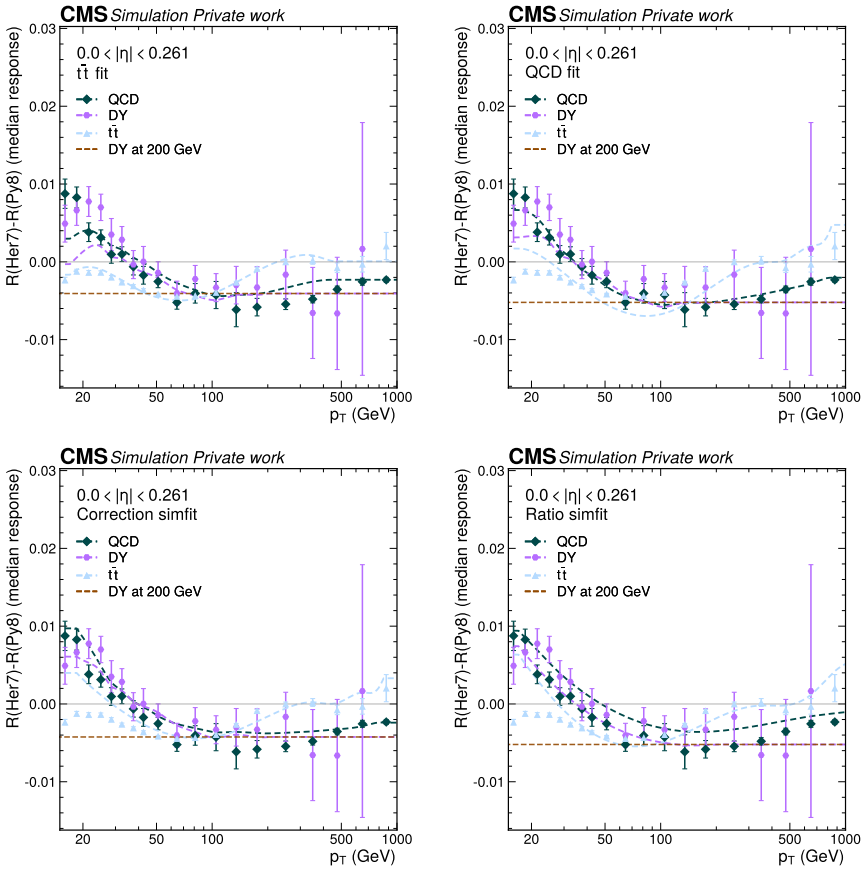

Fig. 6.15. Remixing results of $R_{\mathrm{Her}} - R_{\mathrm{Py}}$ starting from the $t\bar{t}$ fits (top left), QCD fits (top right), the simultaneous fit of the corrections (bottom left) the simultaneous fit of $R_{\mathrm{Her}} - R_{\mathrm{Py}}$ (bottom right). The markers show $R_{\mathrm{Her}} - R_{\mathrm{Py}}$ for each of the physical processes. The dashed curves show the remixing results obtained by Eq. (6.4) starting from the given set of corrections. The dashed brown horizontal line shows the constant factor of Z+jet at 200 GeV, which is used to normalise the individual flavour fits to obtain the flavour uncertainty.

f. These remixed uncertainties are also used to normalise $R_{\mathrm{Her}} - R_{\mathrm{Py}}$ to obtain flavour uncertainties (see., Section 6.4.4).

$\hat{R}_{\mathrm{mix}}$ combines the corrections linearly to obtain the specific flavour mixture and subtracts the one obtained from PYTHIA 8 from the one obtained from HERWIG 7. In the Run 1 analysis, it was assumed that F was the same for both showers. However, as seen in Section 6.3.1, the flavour fractions for the parton flavour were found to be slightly different for the two showers. Thus, Eq. (6.4) now uses $F_{f,\mathrm{sample}}(p_{\mathrm{T}}, \eta)$ corresponding to each of the parton shower. For the combined fit where $R_{\mathrm{Her}} - R_{\mathrm{Py}}$ was fitted directly, the individual remixing for the HERWIG 7 and PYTHIA 8 samples was not possible and the

flavour fractions of each shower, Eq. (6.4′), were replaced with the average of the flavour fractions:

$$\hat{R}_{\text{mix}}(p_{\text{T}},\eta) = \sum_f \left(R_{f,\text{Her}}(p_{\text{T}},\eta) - R_{f,\text{Py}}(p_{\text{T}},\eta)\right) \cdot \left(F_{f,\text{Her}}(p_{\text{T}},\eta) + F_{f,\text{Py}}(p_{\text{T}},\eta)\right)/2, \quad (6.4')$$

where the whole term in the first brackets was obtained from a fit.

Fig. 6.15 (top left) shows the results of the remixing starting from the JEC fits obtained on the $t\bar{t}$ sample. The markers show $R_{\text{Her}} - R_{\text{Py}}$ inclusively in flavour, as summing up all the points for all flavours in Fig. 6.14. The dashed curves show the remixed values obtained by Eq. (6.4) using QCD, $t\bar{t}$ and Z+jet flavour mixes. One sees that the $t\bar{t}$ fit remix agrees well with the $t\bar{t}$ points as both are obtained from the same MC data. The QCD curve has a good agreement with the QCD points showing that the $t\bar{t}$ fits are good at regenerating the response differences, $R_{\text{Her}} - R_{\text{Py}}$, seen in the QCD sample. The agreement with the Z+jet dataset is not as good at $p_{\text{T}} < 100\,\text{GeV}$, the reason being the topological differences between the two physical processes as discussed in Section 6.3.4.

Fig. 6.15 (top right) shows a similar agreement between $t\bar{t}$ and QCD when starting from the QCD fits and shows a slight disagreement with Z+jet. Fig. 6.15 (bottom left and right) shows the agreement when starting from the combined fit of flavour corrections and the combined fit of $R_{\text{Her}} - R_{\text{Py}}$, respectively. Both show a slight disagreement for all the samples due to the averaging effect among all of them. The latter shows an even larger disagreement between the remixed and original values, as the remixing now uses Eq. (6.4′) instead of Eq. (6.4), relying on the average instead of the individual HERWIG 7 and PYTHIA 8 flavour fractions.

6.4.4. Flavour uncertainty

To obtain the flavour uncertainties, ΔR_{flavor}, the flavour differences are normalised using the formula

$$\Delta R_{\text{flavour}}(p_{\text{T}},\eta) = \hat{R}_{\text{mix}}(p_{\text{T}},\eta) - R_{ref}(p_{\text{T}},\eta), \quad (6.5)$$

with

$$R_{ref}(p_{\text{T}},\eta) = \hat{R}_{\text{Z+jet}}(200\,\text{GeV},0) + \left(\hat{R}_{\text{dijet}}(p_{\text{T}},\eta) - \hat{R}_{\text{dijet}}(p_{\text{T}},0)\right), \quad (6.6)$$

where $\hat{R}_{\text{dijet}}$ and $\hat{R}_{\text{Z+jet}}$ are obtained from Eq. (6.4). This ensures that for the Z+jet mix at 200 GeV and $\eta = 0$ the flavour uncertainty is exactly 0, and that for the QCD mix it is independent of η. This is necessary because the global fit is exactly cancelling any data/MC differences for the Z+jet mix at 200 GeV and $\eta = 0$, and residual corrections cancel all the dependence on η for the QCD dataset.

It is more common to apply an uncertainty on each individual flavour in the MC sample than on a whole flavour mix. However, historically flavour uncertainties were also derived for the whole flavour mixes. Therefore, we obtain flavour uncertainties for the

QCD and $t\bar{t}$ flavour mixes as well. For an individual flavour, $\hat{R}_{\text{mix}}(p_{\text{T}}, \eta)$ simplifies to $\hat{R}_f(p_{\text{T}}, \eta)$.

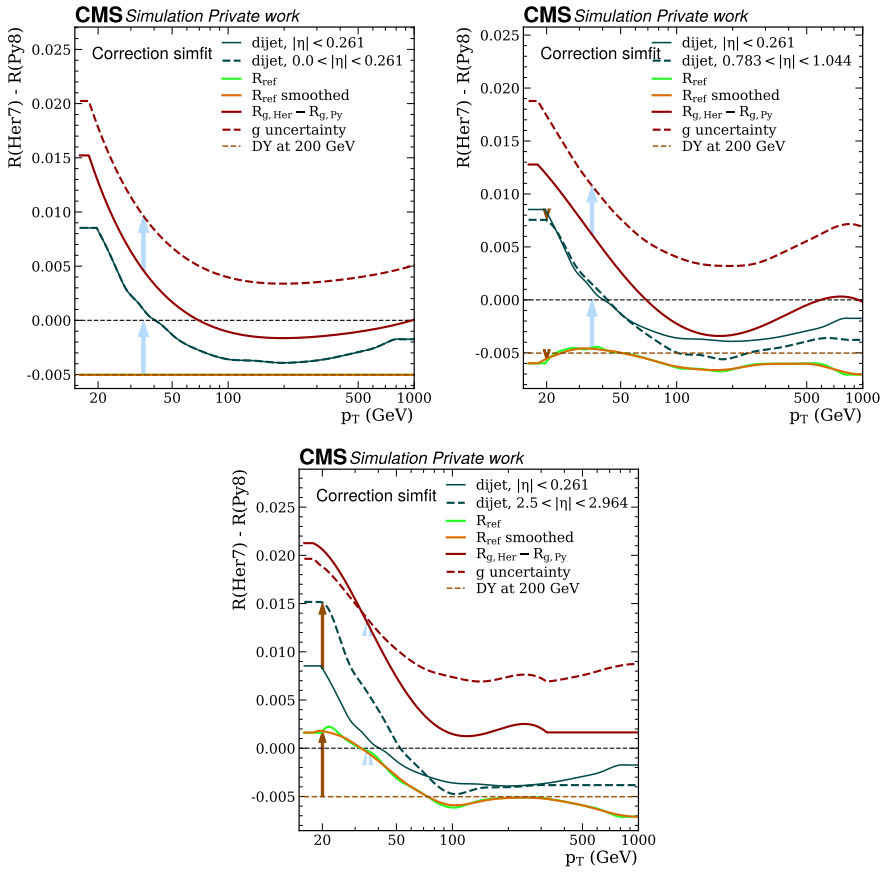

Fig. 6.16. Normalisation of the gluon flavour with respect to the global fit to ensure that for the Z+jet mix at 200 GeV the uncertainty is 0, and that for the QCD mix it is independent of η. Initial response differences of HERWIG 7 and PYTHIA 8 (red solid curve) are normalised to the final gluon flavour uncertainty (dashed red curve).

The transition from flavour response to flavour uncertainty (normalisation) for g jets is shown in Fig. 6.16 for three different $|\eta|$ bins. The top left plot shows the $|\eta| = 0$ result. In that case, $\left(\hat{R}_{\text{dijet}}(p_{\text{T}}, \eta) - \hat{R}_{\text{dijet}}(p_{\text{T}}, 0)\right) = 0$, and there is no contribution from the dijet normalisation. This is represented by the fact that the dashed and the solid dijet lines overlap. The only contribution to the normalisation shift ($R_{\text{ref}}$the bright green curve) comes from the constant factor of the response of the Z+jet mix at 200 GeV (brown dashed horizontal line). This horizontal line shows the shift by which $R_{g,\text{Her}} - R_{g,\text{Py}}$ is increased to make the g uncertainty. For the other two η bins, the dijet normalisation is non-zero. It becomes particularly large for $2.5 < |\eta| < 2.964$. When this contribution is non-zero, the R_{ref} becomes the sum of the constant Z+jet shift and the dijet contribution.

One can see that adding the dijet normalisation leads to statistical fluctuations on R_{ref}. Thus, R_{ref} was smoothed as a running average around the vicinity of the point.

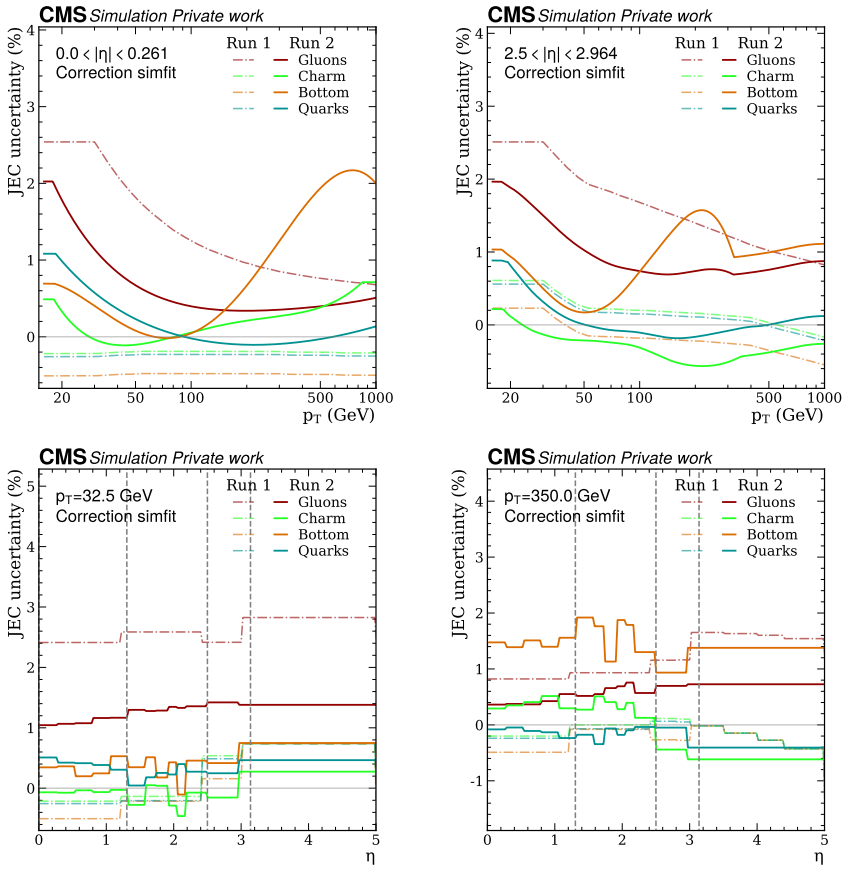

Fig. 6.17. Flavour uncertainty as a function of p_{T} for two different η regions (top), and as a function of η for two different p_{T} regions (bottom). The dash-dotted lines show the flavour uncertainties from Run 1. The solid lines show flavour uncertainties for Run 2.

In Fig. 6.17, the flavour uncertainty obtained using the simultaneous JEC fit approach for different flavours is compared to the flavour uncertainty of Run 1. For gluons, the obtained uncertainty is significantly smaller than in Run 1, and for other flavours, the uncertainty in some regions of p_T becomes slightly larger, while decreasing in others. As in Run 1, gluons were the dominant source of the uncertainty, and due to the limited number of simulated MC events, the rest of the flavours in Run 1 were fitted with a very approximate fit, which often was a simple straight line. This often leads to an underestimation of the uncertainty. For Run 2, we now fit all flavours from a larger number of generated MC events, and an improved dependence over p_T is obtained. The uncertainty for b quarks reaches 2.5 % at $p_{\mathrm{T}} > 100$, compatible with the 3 % in the Autumn18

PYTHIA 8/HERWIG++ analysis [301] which will be studied further in Section 6.4.5. The new flavour uncertainties also offer to split the light quark uncertainties into the individual u, d and s uncertainties. They are presented in appendix C.

6.4.5. Bottom hadron displacement differences in HERWIG 7 and PYTHIA 8

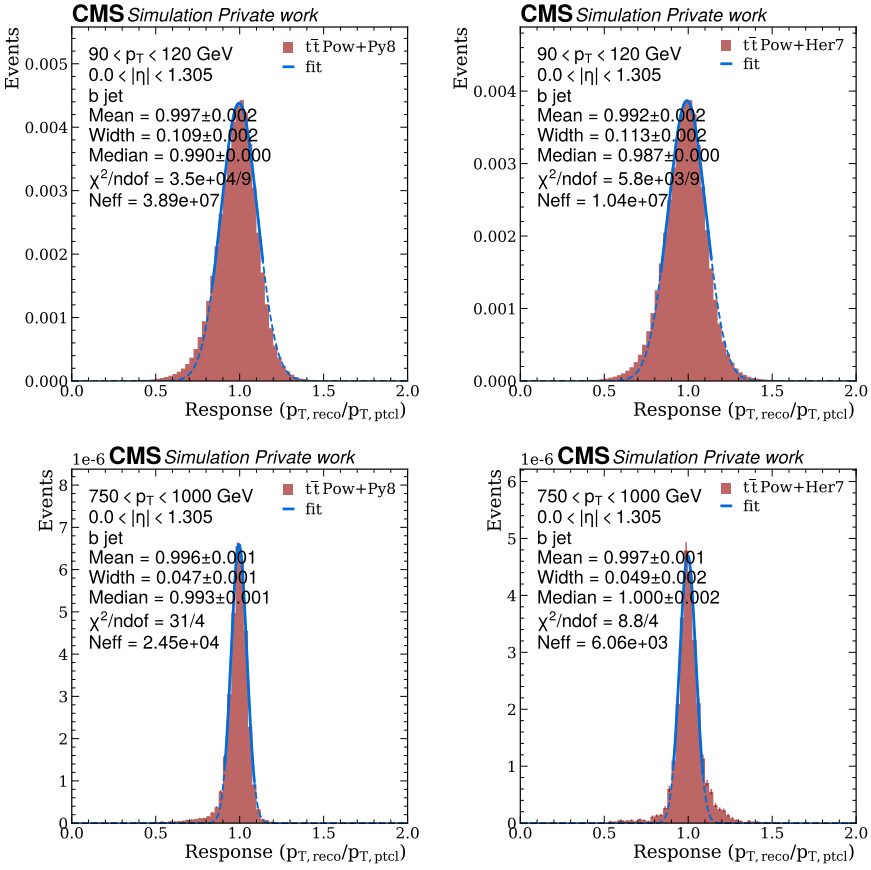

Fig. 6.18. Jet response distributions for the b in the $0 < |\eta| < 1.305$ bin for jets in the $90 < p_{T,\text{ptcl}} < 120\,\text{GeV}$ (top) and $750 < p_{T,\text{ptcl}} < 1000\,\text{GeV}$ (bottom) bin as predicted by PYTHIA 8 (left) and HERWIG 7 (right). The legend explanation is the same as in Fig. 6.5.

In this section, an attempt is made to explain the differences in b jet modelling in PYTHIA 8 and HERWIG 7. The increase in the median response for HERWIG 7 for large p_T jets can be seen to be caused by tails in the response distribution in the HERWIG 7 simulation. Fig. 6.18 shows that at lower p_T values such as $90 < p_{T,\text{ptcl}} < 120\,\text{GeV}$ the response distribution predicted by HERWIG 7 and PYTHIA 8 have the same shape. On the contrary, for $750 < p_{T,\text{ptcl}} < 1000\,\text{GeV}$, HERWIG 7 begins to exhibit tails at large response values, whereas PYTHIA 8 does not.

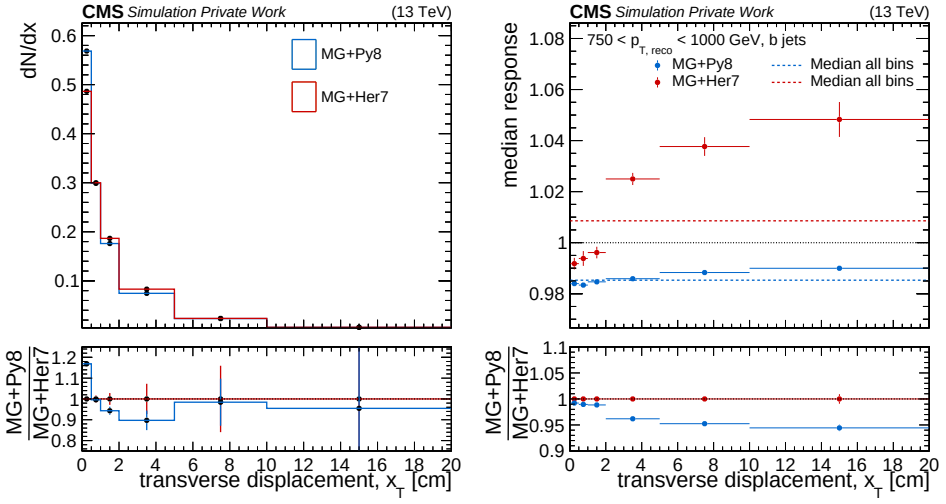

Fig. 6.19. The distribution of the b hadron displacement (left). The jet response vs the b hadron displacement (right). A sharp increase in the response for large displacement is seen for the HERWIG 7 sample but not for the PYTHIA 8 sample.

Previous research has been conducted on the composition of jets with response $0.9 < R < 1.1$ ("normal" jets) and $R > 1.1$ ("tail" jets) [301], [306]. Interestingly, it was found that in HERWIG ++ the reconstructed and matched generated jet neutral energy fraction matches better in "tail" jets than in "neutral" jets. For the charged energy fractions, it was the opposite. This shows that in the "tail" jets the neutral energy fraction could be overestimated, possibly the PF code could be adding additional neutral particles due to the particle momenta not matching the energy deposits well. However, no PYTHIA 8 and HERWIG 7 comparison of the jet composition was made and no particle energy fractions per particle type were made.

Here, we test whether the large tails in the HERWIG 7 responses at large $p_{T,\text{reco}}$ can be explained by a mismodelling of the b hadron decays at large b hadron displacements, which correlates with the long lifetimes of b hadrons. The test is performed on the MiniAOD versions of the HT2000toInf QCD samples generated using MADGRAPH mentioned in Section 6.2.1. The high H_T of the events in the given sample ensures the presence of highp_T jets in the events. Only reconstructed jets that have a matched generated b jet ($\Delta R < 0.4$) with $750\,\text{GeV} < p_{T,\text{ptcl}} < 1000\,\text{GeV}$ are selected, i.e. in the window where there are large PYTHIA 8 vs HERWIG 7 response differences. The response differs by around 2 % in this bin.

All final b hadrons, that is, b hadrons that do not decay into other b hadrons were selected. The final b hadrons were matched with the generated jets within $\Delta R < 0.2$. The transverse displacement of the b hadron, x_T, was calculated as the transverse distance between the production vertex of the b hadron and that of its daughters. No additional

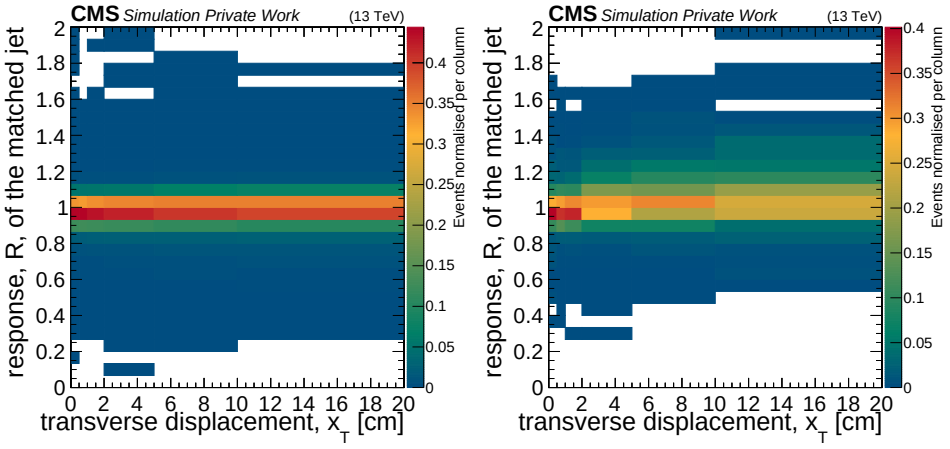

Fig. 6.20. The 2D distribution of the jet response vs the b hadron displacement for the sample showered with PYTHIA 8 (left) and with HERWIG 7 (right).

jet selection was applied. Fig. 6.19 (left) shows the x_T distribution. Around 30 % of the b hadrons travel at least 2 cm, meaning that they have a high probability to enter the first layers of the pixel material at CMS. For the 2017 and 2018 data, after the Phase 1 upgrade, the pixel layers start at 29 mm [240]. Before the Phase 1 upgrade, it started at 44 mm. The tracks of such b hadrons could be missed and misinterpreted as a neutral hadron. In addition, PYTHIA 8 predicts b hadrons to be less displaced. Fig. 6.19 (right) shows the dependence of the median response, R, on the x_T. While for the MADGRAPH+PYTHIA 8 sample R exhibits only a mild dependence on x_T, for the MADGRAPH+HERWIG 7 sample, R increases sharply with x_T. At $10\,\text{cm} < x_T < 20\,\text{cm}$, R is 6 % larger than at $0 < x_T < 0.5$ cm, and it becomes larger than 1 at $x_T \approx 2\,\text{cm}$.

In Fig. 6.20 the 2D distribution of the jet response vs the displacement of b hadron is shown. While for the PYTHIA 8 sample the response looks symmetric around the median, for the HERWIG 7 sample the response is skewed toward larger values for large x_T, and has tails at large R. This study shows that the HERWIG 7 and PYTHIA 8 disagreement for the generated b jet response at large p_T could be brought to less than 1 % by adding a cut on the b hadron displacement within jet. In this way, no more than 30 % large p_T jets would be removed. However, the exact reasons for the b hadron decay differences in PYTHIA 8 and HERWIG 7 are not yet known, and further studies are needed. It is surprising that the largest differences are found in the reconstructed vs generated p_T instead of the fractions of b hadrons, i.e. Fig. 6.19 right instead of left panel. This could mean that the differences are not in the generators themselves, but rather in the detector simulation or reconstruction.

6.5. Gluon-split and prompt bottom and charm jet response

6.5.1. Gluon splitting in bottom jets

As mentioned in Section 5.4, parton flavour does not differentiate between b and c jets that originate from the hard process or decays of heavy resonances (prompt jets) and jets originating from gluon splitting (gluon-split jets). To classify jets into these categories, b jets were matched to the final b hadrons within $\Delta R = 0.4$. Final b hadrons denote hadrons that do not decay into other b hadrons. If more than two b hadrons were matched within the b jet, it was marked as gluon-split. This categorisation misses gluons that split into hadrons at wide angles. Similarly, the c gluon-split category was defined by matching jets to two final c hadrons within $\Delta R < 0.4$.

The relative fraction of the gluon-split b and c jets is illustrated in Fig. 6.21. In the QCD datasets, the fraction of gluon-split jets surpasses 50 % at $p_{T,\text{ptcl}} > 500\,\text{GeV}$ with some modelling differences between PYTHIA 8 and HERWIG 7. The findings are consistent with the observations of the ATLAS Collaboration [307]. Both collaborations see approximately 20 % of gluon-split b jet fraction at $p_{T,\text{ptcl}} = 90\,\text{GeV}$ and approximately 40 % more gluon splittings in HERWIG 7 than in PYTHIA 8. Some milder differences are also observed in the QCD sample generated by PYTHIA 8 and by MADGRAPH, especially at $30 < p_{T,\text{ptcl}} < 100\,\text{GeV}$. In the $t\bar{t}$ dataset the fraction of gluon-split b jets is small. This is due to the large amount of b jets originating in top quark decays. The agreement between PYTHIA 8 and HERWIG 7 for b gluon splitting is better in the DY and $t\bar{t}$ datasets than in the QCD datasets, while for c gluon splitting it is the other way around.

Comparison of the flavour response of the prompt and gluon-split jets in Fig. 6.22 and Fig. 6.23 shows a large difference between b and c jets. Generally, gluon split jets exhibit lower response in comparison to the prompt jets and have a similar response to the gluon jets. Separation of the two categories enhances the consistency of the c response across different physics samples in the region of $50 < p_{T,\text{ptcl}} < 400\,\text{GeV}$. The difference between $t\bar{t}$ and the QCD samples in this interval is reduced to less than 0.5 %, down from approximately 1 %, although the agreement remains outside the error margins. A similar but milder improvement is observed for the b jet response. However, the response in the standalone QCD dataset deviates from the one in the $t\bar{t}$ sample by up to 0.5 %.

6.6. Flavour-antiflavour uncertainties

In precision measurements of potential differences between the properties of matter and antimatter, such as the Δm_t measurement, even small response differences between quark and antiquark jets are important. In the following sections, the author motivates that such differences can arise from different hadron and antihadron content in flavour and antiflavour jets as depicted in Fig. 6.24. These hadrons and antihadrons interact with the detector material that is made out of matter, where the antihadrons lead to a slightly

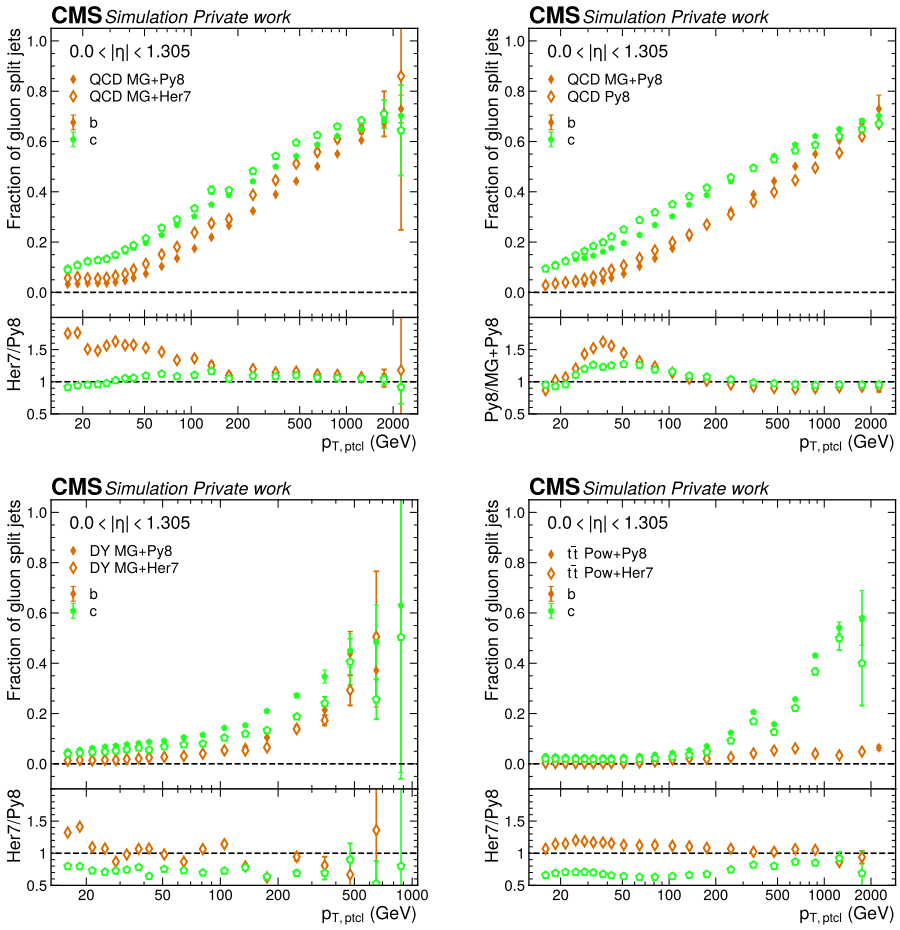

Fig. 6.21. The fraction of gluon split jets for QCD (top), DY (bottom left) and $t\bar{t}$ (bottom right) samples. Shown are both flavour fractions of the sample showered by HERWIG 7 (open markers) and PYTHIA 8 (filled markers), as well as the sample generated with standalone PYTHIA 8 (top right plot).

larger energy deposit in the calorimeters. After a brief discussion of the flavour-antiflavour JES differences, the author presents two sources for flavour-antiflavour uncertainties. The first source of the uncertainty, presented in Section 6.6.4, is the mismodelling of the single-pion responses in the GEANT4 simulation in comparison to the HCAL test beam data. The second uncertainty covers potential mismodelling of the flavour vs antiflavour jet content and fragmentation and decays by the parton showers. This is obtained by a comparison of the HERWIG 7 and PYTHIA 8 parton showers in a similar way as the flavour uncertainties were obtained.

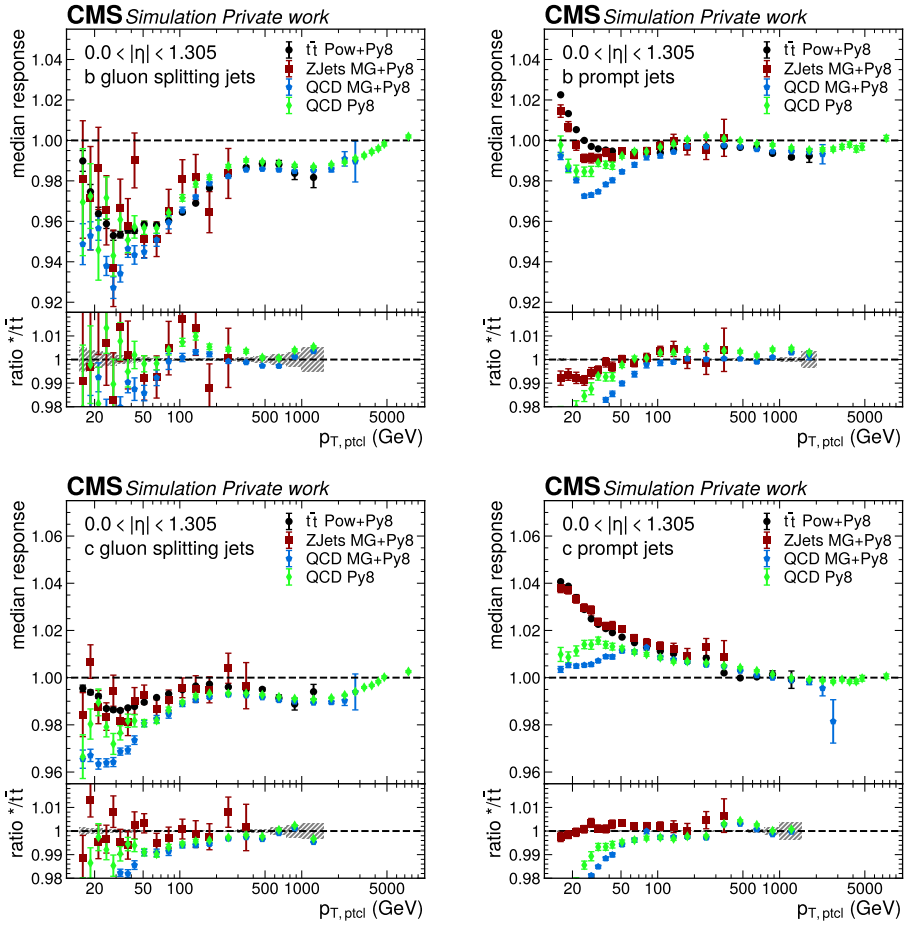

Fig. 6.22. The comparison of the median jet response vs $p_{T,\mathrm{ptcl}}$ for b jets (top) and c jets (bottom) originating in gluon splittings (left) and in prompt jets (right) using the physics datasets showered with PYTHIA 8.

6.6.1. Hadron content differences in flavour and antiflavour jets

This section investigates the hadron energy content in jets of different flavour. The hadron energy content was obtained using a specific NanoAOD version, PFNano, which, in addition to the usual event content, includes information about the PF candidates in the event. The PFNano versions of the $t\bar{t}$ datasets described in Section 6.2.1 were used. A 2D histogram was filled depending on the PDG ID of the PF candidate and the flavour or the matched generated jet, weighting each PF candidate with its p_T. The resulting stacked histograms for the sample showered with PYTHIA 8 and HERWIG 7 are shown in Fig. 6.25 after combining the PF candidates into groups. One can observe that the fractions of π^+ and π^- differ between the flavour and antiflavour jets while the total amount of π^+ and π^-

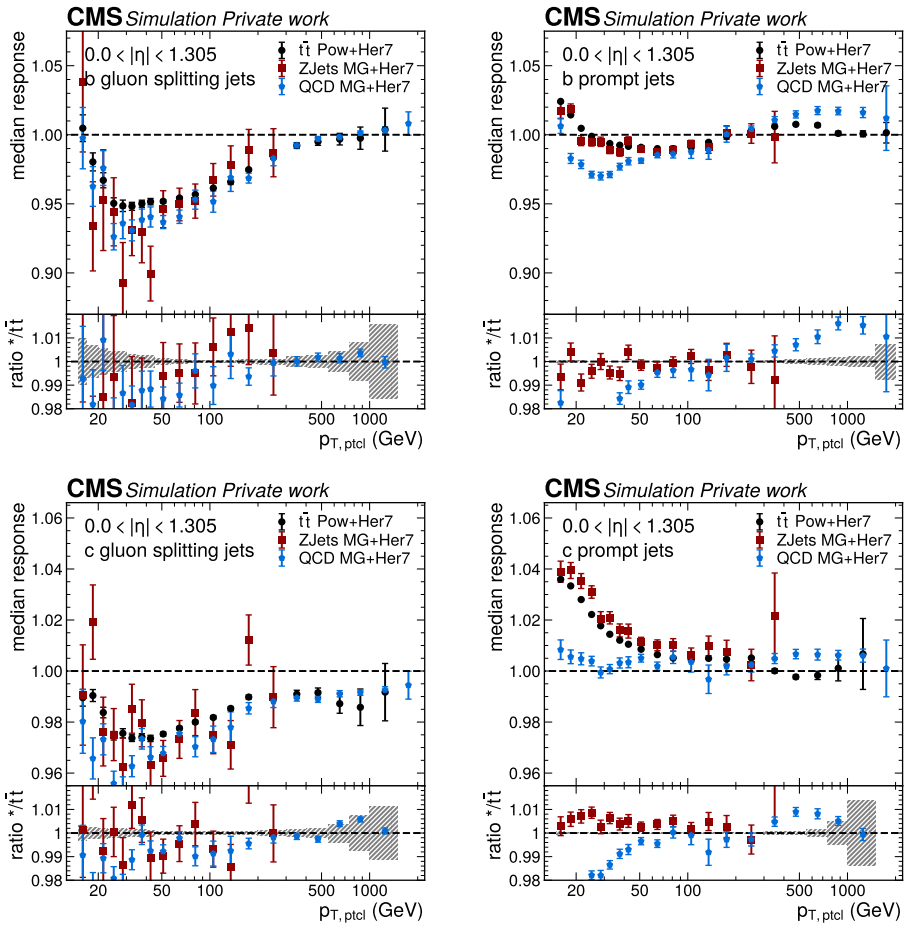

Fig. 6.23. The comparison of the median jet response vs $p_{T,\mathrm{ptcl}}$ for b jets (top) and c jets (bottom) originating in gluon splittings (left) and in prompt jets (right) using datasets showered with HERWIG 7.

stays similar. The largest difference is for u and d jets. The difference is possibly caused by the fact that the information about one initial u quark ($\overline{u}$ quark) remains through the fragmentation, and for hadronization there is one more u quark ($\overline{u}$ quark) available for creating a π^+ (π^-). Likewise, there is some difference for c jets and a smaller one for b jets in their π^+ and π^- energy fractions.

Similar differences are observed in the K^+ and K^- energy fractions. They are most prominently visible in s jets, but also in the other flavours. The flavour-antiflavour asymmetry is also seen in p and n (baryon), $\overline{p}$ and $\overline{n}$ (antibaryon) energy fractions despite the overall flavour fraction being smaller. Quark jets like u and d contain more p and n, while their antiquark jets contain the corresponding antiparticles. Strange baryons were grouped into categories of positively charged baryons $[\Sigma^+, \Theta^+, \Xi^+]$, negatively charged

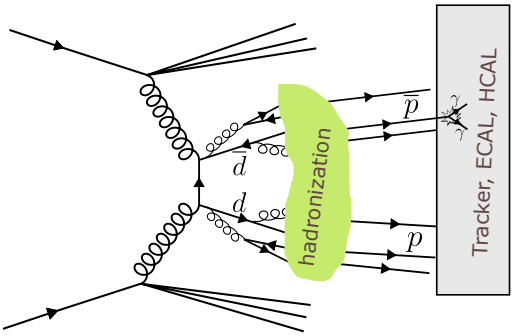

Fig. 6.24. Schematic picture of an event with a quark and antiquark created. The difference in the hadron evolution leaves a different impact in the detector.

baryons $[\Sigma^-, \Theta^-, \Xi^-]$, neutral baryons, $[\Lambda, \Theta^0]$, and the antiparticles of neutral baryons, $[\overline{\Lambda}, \overline{\Theta^0}]$ [19]. The differences in the production of the strange baryons are seen, where quark jets produce almost no strange neutral antibaryons, while antiquark jets produce almost no strange neutral baryons. The trends are similar for the samples showered with either parton shower.

Some difference between the PYTHIA 8 and HERWIG 7 hadron content is visible. HERWIG 7 shower has a larger energy fraction of strange baryons than PYTHIA 8, while for light-quark baryons it is the opposite. Also, the quark-antiquark differences are predicted differently in both showers. PYTHIA 8 predicts more neutrons in s than in $\overline{s}$, while HERWIG 7 predicts it the other way around. On the other hand, the differences between b vs $\overline{b}$ are similar in both PYTHIA 8 and HERWIG 7.

6.6.2. Hadron response differences in the HCAL 2007 test beam data

Before mounting the barrel HCAL and ECAL (EB, HB, and HO) into CMS, a test beam was performed to measure the properties of these subdetectors [308]. Responses to beams of $\pi^\pm$, p, $\overline{p}$, $K^\pm$, $e^\pm$, and $\mu^\pm$ were measured. The experiment used the CERN H2 beam line, where the beams are created when protons from SPS hit a production target. The experimental setup was was composed of the production modules and front-end electronics as they are present in the final CMS detector. The subdetectors were placed on a platform in correspondence to the CMS geometry and the platform was movable in the ϕ and η directions so that the beam could be directed at any angle mimicking the trajectory of a particle from the LHC collision.

The results for the test beam for $\pi^\pm$, $K^\pm$, p and $\overline{p}$, and n and $\overline{n}$ are shown in Fig. 6.26, together with a simulation of the detector response by GEANT4. In this study, GEANT4 version 10.4.p03 [205]–[207] is used together with the physics model configuration (physics

[19] In terms of quark content, $\Sigma^+ = uud$, $\Sigma^- = dds$, $\Theta^+ =$, $\Xi^- = dss$, $\Omega = sss$, $\Lambda = uds$, and $\Xi^0 = uss$.

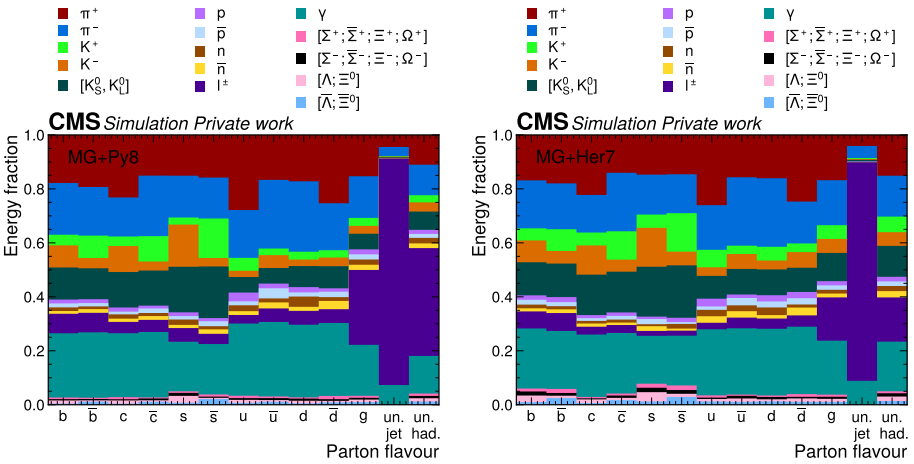

Fig. 6.25. Hadron energy content in jets of different flavours for the QCD datasets showered using PYTHIA 8 (left) and HERWIG 7 (right). Jets that are not ghost matched to any parton and are mostly leptons (un. jet) are included. Unmatched hadrons (un. had.) are hadrons not matched to any jet.

list) `FTFP_BERT_EMM`, as used in the UL18 MC campaign. An alternative physics list `QGSP_FTFP_BERT_EMM` is used for comparison. The initial HCAL calibration had been done with 50 GeV electrons, so the responses are shown relative to the electron response at 50 GeV. The results show a larger response for π^+ than for π^-. At beam energy $p_{\text{Beam}} = 2\,\text{GeV}$, this difference is almost 10 % and slowly decreases with increasing p_{Beam}. This difference is not described by GEANT4. Both of the physics lists used in this study predict approximately the same response of π^+ and π^-, agreeing with the π^+ data. This difference in data could be explained by different probabilities to create π^0 through charge-exchange reactions, $\pi^+ + n \to \pi^0 + p$ (I) and $\pi^- + p \to \pi^0 + n$ (II), taking place in the ECAL. π^0 quickly decays to two photons and in CMS calorimeters leaves around 20 % more signal than $\pi^\pm$. Since $PbWO_4$, the scintillator material in the ECAL consists of 42 % more neutrons than protons, the reaction (I) has a higher probability of taking place, explaining the increased response for π^+.

Another notable disagreement between the test beam results and the simulation of GEANT4 is in kaons. The response for both K^+ and K^- is larger than predicted. The level of disagreement changes in the newer GEANT4 versions [309]. The agreement with π^- becomes better towards GEANT4 version 10.7p01 used for the early Run 3 simulation. On the other hand, the agreement with π^+ does not seem to improve but even deteriorates. Regarding kaons, it was shown that the agreement between the simulation and the particle gun data improves only slightly and there is a remaining disagreement of up to 20 % in the response for $p_{\text{Beam}} > 3\,\text{GeV}$.

There is a large difference between the responses of p and $\overline{p}$, which greatly impacts the overall jet responses of the different jet flavours. However, both are described well

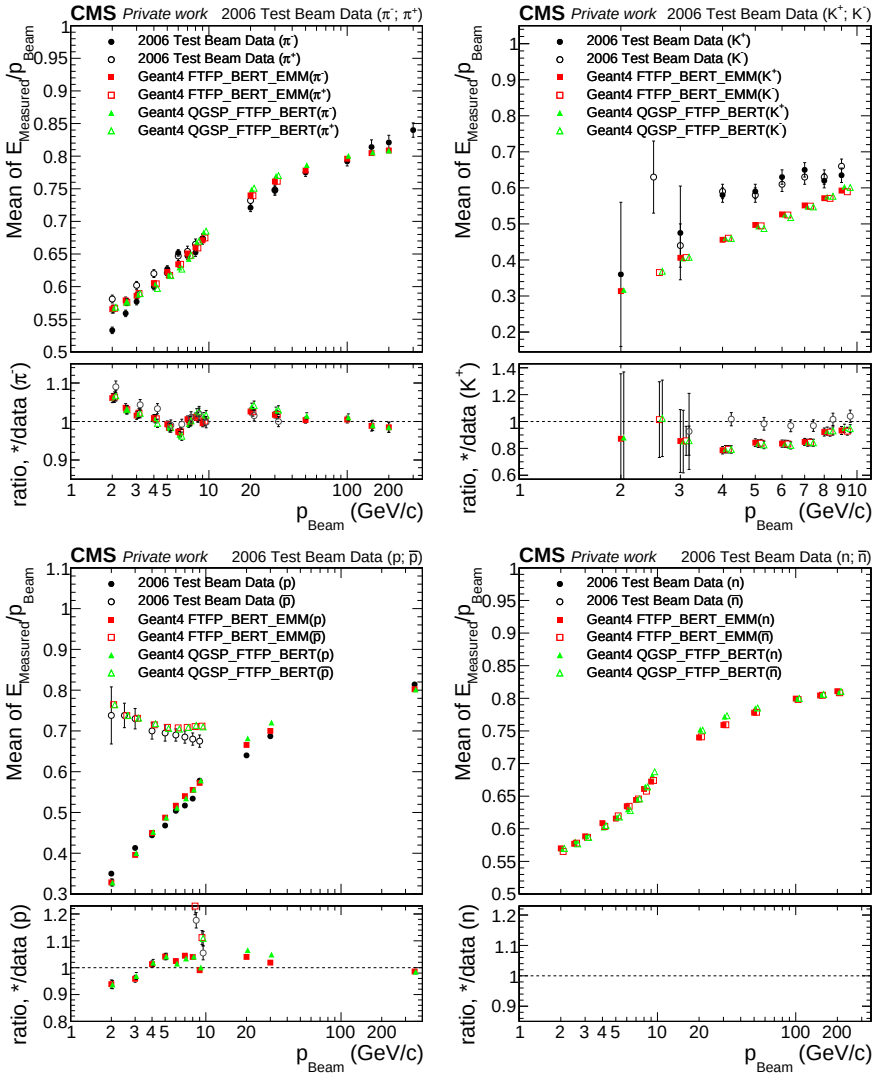

Fig. 6.26. The total ECAL and HCAL response from the test beam and the simulated response using two different physics lists. Top left shows the results for $\pi^{\pm}$, top right for $K^{\pm}$, bottom left for p and $\overline{p}$, and bottom right for n and $\overline{n}$. Data are obtained from [308]. The particle gun simulation is performed using GEANT4 v.10.4.p03.

by GEANT4. For n and $\overline{n}$, there are no data, but the simulation results show similar predictions for n and $\overline{n}$.

In the PF code, the responses of the PF candidates are calibrated with respect to π^0. If different rates of hadrons are predicted in different jet flavours and at different phase space points, this might lead to a disagreement of the JEC for different jet flavours not taken into account in the data-driven JECs. The disagreement of the simulations with the

$\pi-$response can also lead to the disagreement of the JEC between flavour and antiflavour, as tested in Section 6.6.4.

6.6.3. Impact of the single-pion shift on the PF jet energy

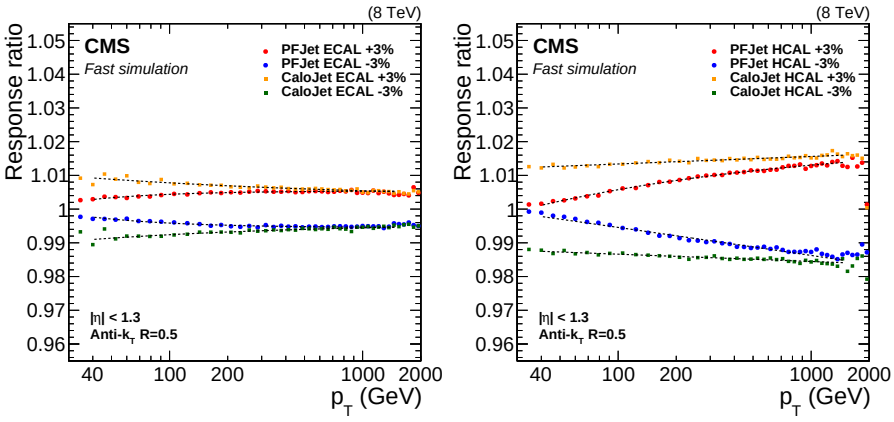

Fig. 6.27. The impact of the 3 % shift in $\pi^{\pm}$ energy in ECAL (left) and in HCAL (right) on the energy of the PF and Calo jets [284].

As demonstrated in an earlier study, the results of which are displayed in Fig. 6.27, miscalibration of the single-pion response has a dampened effect on PF jets due to the fact that jet momentum is determined by combining the track momenta with the energy deposits in the calorimeters. Only at high p_{T}, the effect becomes large because the momentum determination for such high-p_{T} tracks becomes imprecise due to their small curvature. For low-p_{T} jets, the only way to have an impact on the jet p_{T} is if the $\pi^{\pm}$ shift causes the creation or removal of neutral particles in the jet. Since the π^{+}/π^{-} correction developed in this Thesis (see, Section 6.6.4) mainly impacts the low p_{T} tracks, which have a small impact on the large-p_{T} jets, the overall correction is estimated to be small.

6.6.4. Flavour-antiflavour asymmetry due to pion-antipion response differences

To account for the impact of the π^{-} and π^{+} response mismodelling on the flavour-antiflavour JEC seen in the HCAL test beam in Section 6.6.2, the response of the PF candidates formed from negatively charged tracks was scaled and the corrections were then propagated through the JEC code. The goal was to scale the π^{-} response in the simulation to match that in the data. π^{+} response is described better by the simulation and the ratio in the test beam data, $\frac{R(\pi^{+})}{R(\pi^{-})}$, envelopes the variation for both π^{+} and π^{-}. The correction factor for π^{-} was obtained from the fit of $\frac{R(\pi^{+})}{R(\pi^{-})}$ shown in Fig. 6.28. For

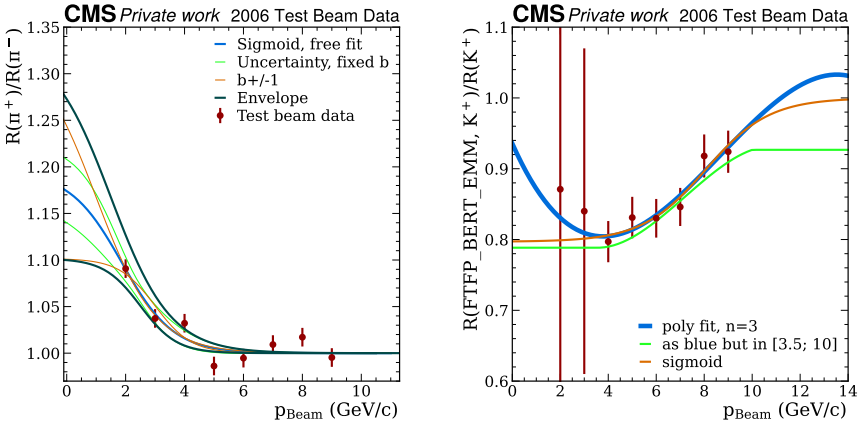

Fig. 6.28. The ratio fit for obtaining the pion (left) and kaon (right) correction factors for PF blocks due to particle response mismodelling. The data points match the ratio plots of Fig. 6.26.

the fit, we use a general sigmoid function

$$y = k + \frac{a}{1 + b\exp(-cx)}, \tag{6.7}$$

but requiring that $y \to 1$ at $x \to \infty$. Thus,

$$y = 1 - a + \frac{a}{1 + \exp(-c \cdot (x - b))}. \tag{6.8}$$

The low momentum data in Fig. 6.28 do not suggest any clear trend towards $p_{\text{Beam}} \to 0$ and under-constrain the sigmoid with 3 input parameters. The parameter b specifies the centre of the transition between the high and low value of the sigmoid. In a free fit allowing b to vary a value of $b = 1.89 \pm 4.42$ was obtained, where the uncertainty does not correspond to the expected transition range of $1 < b < 3$ and is overestimated. To improve the uncertainty estimate for this fit, it was obtained from two factors. First, the fit was performed with fixed parameter $b = 1.89$ (green in the figure). Secondly, two curves with $b \to b \pm 1$ were obtained to estimate the variation due to b parameter. We take the correction factor as the highest envelope of the fits in order to evaluate a conservative systematic uncertainty. The mean values of the fitted parameters and their uncertainties are shown in Fig. 6.1.

The correction factor was applied on the QCD validation sample consisting of 2 million GEN-SIM events (generated events passed through the detector simulation but not the event reconstruction steps; see Fig. 3.2). In the PF algorithm, all tracks were matched to the generated particles with $\Delta R = 0.01$. The closest generated particle to the track was taken as the matched generated particle to the track. Tracks matched to generated π^-

Table 6.1

Fitted parameters, the uncertainties and the covariance matrix of the free fit in Fig. 6.28 (left). The upper and lower envelope curves where obtained by taking the mean fitted parameters, but shifting the p_{Beam} values by 0.5 GeV up and down, respectively

			covariance matrix		
parameter	mean	uncertainty	a	c	b
a	−0.19	0.52	0.27	0.61	2.28
c	1.13	1.23	0.61	1.51	5.24
b	1.87	4.42	2.28	5.24	19.52

were tagged as π^- tracks. Then for each π^- track, the energy of the PF block containing the track was shifted by $E_{\text{new}} = E_{\text{old}} - p_{\text{track}} \cdot (1 - 1/C(p_{\text{track}}))$.

Table 6.2

Fitted parameters, the uncertainties and the covariance matrix of the sigmoid fit in Fig. 6.28 (right)

			covariance matrix		
parameter	mean	uncertainty	a	c	b
a	0.203	0.022	0.0005	−0.0047	-0.007
c	0.75	0.26	−0.0047	0.0679	0.0548
b	8.05	0.40	−0.007	0.0548	0.1613

In a similar way, corrections were implemented for the kaon mismodelling. The fit for the correction factor C is shown in Fig. 6.28 (right). C is obtained by fitting the ratio of GEANT 4 simulation and K^+ response with a sigmoid function. The correction shifts both K^+ and K^- response as $E_{\text{new}} = E_{\text{old}} + p_{\text{track}} \cdot (1 - C(p_{\text{track}}))$. Even though the correction is the same for quark and antiquark jets and thus not used in not used in this analysis, the overall correction factor is important for the precise global JES measurements. The results of the sigmoid fit are shown in Table 6.2.

The effect of the pion correction correction on the jet p_T is expected to be small unless in cases where it allows PF to introduce or remove PF candidates. Since the pion response correction reduces the energy deposit of π^- in HCAL, there are cases where a neutral hadron is no longer introduced. In addition, reducing the HCAL deposit can cause a new non-isolated muon to get introduced. To amplify the effect and to test the non-linearity of the correction, several runs were repeated where the π^- correction was increased by factors of 3, 5, and 10.

The jet energy response of the sample with the scaled π^- response was compared with the sample where the π^- response was kept unchanged (central sample). The comparison for different flavours is illustrated in Fig. 6.29. The error bars correspond to the statistical uncertainty of the MC samples, which is large because only 2 million events were used. Nevertheless, the correlation among jets with and without pion scaling was assessed. The 2D histogram of the jet response with and without pion scaling is shown in Fig. 6.30. The correlation coefficient for the jet response was 1.000. When the pion scaling increased 10

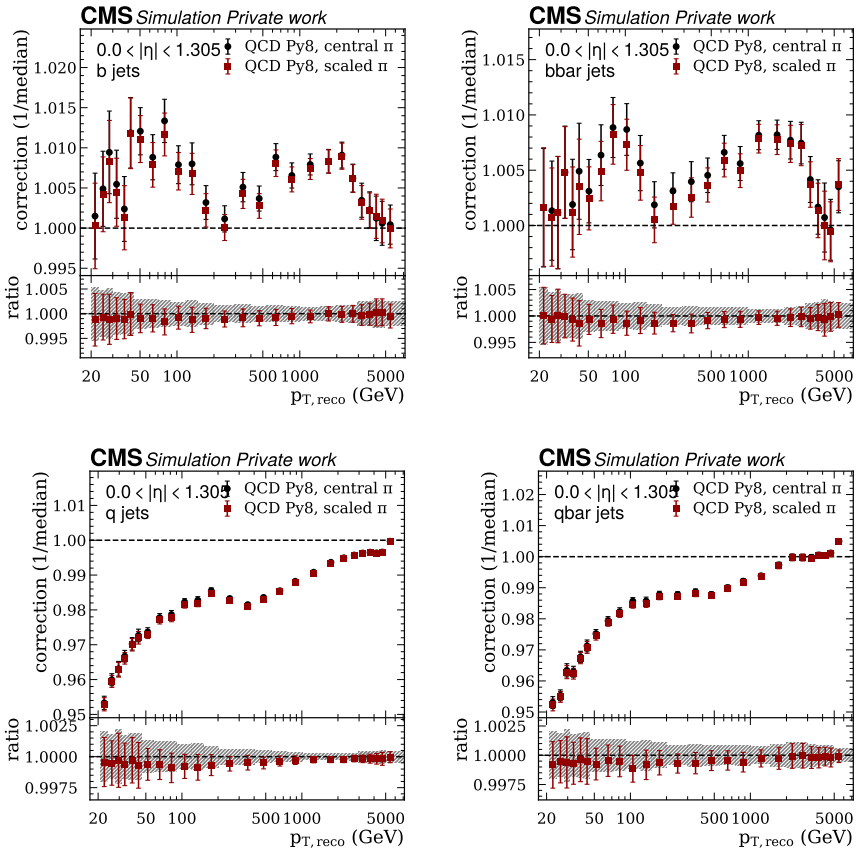

Fig. 6.29. Jet energy response before (black circles) and after (red squares) applying the scaling of the π^- response to match the response seen in the HCAL test beam for quark (left column) and antiquark (right column) jets. The results for b jets (top) and q jets (bottom) are shown.

times the nominal one, the correlation coefficient decreased to 0.997. Due to the large correlations, the statistical uncertainty of the pion scaling was neglected. A shift of up to 0.2 % is observed due to the pion scaling, impacting the JEC for all jets.

The effect of the response shifts seen in Fig. 6.29 is similar on the flavour and antiflavour jets, leaving only a small impact on the flavour-antiflavour uncertainties. The ratio plots from Fig. 6.29 for flavour and antiflavour are overlaid in Fig. 6.31 after merging some of the p_T bins and reducing the statistical uncertainties by a factor of 100 due to the correlations of the scaled and central responses. At low p_T, π^- scaling impacts s jets more than $\overline{s}$ jets, while at large p_T it is the other way around. A similar but opposite trend can be seen for $u + d$ and $\overline{u} + \overline{d}$ jets. For b and c jets, no clear trend of the quark vs antiquark jet relation over p_T is visible. Therefore, it was decided to merge all the p_T bins and unite the uncertainty as an overall scale factor for each of the four $|\eta|$ bins. The

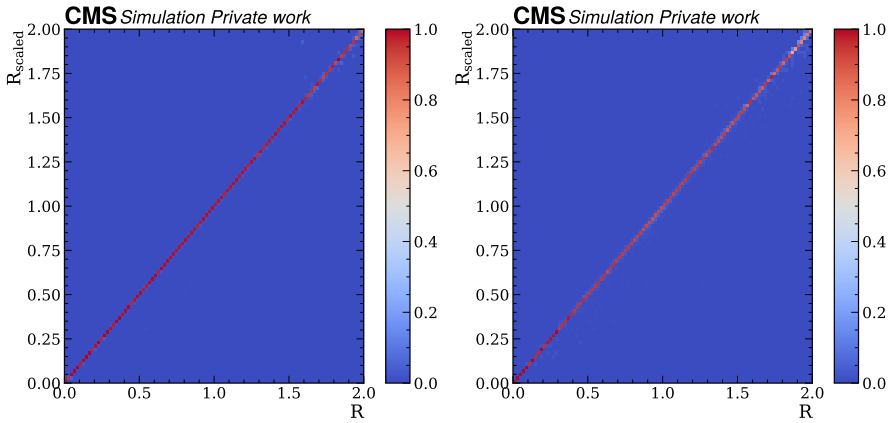

Fig. 6.30. Correlations between the jets with and without correction accounting for π^+ response disagreement with the GEANT 4 simulation. Left shows the correlation matrix for the normal correction and right shows the correlation matrix for the correction increased 10 times.

uncertainty is obtained as the difference of the shift of the jet energy response for quark jets and for antiquark jets. The resulting values are shown in Table 6.3.

Table 6.3

Uncertainty values for each jet flavour and $|\eta|$ bin $\times 10^{-5}$

Jet Flavour	$\lvert\eta\rvert < 1.3$	$1.3 < \lvert\eta\rvert < 2.5$	$2.5 < \lvert\eta\rvert < 3.2$	$3.2 < \lvert\eta\rvert < 5.4$
b	7.7	1.5	-58.1	60.6
$\overline{b}$	-7.7	-1.5	58.1	-60.6
c	-34.6	4.9	-11.3	3.8
$\overline{c}$	34.6	-4.9	11.3	-3.8
s	-3.5	2.2	-1.8	3.4
$\overline{s}$	3.5	-2.2	1.8	-3.4
u/d	7.6	9.3	10.8	7.2
$\overline{u}/\overline{d}$	-7.6	-9.3	-10.8	-7.2

6.6.5. Flavour-antiflavour uncertainties from the parton shower modelling

In this section, the flavour-antiflavour uncertainties are obtained by comparison of PYTHIA 8 and HERWIG 7. The fractions of different jet flavours shown in Fig. 6.4 revealed some differences in modelling by PYTHIA 8 and HERWIG 7 showers. The flavour vs anti-flavour fractions shown in Fig. 6.32, on the other hand, reveal no significant differences, except for a mild difference in the forward direction for u/d quarks. The fractions of most flavours are equal with the corresponding antiflavour fractions, except for u/d and, more mildly, for s quark, where the flavour part starts to dominate over antiflavour at large $p_{T,\mathrm{ptcl}}$. From now on, in this section, writing "inclusive flavour sample" depicts a sample

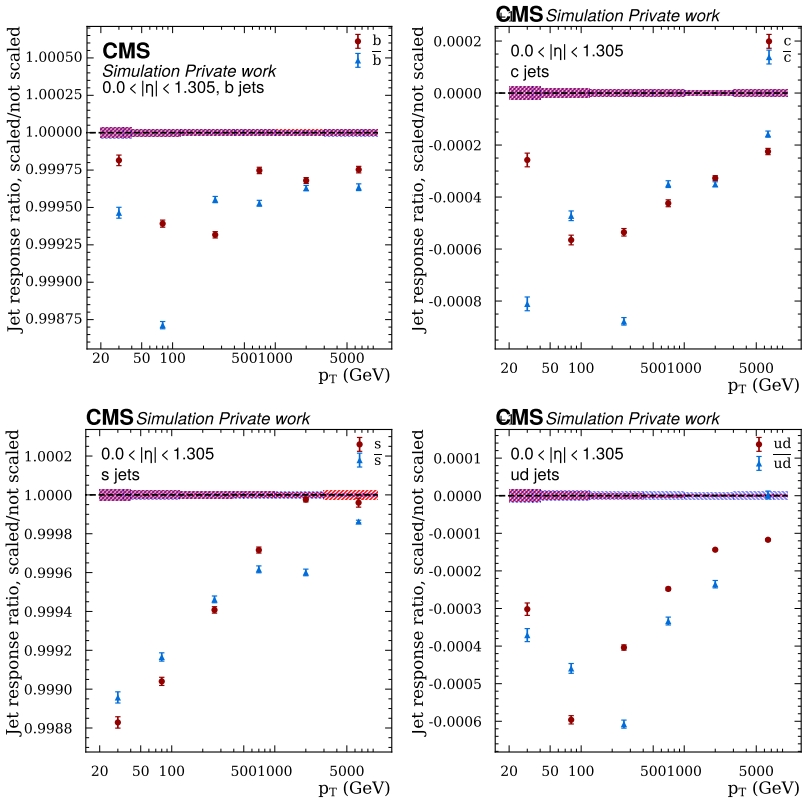

Fig. 6.31. Ratio of the jet energy response scaled and not scaled by the π^- shift. The impact of the shift of the corresponding flavour and antiflavour are overlaid.

where both flavour and antiflavour is included, while solely flavour or antiflavour samples denote exclusive samples. For instance, b sample denotes a sample with b jets and no $\overline{b}$ jets, while b inclusive flavour denotes a sample where both b and $\overline{b}$ are included.

The method used to calculate flavour vs antiflavour uncertainties was derived from the scheme used to determine the flavour uncertainties. Only the $t\bar{t}$ sample was used due to the largest amount of jet data. A fit was performed for each jet flavour and antiflavour, similar to the fits described in Section 6.3.6, but the median response was fitted vs $p_{T,\text{reco}}$ instead of the inverse of the median response. Before the fit, each flavour and antiflavour response was normalised to the inclusive flavour, for example, both b and $\overline{b}$ were normalised by the response of the inclusive b sample. The fit results for the POWHEG+PYTHIA 8 sample for the most central η bin are shown in Fig. 6.33. Two fitting functions were used: a third-order and a fourth-order log-polynomial, and a χ^2 check as in Section 6.3.6 was performed to find the most suitable one. The fit range was limited as in Section 6.3.6 to ensure that the fit is not affected by large statistical uncertainties at high p_T have large statistical uncertainties.

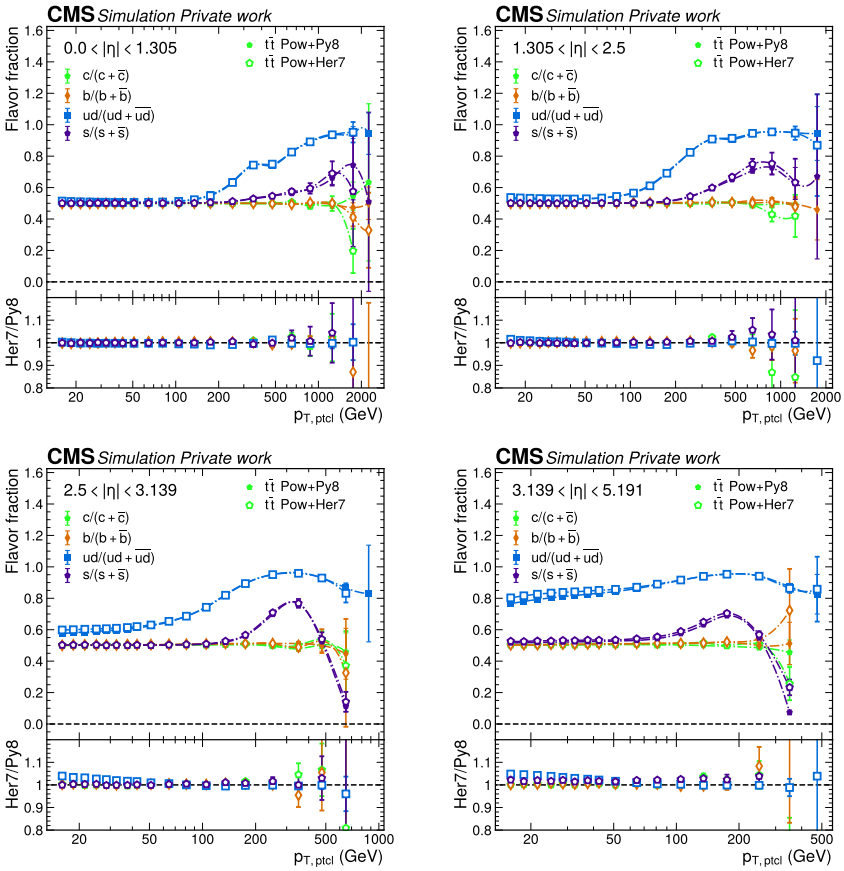

Fig. 6.32. The fractions of each flavour vs the inclusive flavour for the $t\bar{t}$ dataset.

The response of flavour and its corresponding antiflavour jets is nearly opposite because they are normalised to the inclusive flavour. There are some deviations from this pattern in q jets since the pp collisions at LHC yield more u and d jets compared to $\overline{u}$ and $\overline{d}$. It is important to note that the magnitude of the response relative to the inclusive flavour is $\mathcal{O}(10)$ lower than the inclusive response shown in Fig. 6.10, resulting in higher relative statistical uncertainties.

The fits were repeated for the POWHEG+HERWIG 7 sample. The results are shown in Fig. 6.34. Note that the HERWIG 7 sample does not predict a large difference between c and $\overline{c}$ jets, the difference is within 0.04 % for $p_{T,\text{reco}} > 30$ GeV, while PYTHIA 8 predicts a large difference exceeding 0.1 %. This is an example where differences in modelling by the two showers lead to a large flavour-antiflavour uncertainty. In contrast, the differences in b and $\overline{b}$ modelling by the two showers are not as large despite the absolute difference between b and $\overline{b}$ being large in each shower. Note, that PYTHIA 8 predicts a similar trend for both s and $u + d$ jets, while for HERWIG 7 the effect is small and in the opposite directions

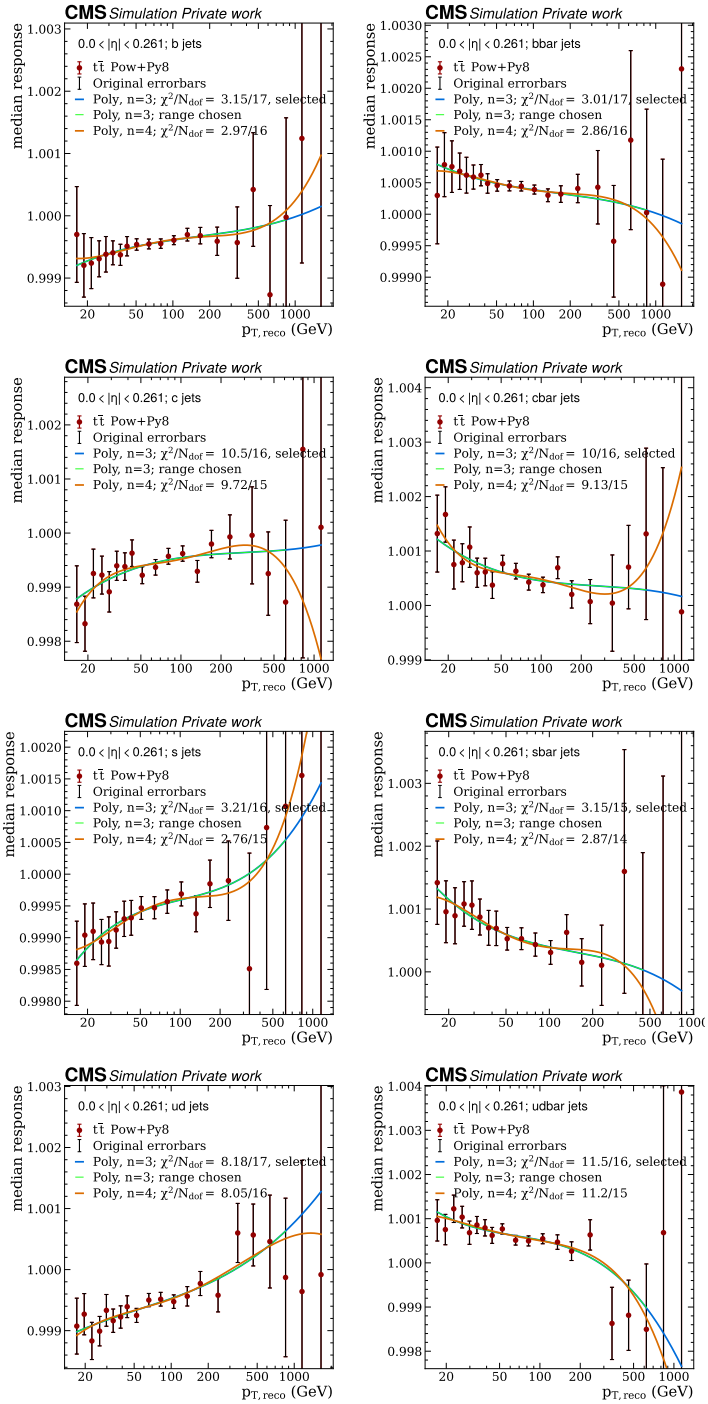

Fig. 6.33. Fits of the median response of b, c, s, and light jets, and their antiflavour jets for the POWHEG+PYTHIA 8 sample in the most central η bin. The χ^2 values is shown on the fits as well as the fit chosen for the further computation.

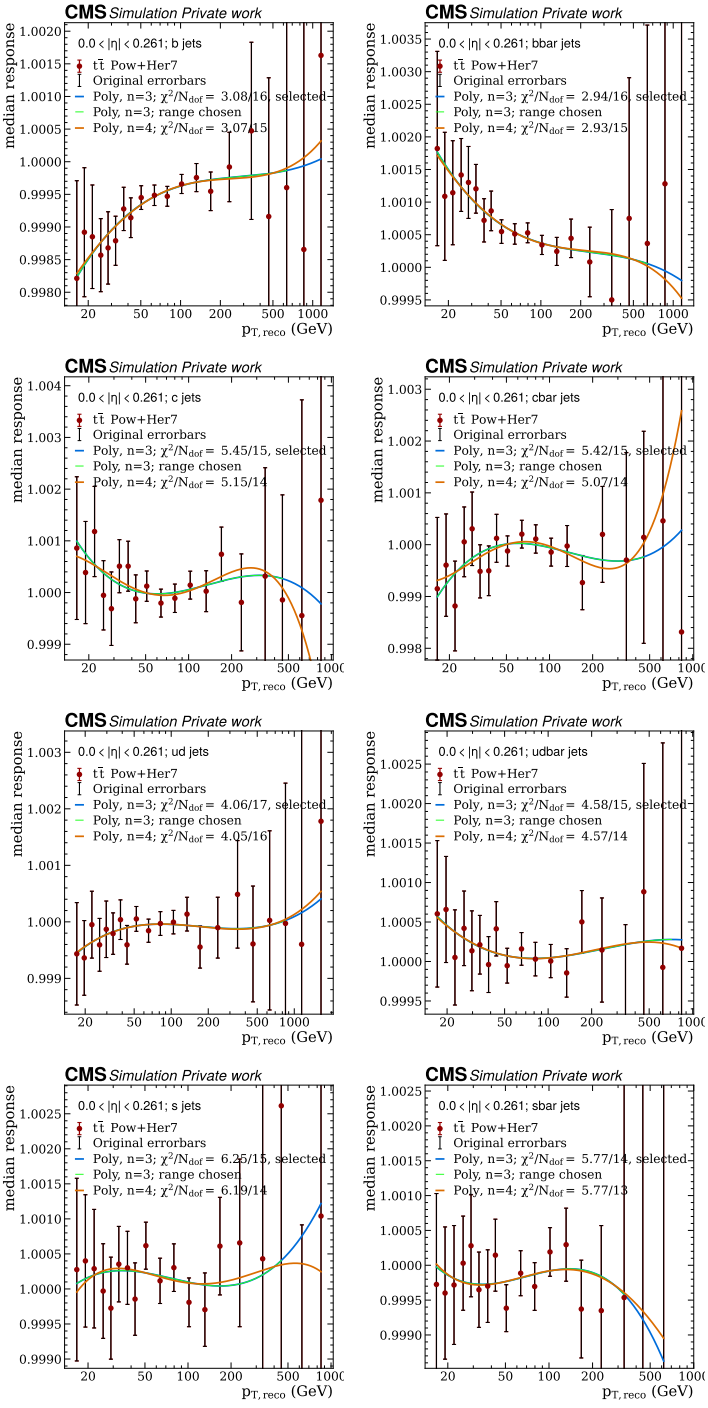

Fig. 6.34. Fits of the median response of b, c, s, and light jets, and their antiflavour jets for the POWHEG+HERWIG 7 sample in the most central η bin.

leading to a large flavour uncertainty. For the Run 1 measurement of Δm_t [30], the b vs $\overline{b}$ uncertainty was estimated by taking the total difference in responses between b and $\overline{b}$ in the same shower, which at that time was PYTHIA 6. However, a good MC generator should model b and $\overline{b}$ response differences as in data, while the potential mismodelling of the different flavour vs antiflavour responses has to be estimated. Thus, this analysis using the predictions of HERWIG 7 and PYTHIA 8 presents a more proper estimate of the flavour-antiflavour uncertainty.

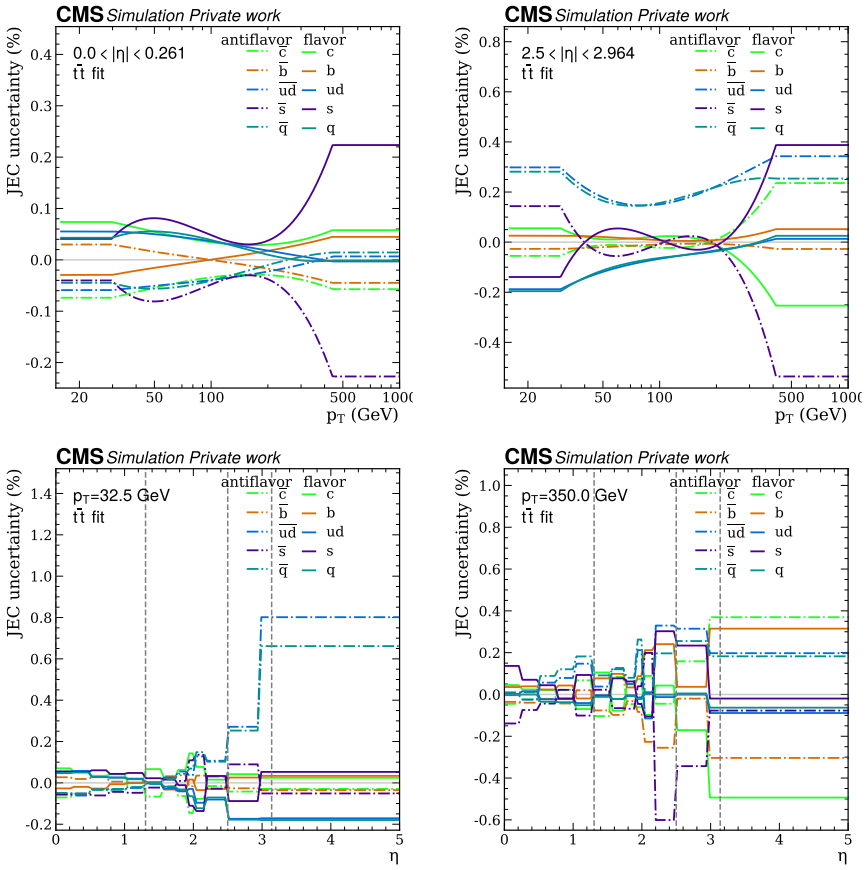

Fig. 6.35. Flavour vs antiflavour uncertainty as a function of p_{T} for two different η regions (top) and as a function of η for two different p_{T} regions (bottom).

The flavour uncertainties were estimated by subtracting the PYTHIA 8 fit from the HERWIG 7 fit. The resulting uncertainty curves can be seen in Fig. 6.35. The dominating uncertainty, especially at the lowest $|\eta|$, is the s vs $\overline{s}$ uncertainty. This agrees with the observations about the hadron energy fraction differences for HERWIG 7 and PYTHIA 8 for s and $\overline{s}$ jets in Section 6.6.1. Due to the u/d flavour fraction dominating over $\overline{u}/\overline{d}$ at large p_T and η, the $\overline{u}/\overline{d}$ uncertainty is much larger than the u/d uncertainty. Thus, at

large p_T and η, where the fraction of $\overline{u}/\overline{d}$ jets is small, the uncertainty for $\overline{u}/\overline{d}$ becomes larger than the u/d uncertainty. The b vs $\overline{b}$ uncertainty changes sign with increasing p_T and $|\eta|$, and is below 0.3 % in the relevant range.

6.7. Summary and conclusions

The derivation of jet flavour corrections and uncertainties was presented. Unlike in Run 1, the flavour corrections are obtained from dijet, $t\bar{t}$ samples individually, and from a combined fit of dijet and $t\bar{t}$, and DY samples. The flavour corrections are derived in a finer binning than the Run 1 corrections and have lower statistical fluctuations. The differences between the Run 1 and newly derived corrections are up to 2 % (for light quark, u/d, jets).

Flavour uncertainties were obtained from a simultaneous fit of all three physics datasets and in a finer binning than in Run 1. Compared to Run 1, flavour uncertainty is significantly reduced for g jets, while for other flavours it remained similar. For b jets, the flavour uncertainty has a rapid increase at large momenta, which is possibly due to the mismodelling of long-lived b hadrons. However, the exact reasons for the issue have yet to be determined. The flavour-antiflavour uncertainty takes into account two different effects. First, the MC modelling of the flavour composition. Second, is the effect of the mismodelling of the hadron and antihadron responses of the GEANT 4 simulation compared to the test beam data.

7. THE MEASUREMENT OF THE MASS DIFFERENCE BETWEEN TOP AND ANTI-TOP QUARK

In this section, the measurement of the mass difference between the top quark and antiquark, $\Delta m_t = m_t - m_{\bar{t}}$, on $t\bar{t}$ events in the lepton+jets decay channel is described.

7.1. Event selection

The event selection is targeting the $t\bar{t}$ lepton+jets decay channel and chooses events that have exactly one isolated lepton (electron or muon) and at least four jets, of which two are b jets. A large $p_{\mathrm{T}}^{\mathrm{miss}}$ is also present. This section sequentially explains the event selection used to obtain $t\bar{t}$ lepton+jets events with a high purity.

An event display of an example event that passes the event selections is shown in Fig. 7.1. The event is obtained from the simulated events and shows four jets, two of which are b tagged, an isolated muon, and a large $p_{\mathrm{T}}^{\mathrm{miss}}$.

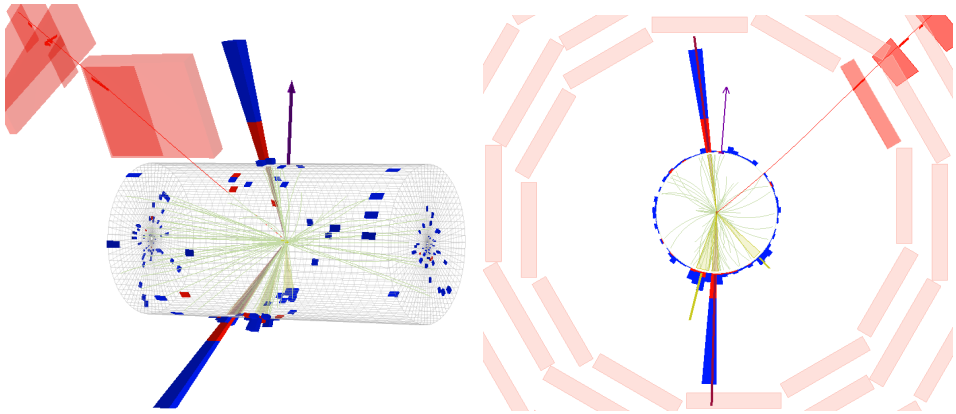

Fig. 7.1. An event display of a $t\bar{t}$ event candidate. The view from an arbitrary plane (left) and in the $\rho - \phi$ plane (right) is shown. The yellow (dark red) cones with same colour lines pointing out represent light (b tagged) jets. The red track shows represents muon going through the muon chambers. The red (blue) stacked blocks represent the energy deposits in the ECAL (HCAL). The violate arrow shows the direction of the $p_{\mathrm{T}}^{\mathrm{miss}}$. The green lines shows the trajectories of the PF candidates.

7.1.1. Triggers

The HLT triggers used are the unprescaled triggers targetting a single electron or single muon. The trigger paths used for each year are listed in Table 7.1 together with the p_{T} thresholds for each of them. The lepton selection then requires thresholds higher than the HLT ones where the trigger efficiency has reached a plateau and does not change significantly. Between 2016 and 2017 the triggers underwent major changes caused by

Table 7.1

The HLT trigger paths used for this analysis

Channel	Trigger	HLT p_T threshold [GeV]	Reco p_T threshold [GeV]
2016 APV e	HLT_Ele27_WPTight_Gsf	27	29
2016 APV μ	HLT_IsoMu24 and HLT_IsoTkMu24	24	26
2016 non-APV e	HLT_Ele27_WPTight_Gsf	27	29
2016 non-APV μ	HLT_IsoMu24 and HLT_IsoTkMu24	24	26
2017 e	HLT_Ele32_WPTight_Gsf_L1DoubleEG	32	35
2017 μ	HLT_IsoMu27	27	29
2018 e	HLT_Ele32_WPTight_Gsf	32	35
2018 μ	HLT_IsoMu24	24	26

the Phase-1 CMS tracker upgrade and the increased luminosity. Note the increase in the p_T threshold for both muons and electrons from 2016 to 2017. The 2017 electron trigger was seeded with single L1 electron + photon (EGamma) trigger seeds and double electron seeds, while for the rest of the years it was only single EGamma seeds. To remove this difference, we require that events passing the 2017 electron trigger must pass an additional L1 filter `hltEGL1SingleEGOrFilter` to match the same requirements as for the other years.

7.1.2. Datasets

The data samples used for this study are listed in appendix D. All datasets are in the MiniAOD v.2 data format and contain ultra legacy (UL) information. UL is the reprocessed CMS Run 2 dataset, which, among other things, benefits from improved tracking and jet reconstruction. The CMS Run 2 dataset from data collected in 2016-2018 is used and corresponds to a total luminosity of 137.62 fb^{-1}. The 2016 dataset is split into two eras, i.e. data collection periods. This is because for the early 2016 runs, also called "APV" (analogue pipeline voltage)[20], the tracker signal-to-noise ratio was mistakenly kept lower and not optimal for the gradually increasing number of pileup (PU) [310]. The large amount of PU created saturation effects in the APV25 readout chips, which caused the tracker to miss some of the hits. The drain speed of the pre-amplifier was changed when collecting the non-APV[21] dataset. Thus, in total four eras of Run 2 are analysed with integrated luminosities 19.52 fb^{-1}, 16.81 fb^{-1}[311], 41.48 fb^{-1}[312] and 59.83 fb^{-1}[313] for the 2016 APV, 2016 non-APV, 2017 and 2018, respectively.

For the MC datasets, $t\bar{t}$ (lepton+jets and dilepton channels) and single-top (tW and t-channel, but not s-channel) are considered signal, since they have substantial event yields and carry a top-mass dependence on their shapes. The default top-quark mass parameter

[20] and also known by names "preVFP" (pre voltage feedback preamplified), or "HIPM" (heavy ionising particle mitigation)

[21] also called 2016postVFP, no-HIPM or late 2016

used for event generation is $m_t = 172.5\,\text{GeV}$. For the signal datasets, additional MC samples with $m_t = 171.5\,\text{GeV}$ and $m_t = 173.5\,\text{GeV}$ were produced. All signal datasets were generated at NLO in α_s using POWHEG, except for the single-top t-channel events that were generated using POWHEG +MADSPIN [314] at NLO.

The backgrounds include $t\bar{t}$ all hadronic decay channel, the single-top s-channel, vector boson, i.e. W+jets and Z+jets, diboson, i.e. WW, WZ and ZZ (VV), and QCD multijet samples. The latter are special electron and muon enriched datasets, since the inclusive QCD datasets contain few events with charged leptons.

7.1.3. Lepton selection

The analysis selects events with one isolated lepton by requiring that exactly one signal electron or muon passes the event selection with no additional veto leptons. The definitions of the signal and veto electrons and muons are shown in Table 7.2. Electrons are selected within the tracker coverage, that is, $|\eta| < 2.4$, which after the Phase-2 upgrade was extended to $|\eta| < 2.5$. In addition, the EE/EB transition region at $1.4442 < |\eta| < 1.566$ is excluded. Muons are selected within the muon detector coverage.

Table 7.2
The options for the signal and veto leptons, their corrections and the scale factors used

	Signal electron	Veto electron	Signal muon	Veto muon
Max $\|\eta\|$ (2016)	2.4	2.4	2.4	2.4
Max $\|\eta\|$ (2017-2018)	2.5	2.5	2.4	2.4
Min p_T [GeV] (2016)	29	15	26	15
Min p_T [GeV] (2017-2018)	35	15	29	15
ID	Tight	Loose	Tight	Loose
ID version	cutbasedElectronID-Fall17-94X-V2		CutBased	CutBased
Isolation	Within ID		PFIsoTight	PFIsoLoose
Extra η cuts	EE/EB transition	-	-	-
Energy corrections	pat::Electron	pat::Electron	Rochester	Rochester
Reco SF	Yes	-	-	-
ID SF	Yes	-	Yes	-
Isolation SF	Within ID SF	-	Yes	-
Trigger SF	Only 2017-2018	-	Yes	-

The signal electrons and muons are required to meet their respective tight ID requirements described in Section 5.7. For muons, the tight relative PF isolation criterion is also added, while for electrons, it is included in the ID requirement. For electrons, an additional impact parameter requirement of $|d_{xy}| < 1\,\text{mm}$, $|d_z| < 2\,\text{mm}$ at $|\eta| \leq 1.479$ and $|d_{xy}| < 0.5\,\text{mm}$, $|d_z| < 1\,\text{mm}$ at $|\eta| > 1.479$ is applied, whereas for muons the cut of $|d_{xy}| < 2\,\text{mm}$, $|d_z| < 5\,\text{mm}$ is already present within the tight ID requirement [315].

As explained in Section 5.7, MC events containing leptons require energy corrections and per-event SFs to match the p_T resolution and efficiencies to those observed in the data. Electron energy corrections are already available within the electron object itself in

the MiniAOD, as marked by "pat::Electron" in Table 7.2. For muons, additional Rochester corrections are applied. All required SF are applied according to Eq. (5.7) and Eq. (5.6), except for the trigger SF for electrons in the 2016 data which have to be added in further studies.

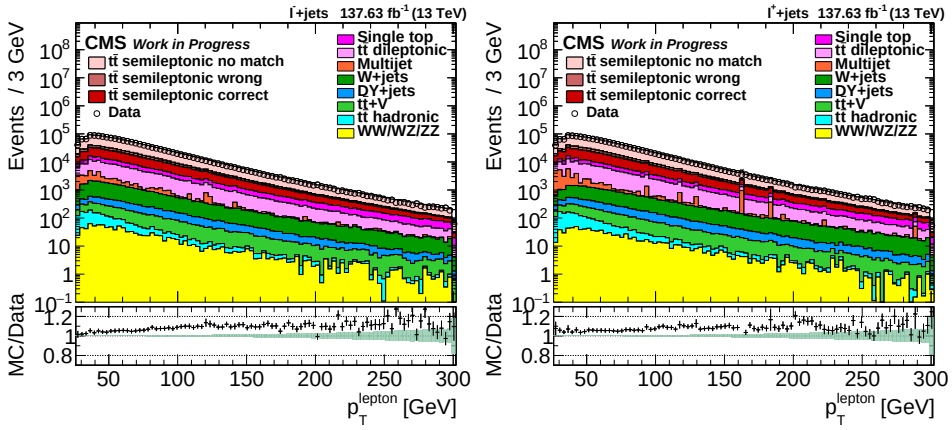

Fig. 7.2. Lepton p_{T} distribution for l^-+jets events (left) and l^++jets events (right). The whole Run 2 dataset is included. The abrupt move of the histogram from the first to the second bin and from the third to the fourth bin at values 29 GeV and 35 GeV is explained by the different p_{T} selection criteria for muons and electrons for different years as shown in Table 7.1. The shaded region in the ratio shows the statistical uncertainties of the data, while the MC error bars show the statistical, cross section and luminosity uncertainty. The data to MC disagreement can be explained by the other MC uncertainties as shown in [92].

The p_{T} distributions for both positive and negative leptons, as depicted in Fig. 7.2, exhibit no notable differences based on charge. In these and the following control plots, for MC, only statistical, luminosity, and cross section uncertainties are shown. An excess in MC events over the data can be seen to increase with increasing lepton p_{T}. This issue is probably related to the disagreement of the NLO predictions for the top-quark p_{T} in $t\bar{t}$ events, seen also in Fig. 3.5 and in [316]–[319]. It is common to perform a top p_{T} spectrum reweighing to correct for this difference. Instead of applying it to the central sample, the reweighing is treated as a separate nuisance parameter in the statistical inference fit, as explained in Section 7.5.2. The overall excess in the event yield for the MC events has been observed in the previous Run 2 analyses of $t\bar{t}$ lepton+jets channel [92], [320] and was found to be around 5 % in the μ+jets and 6 % in the e+jets channel. This excess can be explained by the MC uncertainties that are not included in the uncertainty bars.

It can be seen that some processes, such as the multijet and the $t\bar{t}$ hadronic channel, have a steeper slope in the lepton p_{T} spectrum than other $t\bar{t}$ decay channels and single-top or V+jets, which still contain a significant amount of leptons above 100 GeV. Some multijet events with large event weights and also large uncertainties are seen, in particular

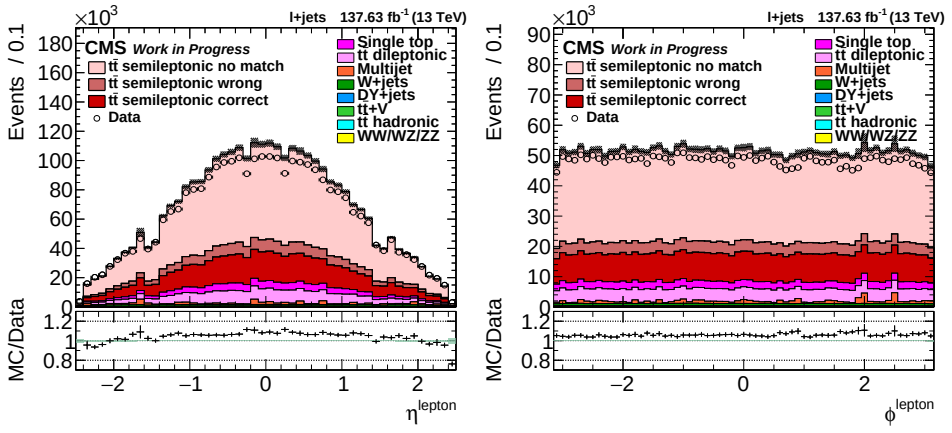

Fig. 7.3. Lepton η (left) and lepton ϕ (right) distributions in the combined l+jets events channel. The whole Run 2 dataset is included. The data to MC disagreement can be explained by the other MC uncertainties as shown in [92].

in the l^++jets distribution. Many of such events will be removed by the event requirements explained in Section 7.2.3, although some of these events will remain an issue for the fit. The lepton η and ϕ distributions presented in Fig. 7.3 are mostly smooth, and the irregularities can be explained by the detector effects, including the EE/EB transition at $1.4442 < |\eta| < 1.566$.

7.1.4. Jet selection

This analysis uses jets clustered from PF candidates after charged hadron subtraction using the anti-k_T algorithm with R=0.4 (AK4PFchs) with $p_T > 30\,\text{GeV}$. In both 2016 eras, we select jets with $|\eta| < 2.4$, while in 2017-2018 we select $|\eta| < 2.5$. The jets are required to pass a tight jet ID as derived by the CMS jet physics object group, including the jet lepton veto [321]. The typical jet energy correctionss (JECs), that is, L1FastJet, L2Relative, and L3Absolute were applied with version 'V7' for 2016, 'V6' for 2017, 'V2' for 2018 data. In addition, flavour corrections are applied as derived in Section 6.3. The impact of flavour corrections on the W boson mass distribution and the procedure to apply them is elaborated in Section 7.2.1. Jet energy resolution (JER) in MC is smeared using the hybrid method as shown in Section 5.6.

The event reconstruction relies on the b-jet identification (b tagging) using the DeepJet algorithm with the Medium WP. The event selection requires at least four jets. In addition, exactly two b-tagged jets among the leading eight are required. This is a stricter requirement than in the previous Δm_t analysis, where at least one b jet was required [30]. This reduces the number of events for the analysis but increases the signal-to-background ratio. Due to the almost ten-fold increase in luminosity between Run 1 and Run 2, the limited amount of data is not expected to be so limiting. The search for the b-tagged jets

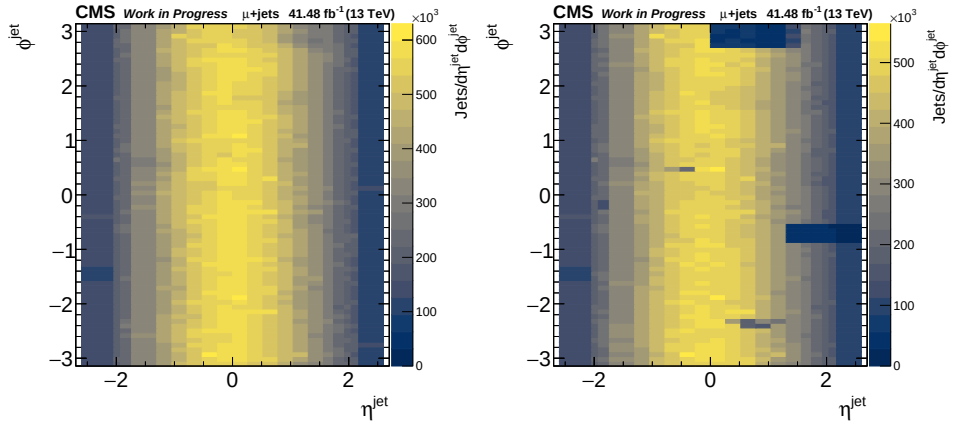

Fig. 7.4. A distribution of the jet ϕ and jet η before the application of jet veto maps (left) and after (right) for the μ+jets 2017 channel.

among the eight leading jets follows the discussion in [320], where it was found to bring a higher signal-to-background ratio. This is different from the Run 2 m_t measurement using the 94X ReReco data [92] and the Run 1 Δm_t measurement [30] where the four leading jets were tested.

Jet veto maps

The strictest of the available jet veto maps, defined in Section 5.6, are applied, where jets aligned with the veto region are vetoed, i.e. removed from data processing. The jet veto maps used are shown in Table 7.3. The veto maps having the greatest impact are those related to the HCAL wedge HEP17 (HCAL Endcap Plus, wedge 17) in the 2017 data and related to the HCAL wedge HEM1516 (HCAL Endcap Minus, wedges 15-16). In addition, rare events with jets fulfilling $p_{\mathrm{T}} > 1000\,\mathrm{GeV}$ are vetoed.

Table 7.3

Names of the jet veto maps used

2016	UL16+HBM2+HBP1+QIE11
2017	UL17+HEP17+HBPW89
2018	UL18+HEM1516+HBP2M1

The vetoed regions can be clearly seen if the jet η and ϕ distributions are compared before and after applying the jet veto maps. Fig. 7.4 shows these distributions for the 2017 μ+jets data and the loss of jets in the HEP17 (at $\phi \approx -0.55$ and $1.305 < \eta < 2.964$) and HBPW89 (at $\phi > 2.7$ and $0 < \eta < 1.479$) can be seen.

Noise filters

Noise filters (sometimes denoted as $p_{\mathrm{T}}^{\mathrm{miss}}$ filters) are applied to remove spurious signals coming from effects such as electronic issues in the calorimeters, beam halo, or other non-physical signal. All recommended noise filters are applied, namely:

`Flag_goodVertices`, `Flag_globalSuperTightHalo2016Filter`, `Flag_HBHENoiseFilter`, `Flag_HBHENoiseIsoFilter`, `EcalDeadCellTriggerPrimitiveFilter`, `Flag_BadPFMuonFilter` and `Flag_eeBadScFilter`. 2017 and 2018 data have an additional `Flag_ecalBadCalibFilter` applied. `Flag_BadPFMuonFilter` filter for historic reasons is added using a separate module within CMSSW, because it was not available in earlier versions of MiniAODv2.

Jet distributions

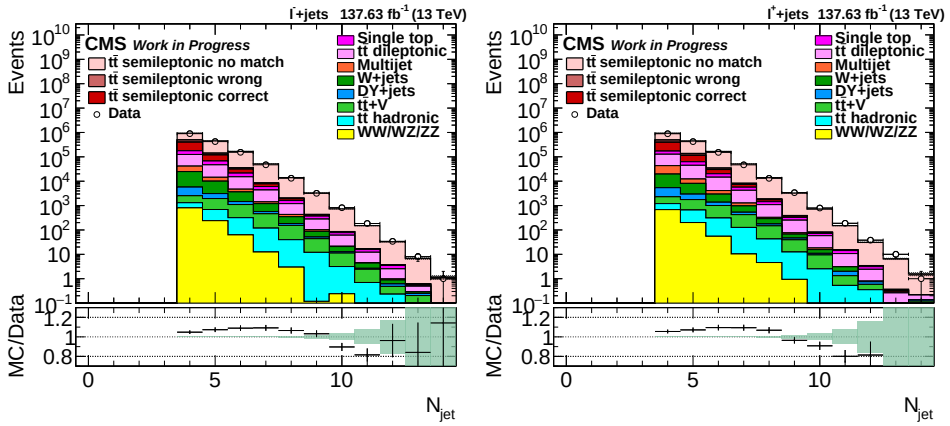

Fig. 7.5. The distribution of the number of jets per event, N_{jet}, in the l^-+jets (left) and l^++jets (right) channel. The whole Run 2 dataset is included.

Several distributions of jet kinematic variables are shown in this section. Fig. 7.5 depicts the distribution of the number of jets per event for the channel with positively and negatively charged lepton. A slight asymmetry in some of the background processes is seen, namely, l^++jets channel contains more multijet, while l^-+jets contains more single-top and W+jets events, even though l^-+jets appears to have longer tail of single-top events. In Fig. 7.6 the p_{T} distributions of the b-tagged and light-tagged (associated with the W boson candidate) jets are shown, showing a similar trend for both charges.

In both channels MC predicts more events with a low number of jets that are harder, as was also seen in the POWHEG+PYTHIA 8 $t\bar{t}$ simulation in Fig. 3.7. The reason for this is probably the same as the slope in the lepton p_{T} distribution (compare with Fig. 7.2), i.e. the lack of high-order calculations of the hard process. Unlike what is seen for lepton p_{T}, the ratio of the jet p_{T} distribution peaks at around $p_{\mathrm{T}} = 100\,\mathrm{GeV}$ and then decreases,

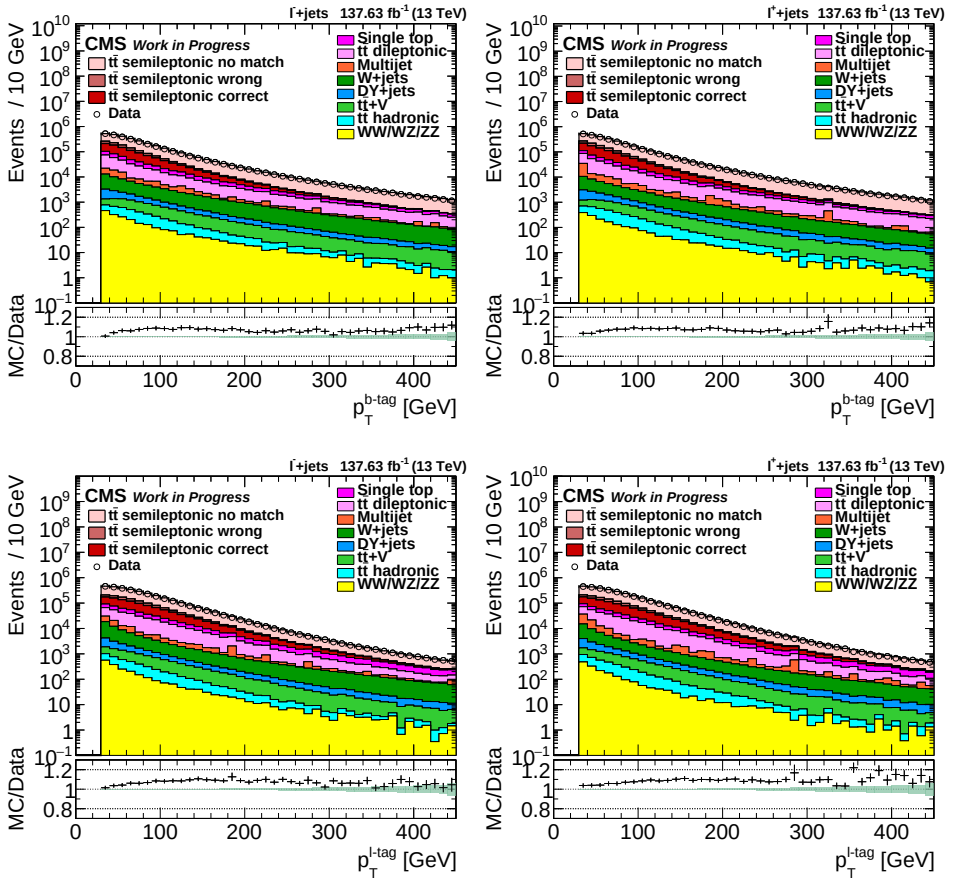

Fig. 7.6. Jet p_{T} distributions for bottom-tagged jets (top) and jets associated with the W boson candidate (bottom) for the l^-+jets events (left) and l^++jets events (right). The whole Run 2 dataset is included.

potentially indicating a non-optimal matching or initial-state radiation (ISR) and final-state radiation (FSR) scale.

The distributions of $p_{\mathrm{T}}^{\mathrm{miss}}$ for events with positive and negative charges are shown in Fig. 7.7. A similar shape of the data-to-MC disagreement as for the jet p_{T} is found, explained by the same effects. No large differences between the lepton charges is seen.

7.1.5. Event weights

Pileup weights

Due to rapidly changing data-taking conditions, such as luminosity, the number of circulating bunches, the number of protons per bunch, and other beam parameters, the exact PU distribution in the data is hard to match when generating the MC events. This

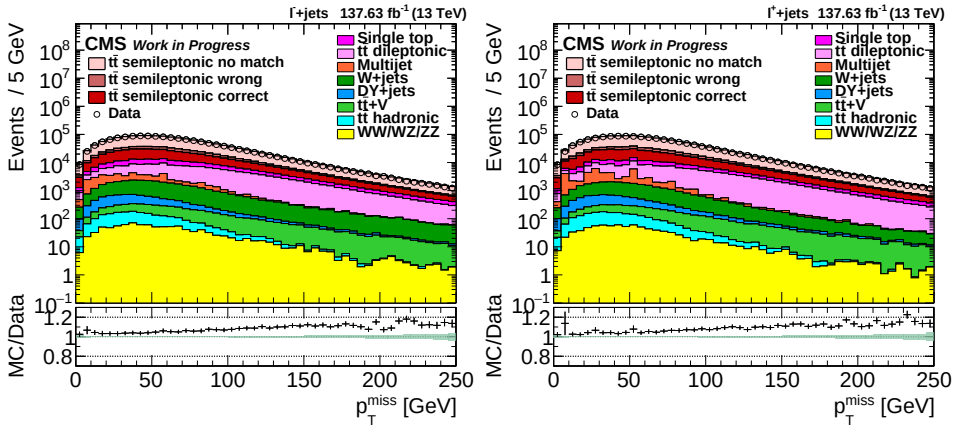

Fig. 7.7. The distribution of $p_{\mathrm{T}}^{\mathrm{miss}}$ in the l^-+jets (left) and l^++jets (right) channel. The whole Run 2 dataset is included.

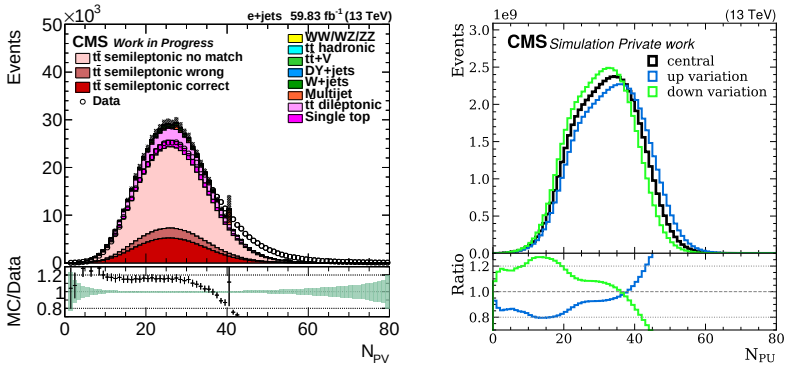

Fig. 7.8. The distribution of the number of primary vertices, N_{PV} in the e+jets channel and 2018 data and MC (left) and the PU distribution in data together with the up and down variations (right).

is mitigated with PU weights that match the number of interactions in the data and MC for each year. The weight depends on the cross section of the inelastic pp collisions (minimum bias, MB events). For this analysis, the LHC recommended value of 69.2 mb at $\sqrt{13}$ TeV was used with a variation of 4.6 % [322], [323].

The distribution of the number of primary vertices in the event, N_{PV}, after applying the PU weights for the 2018 data is shown in Fig. 7.8. Although only the e+jet channel is shown, the distribution is nearly identical to that in the μ+jet channel. In addition, the PU distribution in the data, estimated from the instantaneous luminosity and the MB cross section, is also shown. It is seen that although there are on average more N_{PV} than in the MC still after the application of the pile-up weights, this difference is

approximately within the PU variation. This behaviour is expected and seen in other CMS analyses [324].

7.1.6. b tagging weights

To match the event yields due to different b tagging efficiencies in data and MC, a per-event weight was obtained by formula:

$$w = \frac{P(\text{DATA})}{P(\text{MC})} = \frac{\prod_{i=\text{tagged}} \text{SF}_i \varepsilon_i \prod_{i=\text{not tagged}} (1 - \text{SF}_j \varepsilon_j)}{\prod_{i=\text{tagged}} \varepsilon_i \prod_{i=\text{not tagged}} (1 - \varepsilon_j)},$$

which can be simplified to

$$w = \left(\prod_{i=\text{tagged}} \text{SF}_i \right) \times \left(\prod_{j=\text{not tagged}} \frac{1 - \text{SF}_j \varepsilon_j}{1 - \varepsilon_j} \right), \tag{7.1}$$

where the SF and the b-tagging efficiency ε are functions of p_T and η. The first term in Eq. (7.1) considers both b-tagged jets, while the second term considers all light-tagged (not tagged) jets. Since the b jets are searched within the eight leading jets, the number of light-tagged jets can vary from 2 to 6. SFs are provided by the corresponding CMS physics object group, while ε are obtained for the central signal MC sample. In addition, when applying the flavour uncertainties, for each variation a separate ε corresponding to the given variation is used.

Trigger prefiring

Trigger prefiring is an effect caused by the requirement of L1 that after an accepted event it cannot accept the following two events. If some signal is incorrectly associated with the previous bunch crossing, the following event that is supposed to be accepted ends up not triggering L1. Two sources of L1 prefiring were relevant for Run 2. In the 2016 and 2017 runs, a gradual shift of ECAL timing was not correctly propagated to L1 trigger paths, which caused that the trigger sometimes assigned the effect to the previous bunch crossing. This effect is called L1 ECAL prefiring. For all Run 2, another source of muon prefiring is relevant. It was caused by the muon detector timing resolution not being fine enough to always correctly associate the given muon with the correct bunch crossing [325]. MC simulations do not include prefiring. Instead, the prefiring effect is corrected for by a common weight for both the L1 ECAL prefiring and muon prefiring. The weight is obtained by calculating the probability that the MC event did not prefire [326]. The associated up and down uncertainties on the probability as added as systematic variations.

The impact of L1 prefiring is smaller in 2018 because there was only relevant prefiring due to muons. The ECAL prefiring mostly impacts events with objects in $2.5 < |\eta| < 3.0$ above 100 GeV and therefore has a small impact on this analysis.

7.2. Event reconstruction

The purpose of event reconstruction is to match the reconstructed objects to the $t\bar{t}$ event hypothesis, correct the event kinematic variables, and select events with a higher signal-to-background ratio.

First, reconstructed objects, that is, the lepton, $p_{\mathrm{T}}^{\mathrm{miss}}$, 2-$b$-tagged and two light jets are matched to the parton-level objects in the $t\bar{t}$ event shown in Fig. 2.6. The two leading light jets are assigned to the two light quarks that decay from the W boson, making the W boson candidate. The two b-tagged jets are assigned as the b quark candidates. There are two possible permutations of this assignment.

Based on MC truth information, the jet assignment (permutation) is classified as "correct", when the jet-to-parton level quark matching is correct, "wrong" where the b jet assignment is wrong, but the light jet assignment is correct, and "no match" otherwise. Due to the small mistag rate of the DeepJet algorithm, the "wrong" category arises mostly from the cases where the four jets are selected correctly but the two selected b jets are assigned to the wrong b parton. The "no match" categorises permutations where the four jets do not match the partons arising from the $t\bar{t}$ event, which happens in cases where, for example, an ISR jet is hard enough to appear among the leading light jets. Following [320], the $t\bar{t}$ dilepton, all hadronic channels and $t\bar{t}$ $+V$, where V corresponds for vector bosons (W, Z) are separated out from "no match". It should be noted that "wrong" and "no match" permutations are also sensitive to the generated m_t and thus are useful for the fit, though not in a straightforward way as the correct permutations.

Finally, $p_{\mathrm{T}}^{\mathrm{miss}}$ is assigned to the neutrino. The $|p_z|$ of the neutrino can be found by solving for $(p_\nu + p_l)^2 = (m_{\mathrm{W}}^{\mathrm{pdg}})^2$. This quadratic constraint can lead to two solutions, and an assumption of choosing one of the solutions has to be taken. Reasonable options include taking both solutions, taking the solution with the smallest $|p_z|$, the neutrino solution that is closer to the lepton $|p_z|$, the solution that maximises the cosine of the angle between the lepton and the W, or not solving and keeping $|p_z| = 0$.

7.2.1. Application of flavour-dependent JEC

Typically, in m_t measurements the usage of JEC obtained from the QCD jet mix corrects the light-jet response well enough to enable a good data-to-MC comparison, and no flavour corrections are necessary. However, the reconstruction algorithm described in Section 7.2.3 requires a selection based on the distribution of the reconstructed hadronic W mass m_W^{reco}. The peak of this distribution is shifted due to the light-quark flavour response with respect to the inclusive-quark flavour response. This discrepancy can be removed by applying flavour corrections, derived in Section 6.3.1. The flavour corrections are applied to both the data and the MC datasets. The light-tagged jets are scaled with the light-jet corrections, and the b-tagged jets with the b jet correction.

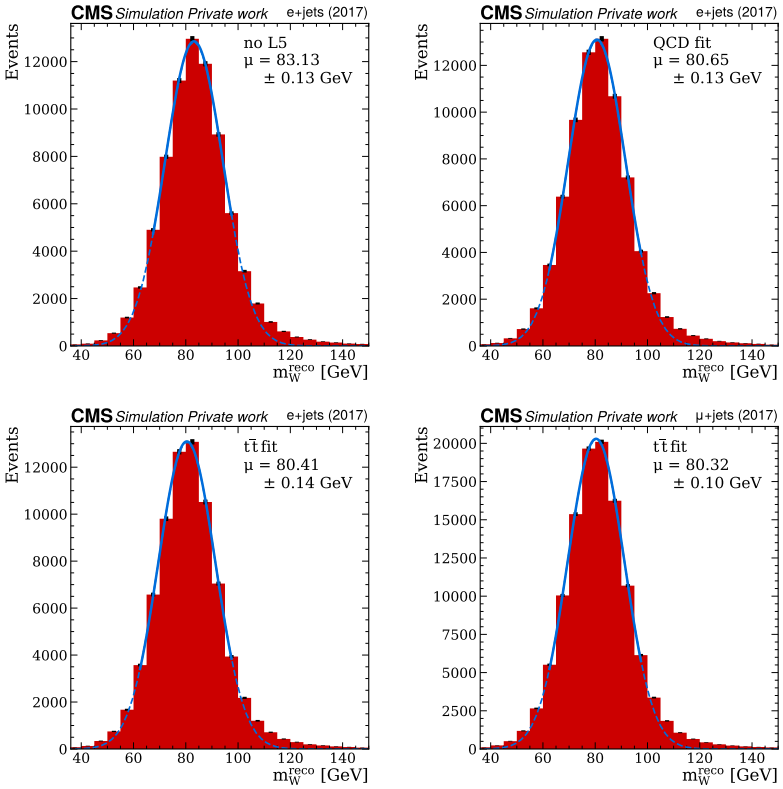

Fig. 7.9. Distribution of the hadronically decaying reconstructed W boson mass, m_W^{reco} for the "correct" jet match of the $t\bar{t}$ lepton+jets events. Top left: the result without the flavour corrections in the e+jets channel, top right: after applying the flavour corrections from the QCD dataset on the e+jets channel, bottom left: after applying the flavour corrections from the $t\bar{t}$ dataset on the e+jets channel, bottom right: after applying the flavour corrections from the $t\bar{t}$ dataset on the μ+jets channel. The blue line shows the result of the Gaussian fit in the range where the fit was conducted and the dashed line shows the whole range of the fit result.

Fig. 7.9 shows the m_W^{reco} distribution from correctly assigned $t\bar{t}$ lepton+jets permutations before and after applying the flavour corrections. The corrections derived from the QCD and $t\bar{t}$ datasets are compared, but for the analysis, only the corrections derived from the $t\bar{t}$ dataset were used. The fit of the peak of the m_W^{reco} is performed 3 times and the results of the final one are shown. The first time the fit is run over the whole range and then twice over the range of 1.5 standard deviations around the previous mean.

The effect of the corrections brings the peak of $m_{\text{W}}^{\text{reco}}$ from $83.13 \pm 0.13\,\text{GeV}$ to $80.41 \pm 0.14\,\text{GeV}$ for the e+ jet events, thus bringing it into agreement with $m_{\text{W}}^{\text{pdg}} = 80.4\,\text{GeV}$. Similarly for events in the μ+ jet channel, the peak position after applying the corrections is $80.31 \pm 0.10\,\text{GeV}$, which is in agreement with $m_{\text{W}}^{\text{pdg}}$. The effect is explained by the light

jets having a response $R > 1$ for the entire range of p_{T} and the jet $|\eta|$ and, so, the flavour correction lowers the p_{T} of the light jets forming the W boson candidate. The flavour corrections derived from the QCD dataset show a slightly worse improvement explained by the differences of the event topologies, as discussed in Section 6.3.4.This shows that although significantly improving p_{T} spectra of the jets of different flavour, one set of flavour corrections may not be ideal for all analyses.

7.2.2. Arguments against the usage of the kinematic fit

Typically, for $t\bar{t}$ event reconstruction in lepton+jets and all-jets channels, a kinematic fit is employed, which is a χ^2 fit of the kinematic properties of the four jets, lepton and neutrino momenta with several constraints [92], [217]. The constraints are added as Lagrange multipliers in the fit and typically include

1. $(p_{q_1} + p_{q_2})^2 \equiv \left(m_{\mathrm{W}}^{\mathrm{reco}}\right)^2 = \left(m_{\mathrm{W}}^{\mathrm{pdg}}\right)^2 = (80.4\,\mathrm{GeV})^2$, i.e. that the invariant mass of the two light jets should match W boson mass, $m_{\mathrm{W}}^{\mathrm{pdg}}$.

2. $(p_\nu + p_l)^2 = \left(m_{\mathrm{W}}^{\mathrm{pdg}}\right)^2 = \left(m_{\mathrm{W,lep}}^{\mathrm{reco}}\right)^2 = (80.4\,\mathrm{GeV})^2$, i.e. neutrino and the lepton system invariant mass should match $m_{\mathrm{W}}^{\mathrm{pdg}}$.

3. $m_t^{\mathrm{reco}} = m_{t,\mathrm{lep}}^{\mathrm{reco}}$, i.e. the hadronically decaying top-quark mass should match the leptonically decaying top-quark mass.

4. Two constraints from the p_{T} balance in the event (p_x and p_y separately).

Note that observables from the hadronically decaying top-quark candidate are denoted without any subscript as only this side is used in the fit, while the observables from the leptonically decaying top quark candidate are denoted with a subscript "lep". Since the constraints are non-linear, they are linearised, and the fit solution is found iteratively, which for analysis targeting the $t\bar{t}$ lepton+jets channel is typically performed using the `HitFit` module [327] as used in previous measurements of m_t at CMS [92], [328]. Usually, jet permutations that provide high enough goodness-of-fit value $P_{\mathrm{gof}} = \exp(-1/2\chi^2) > 0.2$ are stored, although in case of a limited number of events both b jet permutations can be stored. In this way, the kinematic fit is able to select the best matching jet permutation but also to correct the particle momenta for the detector effects.

The total number of constraints is 26, where six constraints come from the invariant masses of the 6 particles, $3 \times 5 = 15$ in the kinematic properties of the particles and 5 in the constraints 1.-4. above. The total number of variables is 24 for the four-momenta of six particles. This leaves two degrees of freedom. In other words, three unknown neutrino momenta are compensated for by the 2 directions of transverse momentum conservation and the three additional constraints. Since the fitting problem should be overconstrained, there should be at least one degree of freedom in the fit. Thus, this allows the $m_t^{\mathrm{reco}} = m_{t,\mathrm{lep}}^{\mathrm{reco}}$ constraint (equal-mass constraint) to be removed. However, in attempts using `HitFit`

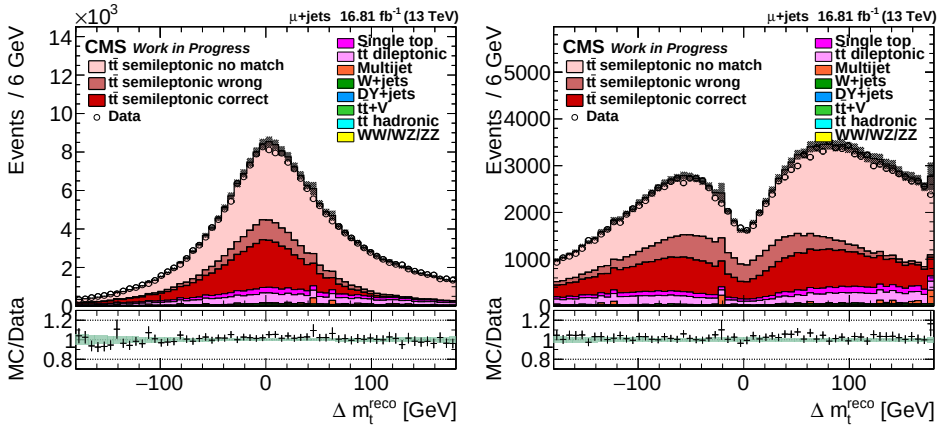

Fig. 7.10. The distribution of $\Delta m_t^{\text{reco}} = m_t^{\text{reco}} - m_{t,\text{lep}}^{\text{reco}}$ for the permutation with the smallest $|\Delta m_t^{\text{reco}}|$ (left) and for the permutation with the largest $|\Delta m_t^{\text{reco}}|$ (right). Distributions are shown for the $\mu + \text{jets}$ channel for the 2016 non-APV data.

without the equal mass constraint, around 35 % of the jet combinations in $t\bar{t}$ events suffered non-convergence.

The equal-mass constraint creates a bias in the top-quark masses in two ways. Firstly, it corrects the b jet momenta and secondly, by selecting events that have the smallest P_{gof}, it selects events that have the smallest $\Delta m_t^{\text{reco}} = m_t^{\text{reco}} - m_{t,\text{lep}}^{\text{reco}}$. Fig. 7.10 shows the distributions of Δm_t^{reco} for the b jet permutation with the smallest and largest Δm_t^{reco}. The distribution for the first permutations is Gaussian with a width of $\mathcal{O}(10\,\text{GeV})$, while the second permutations have long tails extending beyond 50 GeV and contain a larger fraction of wrong jet permutations.

In addition, Fig. 7.11 shows distributions of the leptonic top quark mass, $m_{t,\text{lep}}^{\text{reco}}$, and hadronic top quark mass, m_t^{reco}. It is seen that the width of m_t^{reco} is around 50 GeV, while for the $m_{t,\text{lep}}^{\text{reco}}$, it is larger, around 100 GeV. The effect of the P_{gof} requirement is selecting events that have $\Delta m_t^{\text{reco}} \sim \mathcal{O}(10\,\text{GeV})$ which is orders of magnitude larger than the maximum expected, $\Delta m_t \sim \mathcal{O}(0.1\,\text{GeV})$, to be observed in the data. In other words, the width is so large that it washes out all the differences between the generator top-quark and antiquark masses. On the other hand, the shift of the b jet momenta could create a significant bias.

One option to mitigate this issue is to calibrate the possible Δm_t shift using MC events. Since $m_{t,\text{lep}}^{\text{reco}}$ is not used for statistical inference, another option is to use a $m_{t,\text{lep}}^{\text{reco}} = m_t^{\text{pdg}}$ constraint. Despite these options, in this Thesis, a straightforward approach was chosen, where the kinematic fit was discarded altogether and instead a simpler analyser that is described in Section 7.2.3.

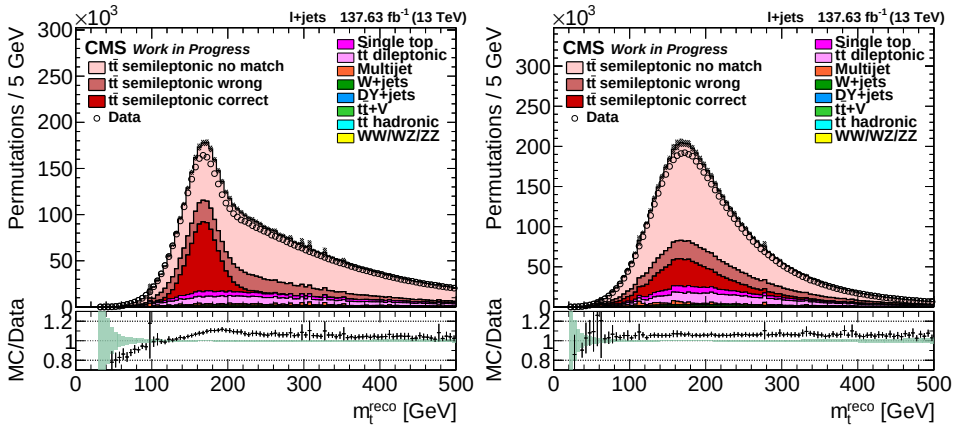

Fig. 7.11. The distribution of the hadronic (left) and leptonic (right) reconstructed top-quark mass for both of the b jet permutations. Distributions are shown for the whole Run 2 dataset.

7.2.3. The simplified analyser, WMassDeltaTopMass

Instead of a kinematic fit, a cut-based reconstruction algorithm, called `WMassDeltaTopMass` (WM-DTM), was used. The aim of the algorithm is to obtain the best possible purity of the correct permutations and the best top mass peak resolution without introducing a bias in Δm_t.

The analysis procedure is as follows. For each event, the two leading light jets are assigned to the W boson candidate. To correct for the detector effects for the light jets, the light-jet four-momenta are scaled, so that their invariant mass is equal to $m_{\mathrm{W}}^{\mathrm{pdg}}$:

$$\begin{aligned} p_{q_1} &\to p_{q_1} \cdot \frac{\sqrt{(p_{q_1}+p_{q_2})^2}}{m_{\mathrm{W}}^{\mathrm{pdg}}} \\ p_{q_2} &\to p_{q_2} \cdot \frac{\sqrt{(p_{q_1}+p_{q_2})^2}}{m_{\mathrm{W}}^{\mathrm{pdg}}} \end{aligned} \tag{7.2}$$

For the neutrino, the solution that minimises the neutrino $|p_z|$ is chosen, that is, the most central one. In the following, observables with superscript "fit" denote observables obtained after the scaling in Eq. (7.2) and choosing the neutrino solution, while "reco" denotes observables before these corrections.

Afterwards, the two permutations of the b jet assignment to the two top-quark candidates are tested, and the one bringing the smallest $|\Delta m_t^{\mathrm{reco}}| = |m_t^{\mathrm{reco}} - m_{t,\mathrm{lep}}^{\mathrm{reco}}|$ is stored.

To increase the ratio of correct permutation to total MC, a condition on m_W^{reco} was added such that $60\,\mathrm{GeV} < m_{\mathrm{W}}^{\mathrm{reco}} < 100\,\mathrm{GeV}$ ($m_{\mathrm{W}}^{\mathrm{reco}}$ requirement) mimics the constraint of $m_{\mathrm{W}}^{\mathrm{reco}}$ in the kinematic fit. Note that with the light jet scaling in Eq. (7.2) the $m_{\mathrm{W}}^{\mathrm{fit}}$ distribution is just a delta function, while $m_{\mathrm{W}}^{\mathrm{reco}}$ remains intact and can be used for the

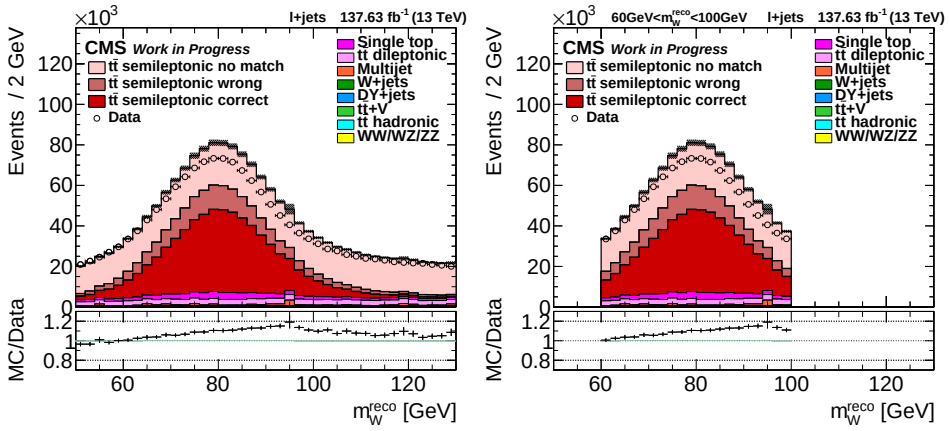

Fig. 7.12. The distribution of the reconstructed hadronic W mass, m_W^{reco}, before applying the $m_{\mathrm{W}}^{\mathrm{reco}}$ requirement (left) and after (right). The leading b-jet permutations in each event are shown.

$m_{\mathrm{W}}^{\mathrm{reco}}$ requirement. The distribution of $m_{\mathrm{W}}^{\mathrm{reco}}$ before and after the $m_{\mathrm{W}}^{\mathrm{reco}}$ requirement is shown in Fig. 7.12. It is possible to see how the $m_{\mathrm{W}}^{\mathrm{reco}}$ requirement removes the tails of the distribution consisting mostly of wrong b jet permutations and backgrounds. Note that the peak of the distribution centres well around 80 GeV due to the usage of the flavour corrections (compare with, e.g. [92], [320]). When compared to the $m_{\mathrm{W}}^{\mathrm{reco}}$ distribution after the P_{gof} cut in the kinematic fit (e.g. [92], [320]), the distributions look similar, except that the sharp cut in Fig. 7.12 is replaced with a continuous transition, where the bin counts fall steeply to 0 within 30 GeV around the peak.

7.2.4. The performance of the WMassDeltaTopMass

In Table 7.4 the number of events obtained for each of the MC samples and data is compared with and without the $m_{\mathrm{W}}^{\mathrm{reco}}$ requirement. Charge asymmetry in the background MC samples can be seen, in particular in the single-top and W+jets samples, which contain more events in l^-+jets events (i.e. in events adding to the hadronic top quark distribution) than in l^++jets events (i.e. in events adding to the hadronic top antiquark distribution). The opposite trend is seen for multijet events. After the $m_{\mathrm{W}}^{\mathrm{reco}}$ requirement, the asymmetry becomes smaller for samples such as single-top and W +jets, while it increases for the multijet sample. The asymmetry is slightly larger in the data than in the simulation.

The $m_{\mathrm{W}}^{\mathrm{reco}}$ requirement is seen to improve the correct permutation purity to above 40 %, which is almost as good as the kinematic fit with the P_{gof} cut, where it was found to be 47 % [92]. As mentioned previously, the MC count exceeds the data count by approximately 6 %, which can be covered by the MC uncertainties, as seen in previous

analyses [92]. The MC-to-data disagreement increases to around 9 % after the $m_{\mathrm{W}}^{\mathrm{reco}}$ requirement.

Table 7.4

Event yields for all the channels and all years with and without the $m_{\mathrm{W}}^{\mathrm{reco}}$ requirement

	No $m_{\mathrm{W}}^{\mathrm{reco}}$ requirement				With the $m_{\mathrm{W}}^{\mathrm{reco}}$ requirement			
	l^-+jets Run 2		l^++jets Run 2		l^-+jets Run 2		l^++jets Run 2	
Dataset	Events [k]	Ratio to signal, %	Events [k]	Ratio to signal, %	Events [k]	Ratio to signal, %	Events [k]	Ratio to signal, %
$t\bar{t}$ l+jets total	1239.7	84.0	1240.6	84.5	530.6	89.4	531.6	89.5
l+jets correct	289.1	19.6	289.5	19.7	255.9	43.1	256.3	43.1
l+jets wrong	115.7	7.8	115.8	7.9	83.0	14.0	83.0	14.0
l+jets no match	834.8	56.6	835.3	56.9	191.7	32.3	192.3	32.4
$t\bar{t}$ dilepton	113.3	7.7	113.4	7.7	26.3	4.4	26.4	4.4
$t\bar{t}$ all hadronic	1.2	0.1	1.3	0.1	0.4	0.1	0.4	0.1
$t\bar{t}$+V	3.1	0.2	2.7	0.2	0.9	0.2	0.8	0.1
single-top	70.3	4.8	61.0	4.2	25.4	4.3	23.3	3.9
DY+jets	4.2	0.3	4.1	0.3	1.0	0.2	1.0	0.2
W+jets	23.4	1.6	17.8	1.2	4.7	0.8	3.7	0.6
VV	1.0	0.1	0.8	0.1	0.3	0.0	0.3	0.0
Multijet	18.8	1.3	26.3	1.8	4.0	0.7	6.8	1.1
Simulation total	1474.9	100.0	1468.0	100.0	593.5	100.0	594.2	100.0
Data	1390.6	94.3	1378.7	93.9	542.8	91.5	540.3	90.9

The distribution of m_t^{reco} with and without the $m_{\mathrm{W}}^{\mathrm{reco}}$ requirement is compared in Fig. 7.13 for the distributions taking only the permutation minimising $|\Delta m_t^{\mathrm{reco}}|$ and taking both permutations. Although the distribution for the correct permutation has a clear peak and is Gaussian distributed, the rest of the MC samples have long tails toward large m_t^{reco}. Applying the $m_{\mathrm{W}}^{\mathrm{reco}}$ requirement removes most of the backgrounds, except for some around the peak. When taking both permutations, the amount of correct permutations increases only slightly compared to the increase in background. When both permutations are kept, the number of wrong and correct permutations is almost the same, the additional wrong permutations being caused by some jets being mistakenly tagged as coming from a b quark. In addition, the contribution from all the other datasets doubles. Thus, using both permutations decreases the data purity while only slightly increasing the amount of good data. Moreover, the $m_{\mathrm{W}}^{\mathrm{reco}}$ requirement is not able to distinguish the correct b jet permutations and thus does not decrease the number of wrong permutations which remains large even after the cut.

The distribution of m_t^{fit} before and after the $m_{\mathrm{W}}^{\mathrm{reco}}$ requirement is compared in Fig. 7.14. The condition in Eq. (7.2) can be seen to significantly reduce the width of the top-quark mass distribution. For all the data samples, except for the correct and wrong $t\bar{t}$ semileptonic permutations, the light-jet scaling is not physical. Thus, instead of the long tail for the backgrounds seen for m_t^{reco}, they create a peak at lower m_t^{fit} values. However, as long as the same correction is applied for the MC and data, they can be used to obtain the generator top-quark mass without a bias.

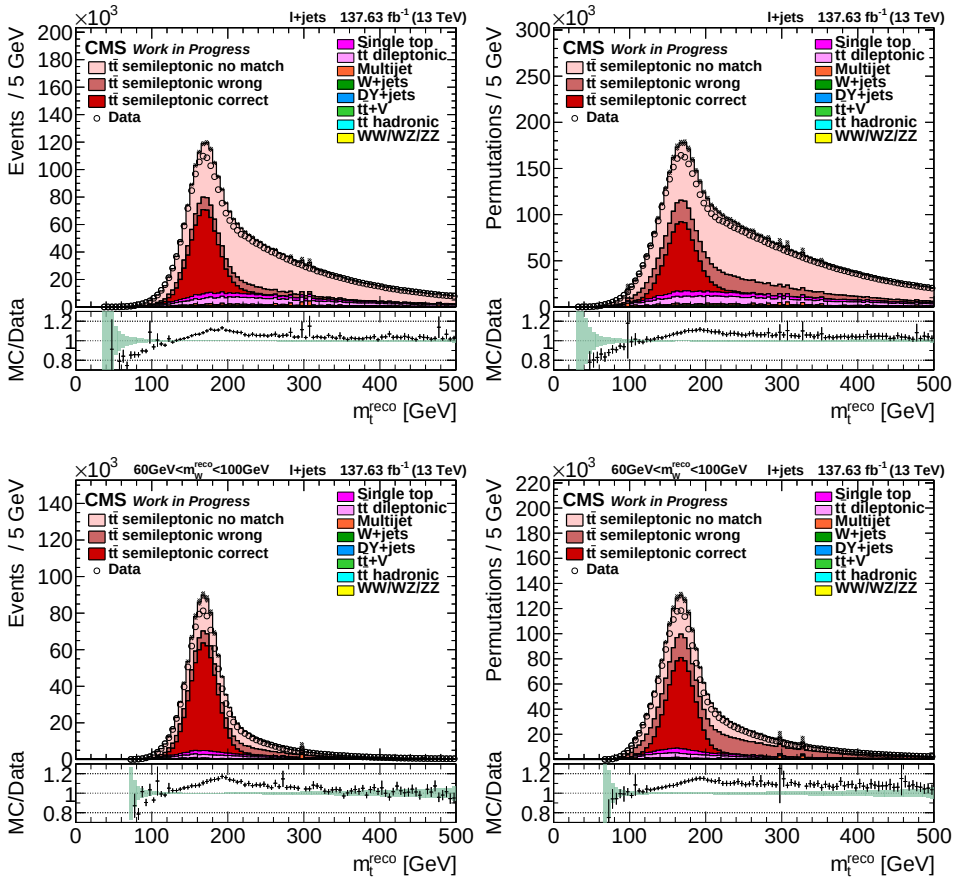

Fig. 7.13. The distribution of the reconstructed top-quark mass, m_t^{reco}, for the first permutation in the event (left) and for both permutations in the event (right). The top row shows events without the $m_{\text{W}}^{\text{reco}}$ requirement, while the bottom row shows events after its application. Distributions are shown for the whole Run 2 dataset. The top right image here is repeated from Fig. 7.10 here for comparison.

The competitive event yields and a good resolution of m_t^{fit} illustrate that WM-DTM serves as a more lightweight cut-based alternative to the kinematic fit while maintaining analogous characteristics. The selection of the $t\bar{t}$ events with WM-DTM leads to a smaller bias for the Δm_t measurement than with the kinematic fit, as there is no explicit shift of the b jet momenta matching the top-quark masses. Selecting only the first permutation does not have a significant impact following a motivation similar to that for the P_{gof} cut for the kinematic fit. The usage of the second permutation would increase the number of events and thus might improve the sensitivity but also worsen the fraction of correctly matched events with respect to all the events. In future revisions of this analysis, the impact of adding the second permutation could be tested.

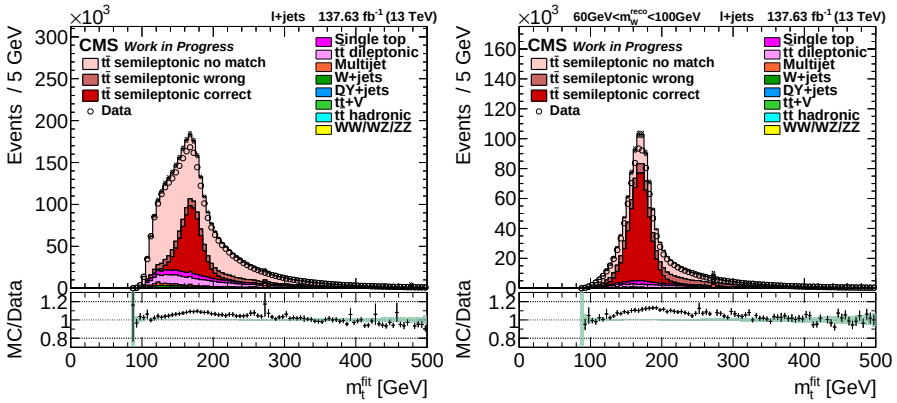

Fig. 7.14. The hadronic fit top-quark mass using the WMassDeltaTopMass algorithm before (left) and after (right) the $m_{\mathrm{W}}^{\mathrm{reco}}$ requirement.

7.3. Profile likelihood fit

The binned profile likelihood fit approach is used to perform the statistical inference. It is performed using the CMS COMBINE tool [329], which has the benefit of ensuring that the results can later be combined with other measurements by correctly calculating the correlations between the systematic uncertainties. In Run 1, early Run 2 m_t and Δm_t measurements, an Ideogram method was used [30], [330], [331]. The method assigns a likelihood per event for the given m_t and the JES factor, which is calibrated using MC events. The method performs well in measurements with large statistical uncertainties, but is computationally expensive because estimating the systematic uncertainties requires the generation of pseudo-experiments for each variation. In addition, it does not include backgrounds in the probability density and requires a calibration of the method. Finally, the correlation between the JES and the modelling uncertainties is not clear.

To mitigate these issues, for the latest Run 2 m_t measurement, a profile likelihood method was used with systematic variations incorporated as nuisance parameters [92]. In this measurement, in addition to the m_t^{fit} distribution, four other uncorrelated observables (projections) were also used as input distributions for the fit. In particular, $m_{\mathrm{W}}^{\mathrm{reco}}$ was used to constrain the light-jet JES, and $m_{lb}^{\mathrm{reco}}/m_t^{\mathrm{fit}}$ and $R_{bq}^{\mathrm{reco}} = (p_T^{b_1} + p_T^{b_2})/(p_T^{q1} + p_T^{q2})$ were used to constrain the b JES. Finally, m_{lb}^{reco} for events that did not pass the cut P_{gof} were also added to gain additional sensitivity to m_t. However, the correlation between these five observables is not guaranteed to be negligible and has to be verified for the correct application of the method. Although the rest of the distributions were grouped in eight bins, the m_t^{fit} distribution in the fit was described by a continuous Voigt distribution. This was meant to ensure that the sensitivity to the narrow peak in the m_t^{fit} distribution is not lost. On the other hand, it has been shown that binning all distributions, including m_t^{fit} in 10 bins, is able to yield at least equally good sensitivity to m_t [320].

For the measurement presented in this Thesis, a method similar to the one performed in [320] was chosen. The sensitivity to Δm_t was ensured by splitting the events according to the lepton charge and constructing the (m_t^{fit}, q) distribution, i.e. m_t^{fit} distribution for events with positive and negative lepton charge, $q = \pm 1$. The events with $q = -1$ are sensitive to top quark mass, m_t^{fit} and the events with $q = +1$ to the top antiquark mass, $m_{\bar{t}}^{\text{fit}}$. The rest of the distributions used in the CMS m_t fit are not used, as the measurement of Δm_t is not affected by a global JES and the residual response differences will be taken into account by specific jet flavour vs antiflavour uncertainties. The sensitivity to the light and b quark JES is already improved by applying the flavour corrections, and in this simpler method, there is no need to verify that all the distributions are independent. The 2 given distributions are independent because the 2 charge categories are mutually exclusive.

Two parameters of interest are defined, m_t and Δm_t. Two independent distributions ensure that m_t and Δm_t can be measured simultaneously. The COMBINE fit obtains the best fit values by comparing the data with MC templates with different m_t and Δm_t. Three MC samples are used with m_t values of 171.5 GeV, 172.5 GeV, and 173.5 GeV (all $\Delta m_t = 0$) to optimise m_t and samples with Δm_t values of -400 MeV, 0, and $+400$ MeV (all with $m_t = 172.5$ GeV) to optimise Δm_t. The m_t variations are obtained from separate MC datasets, while the Δm_t variations are obtained from event reweighing as shown in Section 7.4.1.

7.4. Mathematical formulation

The process of statistical inference is as follows. For each systematic variation, a nuisance parameter θ is introduced. Variations that produce alternative shapes for the distributions used for the fit are described using shape nuisance parameters, θ_i, while variations that vary only the total normalisation, instead of the shape, are described using log-normal nuisance parameters, η_i. The default values $\theta_i = 0$ and $\pm 1\sigma_i$ correspond to the up and down shapes. The probability for θ_i to take a value of $\hat{\theta}_i$ is taken to be $\mathcal{N}(\hat{\theta}_i|\theta_i, \sigma_i = 1)$, where $\mathcal{N}$ is a Gaussian probability distribution with mean θ_i and standard deviation σ_i. In this way, the shape nuisance parameters express the fact that the predicted MC distributions can vary to explain the data, but excessive variation is limited by a Gaussian penalty term.

For the normalisation uncertainty, the default values $\eta_i = 0$ and ± 1 correspond to the increase/decrease of the yield in the sample by κ_i. It is taken to follow the $\mathcal{N}(\hat{\eta}_i|\eta_i, \sigma_i = 1)$ distribution. The vector of all the shape nuisance parameters is further denoted as $\vec{\theta}$ and log-normal parameters as $\vec{\eta}$.

The statistical inference is based on the following binned likelihood

$$\mathcal{L}(\vec{n}|\vec{\theta},\vec{\eta},m_t,\Delta m_t) = \prod_{b\in\text{bins}}\left(P\Big(n_b|\prod_{s\in\text{samples}}(1+\kappa)_s^{\eta}\cdot w_{s,b}(\hat{\vec{\theta}},m_t,\Delta m_t)\Big)\right) \times \prod_{n\in\text{nuisances}}\mathcal{N}(\hat{\theta}_n|\theta_n)\times\prod_{s\in\text{samples}}\mathcal{N}\left(\hat{\eta}_s|\eta_s\right), \tag{7.3}$$

where the first product runs over all the bins, n_b is the observed number of events in the bin b, $w_{s,b}(\hat{\vec{\theta}},m_t,\Delta m_t)$ is the predicted number of events in bin b for the sample s with given m_t, Δm_t and $\hat{\vec{\theta}}$. The function P is the Poisson probability function. Thus, Eq. (7.3) describes the likelihood to observe the number of events n_b in each bin, $\vec{n}$ given the values of θ, η, m_t and Δm_t. The impact of different shape nuisance parameters and parameters of interest on $w_{s,b}$ is further discussed in Section 7.6.

In addition, to estimate the effect of limited bin statistics in the central MC, a simplified Barlow-Beaston approach (Barlow-Beaston lite) is used [329], [332], [333]. We denote $e_{s,b}$ to be the error of $w_{s,b}$ and the total predicted yield in the bin b to be $w_b = \sum_s w_{s,b}$. Further, we denote $e_b^2 = \sum_s (e_{s,b}^2)$ to be the error-squared of w_b. The Barlow-Beaston lite approach can be summarised as follows. For bins with a sufficient effective number of events $w_b^2/e_b^2 > n_{\text{tresh}}$, one Gaussian parameter per bin is introduced, where n_{tresh} is a predefined threshold for the effective number of events. For bins with $w_b^2/e_b^2 > n_{\text{tresh}}$, an additional nuisance parameter per sample is introduced, which can be either normally distributed if for the sample $w_{b,s}^2/e_{b,s}^2 > n_{\text{tresh}}$ is fulfilled or Poisson distributed if not.

The likelihood in Eq. (7.3) is profiled, meaning that for each value of the parameter of interest, m_t and Δm_t, the θ and η values that are the best estimates of the likelihood (denoted with double hat, $\hat{}$) are used, i.e.

$$\mathcal{L}(\vec{n}|m_t,\Delta m_t) = \max_{\vec{\theta},\vec{\eta}}\mathcal{L}(\vec{n}|\vec{\theta},\vec{\eta},m_t,\Delta m_t) \equiv \mathcal{L}(\vec{n}|\hat{\hat{\vec{\theta}}}(m_t,\Delta m_t),\hat{\hat{\vec{\eta}}}(m_t,\Delta m_t),m_t,\Delta m_t). \tag{7.4}$$

A likelihood scan is used to minimise the negative logarithm of the profile likelihood Eq. (7.4).

7.4.1. Reweighed datasets with non-zero top quark mass difference

As no MC samples were available with $|\Delta m_t| > 0$, the mass difference between top quarks and antiquarks was incorporated by adding weights to the simulated events shifting the position of the peak for the top quark and antiquark mass. In this way, events that have mass at the peak can be given a smaller weight than events at a new peak. The event reweighing was done using ratios of Breit-Wigner distributions $B(m_t^{\text{gen}},m_t,\Gamma)$ and

is given as

$$w(m_t^{\text{gen}}, m_{\bar{t}}^{\text{gen}}, m_{t,\text{new}}, m_{\bar{t},\text{new}}, m_{t,\text{old}}, \Gamma) = \left(\frac{B(m_t^{\text{gen}}, m_{t,\text{new}}, \Gamma)}{B(m_t^{\text{gen}}, m_{t,\text{old}}, \Gamma)}\right) \cdot \left(\frac{B(m_{\bar{t}}^{\text{gen}}, M_{\bar{t},\text{new}}, \Gamma)}{B(m_{\bar{t}}^{\text{gen}}, M_{t,\text{old}}, \Gamma)}\right), \tag{7.5}$$

where $m_{t,\text{old}} = 172.5\,\text{GeV}$ and $\Gamma = 1.31\,\text{GeV}$ are top mass and top width parameters used for the event generation, which are the same for top quark and top antiquark, $m_{t,\text{new}}$ and $m_{\bar{t},\text{new}}$ are the values of the top quark and top antiquark mass parameters to which the reweighing should be performed, while m_t^{gen} and $m_{\bar{t}}^{\text{gen}}$ are the generated top-quark and antiquark masses in the event. In other words, the values of m_t^{gen} and $m_{\bar{t}}^{\text{gen}}$ are unique for each top quark and are distributed with a peak at the corresponding m_t and width Γ. The first term on the right-hand side in Eq. (7.5) reweighs the top quark, and the second term reweighs the top antiquark. The Breit-Wigner distribution is given as

$$B(m_t^{\text{gen}}, m_t, \Gamma) = \frac{k}{((m_t^{\text{gen}})^2 - m_t^2)^2 + m_t^2\Gamma^2}, \tag{7.6}$$

where

$$k = \frac{2\sqrt{2}m_t\Gamma\gamma}{\pi\sqrt{m_t^2 + \gamma}} \approx \frac{m_t\Gamma\gamma}{\sqrt{m_t^2 + \gamma}} \tag{7.7}$$

and

$$\gamma = \sqrt{m_t^2(m_t^2 + \Gamma^2)}. \tag{7.8}$$

The constant term, $\frac{2\sqrt{2}}{\pi}$, in front of k in Eq. (7.7) cancels when taking the ratio.

Reweighing is validated by comparing the m_t^{gen} and $m_{\bar{t}}^{\text{gen}}$ distributions, for samples where the initial $m_t = 172.5$ is reweighed to $m_t = 172.5 \pm 1\,\text{GeV}$ with the sample generated specifically with the same m_t values. The results are shown in Fig. 7.15 for the m_t^{gen} distribution. No visible difference is seen between the two samples. A similar agreement was obtained when comparing the $m_{\bar{t}}$ distributions.

For the profile likelihood fit, we use reweighing to $\Delta m_t = \pm 400\,\text{MeV}$, thus each m_t and $m_{\bar{t}}$ is reweighed by $\pm 200\,\text{MeV}$. This covers the 68 % confidence interval of the Run 1 measurement, which was $|\Delta m_t| + |\Delta(\Delta m_t)| = 360\,\text{MeV}$ [30]. Although reweighing can increase the statistical uncertainties in the dataset, if reweighing is performed within Γ of the distribution, the loss of the statistical accuracy is negligible. This trend has also been shown by the results shown in Fig. 7.15.

7.5. Systematic uncertainties

The systematic uncertainties are divided into 3 categories: experimental uncertainties and signal normalisation (I), modelling uncertainties applied as event weights (II), and modelling uncertainties applied as additional uncorrelated samples (III). For the modelling uncertainties, the usage of weights is preferable to applying them as additional

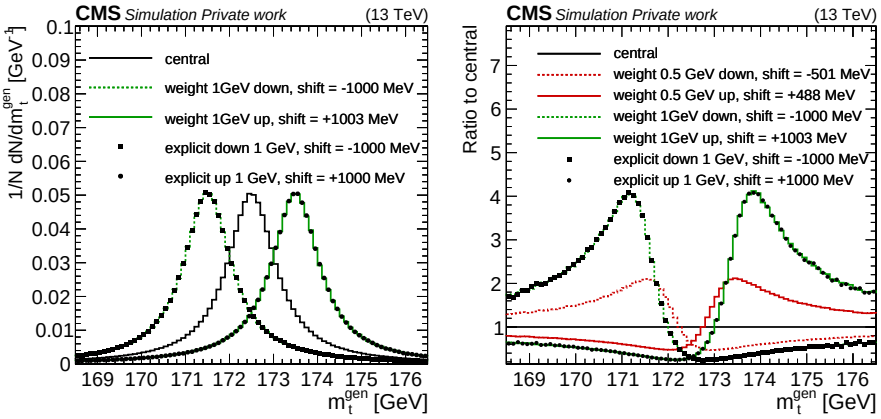

Fig. 7.15. Left: The comparison of the reweighed m_t^{gen} distribution, where m_t values were reweighed to 171.5 GeV and 173.5 GeV (in green) with the sample where the peak was explicitly generated at $m_t = 171.5$ GeV and at $m_t = 173.5$ GeV (the black markers). In addition, the central unreweighed sample generated with $m_t = 172.5$ GeV. Fit mean obtained by fitting distributions with a Voigt distributions is shown in the legend. Right: The ratios of all the samples shown on the left with respect to the central sample. In addition, here also the reweighed distribution to $m_t = 172$ GeV and $m_t = 173$ GeV is also shown (in red).

samples because of a perfect correlation among the variation if applying weights. Since the statistical uncertainties of the type (II) variations are almost fully correlated, then the impact of the variation can be seen even if it occurs within the statistical uncertainties for bins with a small number of events. In addition, when running the MC event generation, the weights are calculated on the fly, which does not increase the computation time as much as generating a new sample. Thus, category (III) uncertainties are used only when an uncertainty using weights is not possible.

Most of the usual systematic uncertainties considered in measurements of m_t are expected to impact m_t and $m_{\bar{t}}$ in a correlated way and thus cancel in the Δm_t measurement. Nevertheless, these uncertainties are kept for completeness and since the profile-likelihood approach allows a simple implementation of these uncertainties without the toy dataset generation. In the following, all systematic uncertainties applied are listed. The uncertainties are either correlated among years or channels, meaning that all the years or channels are varied simultaneously, or uncorrelated, meaning that they are varied independently for each year or channel, effectively having a separate variation for each year or channel. No partially correlated uncertainties are considered. Some of the variations in categories (II) and (III) are one-sided, meaning that there is no up and down variation. The treatment of such variations is explained in Section 7.6.1.

7.5.1. Experimental uncertainties

In this section, all experimental uncertainties are stated.

Jet energy scale uncertainty

The derivation process of JEC contains many steps, as seen in Section 5.6. This leaves a large set of uncertainties. The CMS Run 2 JES uncertainties are split into 26 different components. All partially correlated uncertainties are considered to be fully correlated in this analysis. This results in 16 uncertainties that are fully correlated across the years, while 10 uncertainties remain uncorrelated over the years.

The fully correlated uncertainties are the following: `AbsoluteMPFBias`, `AbsoluteScale`, `Fragmentation`, `PileUpDataMC`, `PileUpPtBB`, `PileUpPtEC1`, `PileUpPtEC2`, `PileUpPtHF`, `PileUpPtRef`, `RelativeFSR`, `RelativeJERHF`, `RelativePtBB`, `RelativePtHF`, `RelativeBal`, `SinglePionECAL`, `SinglePionHCAL`

The uncorrelated uncertainties are as follows: `AbsoluteStat`, `RelativeJEREC1`, `RelativeJEREC2`, `RelativePtEC1`, `RelativePtEC2`, `RelativeSample`, `RelativeStatEC`, `RelativeStatFSR`, `RelativeStatHF`, `TimePtEta`

Jet energy resolution

For JER smearing, the hybrid approach is used as described in Section 5.6. The JER variation is obtained by applying a one σ up and down variation on the JER scale, s_{JER}. When using the stochastic smearing for each of the variations and for the central sample, the same seed is used, assigned to each event. In this way, the variations become correlated. This variation is assumed to be fully correlated between years.

Jet flavour uncertainties

The classical flavour uncertainties that are symmetric for quarks and antiquarks are used for each flavour. In this analysis, new flavour uncertainties derived from $t\bar{t}$ events as described in Section 6.4 are used in this analysis. The uncertainties are applied according to the parton flavour assignment. It is evaluated in an uncorrelated way for each of the jet flavours, b, c, uds, g.

Jet flavour-antiflavour uncertainty

In the Run 1 Δm_t analysis, the b vs $\bar{b}$ JES uncertainty was estimated using MadGraph +pythia as the ratio of b and $\bar{b}$ JEC. It was determined inclusively in p_{T} and η and was found to be $0.078 \pm 0.040\,\%$. The results were verified with a sample generated with mc@nlo +herwig and were found to be similar. This uncertainty resulted in the shift of 51 ± 1 MeV in Δm_t, which was the second largest uncertainty after the method calibration (proportional to MC statistical uncertainty).

In this measurement instead, two sources of flavour-antiflavour uncertainty are estimated. The uncertainty associated with the MC generators is obtained using the procedure described in Section 6.6 by a HERWIG 7 to PYTHIA 8 comparison. The uncertainty associated with the mismodelling of the negative and positive pion response by GEANT 4 is obtained as described in Section 6.6.4. Both of these uncertainty sources are obtained not only for the b quark but also for the ud, s and c quarks.

Missing transverse momentum

The usual jet and lepton scale variations impact $p_{\mathrm{T}}^{\mathrm{miss}}$ because it is the vector ensuring the p_{T} conservation of all objects. An additional $p_{\mathrm{T}}^{\mathrm{miss}}$ up and down scale is applied on the unclustered energy. The unclustered energy arises from particles that are not clustered into jets. Typically, in the PF clustering algorithm, clusters with $p_{\mathrm{T}} < 1\,\mathrm{GeV}$ are not considered as jets. This provides an additional contribution to the p_{T} balance. The uncertainty accounts for the momentum uncertainties of the particles entering the unclustered energy.

b tagging scale factors

The up and down b tagging variation is associated with $\pm 1\sigma$ uncertainty of the tagging and misstagging efficiencies. For both, mistagging and tagging uncertainty, it is split into a component correlated over years and one uncorrelated for each data-taking year. This makes 10 uncertainties, namely `btagSFbc_correlated`, `btagSFlight_correlated`, `btagSFbc_2018`, `btagSFlight_2018`, `btagSFbc_2017`, `btagSFlight_2017`, `btagSFbc_2016postVFP`, `btagSFlight_2016postVFP`, `btagSFbc_2016preVFP`, `btagSFlight_2016preVFP`.

PileUp

For PU, a fully correlated uncertainty over years of $\pm 4.6\,\%$ is used for the 62 mb MB cross section, as mentioned in Section 7.1.5. This shifts the distribution of PU observed in MC.

Electron and muon scale factors

For electrons and muons, the systematic uncertainty associated with the tag-and-probe method used to derive the SF for trigger, ID, and isolation is propagated separately through the analysis. For muons, each of these three uncertainties has a component that is uncorrelated over years and three correlated over the years. For electrons, only trigger SF has a component that is correlated over years and the rest are considered uncorrelated.

The SF associated with the trigger, ID and isolation efficiencies for muons and electrons are obtained in Z +jets events. Therefore, they might differ between the Z +jets topology

and the jet-rich $t\bar{t}$ topology. However, as the SF uncertainty is not major, no additional SF are used.

For the electron energy correction and the resolution SF, the statistical and systematic uncertainty is combined into one up and one down variation for the energy scale and one for the resolution. These uncertainties are considered to be fully correlated between years.

L1 ECAL and muon prefiring

A variation on the prefiring weights as discussed in Section 7.1.5 is applied as an up and down variation.

Luminosity

The luminosity uncertainty is divided into five uncertainties, three uncorrelated uncertainties for each year, and two correlated ones. They are shown in Table 7.5. For the correlated components, one is only correlated for 2017 and 2018 and one is correlated for all three years together. Such a correlation scheme is included because the method to obtain the luminosity in 2016 has been updated and is different from the method used to obtain the luminosities in 2017 and 2018. The impact of the correlated uncertainties on each year differs; for example, the correlated 2016-2018 uncertainty has only an impact of 0.6 % for 2016 but has a 0.9 % and 2.0 % for 2017 and 2018, respectively. This is because the same systematic sources impact the 2017 and 2018 luminosities differently.

Table 7.5

Luminosity uncertainty table for 2016-2018 in %

Uncertainty Name	2016	2017	2018
Uncorrelated (2016)	1.0	0.0	0.0
Uncorrelated (2017)	0.0	2.0	0.0
Uncorrelated (2018)	0.0	0.0	1.5
Correlated 2016-2018	0.6	0.9	2.0
Correlated 2017-2018	0.0	0.6	0.2

Cross section uncertainty

The cross-section uncertainties are implemented using the log-normal nuisance parameters which vary only the normalisation of the distribution. In instances where a theoretical cross section estimate is available, the corresponding uncertainty estimate is used. Otherwise, a generator-based uncertainty is used. For some background processes, such as W+jets, DY+jets or $t\bar{t}$ in dilepton channel, the data-to-MC agreement depends on the number of jets in the event and deteriorates with the larger number of jets [334], [335]. The efficiency of selecting events at the given phase space is accounted for by incorporating an additional uncertainty meant to envelop these differences.

Specifically, for each of the MC samples, the following cross sections and their uncertainties are used.

- For $t\bar{t}$, the cross section calculated at NNLO+NNLL is used, assuming $m_t = 172.5\,\text{GeV}$, i.e. $\sigma(13\,\text{TeV}) = 833.9^{+37.4}_{-43.0}$ pb [336], [337]. The uncertainty includes μ_F and μ_R scale variations, PDF, α_s and mass uncertainty. Thus the scale of 0.94846 down and 1.04803 up is applied for all three decay channels. For the $t\bar{t}$ dilepton channel an additional 5 % uncertainty is added due to the selection efficiency of having events with two additional jets.

- For the single-top tW channel, a 6 % uncertainty obtained from the NNLO theoretical calculations is used, which includes scale and PDF uncertainties [338], [339]. For s-channel and t-channel, the NLO theoretical uncertainty [339] is scaled by 2 to account for the selection efficiency, yielding a ±8 % cross section variation [340]. The uncertainty is correlated for the events with the top quark and with top antiquark

- For W +jets, an uncertainty of ±30 % is used for cover the data-to-MC agreement in events with more than one additional jet [334]. An uncertainty of ±10 % is used for DY+jets [335], $t\bar{t}$ +jets and VV [341], [342].

- For the QCD multijet, a scaling uncertainty of +100 % and 50 % is applied, with these uncertainties being uncorrelated for the muon and electron channel. The two channels are uncorrelated because of the different QCD samples, electron enriched and muon enriched, used for each channel and because of the different sources of electrons and muons in them. Muons predominantly emerge from semileptonic quark decays and pair production processes, whereas electrons, in addition to these mechanisms, are frequently the result of misidentified fake electrons.

7.5.2. Modelling uncertainties applied as weights

In this section, all the theory variations that are applied as weights are discussed. All of these uncertainties are applied as correlated among years.

PDF variations

The central PDF set used is NNPDF3.1 at NNLO [106], [108]. For PDF variations, all default 100 eigenvectors given by the PDF set are varied. In addition, the α_s value is changed from the default 0.118 by $\pm 1\sigma$. Since these variations are not significant, all eigenvariations and α_s are summed quadratically. In addition, alternative PDF sets, i.e. CT14 at NNLO [109] and MMHT2014 at NNLO (68 % CL) [110] are used as a variation. In this case, these are one-sided distributions.

QCD Scale variations

Factorisation and renormalisation scale for ME is varied by a factor of 0.5 (down variation) and 2 (up variation) as two separate variations.

In ISR and FSR, the value of α_s determines the amount of radiation produced and can be tuned to the data. Thus, while $\alpha_s(m_Z)$ should be independent of the physics process, the value might differ in ISR and FSR. The systematic variation of α_s is encompassed by the μ_R and μ_F variations.

Typically in the analyses, to evaluate the ISR and FSR shower uncertainties, μ_R is scaled by 1/2 and 2. However, MC generators allow to vary ISR and FSR for each kind of splitting in an uncorrelated way, i.e. $g \to gg$, $g \to q\bar{q}$, $q \to qg$ and $x \to xg$, where x is either b or t quark. In this analysis, ISR uncertainty has a small impact on the measurement, thus only an overall scale of 0.5 and 2 is utilised. FSR, on the other hand, is varied for all the given splittings. In addition, the variations of non-singular terms (cNS variations) are available, which are complementary to the scale variations, also allowing one to consider all four different splittings separately [126]. Thus, for FSR, there are 4 (splitting types) x 2 (normal vs cNS) x 2 (μ_R and μ_F) = 16 variations.

b jet fragmentation

The b fragmentation as using Boweler-Lund parametrisation in Eq. (3.8) was tuned on LEP data with corresponding uncertainties [343], [344]. An additional Peterson parametrisation of the b fragmentation also tuned on the LEP data is used as a variation. For Peterson variation, only the central value is used as a variation without the corresponding up and down variation in order not to double count experimental LEP-related uncertainties. This way, Bowler-Lund uncertainty is double-sided, having up and down shapes, while Peterson uncertainty is one-sided, as the difference between the Bowler-Lund central shape to Peterson central shape.

Semileptonic branching ratio of the b hadron decays

The uncertainty of the lepton+jets branching ratio (BR) of the b hadron decays significantly impacts the JEC, since a larger BR increases the fraction of neutrinos in the b jet. The variation is applied as weights and the BR value is changed according to [57].

Top transverse momentum mismodelling

In Run 1, in CMS and ATLAS it was discovered and later confirmed in Run 2 that the measured top-quark p_T spectrum is softer than predicted by the MC. This effect can be partially explained by incorporating the NNLO variations [316]–[319]. However, it is often addressed by correcting the disagreement using a data-to-NLO (POWHEG + PYTHIA 8)

fit. It is applied as an event weight on the average of the top-quark p_{T}

$$w = \exp\left(0.0615 - 0.0005 \cdot \frac{p_{T,t_1}^{\mathrm{gen}} + p_{T,t_2}^{\mathrm{gen}}}{2}\right) \tag{7.9}$$

Top p_{T} mismodelling estimates the leftover disagreement. In this measurement, the top p_{T} correction is added as an additional variation, while the central sample is not corrected for this effect. The COMBINE fit is able to interpolate between the two samples and find the optimal shift, as well as assign the corresponding uncertainty. This uncertainty is one-sided.

7.5.3. Modelling uncertainties obtained as additional MC samples

The given variations are not available as weights and require additional independent datasets, uncorrelated to the central one. All the variations are assumed to be uncorrelated among years.

Matrix element to parton shower scale

ME-PS scale associated with the POWHEG h_{damp} parameter, specifies the dampening of the POWHEG real emission by $h_{\mathrm{damp}}^2/(p_T^2 + h_{\mathrm{damp}}^2)$ and the parameter is tuned to the distribution of the leading additional jet p_{T} in $t\bar{t}$ events in $\sqrt{s} = 13\,\mathrm{TeV}$. The optimal value obtained from the fit is $h_{\mathrm{damp}} = 1.379^{+0.9260}_{-0.5052} \cdot m_t$. The variation is obtained by generating two additional samples with the h_{damp} value increased and decreased by the corresponding uncertainty.

CP5 tune variation

The CP5 tune, which is used to describe the underlying event (UE) observables has an associated uncertainty [162], [345]. When obtaining the tune, five free parameters were optimised and, in general, one would require $5{\cdot}2 = 10$ independent variations (eigentunes). Each of the eigentunes is obtained by finding the value of the given parameter that raises the χ^2 distribution by a certain value. However, to limit the number of samples that need to be analysed, in CMS typically only two variations are used, which envelop all the eigentunes added in quadrature. These two are obtained by fitting the UE parameters that best describe each of the variations.

Colour Reconnection and Rarly Resonance Decays on

Besides the so-called QCD-inspired colour reconnection (CR) scheme defined in Section 3.4, PYTHIA 8 allows for two other CR schemes. The central sample uses the MPI-based CR scheme [152]. For the CR variation, two variation samples are obtained with

QCD-inspired and Gluon-move model [346] CR schemes. Changing the CR model impacts the UE distributions, so the CP5 tuning process had to be repeated for both of these models [347].

An additional variation sample includes an MPI-based CR tune with early resonance decays (ERD) on. Nominally with ERD off, in the late resonance decay case, top quarks are assumed to be long-lived enough that all the ISR on the MPI and beam remnants will have already taken place, and the CR then would not impact the decay products of the top quarks. ERD on removes this "protection" for top quarks and lets top decay products be colour-reconnected with the MPI. The physical case is somewhere in-between the two models, but due to the lack of a more precise theoretical model, the two samples are used in COMBINE to find the good middle ground between them.

7.6. The distributions of the systematic uncertainties

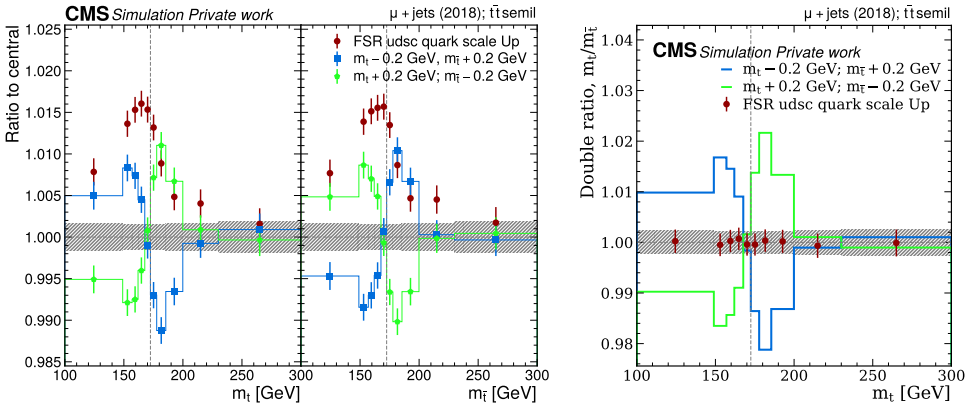

Fig. 7.16. Left: The ratio of the bin count in the FSR light quark scale up variation with respect to the central $t\bar{t}$ lepton+jets dataset. The left panel shows the results for the μ^-+jets sample, while the right panel for the μ^++jets sample. The ratio of the reweighed samples with $\Delta m_t \pm 400\,\text{MeV}$ is overlaid (up/plus variation in green and down/minus variation in blue). The uncertainty band shows the statistical uncertainty for the central sample, and the error bars show the statistical uncertainties for each of the other datasets. The dashed vertical line shows the generated top-quark mass value, $m_t^{\text{gen}} = 172.5\,\text{GeV}$. Results are shown for the 2018 μ+jets channel.
Right: The double ratio $(\text{var}(m_t)/\text{central}(m_t)\ )/(\text{var}(m_{\bar{t}})/\text{central}(m_{\bar{t}}))$, i.e. the ratio of the left panel with respect to the right panel of the left plot.

To compare the impact of the different variations on the event yields, their ratios to the central datasets are shown. Only the $t\bar{t}$ semileptonic signal sample is compared as the contribution of the other samples is small. Fig. 7.16 shows the ratio of the bin count in the $t\bar{t}$ semileptonic up variation of the FSR light quark scale with the central dataset. The ratio is compared with the datasets reweighed to $\Delta m_t = \pm 400\,\text{MeV}$. $\Delta m_t = +400\,\text{MeV}$

corresponds to $m_t \to m_t + 200\,\text{MeV}$ and $m_{\bar{t}} \to m_{\bar{t}} - 200\,\text{MeV}$, while $\Delta m_t = -400\,\text{MeV}$ corresponds to $m_t \to m_t - 200\,\text{MeV}$ and $m_{\bar{t}} \to m_{\bar{t}} + 200\,\text{MeV}$. Note that reweighing shifts m_t and $m_{\bar{t}}$ peaks in the opposite directions. A significant impact is seen on both m_t and $m_{\bar{t}}$, but it is very similar for both m_t and $m_{\bar{t}}$.

To visually compare the differences on how each variation impacts m_t and $m_{\bar{t}}$ a double ratio of the top panel in Fig. 7.16 is constructed, where the values for m_t are divided by the values for $m_{\bar{t}}$. As the effect of the variation is correlated for m_t and $m_{\bar{t}}$, the double ratio shows only a small impact on Δm_t. That is, the double ratio for the variation overlaps almost completely with 1.00. Note that since the variation sample is obtained using weights on the central sample, both samples are correlated. Therefore, the statistical error bars are larger than the exact variation. A small non-cancellation is seen, potentially due to effects like charge asymmetry effects $t\bar{t}$ events, i.e. different η and p_T distributions for top quarks and antiquarks in the LHC [79]. In general, the η distribution is expected to be broader for top quarks than for top antiquarks. This could lead to slightly different jet dynamics after applying the FSR variation. In addition, the deviation from unity can also be a small effect of non-correlation between the central and variation sample, caused by the change in the events passing the m_W^reco requirement and due to some events failing the analysis pipeline.

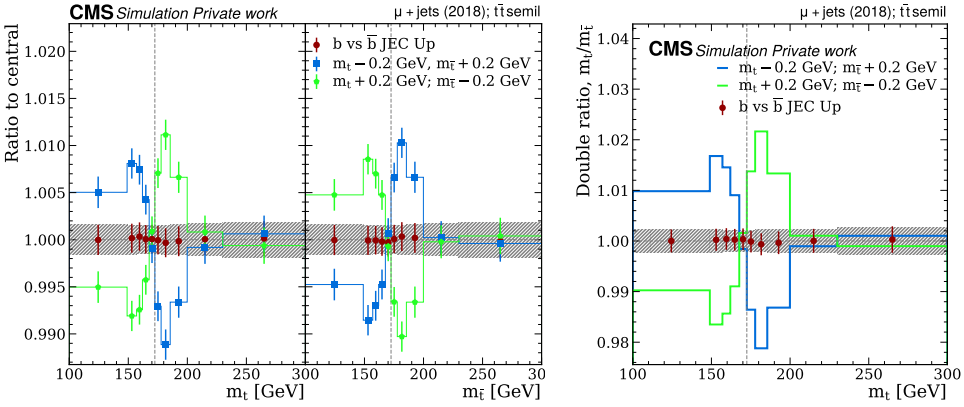

Fig. 7.17. Left: The ratio of the bin count in the b vs $\bar{b}$ up variation with respect to the central $t\bar{t}$ lepton+jets sample for μ^-+jets sample (left) and for μ^++jets sample (right). The legend explanation is the same as in Fig. 7.16.
Right: The double ratio $(\text{var}(m_t)/\text{central}(m_t))/(\text{var}(m_{\bar{t}})/\text{central}(m_{\bar{t}}))$.

An example of a variation that has an anticorrelated effect for m_t and $m_{\bar{t}}$ is the b jet flavour-antiflavour uncertainty, as shown in Fig. 7.17. Although the impact on the overall m_t and $m_{\bar{t}}$ distributions is more than $\mathcal{O}(10)$ smaller, the double ratio shows a small effect of the variation on Δm_t. Moreover, unlike the double ratio in Fig. 7.16, the values in Fig. 7.17 are smoother and thus are more consistent with one of the Δm_t variations, in this case, with the Δm_t up variation. The minimum ratio of the b vs $\bar{b}$ variation is around

0.9995, compared to the effect of Δm_t, which has a minimum of 0.98, and therefore is expected to have no more than a $400/40 = 10$ MeV impact on Δm_t. This can be compared to the 51 MeV impact on the Run 1 measurement [30].

7.6.1. Preparation of the systematic uncertainties for the fits

The variations shown in Fig. 7.16 and Fig. 7.17 are correlated with the central MC dataset. For this reason, the dispersion of the points is smaller than the error bars and the small impact of the variation can be seen. This also reveals how the analysis is more limited by the statistical uncertainty than by the systematic uncertainty, unlike the m_t analysis, where the impact of the variations is usually larger than the statistical uncertainty.

The variations obtained from the independent datasets described in Section 7.5.3 are uncorrelated with the central data set, and thus suffer from large fluctuations. This issue is mitigated in several steps. First, for variations that have up and down variations, an assumption is made that the variation should be symmetric in the both direction. Thus, for the bin i, given the bin value of the central sample, $b_{c,i}$, the new bin value of the up (down) variation histogram $b_{\mathrm{up},i}$ ($b_{\mathrm{dn},i}$) is obtained as

$$\begin{aligned} b_{\mathrm{up}} &\to \Big(1 + (w_{\mathrm{up},i} \cdot c_{\mathrm{up},i} + w_{dn,i} \cdot c_{\mathrm{dn},i})/(w_{\mathrm{up},i} + w_{dn,i})\Big) \cdot b_{c,i} \\ b_{\mathrm{dn}} &\to \Big(1 - (w_{\mathrm{up},i} \cdot c_{\mathrm{up},i} + w_{dn,i} \cdot c_{\mathrm{dn},i})/(w_{\mathrm{up},i} + w_{dn,i})\Big) \cdot b_{c,i} \\ c_{\mathrm{up/dn},i} &= (b_{\mathrm{up/dn},i}/b_{c,i} - 1) \\ w_{\mathrm{up/dn},i} &= (err_{\mathrm{up/dn},i}/b_{c,i})^2, \end{aligned} \tag{7.10}$$

where and $err_{\mathrm{up},i}$ and $err_{\mathrm{dn},i}$ are the errors of the bin i for the up and down variations. In addition, also other variations are symmetrised in this way, not only the ones described in Section 7.5.3.

In addition, it is assumed that for a physical variation, the histogram values are supposed to be smooth and without large bin-to-bin changes. For this reason, all variations described in Section 7.5.3 are smoothed using the 353QH method [348]. This method sequentially replaces the bin values by a running median of some length around the given bin. First, a median of three is applied, that is, for the old values y_i, the new values are found as $z_i = \mathrm{median}(y_{i-1}, y_i, y_{i+1})$. Subsequently, a median of five is used, and then again a median of three. Special treatment is taken at the end points. Following these steps a quadratic interpolation is performed followed by a running average. The mirroring of the variations has the most prominent impact for the UE variation, which is the only variation obtained by separate samples that is two-sided.

Fig. 7.18 and Fig. 7.19 show the impact of the variation before and after applying the symmetrising and smoothing. Unlike the previous plots, here the full Run 2 dataset is combined to see the final impact of the variation. Note that the points are adequately

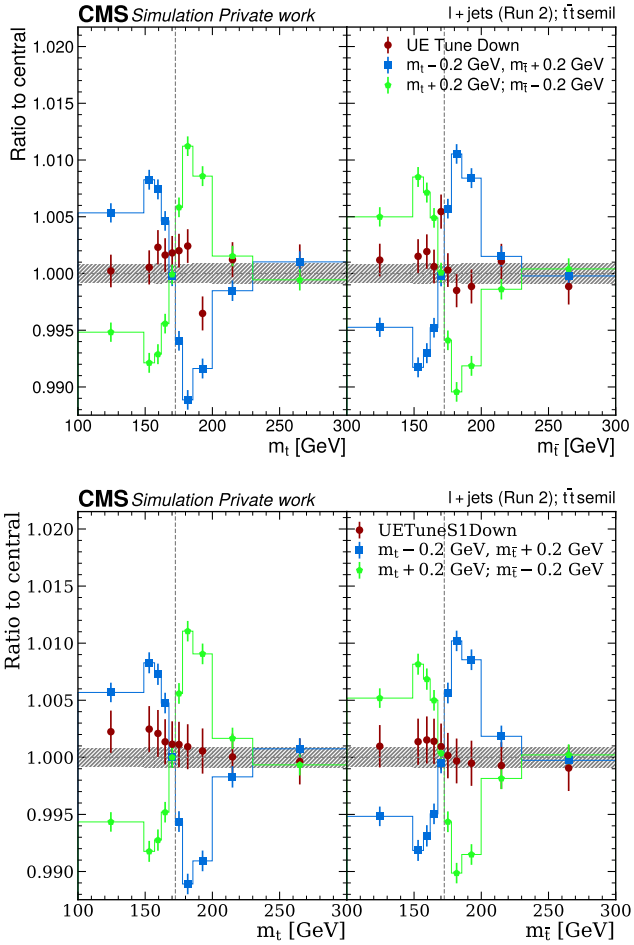

Fig. 7.18. The ratio of the bin count in the UE down variation before (up) and after (down) the bin symmetrizing and bin smoothing with respect to the central $t\bar{t}$ lepton+jets sample for all the l^-+jets (left panel) and for l^++jets sample (right panel). The legend explanation is the same as in Fig. 7.16. Results are shown for the whole Run 2 l+jets dataset.

dispersed according to the error margins, unlike for the correlated variations as in Fig. 7.17. This creates a large random effect in the statistical fit where the fitting procedure finds this random noise as an actual variation. The smoothing distributions, although containing some residual effect, do not have large bin-to-bin variations. The smoothing procedure was found to significantly reduce the impact of these variations.

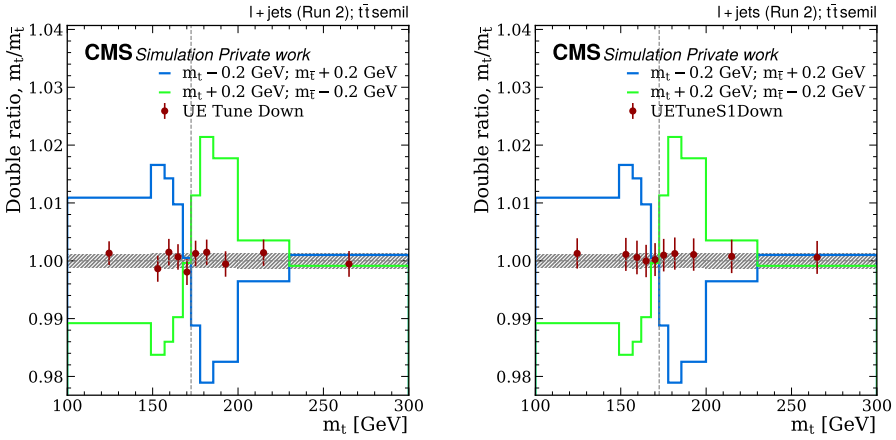

Fig. 7.19. The double ratio (var(m_t)/central(m_t))/(var($m_{\bar{t}}$)/central($m_{\bar{t}}$)), of the ratios shows in Fig. 7.18 for the UE tune down variation before (left) and after (right) the smoothing.

7.6.2. Most important systematic variations

The double ratios introduced above are shown in Fig. 7.20 for some of the most important systematic variations. All of the variations are smaller compared to the statistical uncertainty and far within the shapes of the reweighed samples. The b vs $\overline{b}$ JEC due to pion scaling reveals a prominent shape that is well aligned with the up Δm_t variation. The b jet JEC has a deviation from 1 for some values of m_t, but they are in opposite directions for neighbouring bins and thus do not have an overall effect in the fit. ME-PS scale and ERD-on variations, even after the smoothing, have a large effect on the double ratio, probably a left over noise effect. Nevertheless, these variations have large tails, i.e. at the last two bins, and thus could get constrained by the fit. The BL b Fragmentation and FSR gluon scale has a non-negligible effect on the fit as well.

The double ratios for all the flavours antiflavour uncertainties that have not been previously shown are presented in Fig. 7.21. Since the main source of non-b jets is the W boson, which produces two jets, the effect of these uncertainties is expected to cancel. However, because the ISR and FSR jets impact the energy balances in a non-trivial way, these can have an effect on the overall kinematic properties of the event. Some effect on Δm_t is seen by c vs $\overline{c}$ JEC and pion scaling, possibly due to the few c jets tagged as b and due to the relatively large c vs $\overline{c}$ JES. An interesting effect is seen for s vs $\overline{s}$ JEC which produces overall larger event yield differences for top-quark events than for top-antiquark events. The same normalisation effect was seen for all the decay channels and years. The cause of it is possibly some small asymmetries in s jet production that are amplified by the large s vs $\overline{s}$ uncertainty, possibly for jets coming from W or from ISR. For $t\bar{t}$ lepton+jets events that do not pass the selection criteria, the s vs $\overline{s}$ uncertainty increasing the energy

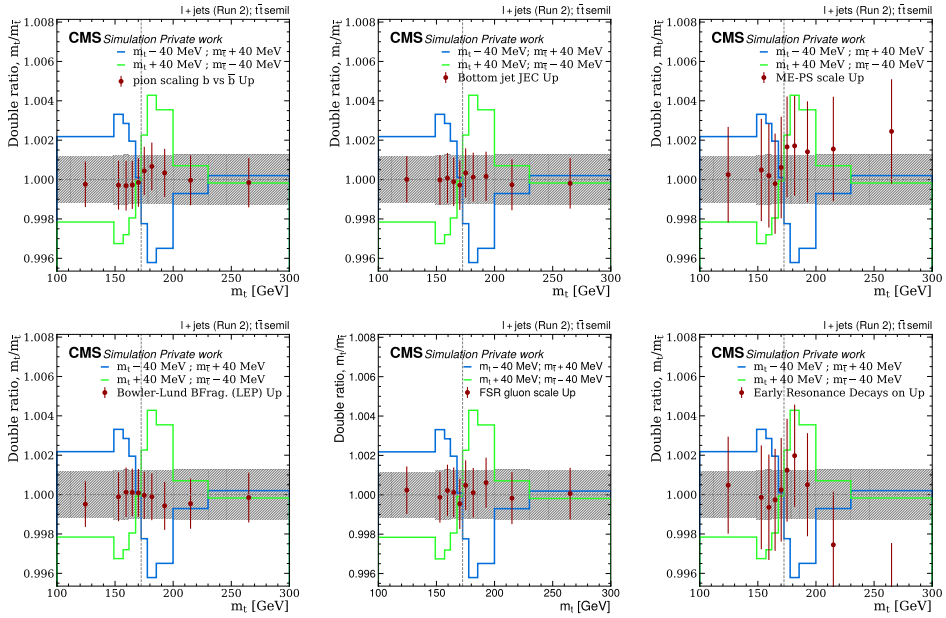

Fig. 7.20. The double ratio (var(m_t)/central(m_t))/(var($m_{\bar{t}}$)/central($m_{\bar{t}}$)) for b vs $\bar{b}$, b jet JEC, ME-PS scale (top) and Bowler-Lund (BL) b fragmetnation, Peterson b ragmentaiton and ERD (bottom) variations. ME-PS scale uncertainty is associated with varying h_{damp} parameter in POWHEG. The legend explanation is the same as in Fig. 7.16. Results are shown for the whole Run 2 l+jets dataset. ME-PS and ERD uncertainties are obtained from separate datasets with limited number of events and thus the statistical uncertainties for the points are large. The default Δm_t variations shown in Fig. 7.19 are scaled by 1/5 to enhance the visual comparison.

of the s jets would allow some of the events to pass them. The event yield differences are largest around the top-quark mass peak.

Double ratios for the most relevant flavour uncertainties (c, g and q) are shown in Fig. 7.22. Some small non-cancellation between the effects on m_t and $m_{\bar{t}}$ is seen, explained by similar effects as for Fig. 7.16.

7.7. Profile likelihood fit

Fig. 7.23 shows the ratio of the m_t^{fit} and $m_{\bar{t}}^{\mathrm{fit}}$ distributions, i.e. distributions in Fig. 7.14 but split into positive and negative lepton charges. Note that since this is a single ratio, not a double ratio as in the previous section, the central prediction (grey line) does not have to coincide with 1. The central prediction shows the expected small (up to 1 %) asymmetry in $t\bar{t}$ events with positive and negative charges with $\Delta m_t = 0$. The asymmetry is predominantly caused by background events, such as single top, W+jets, and QCD events, as shown in Table 7.4. The systematic uncertainties are approximately equal for

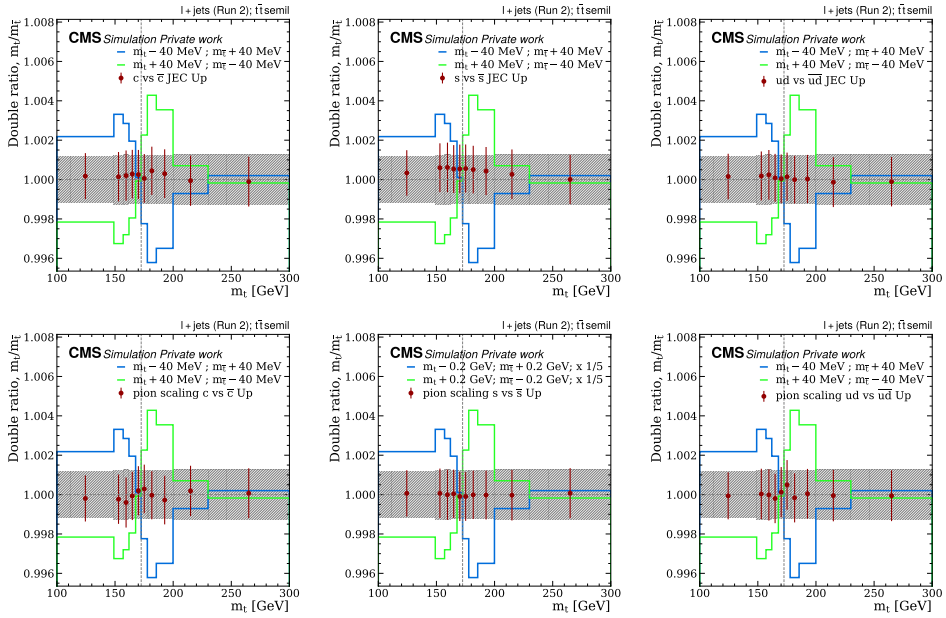

Fig. 7.21. The double ratio (var(m_t)/central(m_t))/(var($m_{\bar{t}}$)/central($m_{\bar{t}}$)), b vs $\bar{b}$ pion scaling uncertainty, b JEC and ME-PS scale (up) and BL fragmentation, Peterson b fragmentation and ERD (bottom) uncertainty. The legend explanation is the same as in Fig. 7.16. Results are shown for the whole Run 2 l+jets dataset. The Δm_t variations are scaled by 1/5.

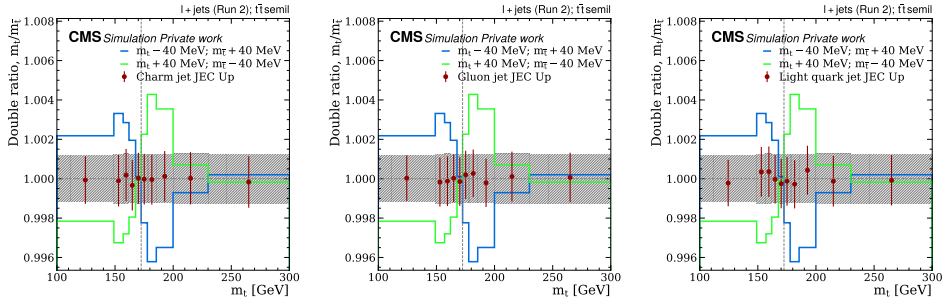

Fig. 7.22. The double ratio (var(m_t)/central(m_t))/(var($m_{\bar{t}}$)/central($m_{\bar{t}}$)) for c, g and q flavour uncertainties. The legend explanation is the same as in Fig. 7.16. Results are shown for the whole Run 2 l+jets dataset. The Δm_t variations are scaled by 1/5.

all the data points because of the approximately equal amount of data chosen for each bin. Conversely, in the MC events, the uncertainty bars differ bin to bin because some of the background processes that contribute more at the tails have larger weights. Comparing the data with the MC, it can be seen that some points, e.g. those around 175 GeV and

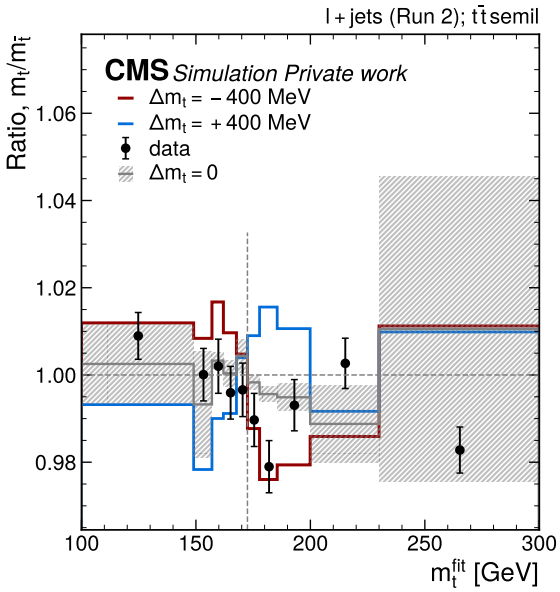

Fig. 7.23. The ratio of the m_t^{fit} and $m_{\bar{t}}^{\text{fit}}$ distributions. The gray line shows the ratio with $\Delta m_t = 0$, with the shaded boxes corresponding to the statistical uncertainty of the simulation. Blue and red lines show the $\Delta m_t \pm 400\,\text{MeV}$, respectively. The markers show the result in data.

180 GeV are shifted towards $\Delta m_t = 400\,\text{MeV}$ and do not agree with the central simulation with the error bars, while some lower points are shifted towards $\Delta m_t = -400\,\text{MeV}$.

The fit described in Section 7.3 was performed in two steps. First, it was performed on the Asimov dataset, namely, taking the nominal MC result as the data, normalising the event yields to data. In other words, the values of the parameters of interest and nuisance parameters in the Asimov dataset are equal to the values used to generate the dataset. This gives the result consistent with $\Delta m_t = 0$, but enables the validation of the fit and the estimation of statistical and systematic uncertainties associated with the result without unblinding, i.e. revealing the actual result in the data. After that, a fit was made on the collision data to obtain the final result. Only the result for Δm_t was unblinded because a different high-precision measurement is in process targeting only the m_t fit in CMS using the same dataset. The fit was performed for Δm_t as the parameter of interest, letting m_t float freely. The whole Run 2 MC dataset was used for the fit, as well as for each year and decay channel separately. The uncertainties for nuisance parameters are estimated sequentially by finding the upper and lower bound of 68 % CL interval, where the negative profile log-likelihood ratio $q = -\ln\left(\frac{\mathcal{L}(\vec{n}|\Delta m_t, \hat{\hat{\vec{\theta}}}, \hat{\hat{\vec{n}}})}{\mathcal{L}(\vec{n}|\Delta m_t, \hat{\vec{\theta}}, \hat{\vec{n}})}\right)$ increases by $1/2$. The `minuit midgrad` algorithm is used for minimisation within COMBINE.

The profile likelihood fit was validated by performing the fit with datasets with different reweighted $\Delta m_{t,\mathrm{gen}}$ values taken as Asimov datasets. The agreement between the optimisation output $\Delta m_{t,\mathrm{extr}}$ and $\Delta m_{t,\mathrm{gen}}$ was tested. Fig. 7.24 (left) depicts the results for $\Delta m_{t,\mathrm{extr}}$ depending on $\Delta m_{t,\mathrm{gen}}$. The test was performed in a large range of $-2000 < \Delta m_t < 2000\,\mathrm{MeV}$ to see the breaking point of the method. For $\Delta m_{t,\mathrm{extr}}$ vs $\Delta m_{t,\mathrm{gen}}$ no deviation from the diagonal is visible in the entire range, except at $|\Delta m_t| = 2000\,\mathrm{MeV}$. This shows a nearly perfect closure of the method. All the deviations are negligible compared to the statistical uncertainties of the fit.

Fig. 7.24 (right) depicts $\Delta m_{t,\mathrm{extr}} - \Delta m_{t,\mathrm{gen}}$ (bias) vs $\Delta m_{t,\mathrm{gen}}$ and shows that the bias of the method is within 1 MeV for the relevant range of $-400 < \Delta m_t < 400\,\mathrm{MeV}$, which includes the 64% CI of the previous CMS measurement. The bias in this range is also two orders of magnitude smaller than the statistical uncertainty in the fits. These tests show that no specific calibration of the method is necessary.

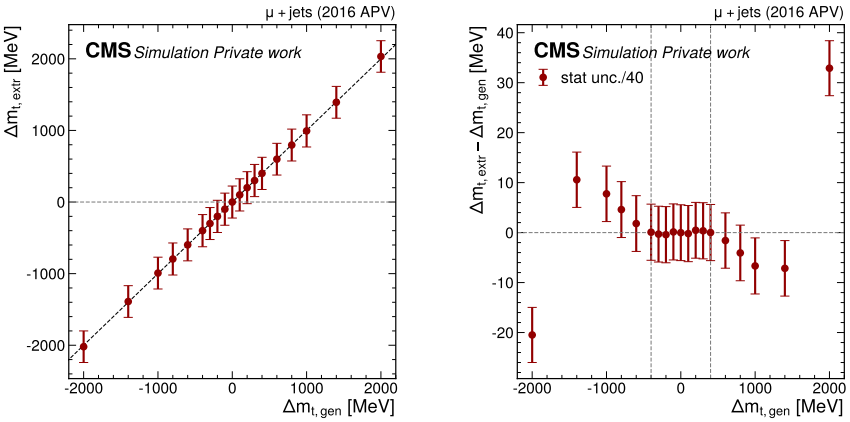

Fig. 7.24. Method validation showing the extracted top mass difference $\Delta m_{t,\mathrm{extr}}$ vs the generated top mass difference $\Delta m_{t,\mathrm{gen}}$ (left) and the obtained bias $\Delta m_{t,\mathrm{extr}} - \Delta m_{t,\mathrm{gen}}$ vs $\Delta m_{t,\mathrm{gen}}$. The left plot shows the full statistical uncertainties on the points while the right plot shows statistical uncertainties reduced by a factor of 40. Results are obtained for the simulated dataset for 2016 in μ+jets channel

7.8. Fit result

The impact of each nuisance parameter is obtained by

$$\Delta(\Delta m_t) = \widehat{\Delta m_t}(\hat{\theta}_k + \Delta^{\pm}\theta_k) - \widehat{\Delta m_t}, \tag{7.11}$$

where $\widehat{\Delta m_t}(\hat{\theta}_k + \Delta^{\pm}\theta_k)$ is the value of m_t obtained by the likelihood fit when the nuisance parameter is shifted to $\hat{\theta}_k + \Delta^{\pm}\theta_k$. The impact distribution of the main nuisance parameters for the measurement is shown in Fig. 7.25 together with the constraints and pulls

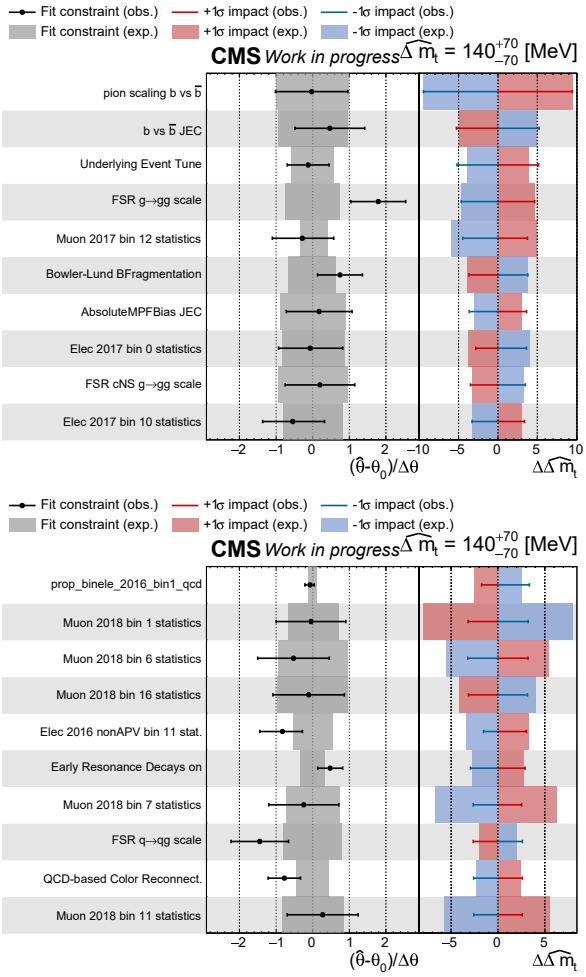

Fig. 7.25. The constraints and pulls of the main nuisance parameters (middle panel) and the nuisance parameter impacts on Δm_t (right panel). The shaded boxes show the results performed on the Asimov dataset (expected results), while the error bars show the results on the data (observed results). The red (blue) shaded boxes and error bars correspond to the positive (negative) impacts.

on the nuisance parameters, relative to their prefit uncertainties, $(\hat{\theta}_i - \theta_i)/\sigma_i$, where σ_i is the standard deviation of the nuisance parameter before the fit. The expected results are shown as shaded boxes, while the observed results are shown as error bars. The expected results contain no pulls because the Asimov dataset is used for the fit. The leading uncertainties are the two b vs $\bar{b}$ JES sources, from the pion scaling, the effect being larger and of the order of 10 MeV. Further important uncertainties include variations obtained from independent datasets that possibly contain large statistical fluctuations.

Multiple variations are associated with the MC statistical uncertainty estimated using the Barlow-Beaston approach, indicated as `<sample> bin <bin_number> statistics`. This shows that the analysis, similarly to the Run 1 analysis, is dominated by the statistical uncertainty. The greatest impact has the signal MC statistical uncertainty and the QCD background statistical uncertainty. Finally, there is a large impact from the FSR variation for the $g \to gg$ and cNS $g \to gg$ splitting, where the former is pulled towards larger values. Pulls for FSR variations have also been observed in the previous CMS m_t measurement [92]. The impacts of these variations on the Δm_t measurement could be a fluctuation in the MC weights and an effect of $t\bar{t}$ charge asymmetry, which is further studied in appendix G. The effect of $g \to gg$ can be seen in Fig. 7.20, where there is a fluctuation in the two most central bins that are particularly sensitive to the Δm_t variation. The nuisance parameter for the ME-PS scale variation was removed from the fit because the tests including that ME-PS nuisance parameter would have a non-physically large pull. As discussed in the text surrounding Fig. 7.20, the ME-PS scale has an unexpectedly large impact on Δm_t, probably because it is obtained from a dataset with a limited number of events. Future revision of this analysis should include the estimation of the ME-PS uncertainty using the ML event reweighing, as introduced in Section 3.5.5. The impact of this variation is not expected to be larger than a few MeV.

Table 7.6

Mean value, as well as the statistical, systematic and total uncertainty of the Δm_t measurement for each of the data taking period and channel

Channel	e+jets [MeV]				μ+jets [MeV]				l+jets [MeV]			
	mean	stat.	syst.	tot.	mean	stat.	syst.	tot.	mean	stat.	syst.	tot.
2016APV	350	$^{+262}_{-262}$	$^{+175}_{-176}$	$^{+315}_{-315}$	276	$^{+200}_{-201}$	$^{+186}_{-183}$	$^{+273}_{-271}$	281	$^{+159}_{-159}$	$^{+128}_{-127}$	$^{+204}_{-204}$
2016	-355	$^{+280}_{-280}$	$^{+183}_{-183}$	$^{+335}_{-335}$	303	$^{+219}_{-219}$	$^{+426}_{-424}$	$^{+479}_{-477}$	1	$^{+174}_{-174}$	$^{+191}_{-192}$	$^{+258}_{-259}$
2017	-111	$^{+184}_{-184}$	$^{+135}_{-135}$	$^{+228}_{-228}$	-68	$^{+147}_{-147}$	$^{+135}_{-144}$	$^{+199}_{-205}$	-62	$^{+115}_{-115}$	$^{+84}_{-87}$	$^{+142}_{-144}$
2018	444	$^{+153}_{-153}$	$^{+117}_{-117}$	$^{+193}_{-193}$	75	$^{+120}_{-120}$	$^{+150}_{-149}$	$^{+193}_{-192}$	198	$^{+94}_{-94}$	$^{+61}_{-61}$	$^{+112}_{-112}$
all	125	$^{+100}_{-100}$	$^{+54}_{-54}$	$^{+113}_{-113}$	110	$^{+79}_{-79}$	$^{+53}_{-51}$	$^{+95}_{-94}$	139	$^{+62}_{-62}$	$^{+25}_{-25}$	$^{+67}_{-67}$

The final result of the measurement is $\Delta m_t = 139^{+67}_{-67}$ MeV. The breakdown of the uncertainty into statistical and systematic uncertainty is shown in Table 7.6, where the comparison is shown for all the separate data channels as well as for the combined dataset. The statistical uncertainty is obtained by freezing all nuisance parameters and repeating the search for the upper and lower bounds of the 68 % CL interval. When compared to the Run 1 19.6 fb^{-1} result, the statistical uncertainty is reduced from 190 MeV to 62 MeV, that is, more than by a factor of 3. This is slightly better than predicted from the luminosity increase but can be explained by the improved b-tagging efficiency and the usage of a profile-likelihood fit for statistical inference instead of the Ideogram method. The systematic uncertainty is reduced from 90 MeV to 25 MeV, mostly due to the improved flavour vs antiflavour JES measurement. It can be seen that not only the statistical

uncertainty is roughly proportional to the luminosity in each data-taking period but also the systematic uncertainty. This comes from the fact that COMBINE is able to better constrain each variation with an increasing amount of data.

7.9. Summary

In this section, the measurement of Δm_t has been described. The measurement technique yielded a result with a total uncertainty of $\pm 67\,\text{MeV}$ which is an improvement by a factor of more than 3 with respect to the Run 1 measurement of the same parameter. This leads to the world-leading Δm_t measurement to date. The measurement excludes the effect of the ME-PS scale, which should be included in subsequent iterations using event reweighing based on ML.

8. CONCLUSION AND OUTLOOK

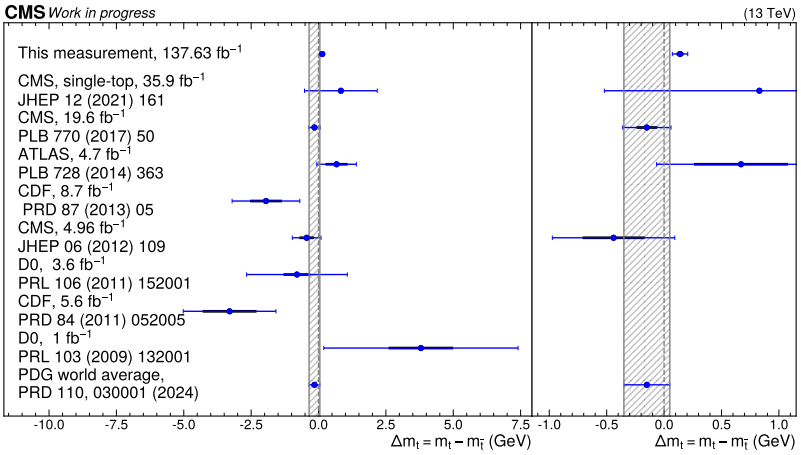

Fig. 8.1. The different measurements of the mass difference between the top quark and antiquark, including the result of this Thesis. The legend is identical to the legend of Fig. 1.2.

In this Thesis, the measurement of the mass difference between the top quark and antiquark was presented, yielding a result of $\Delta m_t = 139 \pm 67\,\text{MeV} = 139 \pm 62\,(\text{stat.}) \pm 25\,(\text{syst.})\,\text{MeV}$. This presents the most precise Δm_t measurement to date. The comparison of this measurement with other measurements of Δm_t is shown in Fig. 8.1. There is a slight disagreement with the CMS measurement at $\sqrt{s} = 8\,\text{TeV}$ and with the world average. Otherwise, the measurements exhibit general consistency. The result deviates from the SM prediction of $\Delta m_t = 0$ by 2.1σ, which is lower than 3σ, which is the accepted minimal threshold in particle physics for substantiating evidence of a discovery, and much less than 5σ required for a discovery. Thus, the measurement does not prove the violation of CPT symmetry.

The precision of this measurement relies on the improved prescription for the flavour-antiflavour JES uncertainty. Due to improved technique for the systematic uncertainties, the measurement is statistically limited just like the CMS Run 1 measurement. Adding the CMS Run 3 dataset would improve the statistical uncertainty by around a factor $\sqrt{2}$ due to the double luminosity (2023 data-taking period has $29\,\text{fb}^{-1}$, 2022 has recorded $35\,\text{fb}^{-1}$ luminosity, while in the 2024 data-taking period, CMS has recorded $113.32\,\text{fb}^{-1}$ luminosity). The leading uncertainty is the b vs $\bar{b}$ uncertainty due to pion scaling, which estimates the mismodelling of GEANT 4 hadron interactions.

The uncertainty could be reduced by adding additional observables to the fit, as was performed in [92]. Further improvements could be achieved by repeating the study shown in Section 6.6.4 with a larger MC dataset, enabling the variation to be jet p_T dependent

instead of only being jet $|\eta|$ dependent. An alternative approach of the measurement is to measure the mass difference from m_{lb}. Despite the lower m_t resolution, the sensitivity for Δm_t could be higher, based on the precise μ^+ and μ^- resolution in the CMS.

The flavour-antiflavour uncertainty due to event generator mismodelling can be improved by implementing the factorized scheme for flavour uncertainties as described in [303]. The SHERPA $t\bar{t}$ dataset presented in Section 3.7.2 could be used for the estimation of the hadronization uncertainty if an additional dataset with the Lund string hadronization model is generated.

ACKNOWLEDGMENTS

My gratitude is overflowing to all the people who contributed directly or indirectly to this Thesis and my doctoral studies. Naming everyone individually would exceed the limits of this page.

First and foremost, I am thankful to my RTU supervisor Kārlis Dreimanis for his mentoring, guidance, and ensuring I had all the necessary resources throughout my research. I am equally grateful to my CERN supervisor Martijn Mulders for his support, especially for guiding me through the world of the CERN CMS group humming with cutting-edge physics ideas. Heartfelt thanks to my scientific advisor Markus Seidel. Whether it was scientific advice, practical help with some analysis tools, or proofreading my texts, he was always generous. Markus was unfailingly patient when discussing meticulous details of my work, including when I was often mistakenly sending him wrong links to results or messing up the plot legends.

I warmly thank my family, mom, dad, and brother, for being patient through the times of my absence, even when living in the same city. My father's unceasing support and encouragement in all the stages of my studies laid the foundation for where I stand today.

My gratitude goes to all my colleagues, but particularly to Antra, Normunds, and Robert. Each at a different spacetime point was interacting with me strongly, where the interaction was mediated by common complaints and frustrations, meaningful lunch breaks, or just silence.

I extend my deep appreciation to everyone who helped me to adjust and survive in different countries and environments. In a gray February day of 2022, with me hiding in my room due to COVID positivity and when my Doctoral studies were hanging on a tiny thread, our 7-room shared house was accompanied by Ana María. Out of nowhere it felt she came, and at the right moment had good talks and encouragement to look for help, advice, and prayer. Thanks to God for being faithful when we are not.

Thanks to Sandijs for being available for spontaneous calls even after getting married (I am so happy). Thanks to Paula for bringing joy into the writing process and teaching me so much. Thanks to St. Matthew's church home group for renewing my goals and purpose. To Agape student organization for doing fun things with me at the uni, and Crossroads and Communitas international churches for welcoming me and being ready to listen and pray for me.

I am grateful to my outdoor friends, especially Andrew for making me renew my promise of love to mountains and getting me out of my house almost more than my body could sustain. Thanks to Juan and Tom for the continuation of this wholesome work.

Thanks to my electric guitar, Nelly (Epiphone ES-335), for always sounding so great when fingers and ears collaborate. And though unexpected, thanks also to COVID for teaching me valuable life lessons.

APPENDIX

A. CUTFLOW OF THE NUMBER OF JETS PER EVENT FOR DIFFERENT DATASETS

This section states the MC dataset names used for the derivation of the flavour corrections and flavour uncertainties described in Chapter 6. The names are stated as appearing in the CMS data aggregation system. All the MC samples are obtained from the SUMMER20UL18 data campaign and are present in the JMENANOAOD version of the NANOAOD format. The HERWIG 7 samples were reprocessed with the *HerwigJetPartonBugFix*, a version with a repaired bug to include *Jet_partonFlavour* and *GenJet_partonFlavour* branches.

The QCD samples have the hard process generated by the MADGRAPH 5_aMC@NLO v2.6.1 program [122] and are matched to a parton shower using the MLM matching ($q_{\text{cut}} = 14\,\text{GeV}$). The cross sections for the MADGRAPH+HERWIG 7 sample were tuned to make smooth transitions of H_{T} between the samples, while for MADGRAPH+PYTHIA 8 the cross sections given in the CMS cross sections database were found to directly provide a good matching between the samples.

- /QCD_HT*_TuneCP5_PSWeights_13TeV-madgraph-pythia8/RunIISummer20UL18NanoAODv9-20UL18JMENano_106X_upgrade2018_realistic_v16_L1v1-v1/NANOAODSIM

- /QCD_HT*_TuneCH3_13TeV-madgraphMLM-herwig7/RunIISummer20UL16NanoAODAPVv9-20UL16APVJMENano_HerwigJetPartonBugFix_106X_mcRun2_asymptotic_preVFP_v11-v1/NANOAODSIM ,

where * corresponds to the samples of different jet momentum scalar, H_{T}. The cross sections used to stitch together the different H_{T} bins are given in Table A.1 for the MADGRAPH+HERWIG 7 sample and in Table A.2 for the MADGRAPH+PYTHIA 8 sample.

The p_{T} spectra of the jets from the two QCD MADGRAPH samples, after performing the jet selection as described in Section 6.2.2, are shown in Fig. A.1. This figure also shows the contribution from each of the bins. A smooth transition between the samples is observed. Fig. A.2 (left) shows the H_{T} spectrum of the stitched QCD samples and shows no jumps between the edges of the H_{T} bins.

In addition, a QCD sample generated by standalone PYTHIA 8 at LO is used only for the flavour corrections:

- /QCD_Pt-15to7000_TuneCP5_Flat2018_13TeV_pythia8/RunIISummer20UL18NanoAODv9-20UL18JMENano_106X_upgrade2018_realistic_v16_L1v1-v1/NANOAODSIM .

Table A.1

Cross sections used for the madgraphMLM+HERWIG 7 sample.

H_T bin	Cross section (pb)
HT50to100	56530.0
HT100to200	10801.5
HT200to300	971.85
HT300to500	241.4
HT500to700	25.05
HT700to1000	5.685
HT1000to1500	1.0818
HT1500to2000	0.10904
HT2000toInf	0.021787

Table A.2

Cross sections used for the madgraphMLM+PYTHIA 8 sample.

H_T bin	Cross section (pb)
HT50to100	186100.0
HT100to200	23630.0
HT200to300	1554.0
HT300to500	323.8
HT500to700	30.28
HT700to1000	6.392
HT1000to1500	1.118
HT1500to2000	0.1098
HT2000toInf	0.02193

Fig. A.2 (right) shows that, except for the low p_T bins impacted by the missing contributions from the $H_T < 50\,\text{GeV}$ samples, the weighted PYTHIA 8 sample has a reasonable agreement with the MADGRAPH samples. For flavour corrections the unweighted PYTHIA 8 sample was used, as no significant difference was found in the responses in the relevant p_T range between the weighted and unweighted samples, if selecting only the leading three generated jets.

The $t\bar{t}$ samples have the hard process generated by the hvq programme that is part of POWHEG-Box v2:

- /TTToSemiLepton_TuneCP5_13TeV-powheg-pythia8/RunIISummer20UL18NanoAODv9-JMENano_106X_upgrade2018_realistic_v16_L1v1-v1/NANOAODSIM
- /TTToHadronic_TuneCP5_13TeV-powheg-pythia8/RunIISummer20UL18NanoAODv9-JMENano_106X_upgrade2018_realistic_v16_L1v1-v1/NANOAODSIM
- /TTTo2L2Nu_TuneCP5_13TeV-powheg-pythia8/RunIISummer20UL18NanoAODv9-JMENano_106X_upgrade2018_realistic_v16_L1v1-v1/NANOAODSIM

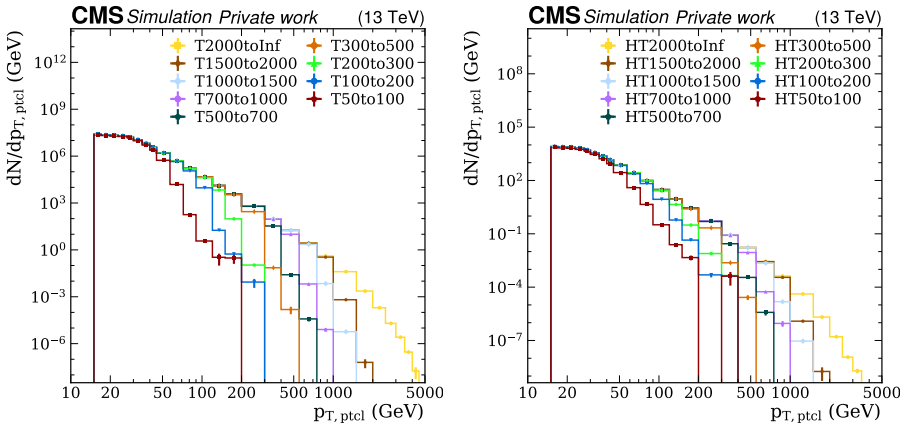

Fig. A.1. The p_T of the AK4 jets passing the selection criteria described in Section 6.2.2 for the QCD sample generated by MADGRAPH + PYTHIA 8 (left) and by MADGRAPH + HERWIG 7 (right). The contributions from each H_T bin are stacked.

- /TT_TuneCH3_13TeV-powheg-herwig7/RunIISummer20UL18NanoAODv9-20UL18JMENano_HerwigJetPartonBugFix_106X_upgrade2018_realistic_v16_L1v1-v1/NANOAODSIM .

The HERWIG 7 $t\bar{t}$ sample is inclusive in the $t\bar{t}$ decay channels while the PYTHIA 8 samples have each channel in each dataset separately.

The Z+jets samples are generated by MADGRAPH 5_aMC@NLO and matched to a parton shower using MLM matching:

- /DYJetsToLL_M-50_TuneCP5_13TeV-madgraphMLM-pythia8/RunIISummer20UL18NanoAODv9-20UL18JMENano_106X_upgrade2018_realistic_v16_L1v1-v1/NANOAODSIM
- /DYJetsToLL_M-50_TuneCH3_13TeV-madgraphMLM-herwig7/RunIISummer20UL18NanoAODv9-20UL18JMENano_HerwigJetPartonBugFix_106X_upgrade2018_realistic_v16_L1v1-v1/NANOAODSIM .

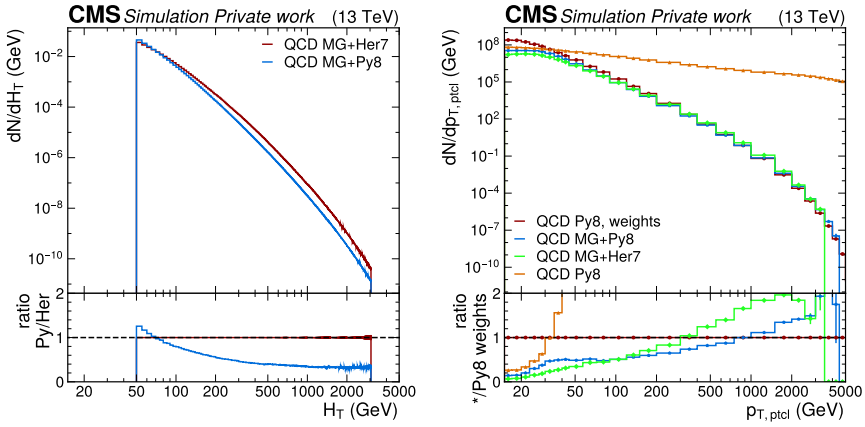

Fig. A.2. The event transverse momentum scalar, H_T, for the stitched QCD samples generated by MADGRAPH +PYTHIA 8 and generated by MADGRAPH +HERWIG 7 (left). Comparison of the p_T spectra of the samples shown in Fig. A.1, as well as the weighted and unweighted QCD samples generated by PYTHIA 8 (right).

B. COMPARISON OF THE MEDIAN RESPONSES BETWEEN THE TOP-PAIR, Z+JETS AND QCD DATA SETS SHOWERED BY THE HERWIG 7 PARTON SHOWER

In this section, we show the jet median response for the samples showered by HERWIG 7 in four different η bins. The results are shown in Fig. B.1.

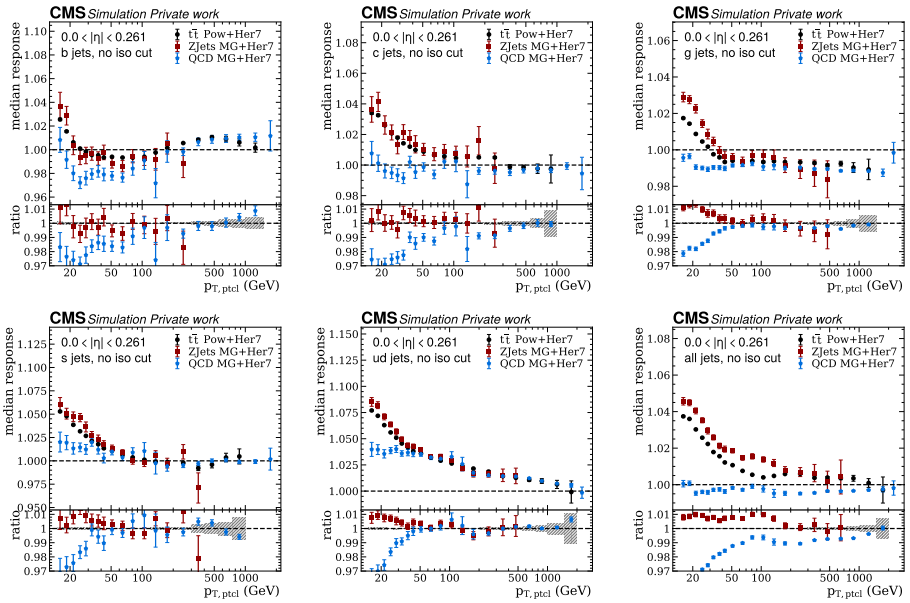

Fig. B.1. Comparison of the inverse median of the jet energy response for three MC physics samples showered by HERWIG 7. Results are shown in the $0.0 < |\eta| < 0.261$ bin for six different jet flavors.

C. THE COMPARISON OF THE FLAVOUR UNCERTAINTIES INCLUDING THE RESULTS AFTER SEPARATING THE LIGHT FLAVOUR INTO UP, DOWN AND STRANGE.

This section contains the results of the flavour uncertainties, including the results after separating the light quark (quark) flavour into uncorrelated uncertainties for up, down, and strange flavour. In Run 1, these separated uncertainties were not obtained. The results are shown in Fig. C.1. A notable difference between the up, down, and strange is seen, with the up having a small uncertainty, not exceeding 0.5 %, while the

down having the largest uncertainty. The strange uncertainty is similar to the inclusive quark uncertainty. The plot also shows how the inclusive QCD uncertainty, which mainly contains gluon jets, decreases with respect to Run 1, while DY stays similar to the Run 1 uncertainty.

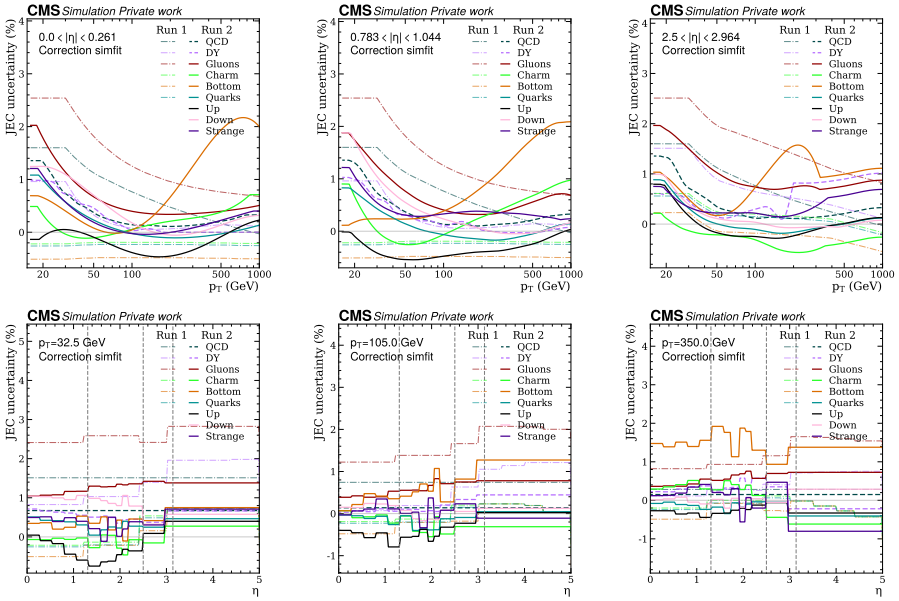

Fig. C.1. Flavour uncertainty as a function of p_{T} for three different η regions (top) and as a function of η for three different p_{T} regions (bottom). The dash-dotted lines show the flavour uncertainties from Run 1. The solid lines show flavour uncertainties for Run 2 for pure flavours and the dashed lines show the flavour uncertainties for Run 2 for the QCD and Z+jet mixes.

D. DATASETS

The datasets used in the analysis presented in Chapter 7 are shown in this section.

Table D.1

Single lepton datasets for Run2 UL16-UL18 data at 13 TeV. The "/MINIAOD" tag at the end of dataset names is skipped for readability.

Dataset	Event count	$\mathcal{L}^{\text{Data}}[\text{fb}^{-1}]$
/SingleMuon/Run2016B-ver2_HIPM_UL2016_MiniAODv2-v2	158 145 722	5.83
/SingleMuon/Run2016C-HIPM_UL2016_MiniAODv2-v2	67 441 308	2.60
/SingleMuon/Run2016D-HIPM_UL2016_MiniAODv2-v2	98 017 996	4.29
/SingleMuon/Run2016E-HIPM_UL2016_MiniAODv2-v2	90 984 718	4.07
/SingleMuon/Run2016F-HIPM_UL2016_MiniAODv2-v2	57 465 359	2.72
/SingleMuon/Run2016F-UL2016_MiniAODv2-v2	8 024 195	0.42
/SingleMuon/Run2016G-UL2016_MiniAODv2-v2	149 916 849	7.65
/SingleMuon/Run2016H-UL2016_MiniAODv2-v2	174 035 164	8.74
/SingleMuon/Run2017B-UL2017_MiniAODv2-v1	136 300 266	4.80
/SingleMuon/Run2017C-UL2017_MiniAODv2-v1	165 652 756	9.57
/SingleMuon/Run2017D-UL2017_MiniAODv2-v1	70 361 660	4.25
/SingleMuon/Run2017E-UL2017_MiniAODv2-v1	154 618 774	9.31
/SingleMuon/Run2017F-UL2017_MiniAODv2-v1	242 140 980	13.54
/SingleMuon/Run2018A-UL2018_MiniAODv2-v3	241 613 524	14.03
/SingleMuon/Run2018B-UL2018_MiniAODv2-v2	119 918 017	7.07
/SingleMuon/Run2018C-UL2018_MiniAODv2-v2	109 986 009	6.90
/SingleMuon/Run2018D-UL2018_MiniAODv2-v3	513 909 894	31.94
$\sum$ Single Muon Data 2016 APV	472 055 103	19.52
$\sum$ Single Muon Data 2016 non-APV	331 976 208	16.81
$\sum$ Single Muon Data 2017	769 074 436	41.48
$\sum$ Single Muon Data 2018	985 427 444	59.83
$\sum$ Single Muon Data Full Run2	2 558 533 191	137.62
/SingleElectron/Run2016B-ver2_HIPM_UL2016_MiniAODv2-v2	246 440 440	5.83
/SingleElectron/Run2016C-HIPM_UL2016_MiniAODv2-v2	97 259 854	2.60
/SingleElectron/Run2016D-HIPM_UL2016_MiniAODv2-v2	148 167 727	4.29
/SingleElectron/Run2016E-HIPM_UL2016_MiniAODv2-v5	117 269 446	4.07
/SingleElectron/Run2016F-HIPM_UL2016_MiniAODv2-v2	61 735 326	2.72
/SingleElectron/Run2016F-UL2016_MiniAODv2-v2	8 858 206	0.42
/SingleElectron/Run2016G-UL2016_MiniAODv2-v2	153 363 109	7.65
/SingleElectron/Run2016H-UL2016_MiniAODv2-v2	129 021 893	8.74
/SingleElectron/Run2017B-UL2017_MiniAODv2-v1	60 537 490	4.80
/SingleElectron/Run2017C-UL2017_MiniAODv2-v1	136 637 888	9.57
/SingleElectron/Run2017D-UL2017_MiniAODv2-v1	51 526 521	4.25
/SingleElectron/Run2017E-UL2017_MiniAODv2-v1	102 122 055	9.31
/SingleElectron/Run2017F-UL2017_MiniAODv2-v1	128 467 223	13.54
/EGamma/Run2018A-UL2018_MiniAODv2-v1	339 013 231	14.03
/EGamma/Run2018B-UL2018_MiniAODv2-v1	153 792 795	7.07
/EGamma/Run2018C-UL2018_MiniAODv2-v1	147 827 904	6.90
/EGamma/Run2018D-UL2018_MiniAODv2-v2	752 524 583	31.94
$\sum$ Single Electron Data 2016 APV	670 872 793	19.52
$\sum$ Single Electron Data 2016 non-APV	291 243 208	16.81
$\sum$ Single Electron Data 2017	479 291 177	41.48
$\sum$ Single Electron Data 2018	1 393 158 513	59.83
$\sum$ Single Electron Data Full Run2	2 834 565 691	137.62

D.1. Baseline samples

Table D.2

List of top quark production baseline samples. The full entries to the datasets as used for CMS data aggregation system are shortened for readability. All the datasets are from 20UL campaign in MINIAODv2. The same detector conditions are used for all the datasets, namely tag `106X_mcRun2_asymptotic_preVFP_v11` for 2016 APV samples, `106X_mcRun2_asymptotic_v17` for 2016 non-APV samples, `106X_mc2017_realistic_v9` for 2017 samples and `106X-upgrade2018_realistic_v16_L1v1` for 2018 samples. All datasets are in CP5 UE tune and showered using PYTHIA 8. In the first rows of each group also the inclusive cross section is snown.

Dataset name	Events				σ [pb]	$\mathcal{L}_{\text{eff}}$[fb^{-1}]			
	16 APV	16 non-APV	17	18		16 APV	16 non-APV	17	18
$t\bar{t}$ samples: Tune CP5 (POWHEG+PYTHIA 8 NLO)					831.8				
TTToSemiLeptonic	132.18 M	144.97 M	355.33 M	478.98 M	365.5	355.8	390.3	948.5	1 282.5
TTTo2L2Nu	37.51 M	43.63 M	106.72 M	146.01 M	88.3	417.7	485.4	1 185.0	1 573.3
TTToHadronic	97.60 M	109.38 M	235.72 M	343.25 M	378.0	253.9	284.7	613.5	864.5
TTW samples: Tune CP5 (MC@NLO FXFX-MADSPIN+PYTHIA 8 NLO)									
TTWJetsToLNu	2.85 M	3.32 M	7.46 M	10.52 M	0.2	3 863.4	4 512.3	10 138.5	14 296.9
TTWJetsToQQ	0.27 M	0.31 M	0.66 M	0.97 M	0.4	186.9	211.5	450.6	663.8
TTZ samples: Tune CP5 (MC@NLO +PYTHIA 8 NLO)									
TTZToLLNuNu_M-10	5.79 M	6.06 M	14.20 M	19.61 M	0.2	5 776.5	6 020.9	14 113.8	19 479.4
TTZToQQ	6.28 M	5.40 M	13.98 M	19.82 M	0.5	3 029.7	2 605.7	6 748.8	9 584.1
single top samples tW channel (not inclusive): Tune CP5 (POWHEG+PYTHIA 8 NLO)					263.7				
ST_tW_top_5f_NoFullyHadronicDecays	3.29 M	3.37 M	8.32 M	12.38 M	21.7	151.9	155.3	383.7	570.8
ST_tW_antitop_5f_NoFullyHadronicDecays	3.18 M	3.65 M	8.33 M	11.78 M	21.7	146.5	168.5	383.9	543.1
single top samples t-channel Tune CP5 (POWHEG-MADSPIN+PYTHIA NLO)									
ST_t-channel_top_4f_inclusiveDecays	55.96 M	63.07 M	129.90 M	178.76 M	136.0	361.2	407.1	815.5	1 151.4
ST_t-channel_antitop_4f_inclusiveDecays	31.02 M	30.61 M	69.92 M	95.83 M	81.0	339.6	335.1	760.3	1 047.6
single top samples s-channel. Tune CP5 (MC@NLO +PYTHIA NLO)									
ST_s-channel_4f_leptonDecays	5.52 M	5.47 M	13.88 M	19.37 M	3.4	695.5	689.9	1 730.1	2 402.0

D.2. Simulated Vector Boson Production

Table D.3

List of HT-binned background samples.

Dataset	Events				σ [pb]	$\mathcal{L}_{\text{eff}}$[fb^{-1}]			
	16 APV	16 non-APV	17	18		16 APV	16 non-APV	17	18
W+Jets samples: Tune CP5 (MADGRAPH-MLM+PYTHIA LO)									
WJetsToLNu_HT-70To100	16.93 M	19.44 M	44.74 M	66.57 M	1 272.0	13.3	15.3	34.8	51.8
WJetsToLNu_HT-100To200	21.73 M	19.75 M	47.42 M	51.54 M	1 254.0	17.3	15.8	37.8	41.1
WJetsToLNu_HT-200To400	17.87 M	15.07 M	42.60 M	58.33 M	336.2	53.2	44.8	126.7	173.5
WJetsToLNu_HT-400To600	2.47 M	2.12 M	5.47 M	7.44 M	45.2	54.5	46.8	114.5	164.5
WJetsToLNu_HT-600To800	2.34 M	2.25 M	5.55 M	7.72 M	11.0	213.1	204.7	504.1	701.7
WJetsToLNu_HT-800To1200	2.51 M	2.13 M	5.09 M	7.31 M	4.9	510.0	433.1	1 033.4	1 484.1
WJetsToLNu_HT-1200To2500	2.12 M	2.09 M	4.96 M	6.48 M	1.2	1 833.9	1 808.4	4 213.5	5 606.8
WJetsToLNu_HT-2500ToInf	0.81 M	0.71 M	1.19 M	2.10 M	0.03	30 840.9	27 060.0	45 221.2	80 001.8
DY+jets samples: Tune CP5 (MADGRAPH-MLM+PYTHIA 8 LO)									
DYJetsToLL_M-10to50	25.80 M	23.71 M	68.48 M	99.29 M	18 610.0	1.4	1.3	3.7	5.3
DYJetsToLL_M-50_HT-70to100	6.72 M	5.89 M	12.21 M	17.00 M	159.0	48.1	42.1	76.7	106.9
DYJetsToLL_M-50_HT-100to200	9.57 M	8.32 M	18.96 M	26.20 M	159.5	68.2	59.3	118.8	164.2
DYJetsToLL_M-50_HT-200to400	5.86 M	5.65 M	12.51 M	18.46 M	43.6	152.8	147.3	286.8	401.7
DYJetsToLL_M-50_HT-400to600	2.72 M	2.49 M	5.54 M	8.91 M	5.9	521.0	477.7	935.1	1 502.7
DYJetsToLL_M-50_HT-600to800	2.68 M	2.30 M	5.28 M	7.04 M	1.4	2 116.5	1 815.2	3 664.8	4 885.1
DYJetsToLL_M-50_HT-800to1200	2.41 M	2.39 M	4.51 M	6.68 M	0.6	4 244.9	4 214.7	6 980.0	10 342.5
DYJetsToLL_M-50_HT-1200to2500	2.19 M	1.97 M	4.80 M	6.17 M	0.2	16 451.3	14 807.3	29 203.5	40 441.1
DYJetsToLL_M-50_HT-2500toInf	0.72 M	0.70 M	1.48 M	1.98 M	0.003	241 514.6	233 281.2	435 307.9	552 632.9

D.3. Simulated QCD Multijet Production

Table D.4

List of QCD background samples.

Dataset	Events				σ [pb]	$\mathcal{L}_{\text{eff}}$ [fb^{-1}]				$\mathcal{L}_{\text{eff}}$ [fb^{-1}]			
	16 APV	16 non-APV	17	18		16 APV	16 non-APV	17	18	16 APV	16 non-APV	17	18
QCD Muon Enriched samples: Tune CP5 (PYTHIA 8 LO)													
QCD_Pt-15To20_MuEnrichedPt5													
QCD_Pt-20To30_MuEnrichedPt5	-	-	64.34 M	60.64 M	3 987 854.9	-	-	0.025	0.024	-	-	0.645	0.635
QCD_Pt-30To50_MuEnrichedPt5	28.66 M	35.47 M	58.36 M	58.63 M	1 368 000.0	0.024	0.026	0.043	0.043	0.419	0.519	1.145	0.366
QCD_Pt-50To80_MuEnrichedPt5	19.72 M	21.49 M	40.38 M	40.02 M	377 800.0	0.030	0.021	0.107	0.105	1.044	1.138	1.927	1.941
QCD_Pt-80To120_MuEnrichedPt5	21.98 M	22.01 M	45.98 M	45.57 M	88 490.0	0.248	0.249	0.516	0.509	8.280	8.551	10.446	11.231
QCD_Pt-120To170_MuEnrichedPt5	19.14 M	19.77 M	39.39 M	39.11 M	21 190.0	0.903	0.933	1.852	1.846	24.452	27.109	36.141	37.835
QCD_Pt-170To300_MuEnrichedPt5	34.29 M	34.29 M	73.07 M	71.93 M	7 039.0	4.871	4.872	10.373	10.147	140.516	135.836	157.025	164.137
QCD_Pt-300To470_MuEnrichedPt5	24.94 M	29.91 M	58.69 M	58.95 M	620.5	40.192	48.201	94.501	94.111	941.347	1 098.228	1 243.632	1 246.059
QCD_Pt-470To600_MuEnrichedPt5	19.70 M	19.77 M	39.49 M	38.45 M	59.0	333.762	335.053	668.301	636.769	6 800.729	5 943.627	8 685.195	7 552.609
QCD_Pt-600To800_MuEnrichedPt5	19.60 M	18.76 M	39.32 M	38.41 M	18.2	1 077.450	1 031.508	2 140.579	2 095.289	18 420.484	17 717.800	22 567.194	23 346.524
QCD_Pt-800To1000_MuEnrichedPt5	39.09 M	38.92 M	78.17 M	78.94 M	3.3	11 944.077	11 891.698	23 817.427	24 068.812	168 828.131	184 792.157	247 465.689	231 835.238
QCD_Pt-1000_MuEnrichedPt5	13.66 M	14.20 M	27.48 M	27.43 M	1.1	12 672.541	13 170.272	25 289.228	25 196.572	193 484.911	194 130.801	220 193.399	223 171.767
QCD EM Enriched samples: Tune CP5 (PYTHIA 8 LO)													
QCD_Pt-30to50_EMEnriched	4.36 M	4.35 M	8.78 M	8.57 M	6 418 000.0	0.001	0.001	0.001	0.001	0.453	0.452	0.878	0.891
QCD_Pt-50to80_EMEnriched	5.44 M	5.44 M	10.21 M	10.52 M	1 987 000.0	0.037	0.003	0.005	0.005	1.369	1.370	2.528	2.648
QCD_Pt-80to120_EMEnriched	4.85 M	4.80 M	9.62 M	9.47 M	366 100.0	0.013	0.013	0.026	0.026	6.620	6.562	12.650	12.820
QCD_Pt-120to170_EMEnriched	4.85 M	5.01 M	9.90 M	9.68 M	66 520.0	0.083	0.038	0.146	0.145	36.475	37.638	50.113	48.982
QCD_Pt-170to300_EMEnriched	1.86 M	1.86 M	3.68 M	3.71 M	16 550.0	0.070	0.112	0.222	0.224	56.056	20.463	51.161	68.844
QCD_Pt-300toInf_EMEnriched	1.14 M	1.14 M	2.21 M	2.22 M	1 099.0	1.037	1.036	2.015	2.016	147.543	115.836	262.584	366.849
QCD bcToE (b/c to electron) samples: Tune CP5 (PYTHIA 8 LO)													
QCD_Pt_20to30_bcToE	-	-	15.24 M	15.36 M	305 400.0	-	-	0.046	0.046	-	-	30.935	30.935
QCD_Pt_30to80_bcToE	7.97 M	7.71 M	15.24 M	15.36 M	362 300 000.0	0.022	0.229	0.042	0.042	11.047	10.696	21.129	2.571
QCD_Pt_80to170_bcToE	7.69 M	7.88 M	15.57 M	15.19 M	33 700 000.0	0.227	0.233	0.436	0.449	47.605	32.347	98.169	61.121
QCD_Pt_170to250_bcToE	7.34 M	7.86 M	15.50 M	15.74 M	2 125 000.0	3.451	3.695	7.174	7.340	427.009	426.165	1 123.094	813.421
QCD_Pt_250toInf_bcToE	6.86 M	8.15 M	15.56 M	15.77 M	562 500.0	12.179	14.481	27.483	28.007	1 164.631	988.823	2 516.810	2 082.436

E. THE COMPARISON OF THE FITTED TOP QUARK MASS FOR DIFFERENT DECAY CHANNELS

This appendix shows the distributions of the hadronically decaying fit top-quark mass, m_t^{fit} using the WMassDeltaTopMass as in Fig. 7.14 but split into all the different decay channels and years.

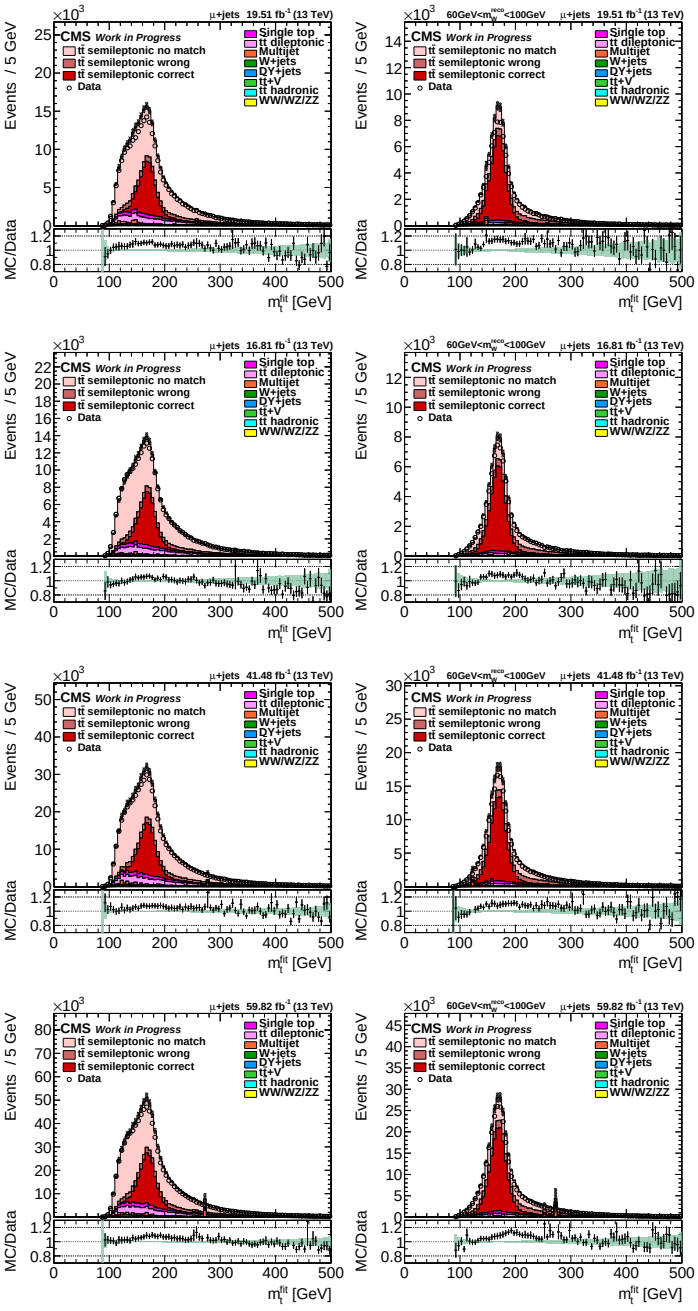

Fig. E.1. The fit top quark mass before (left) and after (right) the W boson mass requirement for the single muon channel. From top to bottom 2016, 2016APV, 2017, and 2018 are shown.

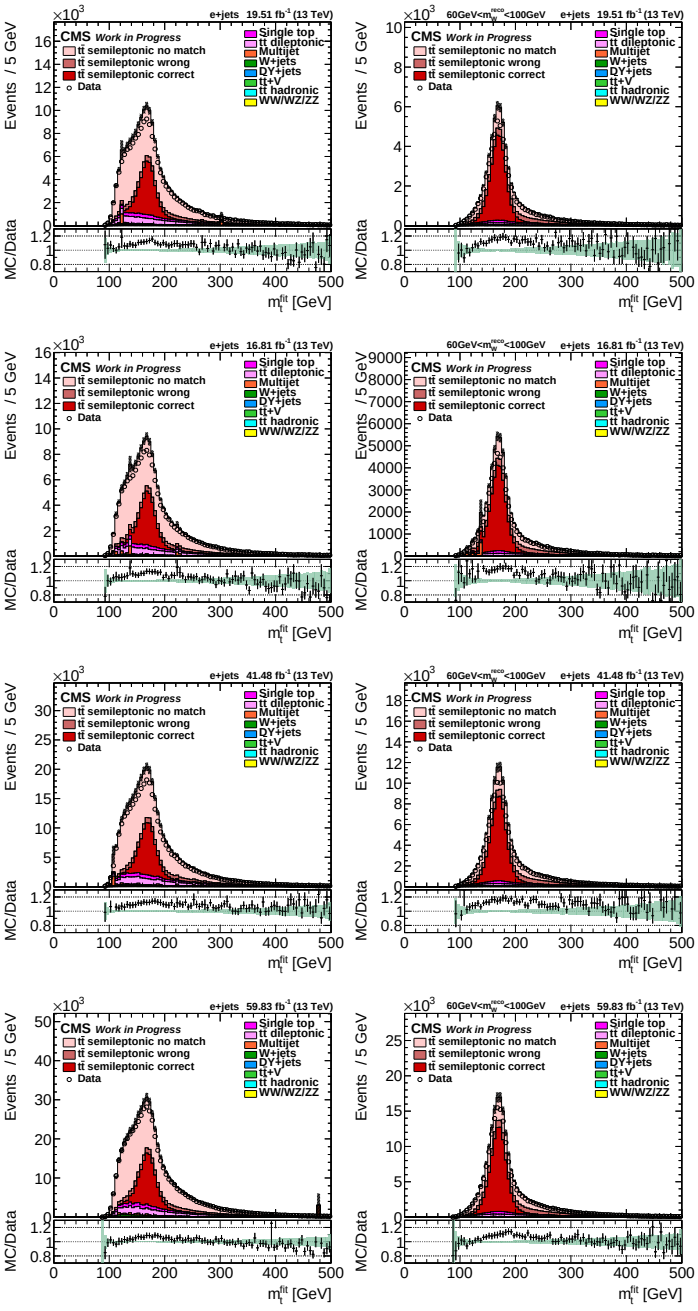

Fig. E.2. The fit top quark mass before (left) and after (right) the W boson mass requirement for the single electron channel. From top to bottom 2016, 2016APV, 2017, and 2018 are shown.

F. IMPACTS OF IMPORTANT SYSTEMATIC VARIATIONS

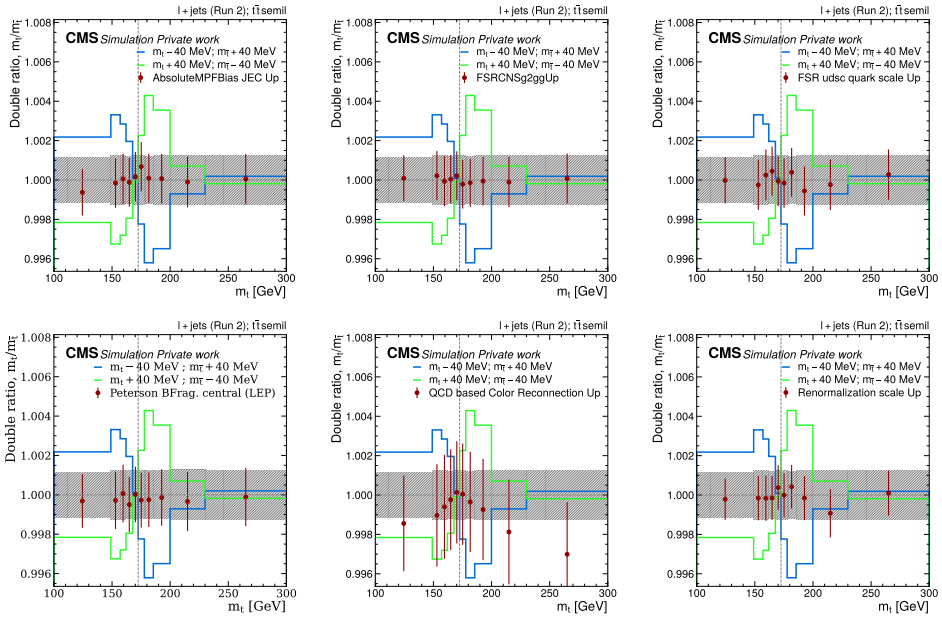

Fig. F.1. The double ratio (var(m_t)/central(m_t))/(var($m_{\bar{t}}$)/central($m_{\bar{t}}$)) for MPF bias JEC, FSR CNS gluon to gluon, FSR light quark scale variation (top) and Peterson bfragmentation, QCD-bases CR and renormalization scale variation (bottom). Results are shown for the whole Run 2 l+jets dataset. QCD-based CR variation is obtained from a separate MC dataset and is smoothed, while others are obtained as weights. The default Δm_t variations shown in Fig. 7.19 are scaled by 1/5 to enhance the visual comparison.

This section shows the double rations as introduced in Section 7.6 for the sub-leading systematic variations not shown already in Section 7.6.2.

G. IMPACT OF THE FSR GLUON SCALE VARIATION ON THE TOP QUARK MASS DISTRIBUTION

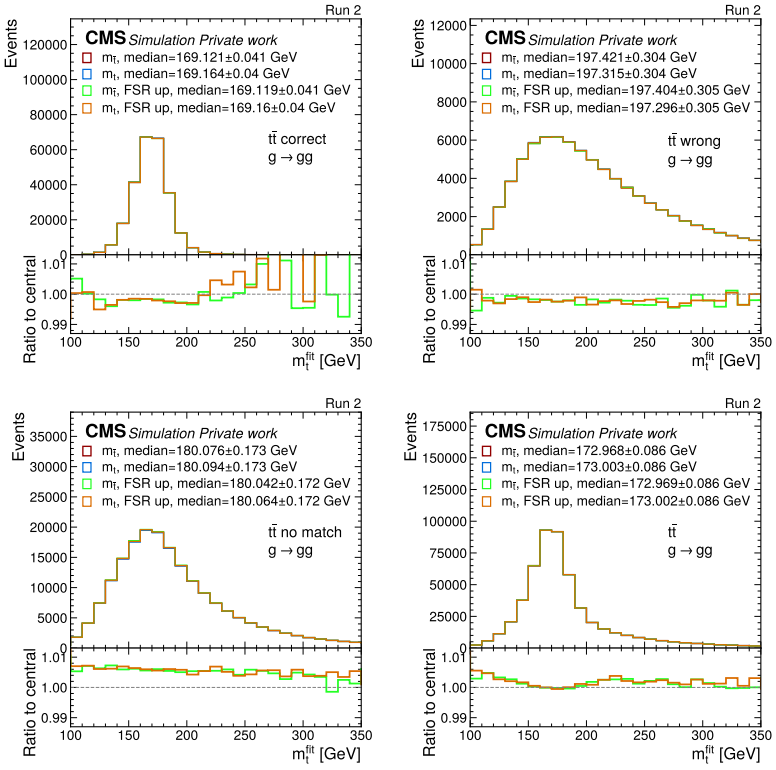

Fig. G.1. Impact of the FSR $g \to gg$ variation on the top quark and antiquark mass distribution in $t\bar{t}$ events for the correct (top left), wrong (top right), no match (bottom left) permutations and for all the permutations (bottom right).

This section shows the dependence of different FSR variations on the events yields in the $t\bar{t}$ event simulation. Fig. G.1 shows the impact of the FSR $g \to gg$ variation on the top quark mass distribution in the $t\bar{t}$ events with correct, wrong, and no match permutations generated with $m_t = 172.5\,\text{GeV}$ and $\Delta m_t = 0$. The median of the distributions is also shown. A slight asymmetry in the given variation is observed, shifting $m_{\bar{t}}$ more towards higher values than m_t. This is probably caused by small variations in the MC weights and amplified by the charge asymmetry of the $t\bar{t}$ events. However, the shifts are within the error margins of the medians. The variation predominantly affects the no match permutations, as for these permutations, an energetic gluon originating from FSR is frequently misidentified as the light jet associated with the W boson candidate.

The difference Δm_t in the median values in the no match events is increased from 18 MeV to 22 MeV. Since the no match category presents 32% of event yields in simulation

(see Fig. 7.4) and is pulled by 1.8σ (see Fig. 7.25), such a shift could correspond to the impact of 5 MeV seen in Fig. 7.25. The double ratios of these distributions in the binning used in the Δm_t measurement are shown in Fig. 7.20 and no clear effect can be seen, except for larger fluctuations in the two most central bins, which are particularly sensitive to the Δm_t variation.

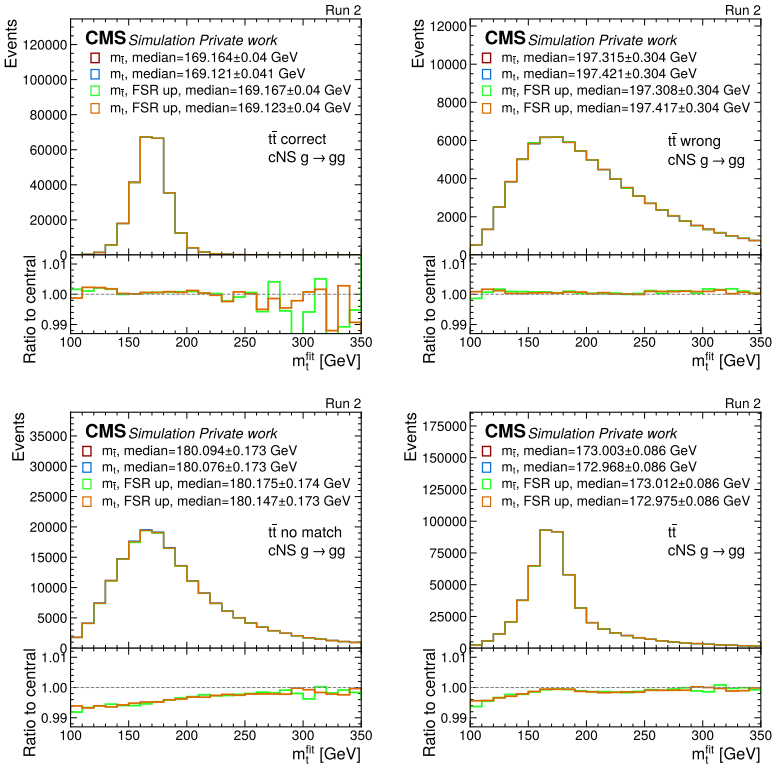

Fig. G.2. Impact of the cNS FSR $g \to gg$ variation on the top quark and antiquark mass distribution in $t\bar{t}$ events for the correct (top left), wrong (top right), no match (bottom left) permutations and for all the permutations (bottom right).

Similar plots for the cNS $g \to gg$ FSR variation are shown in Fig. G.2. They present a similar pattern as for the $g \to gg$ variation, mainly impacting the no match permutations and also presenting a slight asymmetry for m_t vs $m_{\bar{t}}$.

References

[1] C. E. Gerber, "LHC Highlights and Prospects", doi:10.23730/CYRSP-2021-002.161, arXiv:1909.10919. 38 pages, 31 figures, Lecture notes for the 10th CERN Latin-American School of High-Energy Physics (CLASHEP2019), 13 to 26 March 2019 in Villa General Belgrano, Cordoba Province, Argentina.

[2] CMS Collaboration, "Stairway to discovery: A report on the CMS programme of cross section measurements from millibarns to femtobarns", May 2024, doi:10.48550/arXiv.2405.18661.

[3] ATLAS Collaboration, "Summary plots from the ATLAS Standard Model physics group", 2024, https://atlas.web.cern.ch/Atlas/GROUPS/PHYSICS/CombinedSummaryPlots/SM/index.html.

[4] L. Canetti, M. Drewes, and M. Shaposhnikov, "Matter and Antimatter in the Universe", *New J. Phys.*, **14** (September 2012) 095012, doi:10.1088/1367-2630/14/9/095012, arXiv:1204.4186.

[5] SNO Collaboration et al., "Direct Evidence for Neutrino Flavor Transformation from Neutral-Current Interactions in the Sudbury Neutrino Observatory", *Phys. Rev. Lett.*, **89** (June 2002) 011301, doi:10.1103/PhysRevLett.89.011301.

[6] The Super-Kamiokande Collaboration, "Evidence for oscillation of atmospheric neutrinos", *Phys. Rev. Lett.*, **81** (August 1998) 1562–1567, doi:10.1103/PhysRevLett.81.1562, arXiv:hep-ex/9807003.

[7] G. Bertone, "History of dark matter", *Rev. Mod. Phys.*, **90** (2018),, no. 4, doi:10.1103/RevModPhys.90.045002.

[8] J. G. de Swart, G. Bertone, and J. van Dongen, "How dark matter came to matter", *Nat Astron*, **1** (March 2017) 1–9, doi:10.1038/s41550-017-0059.

[9] C. Rovelli, "Notes for a brief history of quantum gravity", January 2001, doi:10.48550/arXiv.gr-qc/0006061.

[10] A. Zee, "Quantum Field Theory in a Nutshell". Princeton University Press, second edition edition, 2010. ISBN 978-0-691-14034-6, https://www.amazon.com/Quantum-Field-Theory-Nutshell-nutshell/dp/0691140340.

[11] ATLAS Collaboration, "ATLAS Run 1 searches for direct pair production of third-generation squarks at the Large Hadron Collider", *Eur. Phys. J. C*, **75** (October 2015) 510, doi:10.1140/epjc/s10052-015-3726-9, arXiv:1506.08616.

[12] CMS Collaboration, "Search for single production of scalar leptoquarks in proton-proton collisions at $\sqrt{s} = 8\ TeV$", *Phys. Rev. D*, **93** (2016)„ no. 3, 032005, doi:10.1103/PhysRevD.93.032005, arXiv:1509.03750. [Erratum: Phys.Rev.D 95, 039906 (2017)].

[13] C. P. Salemi et al., "Search for Low-Mass Axion Dark Matter with ABRACADABRA-10 cm", *Phys. Rev. Lett.*, **127** (2021)„ no. 8, 081801, doi:10.1103/PhysRevLett.127.081801, arXiv:2102.06722.

[14] A. Gómez-Bañón, K. Bartnick, K. Springmann, and J. A. Pons, "Constraining light QCD axions with isolated neutron star cooling", arXiv:2408.07740.

[15] J. S. Bell, "Time reversal in field theory", *Proc. R. Soc. Lond.*, **A** (1955)„ no. 231, 479–495.

[16] R. F. Streater and A. S. Wightman, "PCT, Spin and Statistics, and All That". Princeton University Pressrsity, 2001. ISBN 978-0-691-07062-9, https://press.princeton.edu/books/paperback/9780691070629/pct-spin-and-statistics-and-all-that.

[17] V. N. Gribov and J. Nyiri, "Quantum electrodynamics: Gribov lectures on theoretical physics", volume 13. Cambridge University Press, 7 2005. ISBN 978-0-521-67569-7.

[18] D. Colladay and V. A. Kostelecky, "CPT violation and the standard model", *Phys. Rev. D*, **55** (1997), 6760–6774, doi:10.1103/PhysRevD.55.6760.

[19] S. Mukohyama and S. C. Park, "Ghost condensation and *CPT* violation in neutrino sector", *Physics Letters B*, **696** (February 2011) 505–508, doi:10.1016/j.physletb.2011.01.014.

[20] G. Barenboim and J. Lykken, "A model of CPT violation for neutrinos", *Physics Letters B*, **554** (February 2003) 73–80, doi:10.1016/S0370-2693(02)03262-8, arXiv:hep-ph/0210411.

[21] Particle Data Group Collaboration, "Review of particle physics", *Phys. Rev. D*, **110** (2024)„ no. 3, 030001, doi:10.1103/PhysRevD.110.030001.

[22] CPLEAR Collaboration, "K0 anti-K0 mass and decay width differences: CPLEAR evaluation", *Phys. Lett. B*, **471** (1999), 332–338, doi:10.1016/S0370-2693(99)01333-7.

[23] A. Belyaev et al., "Probing CPT invariance with top quarks at the LHC", November 2024, doi:10.48550/arXiv.2405.12162.

[24] CMS Collaboration, "Searches for violation of Lorentz invariance in top quark pair production using dilepton events in 13 TeV proton-proton collisions", *Phys. Lett. B*, **857** (2024), 138979, doi:10.1016/j.physletb.2024.138979, arXiv:2405.14757.

[25] M. S. Fee et al., "Measurement of the positronium 1 S-31-2 S-31 interval by continuous-wave two-photon excitation", *Phys. Rev. A*, **48** (1993), 192–219, doi:10.1103/PhysRevA.48.192.

[26] Belle Collaboration, "Measurement of the mass of the tau-lepton and an upper limit on the mass difference between tau+ and tau-", *Phys. Rev. Lett.*, **99** (2007), 011801, doi:10.1103/PhysRevLett.99.011801, arXiv:hep-ex/0608046.

[27] D. S. Ayers et al., "Measurements of the lifetimes of positive and negative pions", *Phys. Rev. D*, **3** (1971), 1051–1063, doi:10.1103/PhysRevD.3.1051.

[28] DELPHI Collaboration, "Masses, Lifetimes and Production Rates of Xi- and anti-Xi+ at LEP 1", *Phys. Lett. B*, **639** (2006), 179–191, doi:10.1016/j.physletb.2006.06.029, arXiv:hep-ex/0606030.

[29] E756 Collaboration, "Measurement of the Properties of the $\bar{\Omega}^+$ and Ω^- hyperons", *Phys. Rev. D*, **58** (1998), 072002, doi:10.1103/PhysRevD.58.072002.

[30] CMS Collaboration, "Measurement of the mass difference between top quark and antiquark in pp collisions at $\sqrt{s} = 8$ TeV", *Phys. Lett. B*, **770** (2017), 50–71, doi:10.1016/j.physletb.2017.04.028, arXiv:1610.09551.

[31] CMS Collaboration, "Measurement of the Mass Difference between Top and Antitop Quarks", *JHEP*, **06** (2012), 109, doi:10.1007/JHEP06(2012)109, arXiv:1204.2807.

[32] CMS Collaboration, "Measurement of the top quark mass using events with a single reconstructed top quark in pp collisions at $\sqrt{s} = 13$ TeV", *JHEP*, **12** (2021), 161, doi:10.1007/JHEP12(2021)161, arXiv:2108.10407.

[33] ATLAS Collaboration, "Measurement of the mass difference between top and anti-top quarks in pp collisions at $\sqrt{s} = 7$ TeV using the ATLAS detector", *Phys. Lett. B*, **728** (2014), 363–379, doi:10.1016/j.physletb.2013.12.010, arXiv:1310.6527.

[34] CDF Collaboration, "Measurement of the Mass Difference between Top and Anti-top Quarks", *Phys. Rev. D*, **87** (2013)„ no. 5, 052013, doi:10.1103/PhysRevD.87.052013, arXiv:1210.6131.

[35] D0 Collaboration, "Direct measurement of the mass difference between top and antitop quarks", *Phys. Rev. D*, **84** (2011), 052005, doi:10.1103/PhysRevD.84.052005, arXiv:1106.2063.

[36] CDF Collaboration, "Measurement of the Mass Difference between t and $\bar{t}$ Quarks", *Phys. Rev. Lett.*, **106** (2011), 152001, doi:10.1103/PhysRevLett.106.152001, arXiv:1103.2782.

[37] D0 Collaboration, "Direct measurement of the mass difference between top and antitop quarks", *Phys. Rev. Lett.*, **103** (2009), 132001, doi:10.1103/PhysRevLett.103.132001, arXiv:0906.1172.

[38] ATLAS and CMS Collaboration, "Improved Common $t\bar{t}$ Monte-Carlo Settings for ATLAS and CMS", technical report, CERN, Geneva, 2023, cds:2861366.

[39] ATLAS Collaboration, "Improved Common $t\bar{t}$ Monte-Carlo Settings for ATLAS and CMS", technical report, CERN, Geneva, 2023, cds:2862524.

[40] A. Potrebko, "Flavor dependent (L5) MC truth jet energy corrections and flavor uncertainties in Run 2", Technical Report CMS AN-2023/074, CERN, 2024.

[41] A. Potrebko, M. Seidel, M. Mulders, and K. Dreimanis, "Measurement of the mass difference between the top quark and antiquark in $t\bar{t}$ events with lepton+jets final states in 13 TeV proton-proton collisions", Technical Report CMS AN-2023/074, 2025.

[42] J. J. Thomson, "XL. Cathode Rays", *Lond. Edinb. Dublin Philos. Mag. J. Sci.*, **44** (October 1897) 293–316, doi:10.1080/14786449708621070.

[43] ATLAS Collaboration, "Observation of a new particle in the search for the Standard Model Higgs boson with the ATLAS detector at the LHC", *Phys. Lett. B*, **716** (2012), 1–29, doi:10.1016/j.physletb.2012.08.020, arXiv:1207.7214.

[44] CMS Collaboration, "Observation of a New Boson at a Mass of 125 GeV with the CMS Experiment at the LHC", *Phys. Lett. B*, **716** (2012), 30–61, doi:10.1016/j.physletb.2012.08.021, arXiv:1207.7235.

[45] LHCb Collaboration, "Observation of the resonant character of the $Z(4430)^-$ state", *Phys. Rev. Lett.*, **112** (2014),, no. 22, 222002, doi:10.1103/PhysRevLett.112.222002, arXiv:1404.1903.

[46] LHCb Collaboration, "Observation of $J/\psi p$ Resonances Consistent with Pentaquark States in $\Lambda_b^0 \to J/\psi K^- p$ Decays", *Phys. Rev. Lett.*, **115** (2015), 072001, doi:10.1103/PhysRevLett.115.072001, arXiv:1507.03414.

[47] M. E. Peskin and D. V. Schroeder, "An Introduction to Quantum Field Theory". Addison-Wesley, Reading, USA, 1995. ISBN 978-0-201-50397-5.

[48] G. Kane, "Modern Elementary Particle Physics". Cambridge University Press, February 2017. doi:10.1017/9781316691434, ISBN 978-1-107-16508-3.

[49] J. J. Sakurai and J. Napolitano, "Modern Quantum Mechanics". Cambridge University Press, 2 edition, 2017. doi:10.1017/9781108499996, ISBN 978-1-108-49999-6.

[50] T. Kinoshita, "Mass Singularities of Feynman Amplitudes", *Journal of Mathematical Physics*, **3** (July 1962) 650–677, doi:10.1063/1.1724268.

[51] T. D. Lee and M. Nauenberg, "Degenerate Systems and Mass Singularities", *Phys. Rev.*, **133** (March 1964) B1549–B1562, doi:10.1103/PhysRev.133.B1549.

[52] E. Noether, "Invariante variationsprobleme", *Nachrichten von der Gesellschaft der Wissenschaften zu Göttingen, Mathematisch-Physikalische Klasse*, **1918** (1918), 235–257.

[53] C. S. Wu et al., "Experimental Test of Parity Conservation in Beta Decay", *Phys. Rev.*, **105** (February 1957) 1413–1415, doi:10.1103/PhysRev.105.1413.

[54] J. W. Blanchard et al., "Molecular parity nonconservation in nuclear spin couplings", *Phys. Rev. Res.*, **2** (Jun 2020) 023258, doi:10.1103/PhysRevResearch.2.023258.

[55] M.-A. Bouchiat, "Atomic Parity Violation. Early days, present results, prospects", *Il Nuovo Cimento C*, **35** (September 2012) 78–84, doi:10.1393/ncc/i2012-11269-6, arXiv:1111.2172.

[56] J. H. Christenson, J. W. Cronin, V. L. Fitch, and R. Turlay, "Evidence for the 2π Decay of the K_2^0 Meson", *Phys. Rev. Lett.*, **13** (1964), 138–140, doi:10.1103/PhysRevLett.13.138.

[57] Particle Data Group Collaboration, "Review of particle physics", *PTEP*, **2022** (2022), 083C01, doi:10.1093/ptep/ptac097.

[58] H. Burkhardt et al., "First evidence for direct *CP* violation", *Physics Letters B*, **206** (May 1988) 169–176, doi:10.1016/0370-2693(88)91282-8.

[59] G. D. Barr et al., "A new measurement of direct CP violation in the neutral kaon system", *Physics Letters B*, **317** (November 1993) 233–242, doi:10.1016/0370-2693(93)91599-I.

[60] LHCb Collaboration, "First observation of CP violation in the decays of B_s^0 mesons", *Phys. Rev. Lett.*, **110** (2013),, no. 22, 221601, doi:10.1103/PhysRevLett.110.221601, arXiv:1304.6173.

[61] LHCb Collaboration, "Measurement of the Time-Integrated CP Asymmetry in D0→K-K+ Decays", *Phys. Rev. Lett.*, **131** (2023),, no. 9, 091802, doi:10.1103/PhysRevLett.131.091802, arXiv:2209.03179.

[62] R. D. Peccei and H. R. Quinn, "CP conservation in the presence of pseudoparticles", *Phys. Rev. Lett.*, **38** (Jun 1977) 1440–1443, doi:10.1103/PhysRevLett.38.1440.

[63] S. Weinberg, "A new light boson?", *Phys. Rev. Lett.*, **40** (Jan 1978) 223–226, doi:10.1103/PhysRevLett.40.223.

[64] D. Colladay and A. Kostelecky, "Lorentz-Violating Extension of the Standard Model", *Phys. Rev. D*, **58** (October 1998) 116002, doi:10.1103/PhysRevD.58.116002, arXiv:hep-ph/9809521.

[65] S. L. Glashow, "The renormalizability of vector meson interactions", *Nuclear Physics*, **10** (February 1959) 107–117, doi:10.1016/0029-5582(59)90196-8.

[66] A. Salam and J. C. Ward, "Weak and electromagnetic interactions", *Nuovo Cim*, **11** (February 1959) 568–577, doi:10.1007/BF02726525.

[67] S. Weinberg, "A model of leptons", *Phys. Rev. Lett.*, **19** (Nov 1967) 1264–1266, doi:10.1103/PhysRevLett.19.1264.

[68] G. 't Hooft and M. J. G. Veltman, "Regularization and Renormalization of Gauge Fields", *Nucl. Phys. B*, **44** (1972), 189–213, doi:10.1016/0550-3213(72)90279-9.

[69] F. Englert, "Broken Symmetry and the Mass of Gauge Vector Mesons", *Phys. Rev. Lett.*, **13** (1964),, no. 9, 321–323, doi:10.1103/PhysRevLett.13.321.

[70] P. W. Higgs, "Broken Symmetries and the Masses of Gauge Bosons", *Phys. Rev. Lett.*, **13** (1964),, no. 16, 508–509, doi:10.1103/PhysRevLett.13.508.

[71] G. S. Guralnik, "Global Conservation Laws and Massless Particles", *Phys. Rev. Lett.*, **13** (1964),, no. 20, 585–587, doi:10.1103/PhysRevLett.13.585.

[72] L. Cruz, "The higgs profile in the standard model and beyond", *Revista Mexicana de Física*, **65** (09 2019) 419, doi:10.31349/RevMexFis.65.419.

[73] M. D'Onofrio and K. Rummukainen, "The Standard Model cross-over on the lattice", *Phys. Rev. D*, **93** (January 2016) 025003, doi:10.1103/PhysRevD.93.025003, arXiv:1508.07161.

[74] H. E. Haber, "Introductory low-energy supersymmetry", in *Theoretical Advanced Study Institute (TASI 92): From Black Holes and Strings to Particles*, pp. 589–686. 4 1993. arXiv:hep-ph/9306207.

[75] Y. Dokshitzer, V. Khoze, A. Mueller, and S. Troyan, "Basics of Perturbative QCD". Editions Frontières, 1991. ISBN 2-86332-101-3, http://www.lpthe.jussieu.fr/~yuri/BPQCD/BPQCD-print.pdf.

[76] T. Stelzer and S. Willenbrock, "Spin correlation in top-quark production at hadron colliders", *Physics Letters B*, **374** (5 1996) 169–172, doi:10.1016/0370-2693(96)00178-5.

[77] CMS Collaboration, "Observation of quantum entanglement in top quark pair production in proton–proton collisions at $\sqrt{s} = 13$ TeV", *Rept. Prog. Phys.*, **87** (2024),, no. 11, 117801, doi:10.1088/1361-6633/ad7e4d, arXiv:2406.03976.

[78] S. J. Parke, "Top quark spin correlations - theory", *Nuovo Cimento della Societa Italiana di Fisica C*, **35** (2 2012) 111–114, doi:10.1393/ncc/i2012-11229-2.

[79] CMS Collaboration, "Measurement of the $\mathrm{t\bar{t}}$ charge asymmetry in events with highly Lorentz-boosted top quarks in pp collisions at $\sqrt{s} = 13\,\text{TeV}$", *Phys. Lett. B*, **846** (2023), 137703, doi:10.1016/j.physletb.2023.137703, arXiv:2208.02751.

[80] G. Degrassi et al., "Higgs mass and vacuum stability in the Standard Model at NNLO", *J. High Energ. Phys.*, **2012** (August 2012) 98, doi:10.1007/JHEP08(2012)098, arXiv:1205.6497.

[81] F. Bezrukov, M. Y. Kalmykov, B. A. Kniehl, and M. Shaposhnikov, "Higgs boson mass and new physics", *J. High Energ. Phys.*, **2012** (October 2012) 140, doi:10.1007/JHEP10(2012)140, arXiv:1205.2893.

[82] M. Baak et al., "The global electroweak fit at NNLO and prospects for the LHC and ILC", *Eur. Phys. J. C*, **74** (September 2014) 3046, doi:10.1140/epjc/s10052-014-3046-5, arXiv:1407.3792.

[83] T. A. Collaboration et al., "Electroweak Measurements in Electron-Positron Collisions at W-Boson-Pair Energies at LEP", *Physics Reports*, **532** (November 2013) 119–244, doi:10.1016/j.physrep.2013.07.004, arXiv:1302.3415.

[84] M. Baak et al., "The Electroweak Fit of the Standard Model after the Discovery of a New Boson at the LHC", *Eur. Phys. J. C*, **72** (November 2012) 2205, doi:10.1140/epjc/s10052-012-2205-9, arXiv:1209.2716.

[85] P. Nason, "The Top Mass in Hadronic Collisions", January 2018, doi:10.48550/arXiv.1712.02796.

[86] J. Kieseler, K. Lipka, and S.-O. Moch, "Calibration of the Top-Quark Monte-Carlo Mass", *Phys. Rev. Lett.*, **116** (April 2016) 162001, doi:10.1103/PhysRevLett.116.162001, arXiv:1511.00841.

[87] P. Marquard, A. V. Smirnov, V. A. Smirnov, and M. Steinhauser, "Quark Mass Relations to Four-Loop Order in Perturbative QCD", *Phys. Rev. Lett.*, **114** (2015),, no. 14, 142002, doi:10.1103/PhysRevLett.114.142002, arXiv:1502.01030.

[88] A. H. Hoang and I. W. Stewart, "Top Mass Measurements from Jets and the Tevatron Top-Quark Mass", *Nuclear Physics B - Proceedings Supplements*, **185** (December 2008) 220–226, doi:10.1016/j.nuclphysbps.2008.10.028, arXiv:0808.0222.

[89] M. Butenschoen et al., "Top quark mass calibration for Monte-Carlo event generators", *PoS*, **DIS2016** (2016), 153, doi:10.22323/1.265.0153.

[90] B. Dehnadi, A. H. Hoang, O. L. Jin, and V. Mateu, "Top quark mass calibration for Monte Carlo event generators — an update", *JHEP*, **12** (2023), 065, doi:10.1007/JHEP12(2023)065, arXiv:2309.00547.

[91] ATLAS, CMS Collaboration, "Combination of Measurements of the Top Quark Mass from Data Collected by the ATLAS and CMS Experiments at s=7 and 8 TeV", *Phys. Rev. Lett.*, **132** (2024),, no. 26, 261902, doi:10.1103/PhysRevLett.132.261902, arXiv:2402.08713.

[92] CMS Collaboration, "Measurement of the top quark mass using a profile likelihood approach with the lepton + jets final states in proton–proton collisions at $\sqrt{s} = 13\,\text{TeV}$", *Eur. Phys. J. C*, **83** (2023),, no. 10, 963, doi:10.1140/epjc/s10052-023-12050-4, arXiv:2302.01967.

[93] CMS Collaboration, "Measurement of $\mathrm{t\bar{t}}$ normalised multi-differential cross sections in pp collisions at $\sqrt{s} = 13$ TeV, and simultaneous determination of the strong coupling strength, top quark pole mass, and parton distribution functions", *Eur. Phys. J. C*, **80** (2020),, no. 7, 658, doi:10.1140/epjc/s10052-020-7917-7, arXiv:1904.05237.

[94] CMS Collaboration, "Measurement of the top quark pole mass using $\mathrm{t\bar{t}}$+jet events in the dilepton final state in proton-proton collisions at $\sqrt{s} = 13$ TeV", *JHEP*, **07** (2023), 077, doi:10.1007/JHEP07(2023)077, arXiv:2207.02270.

[95] CMS Collaboration, "Measurement of the differential $\mathrm{t\bar{t}}$ production cross section as a function of the jet mass and extraction of the top quark mass in hadronic decays of boosted top quarks", *Eur. Phys. J. C*, **83** (2023),, no. 7, 560, doi:10.1140/epjc/s10052-023-11587-8, arXiv:2211.01456.

[96] A. Buckley et al., "General-purpose event generators for LHC physics", *Physics Reports*, **504** (July 2011) 145–233, doi:10.1016/j.physrep.2011.03.005, arXiv:1101.2599.

[97] P. Skands, "Introduction to QCD", in *Theor. Adv. Study Inst. Elem. Part. Phys. Search. New Phys. Small Large Scales TASI 2023*, pp. 341–420. November 2013. arXiv:1207.2389. doi:10.1142/9789814525220_0008.

[98] F. Gross et al., "50 Years of Quantum Chromodynamics", *Eur. Phys. J. C*, **83** (December 2023) 1125, doi:10.1140/epjc/s10052-023-11949-2, arXiv:2212.11107.

[99] J. M. Campbell et al., "Event generators for high-energy physics experiments", *SciPost Phys.*, **16** (May 2024) 130, doi:10.21468/SciPostPhys.16.5.130.

[100] The HSF Physics Event Generator WG et al., "HL-LHC Computing Review Stage-2, Common Software Projects: Event Generators", arXiv:2109.14938.

[101] E. Bothmann et al., "Event Generation with Sherpa 2.2", *SciPost Phys.*, **7** (September 2019) 034, doi:10.21468/SciPostPhys.7.3.034, arXiv:1905.09127.

[102] G. Altarelli and G. Parisi, "Asymptotic freedom in parton language", *Nuclear Physics B*, **126** (August 1977) 298–318, doi:10.1016/0550-3213(77)90384-4.

[103] V. N. Gribov and L. N. Lipatov, "Deep inelastic e p scattering in perturbation theory", *Sov. J. Nucl. Phys.*, **15** (1972), 438–450.

[104] Y. L. Dokshitzer, "Calculation of the Structure Functions for Deep Inelastic Scattering and e+ e- Annihilation by Perturbation Theory in Quantum Chromodynamics.", *Sov. Phys. JETP*, **46** (1977), 641–653.

[105] A. Vogt, S. Moch, and J. Vermaseren, "The Three-Loop Splitting Functions in QCD", July 2004, doi:10.48550/arXiv.hep-ph/0407321.

[106] J. Butterworth et al., "PDF4LHC recommendations for LHC Run II", *J. Phys. G: Nucl. Part. Phys.*, **43** (February 2016) 023001, doi:10.1088/0954-3899/43/2/023001, arXiv:1510.03865.

[107] A. Buckley et al., "LHAPDF6: Parton density access in the LHC precision era", *Eur. Phys. J. C*, **75** (March 2015) 132, doi:10.1140/epjc/s10052-015-3318-8, arXiv:1412.7420.

[108] The NNPDF Collaboration et al., "Parton distributions from high-precision collider data", *Eur. Phys. J. C*, **77** (October 2017) 663, doi:10.1140/epjc/s10052-017-5199-5, arXiv:1706.00428.

[109] S. Dulat et al., "New parton distribution functions from a global analysis of quantum chromodynamics", *Phys. Rev. D*, **93** (February 2016) 033006, doi:10.1103/PhysRevD.93.033006, arXiv:1506.07443.

[110] L. A. Harland-Lang, A. D. Martin, P. Motylinski, and R. S. Thorne, "Parton distributions in the LHC era: MMHT 2014 PDFs", *Eur. Phys. J. C*, **75** (May 2015) 204, doi:10.1140/epjc/s10052-015-3397-6, arXiv:1412.3989.

[111] S. Catani and M. H. Seymour, "The Dipole Formalism for the Calculation of QCD Jet Cross Sections at Next-to-Leading Order", *Physics Letters B*, **378** (June 1996) 287–301, doi:10.1016/0370-2693(96)00425-X, arXiv:hep-ph/9602277.

[112] S. Catani and M. H. Seymour, "A General Algorithm for Calculating Jet Cross Sections in NLO QCD", *Nuclear Physics B*, **485** (February 1997) 291–419, doi:10.1016/S0550-3213(96)00589-5, arXiv:hep-ph/9605323.

[113] S. Höche and S. Prestel, "Triple collinear emissions in parton showers", *Phys. Rev. D*, **96** (October 2017) 074017, doi:10.1103/PhysRevD.96.074017, arXiv:1705.00742.

[114] S. Höche, F. Krauss, and S. Prestel, "Implementing NLO DGLAP evolution in Parton Showers", *J. High Energ. Phys.*, **2017** (October 2017) 93, doi:10.1007/JHEP10(2017)093, arXiv:1705.00982.

[115] F. Dulat, S. Höche, and S. Prestel, "Leading-color fully differential two-loop soft corrections to QCD dipole showers", *Phys. Rev. D*, **98** (October 2018) 074013, doi:10.1103/PhysRevD.98.074013, arXiv:1805.03757.

[116] J. Bellm et al., "Herwig 7.0/Herwig++ 3.0 release note", *Eur. Phys. J. C*, **76** (April 2016) 196, doi:10.1140/epjc/s10052-016-4018-8.

[117] D. A. Kosower, "Antenna Factorization of Gauge-Theory Amplitudes", *Phys. Rev. D*, **57** (May 1998) 5410–5416, doi:10.1103/PhysRevD.57.5410, arXiv:hep-ph/9710213.

[118] W. T. Giele et al., "The Vincia Parton Shower", July 2013, doi:10.48550/arXiv.1307.1060.

[119] S. Frixione, Z. Kunszt, and A. Signer, "Three-jet cross sections to next-to-leading order", *Nuclear Physics B*, **467** (May 1996) 399–442, doi:10.1016/0550-3213(96)00110-1, arXiv:hep-ph/9512328.

[120] S. Frixione, G. Ridolfi, and P. Nason, "A positive-weight next-to-leading-order Monte Carlo for heavy flavour hadroproduction", *J. High Energy Phys.*, **2007** (September 2007) 126, doi:10.1088/1126-6708/2007/09/126.

[121] S. Alioli, P. Nason, C. Oleari, and E. Re, "A general framework for implementing NLO calculations in shower Monte Carlo programs: The POWHEG BOX", *J. High Energ. Phys.*, **2010** (June 2010) 43, doi:10.1007/JHEP06(2010)043, arXiv:1002.2581.

[122] J. Alwall et al., "The automated computation of tree-level and next-to-leading order differential cross sections, and their matching to parton shower simulations", *J. High Energ. Phys.*, **2014** (July 2014) 79, doi:10.1007/JHEP07(2014)079, arXiv:1405.0301.

[123] M. Seidel, "Tuning of generators", in *QCD@LHC2022*. October 2022.

[124] T. Sjöstrand, S. Mrenna, and P. Skands, "A Brief Introduction to PYTHIA 8.1", *Computer Physics Communications*, **178** (June 2008) 852–867, doi:10.1016/j.cpc.2008.01.036, arXiv:0710.3820.

[125] T. Sjöstrand et al., "An Introduction to PYTHIA 8.2", *Computer Physics Communications*, **191** (June 2015) 159–177, doi:10.1016/j.cpc.2015.01.024, arXiv:1410.3012.

[126] S. Mrenna and P. Skands, "Automated parton-shower variations in pythia 8", *Phys. Rev. D*, **94** (October 2016) 074005, doi:10.1103/PhysRevD.94.074005.

[127] J. Bellm et al., "Parton-shower uncertainties with Herwig 7: Benchmarks at leading order", *Eur. Phys. J. C*, **76** (December 2016) 665, doi:10.1140/epjc/s10052-016-4506-x.

[128] M. van Beekveld et al., "PanScales showers for hadron collisions: All-order validation", *J. High Energ. Phys.*, **2022** (November 2022) 20, doi:10.1007/JHEP11(2022)020.

[129] M. van Beekveld et al., "A new standard for the logarithmic accuracy of parton showers", June 2024, doi:10.48550/arXiv.2406.02661.

[130] M. van Beekveld and S. F. Ravasio, "Next-to-leading-logarithmic PanScales showers for Deep Inelastic Scattering and Vector Boson Fusion", *J. High Energ. Phys.*, **2024** (February 2024) 1, doi:10.1007/JHEP02(2024)001, arXiv:2305.08645.

[131] G. Bewick, S. F. Ravasio, P. Richardson, and M. H. Seymour, "Logarithmic Accuracy of Angular-Ordered Parton Showers", March 2020, doi:10.48550/arXiv.1904.11866.

[132] G. Bewick, S. F. Ravasio, P. Richardson, and M. H. Seymour, "Initial State Radiation in the Herwig 7 Angular-Ordered Parton Shower", *J. High Energ.*

Phys., **2022** (January 2022) 26, doi:10.1007/JHEP01(2022)026, arXiv:2107.04051.

[133] R. K. Ellis, G. Marchesini, and B. R. Webber, "Soft radiation in parton-parton scattering", *Nuclear Physics B*, **286** (January 1987) 643–656, doi:10.1016/0550-3213(87)90456-1.

[134] C. Degrande et al., "UFO - The Universal FeynRules Output", *Computer Physics Communications*, **183** (June 2012) 1201–1214, doi:10.1016/j.cpc.2012.01.022, arXiv:1108.2040.

[135] R. Frederix and P. Torrielli, "A new way of reducing negative weights in MC@NLO", arXiv:2310.04160.

[136] S. Jadach et al., "New simpler method of matching NLO corrections with parton shower Monte Carlo", August 2016, doi:10.48550/arXiv.1607.00919.

[137] S. Catani, F. Krauss, R. Kuhn, and B. R. Webber, "QCD Matrix Elements + Parton Showers", *J. High Energy Phys.*, **2001** (November 2001) 063–063, doi:10.1088/1126-6708/2001/11/063, arXiv:hep-ph/0109231.

[138] J. Alwall et al., "Comparative study of various algorithms for the merging of parton showers and matrix elements in hadronic collisions", *Eur. Phys. J. C*, **53** (February 2008) 473–500, doi:10.1140/epjc/s10052-007-0490-5.

[139] L. Lonnblad, "Correcting the Colour-Dipole Cascade Model with Fixed Order Matrix Elements", *J. High Energy Phys.*, **2002** (May 2002) 046–046, doi:10.1088/1126-6708/2002/05/046, arXiv:hep-ph/0112284.

[140] R. Frederix and S. Frixione, "Merging meets matching in MC@NLO", *J. High Energ. Phys.*, **2012** (December 2012) 61, doi:10.1007/JHEP12(2012)061, arXiv:1209.6215.

[141] L. Lönnblad and S. Prestel, "Merging multi-leg NLO matrix elements with parton showers", *J. High Energ. Phys.*, **2013** (March 2013) 166, doi:10.1007/JHEP03(2013)166.

[142] L. Lönnblad and S. Prestel, "Unitarising matrix element + parton shower merging", *J. High Energ. Phys.*, **2013** (February 2013) 94, doi:10.1007/JHEP02(2013)094.

[143] H.-U. Bengtsson and T. Sjostrand, "The Lund Monte Carlo for Hadronic Processes: Pythia Version 4.8", *Comput. Phys. Commun.*, **46** (1987), 43, doi:10.1016/0010-4655(87)90036-1.

[144] B. Andersson, "The Lund Model". Cambridge Monographs on Particle Physics, Nuclear Physics and Cosmology. Cambridge University Press, Cambridge, 1998. doi:10.1017/CBO9780511524363.

[145] T. D. Gottschalk, "A realistic model for e+e- annihilation including parton bremsstrahlung effects", *Nuclear Physics B*, **214** (April 1983) 201–222, doi:10.1016/0550-3213(83)90658-2.

[146] T. D. Gottschalk, "An improved description of hadronization in the QCD cluster model for e+e- annihilation", *Nuclear Physics B*, **239** (July 1984) 349–381, doi:10.1016/0550-3213(84)90253-0.

[147] B. Andersson, G. Gustafson, and B. Söderberg, "A general model for jet fragmentation", *Z. Phys. C - Particles and Fields*, **20** (December 1983) 317–329, doi:10.1007/BF01407824.

[148] M. G. Bowler, "e+ e- Production of Heavy Quarks in the String Model", *Z. Phys. C*, **11** (1981), 169, doi:10.1007/BF01574001.

[149] C. Peterson, D. Schlatter, I. Schmitt, and P. M. Zerwas, "Scaling violations in inclusive e^+e^- annihilation spectra", *Phys. Rev. D*, **27** (Jan 1983) 105–111, doi:10.1103/PhysRevD.27.105.

[150] H. Wittig, "QCD on the Lattice", in *Particle Physics Reference Library: Volume 1: Theory and Experiments*, H. Schopper, ed., pp. 137–262. Springer International Publishing, Cham, 2020. doi:10.1007/978-3-030-38207-0_5.

[151] C. Gattringer and C. B. Lang, "Quantum Chromodynamics on the Lattice: An Introductory Presentation", volume 788 of *Lecture Notes in Physics*. Springer, Berlin, Heidelberg, 2010. doi:10.1007/978-3-642-01850-3, ISBN 978-3-642-01849-7 978-3-642-01850-3.

[152] T. Sjöstrand and M. van Zijl, "A multiple-interaction model for the event structure in hadron collisions", *Phys. Rev. D*, **36** (October 1987) 2019–2041, doi:10.1103/PhysRevD.36.2019.

[153] P. Bartalini et al., "Multi-Parton Interactions at the LHC", November 2011, doi:10.48550/arXiv.1111.0469.

[154] A. Tumasyan et al., "Observation of triple J/ψ meson production in proton-proton collisions", *Nat. Phys.*, **19** (March 2023) 338–350, doi:10.1038/s41567-022-01838-y.

[155] J. R. Andersen et al., "Exploring High-Purity Multiparton Scattering at Hadron Colliders", *Phys. Rev. Lett.*, **132** (January 2024) 041901, doi:10.1103/PhysRevLett.132.041901.

[156] CMS Collaboration, "Measurement of the underlying event activity using charged-particle jets in proton-proton collisions at sqrt(s) = 2.76 TeV", *J. High Energ. Phys.*, **2015** (September 2015) 137, doi:10.1007/JHEP09(2015)137, arXiv:1507.07229.

[157] CMS Collaboration, "Underlying Event Measurements with Leading Particles and Jets in pp collisions at $\sqrt{s} = 13$ TeV", technical report, CERN, Geneva, 2015, cds:2104473.

[158] CMS Collaboration, "Study of the underlying event in top quark pair production in pp collisions at 13 TeV", *Eur. Phys. J. C*, **79** (February 2019) 123, doi:10.1140/epjc/s10052-019-6620-z, arXiv:1807.02810.

[159] UA1 Collaboration, "Production of Low Transverse Energy Clusters in anti-p p Collisions at s**(1/2) = 0.2-TeV to 0.9-TeV and their Interpretation in Terms of QCD Jets", *Nucl. Phys. B*, **309** (1988), 405–425, doi:10.1016/0550-3213(88)90450-6.

[160] CDF Collaboration et al., "Charged jet evolution and the underlying event in proton-antiproton collisions at 1.8 TeV", *Phys. Rev. D*, **65** (April 2002) 092002, doi:10.1103/PhysRevD.65.092002.

[161] P. Skands, S. Carrazza, and J. Rojo, "Tuning PYTHIA 8.1: The Monash 2013 Tune", *Eur. Phys. J. C*, **74** (August 2014) 3024, doi:10.1140/epjc/s10052-014-3024-y, arXiv:1404.5630.

[162] CMS Collaboration, "Extraction and validation of a new set of CMS PYTHIA8 tunes from underlying-event measurements", *Eur. Phys. J. C*, **80** (January 2020) 4, doi:10.1140/epjc/s10052-019-7499-4, arXiv:1903.12179.

[163] The ATLAS collaboration, "ATLAS Pythia 8 Tunes to 7 TeV Data", technical report, CERN, Geneva, 2014, cds:1966419.

[164] UA1 Collaboration, "A Study of the General Characteristics of $p\bar{p}$ Collisions at $\sqrt{s}$ = 0.2-TeV to 0.9-TeV", *Nucl. Phys. B*, **335** (1990), 261–287, doi:10.1016/0550-3213(90)90493-W.

[165] E735 Collaboration, "Multiplicity dependence of transverse momentum spectra of centrally produced hadrons in anti-p p collisions at 0.3-TeV, 0.54-TeV, 0.9-TeV, and 1.8-TeV center-of-mass energy", *Phys. Lett. B*, **336** (1994), 599–604, doi:10.1016/0370-2693(94)90578-9.

[166] The ATLAS Collaboration, "Charged-particle multiplicities in pp interactions measured with the ATLAS detector at the LHC", *New J. Phys.*, **13** (May 2011) 053033, doi:10.1088/1367-2630/13/5/053033, arXiv:1012.5104.

[167] J. R. Christiansen and P. Z. Skands, "String Formation Beyond Leading Colour", *J. High Energ. Phys.*, **2015** (August 2015) 3, doi:10.1007/JHEP08(2015)003, arXiv:1505.01681.

[168] H. Brooks, P. Skands, and R. Verheyen, "Interleaved Resonance Decays and Electroweak Radiation in Vincia", January 2022, doi:10.48550/arXiv.2108.10786.

[169] C. Bierlich et al., "A comprehensive guide to the physics and usage of PYTHIA 8.3", March 2022, doi:10.48550/arXiv.2203.11601.

[170] H. Brooks and C. T. Preuss, "Efficient multi-jet merging with the Vincia sector shower", *Computer Physics Communications*, **264** (July 2021) 107985, doi:10.1016/j.cpc.2021.107985, arXiv:2008.09468.

[171] J. Bellm et al., "Herwig 7.1 Release Note", May 2017, doi:10.48550/arXiv.1705.06919.

[172] S. Plätzer and S. Gieseke, "Dipole showers and automated NLO matching in Herwig++", *Eur. Phys. J. C*, **72** (November 2012) 2187, doi:10.1140/epjc/s10052-012-2187-7.

[173] M. Bahr et al., "Herwig++ Physics and Manual", *Eur. Phys. J. C*, **58** (December 2008) 639–707, doi:10.1140/epjc/s10052-008-0798-9, arXiv:0803.0883.

[174] C. F. Berger et al., "An Automated Implementation of On-Shell Methods for One-Loop Amplitudes", *Phys. Rev. D*, **78** (August 2008) 036003, doi:10.1103/PhysRevD.78.036003, arXiv:0803.4180.

[175] J. Campbell and T. Neumann, "Precision phenomenology with MCFM", September 2019, doi:10.1007/JHEP12(2019)034.

[176] F. Cascioli, P. Maierhöfer, and S. Pozzorini, "Scattering Amplitudes with Open Loops", *Phys. Rev. Lett.*, **108** (March 2012) 111601, doi:10.1103/PhysRevLett.108.111601, arXiv:1111.5206.

[177] S. Actis et al., "RECOLA: REcursive Computation of One-Loop Amplitudes", *Computer Physics Communications*, **214** (May 2017) 140–173, doi:10.1016/j.cpc.2017.01.004, arXiv:1605.01090.

[178] B. Biedermann et al., "Automation of NLO QCD and EW corrections with Sherpa and Recola", *Eur. Phys. J. C*, **77** (July 2017) 492, doi:10.1140/epjc/s10052-017-5054-8, arXiv:1704.05783.

[179] F. Krauss, R. Kuhn, and G. Soff, "AMEGIC++ 1.0, A Matrix Element Generator In C++", *J. High Energy Phys.*, **2002** (February 2002) 044–044, doi:10.1088/1126-6708/2002/02/044, arXiv:hep-ph/0109036.

[180] T. Gleisberg and S. Hoeche, "Comix, a new matrix element generator", *J. High Energy Phys.*, **2008** (December 2008) 039–039, doi:10.1088/1126-6708/2008/12/039, arXiv:0808.3674.

[181] S. Höche, S. Kuttimalai, S. Schumann, and F. Siegert, "Beyond Standard Model calculations with Sherpa", *Eur. Phys. J. C*, **75** (March 2015) 135, doi:10.1140/epjc/s10052-015-3338-4, arXiv:1412.6478.

[182] S. Schumann and F. Krauss, "A parton shower algorithm based on Catani-Seymour dipole factorisation", *J. High Energy Phys.*, **2008** (March 2008) 038–038, doi:10.1088/1126-6708/2008/03/038, arXiv:0709.1027.

[183] S. Höche and S. Prestel, "The midpoint between dipole and parton showers", *Eur. Phys. J. C*, **75** (September 2015) 461, doi:10.1140/epjc/s10052-015-3684-2, arXiv:1506.05057.

[184] M. L. Mangano, M. Moretti, F. Piccinini, and M. Treccani, "Matching matrix elements and shower evolution for top-quark production in hadronic collisions", *J. High Energy Phys.*, **2007** (January 2007) 013–013, doi:10.1088/1126-6708/2007/01/013, arXiv:hep-ph/0611129.

[185] S. Höche, J. Krause, and F. Siegert, "Multijet merging in a variable flavor number scheme", *Phys. Rev. D*, **100** (July 2019) 014011, doi:10.1103/PhysRevD.100.014011.

[186] T. Ježo et al., "An NLO+PS generator for $t\bar{t}$ and Wt production and decay including non-resonant and interference effects", *Eur. Phys. J. C*, **76** (December 2016) 691, doi:10.1140/epjc/s10052-016-4538-2.

[187] CMS Collaboration, "Measurement of the top quark polarization and $\mathrm{t\bar{t}}$ spin correlations using dilepton final states in proton-proton collisions at $\sqrt{s} = 13$ TeV", *Phys. Rev. D*, **100** (2019),, no. 7, 072002, doi:10.1103/PhysRevD.100.072002, arXiv:1907.03729.

[188] CMS Collaboration, "Measurements of polarization and spin correlation and observation of entanglement in top quark pairs using lepton+jets events from proton-proton collisions at s=13 TeV", *Phys. Rev. D*, **110** (2024),, no. 11, 112016, doi:10.1103/PhysRevD.110.112016, arXiv:2409.11067.

[189] V. Fadin, V. Khoze, and T. Sjöstrand, "On the threshold behaviour of heavy top production", *Z. Phys. C - Particles and Fields*, **48** (December 1990) 613–621, doi:10.1007/BF01614696.

[190] W.-L. Ju et al., "Top quark pair production near threshold: Single/double distributions and mass determination", *J. High Energ. Phys.*, **2020** (June 2020) 158, doi:10.1007/JHEP06(2020)158.

[191] P. F. Monni, E. Re, and M. Wiesemann, "MiNNLO$_{\rm PS}$: optimizing $2 \to 1$hadronic processes", *Eur. Phys. J. C*, **80** (November 2020) 1075, doi:10.1140/epjc/s10052-020-08658-5.

[192] P. F. Monni et al., "MiNNLOPS: A new method to match NNLO QCD to parton showers", *J. High Energ. Phys.*, **2020** (May 2020) 143, doi:10.1007/JHEP05(2020)143.

[193] S. Alioli et al., "Drell-yan production at NNLL$'$ + NNLO matched to parton showers", *Phys. Rev. D*, **92** (November 2015) 094020, doi:10.1103/PhysRevD.92.094020.

[194] S. Alioli et al., "Combining higher-order resummation with multiple NLO calculations and parton showers in GENEVA", *J. High Energ. Phys.*, **2013** (September 2013) 120, doi:10.1007/JHEP09(2013)120.

[195] G. Aad et al., "Measurement of the top-quark mass using a leptonic invariant mass in pp collisions at $\sqrt{s}$= 13 TeV with the ATLAS detector", *J. High Energ. Phys.*, **2023** (June 2023) 19, doi:10.1007/JHEP06(2023)019.

[196] E. Bothmann et al., "Exploring phase space with Neural Importance Sampling", *SciPost Physics*, **8** (April 2020) 069, doi:10.21468/SciPostPhys.8.4.069.

[197] N. Deutschmann and N. Götz, "Accelerating HEP simulations with Neural Importance Sampling", *J. High Energ. Phys.*, **2024** (March 2024) 83, doi:10.1007/JHEP03(2024)083.

[198] C. Bierlich et al., "Reweighting Monte Carlo Predictions and Automated Fragmentation Variations in Pythia 8", *SciPost Phys.*, **16** (May 2024) 134, doi:10.21468/SciPostPhys.16.5.134, arXiv:2308.13459.

[199] A. Andreassen and B. Nachman, "Neural Networks for Full Phase-space Reweighting and Parameter Tuning", *Phys. Rev. D*, **101** (May 2020) 091901, doi:10.1103/PhysRevD.101.091901, arXiv:1907.08209.

[200] CMS Collaboration, "Reweighting of simulated events using machine learning techniques in CMS", technical report, CERN, Geneva, 2024, cds:2904938.

[201] J. Alwall et al., "MadGraph 5 : Going Beyond", *J. High Energ. Phys.*, **2011** (June 2011) 128, doi:10.1007/JHEP06(2011)128, arXiv:1106.0522.

[202] A. Potrebko, "A Program for SU(N) Color Structure Decomposition into Multiplet Bases Using Wigner 3j and 6j Coefficients". Master's thesis, Lund U., 2020.

[203] S. Keppeler, S. Plätzer, and M. Sjodahl, "Wigner 6j symbols with gluon lines: Completing the set of 6j symbols required for color decomposition", *J. High Energ. Phys.*, **2024** (May 2024) 51, doi:10.1007/JHEP05(2024)051.

[204] R. Brun and F. Rademakers, "ROOT — An object oriented data analysis framework", *Nuclear Instruments and Methods in Physics Research Section A: Accelerators, Spectrometers, Detectors and Associated Equipment*, **389** (April 1997) 81–86, doi:10.1016/S0168-9002(97)00048-X.

[205] S. Agostinelli et al., "Geant4—a simulation toolkit", *Nuclear Instruments and Methods in Physics Research Section A: Accelerators, Spectrometers, Detectors and Associated Equipment*, **506** (July 2003) 250–303, doi:10.1016/S0168-9002(03)01368-8.

[206] J. Allison et al., "Recent developments in Geant4", *Nuclear Instruments and Methods in Physics Research Section A: Accelerators, Spectrometers, Detectors and Associated Equipment*, **835** (November 2016) 186–225, doi:10.1016/j.nima.2016.06.125.

[207] J. Allison et al., "Geant4 developments and applications", *IEEE Trans. Nucl. Sci.*, **53** (February 2006) 270–278, doi:10.1109/TNS.2006.869826.

[208] CMS Collaboration, "CMS Open data docmentation". http://opendata.cern.ch/docs/cms-guide-event-production, Dec 2023.

[209] S. Schmitt, "TUnfold: An algorithm for correcting migration effects in high energy physics", *J. Inst.*, **7** (October 2012) T10003–T10003, doi:10.1088/1748-0221/7/10/T10003, arXiv:1205.6201.

[210] A. Buckley et al., "Rivet user manual", *Computer Physics Communications*, **184** (December 2013) 2803–2819, doi:10.1016/j.cpc.2013.05.021, arXiv:1003.0694.

[211] "LHC TOP WG: WG on Top Physics at the LHC | LPCC". https://lpcc.web.cern.ch/content/lhc-top-wg.

[212] W.-M. Yao et al., "Review of Particle Physics", *Journal of Physics G*, **33** (2007), 1+.

[213] The NNPDF Collaboration et al., "Parton distributions for the LHC Run II", *J. High Energ. Phys.*, **2015** (April 2015) 40, doi:10.1007/JHEP04(2015)040, arXiv:1410.8849.

[214] ATLAS Collaboration, "Measurements of top-quark pair differential and double-differential cross-sections in the ℓ+jets channel with pp collisions at $\sqrt{s} = 13$TeV using the ATLAS detector", *Eur. Phys. J. C*, **79** (December 2019) 1028, doi:10.1140/epjc/s10052-019-7525-6.

[215] ATLAS Collaboration, "Measurements of $t\bar{t}$ differential cross-sections of highly boosted top quarks decaying to all-hadronic final states in pp collisions at $\sqrt{s} = 13$ TeV using the ATLAS detector", *Phys. Rev. D*, **98** (2018),, no. 1, 012003, doi:10.1103/PhysRevD.98.012003, arXiv:1801.02052.

[216] CMS Collaboration, "Measurement of differential cross sections for the production of top quark pairs and of additional jets in lepton+jets events from pp collisions at $\sqrt{s} = 13$ TeV", *Phys. Rev. D*, **97** (2018),, no. 11, 112003, doi:10.1103/PhysRevD.97.112003, arXiv:1803.08856.

[217] A. Hayrapetyan et al., "Review of top quark mass measurements in CMS",.

[218] CMS Collaboration, "Measurements of differential cross sections of top quark pair production as a function of kinematic event variables in proton-proton collisions at $\sqrt{s} = 13$ TeV", *JHEP*, **06** (2018), 002, doi:10.1007/JHEP06(2018)002, arXiv:1803.03991.

[219] G. S. Chahal and F. Krauss, "Cluster Hadronisation in Sherpa", *SciPost Phys.*, **13** (August 2022) 019, doi:10.21468/SciPostPhys.13.2.019.

[220] ATLAS Collaboration, "Dependence of the Jet Energy Scale on the Particle Content of Hadronic Jets in the ATLAS Detector Simulation", technical report, CERN, Geneva, 2022, cds:2808016.

[221] O. S. Brüning et al., "LHC Design Report", technical report, CERN, Geneva, 2004, doi:10.5170/CERN-2004-003-V-2.

[222] L. Evans and P. Bryant, "LHC Machine", *J. Instrum.*, **3** (2008),, no. 08, S08001–S08001, doi:10.1088/1748-0221/3/08/s08001.

[223] CERN, "LEP design report", technical report, CERN, Geneva, 1984, cds:102083. Copies shelved as reports in LEP, PS and SPS libraries.

[224] Laurent Guiraud, "Plan of sps to lhc transfer tunnels. plan des accélérateurs lhc et sps ainsi que le plan des deux nouveaux tunnels de transfert ti2 et ti8", technical report, CERN, Aug 2001, cds:42387.

[225] CERN, "LHC Guide", Mar 2017, cds:2255762.

[226] R. "Scrivens et al., "Overview of the status and developments on primary ion sources at CERN*", technical report, CERN, Sep 2011, cds:1382102.

[227] C. E. Hill, A. M. Lombardi, E. Tanke, and M. Vretenar, "Present performance of the CERN proton linac",.

[228] The ALICE Collaboration et al., "The ALICE experiment at the CERN LHC", *J. Inst.*, **3** (August 2008) S08002, doi:10.1088/1748-0221/3/08/S08002.

[229] ALICE Collaboration, "Performance of the ALICE Experiment at the CERN LHC", August 2015, doi:10.48550/arXiv.1402.4476.

[230] The ATLAS Collaboration et al., "The ATLAS Experiment at the CERN Large Hadron Collider", *J. Inst.*, **3** (August 2008) S08003, doi:10.1088/1748-0221/3/08/S08003.

[231] The CMS Collaboration et al., "The CMS experiment at the CERN LHC", *J. Inst.*, **3** (August 2008) S08004, doi:10.1088/1748-0221/3/08/S08004.

[232] The LHCb Collaboration et al., "The LHCb Detector at the LHC", *J. Inst.*, **3** (August 2008) S08005, doi:10.1088/1748-0221/3/08/S08005.

[233] LHCb collaboration et al., "LHCb Detector Performance", March 2015, doi:10.48550/arXiv.1412.6352.

[234] G. Arduini, "Specification of machine and beam parameters: Deliverable: D2.6", technical report, CERN, Nov 2014, cds:1972603.

[235] O. Aberle et al., "High-Luminosity Large Hadron Collider (HL-LHC): Technical design report", technical report, CERN, Geneva, 2020, doi:10.23731/CYRM-2020-0010, cds:2749422.

[236] CMS Collaboration, "Particle-flow reconstruction and global event description with the CMS detector", *J. Instrum.*, **12** (October 2017) P10003–P10003, doi:10.1088/1748-0221/12/10/P10003, arXiv:1706.04965.

[237] I. Neutelings, "CMS coordinate system", July 2024, https://tikz.net/axis3d_cms/.

[238] CMS Collaboration, "ECAL Technical Design Report (TDR) Figures from Chapter 3", technical report, CERN, 1997, cds:1327664.

[239] CMS Collaboration, "The CMS magnet project: Technical Design Report", technical report, CERN, Geneva, 1997, doi:10.17181/CERN.6ZU0.V4T9, cds:331056.

[240] The Tracker Group of the CMS Collaboration, "The CMS Phase-1 Pixel Detector Upgrade", December 2020, doi:10.48550/arXiv.2012.14304.

[241] CMS Collaboration, "The CMS tracker system project: Technical Design Report", technical report, CERN, Geneva, 1997, cds:368412.

[242] CMS Collaboration, "The CMS electromagnetic calorimeter project: Technical Design Report", technical report, CERN, Geneva, 1997, cds:349375.

[243] CMS Collaboration, "The CMS hadron calorimeter project: Technical Design Report", technical report, CERN, Geneva, 1997, cds:357153.

[244] CMS Collaboration, "Electromagnetic physics objects commissioning with first LHC data", technical report, CERN, Geneva, 2010, cds:1247384.

[245] J. Mans et al., "CMS Technical Design Report for the Phase 1 Upgrade of the Hadron Calorimeter", technical report, CERN, 2012, cds:1481837.

[246] CMS Collaboration, "Performance of the local reconstruction algorithms for the CMS hadron calorimeter with Run 2 data", *J. Inst.*, **18** (November 2023) P11017, doi:10.1088/1748-0221/18/11/P11017, arXiv:2306.10355.

[247] CMS Collaboration, "The Performance of the CMS Muon Detector in Proton-Proton Collisions at $\sqrt{s} = 7$ TeV at the LHC", *JINST*, **8** (2013), P11002, doi:10.1088/1748-0221/8/11/P11002, arXiv:1306.6905.

[248] CMS Collaboration, "The CMS muon project: Technical Design Report", technical report, CERN, Geneva, 1997, cds:343814.

[249] A. Sirunyan, A. Tumasyan, and Adam, "Performance of the CMS muon detector and muon reconstruction with proton-proton collisions at $\sqrt{s}$ =13 TeV", *Journal of Instrumentation*, **13** (June 2018) P06015–P06015, doi:10.1088/1748-0221/13/06/p06015.

[250] CMS Collaboration, "Charged particle detection performance of gas electron multiplier detector for the upgrade of CMS endcap muon system at the CERN LHC", technical report, CERN, 2015, cds:2162881.

[251] LHCb Collaboration, "Charged hadron identification performance with early Run 3 data", technical report, CERN, 2023, cds:2868904.

[252] CMS Collaboration, "Measurement of time-dependent CP violation in $B_s^0 \to J/\psi\,\phi(1020)$ decays with the CMS detector", technical report, CERN, Geneva, 2024, cds:2894821.

[253] CMS Collaboration, "Search for CP violation in $\mathrm{D}^0 \to \mathrm{K}^0_\mathrm{S}\mathrm{K}^0_\mathrm{S}$ decay from proton-proton collisions at 13 TeV", technical report, CERN, Geneva, 2024, cds:2893166.

[254] CMS Collaboration, "The CMS trigger system", September 2016, doi:10.1088/1748-0221/12/01/P01020.

[255] CMS Collaboration, "Enriching the physics program of the CMS experiment via data scouting and data parking", March 2024, doi:10.48550/arXiv.2403.16134.

[256] A. M. Sirunyan et al., "Pileup mitigation at CMS in 13 TeV data", *J. Instrum.*, **15** (2020)„ no. 09, P09018, doi:10.1088/1748-0221/15/09/P09018.

[257] CMS Collaboration, "Description and performance of track and primary-vertex reconstruction with the CMS tracker", *J. Inst.*, **9** (October 2014) P10009–P10009, doi:10.1088/1748-0221/9/10/P10009, arXiv:1405.6569.

[258] R. Mankel, "A concurrent track evolution algorithm for pattern recognition in the HERA-B main tracking system", *Nuclear Instruments and Methods in Physics Research Section A: Accelerators, Spectrometers, Detectors and Associated Equipment*, **395** (August 1997) 169–184, doi:10.1016/S0168-9002(97)00705-5.

[259] ATLAS Collaboration, "The performance of missing transverse momentum reconstruction and its significance with the ATLAS detector using 140 fb^{-1} of $\sqrt{s} = 13$ TeV pp collisions", arXiv:2402.05858.

[260] CMS Collaboration, "Performance of CMS Muon Reconstruction in pp Collision Events at $\sqrt{s} = 7$ TeV", *JINST*, **7** (2012), P10002, doi:10.1088/1748-0221/7/10/P10002, arXiv:1206.4071.

[261] G. P. Salam and G. Soyez, "A practical Seedless Infrared-Safe Cone jet algorithm", *J. High Energy Phys.*, **2007** (May 2007) 086–086, doi:10.1088/1126-6708/2007/05/086, arXiv:0704.0292.

[262] Y. L. Dokshitzer, G. D. Leder, S. Moretti, and B. R. Webber, "Better jet clustering algorithms", *JHEP*, **08** (1997), 001, doi:10.1088/1126-6708/1997/08/001.

[263] M. Cacciari, Gavin P. Salam, and Gregory Soyez, "The anti-kt jet clustering algorithm", *J. High Energy Phys.*, **2008** (April 2008) 063, doi:10.1088/1126-6708/2008/04/063.

[264] CMS Collaboration, "Measurement of jet substructure observables in $\text{t}\bar{\text{t}}$ events from proton-proton collisions at $\sqrt{s} = 13$ TeV", *Phys. Rev. D*, **98** (2018)„ no. 9, 092014, doi:10.1103/PhysRevD.98.092014, arXiv:1808.07340.

[265] CMS Collaboration, "Measurement of the primary Lund jet plane density in proton-proton collisions at $\sqrt{\text{s}} = 13$ TeV", *JHEP*, **05** (2024), 116, doi:10.1007/JHEP05(2024)116, arXiv:2312.16343.

[266] A. J. Larkoski, S. Marzani, G. Soyez, and J. Thaler, "Soft Drop", *J. High Energ. Phys.*, **2014** (May 2014) 146, doi:10.1007/JHEP05(2014)146, arXiv:1402.2657.

[267] A. Banfi, G. Salam, and G. Zanderighi, "Infrared-safe definition of jet flavour", *Eur. Phys. J. C*, **47** (July 2006) 113–124, doi:10.1140/epjc/s2006-02552-4.

[268] P. T. Komiske, E. M. Metodiev, and J. Thaler, "An operational definition of quark and gluon jets", *J. High Energ. Phys.*, **2018** (November 2018) 59, doi:10.1007/JHEP11(2018)059.

[269] S. Caletti, A. J. Larkoski, S. Marzani, and D. Reichelt, "A fragmentation approach to jet flavor", *J. High Energy Phys.* (October 2022) 158, doi:10.1007/JHEP10(2022)158.

[270] CMS Collaboration, "Measurement of the Cross Section and Angular Correlations for Associated Production of a Z Boson with b Hadrons in pp Collisions at $\sqrt{s} = 7$ TeV", *JHEP*, **12** (2013), 039, doi:10.1007/JHEP12(2013)039, arXiv:1310.1349.

[271] J. Gallicchio and M. D. Schwartz, "Seeing in Color: Jet Superstructure", *Phys. Rev. Lett.*, **105** (July 2010) 022001, doi:10.1103/PhysRevLett.105.022001.

[272] M. Cacciari, G. P. Salam, and G. Soyez, "The Catchment Area of Jets", *J. High Energy Phys.*, **2008** (April 2008) 005–005, doi:10.1088/1126-6708/2008/04/005, arXiv:0802.1188.

[273] E. M. Metodiev and J. Thaler, "Jet Topics: Disentangling Quarks and Gluons at Colliders", *Phys. Rev. Lett.*, **120** (June 2018) 241602, doi:10.1103/PhysRevLett.120.241602.

[274] T. Lenz, "Measurement of jet substructure observables and jet fragmentation properties using the ATLAS detector", *Nuclear and Particle Physics Proceedings*, **309–311** (January 2020) 1–8, doi:10.1016/j.nuclphysbps.2019.11.002.

[275] P. T. Komiske, S. Kryhin, and J. Thaler, "Disentangling quarks and gluons in CMS open data", *Phys. Rev. D*, **106** (November 2022) 094021, doi:10.1103/PhysRevD.106.094021.

[276] A. Tumasyan et al., "Study of quark and gluon jet substructure in Z+jet and dijet events from pp collisions", *J. High Energ. Phys.*, **2022** (January 2022) 188, doi:10.1007/JHEP01(2022)188.

[277] CMS Collaboration, "Identification of heavy-flavour jets with the CMS detector in pp collisions at 13 TeV", *J. Instrum.*, **13** (2018),, no. CMS-BTV-16-002, CERN-EP-2017-326, P05011, doi:10.1088/1748-0221/13/05/P05011, arXiv:1712.07158.

[278] C. Tarantino, "Beauty Hadron Lifetimes and B-Meson CP-Violation Parameters from Lattice QCD", October 2003, doi:10.48550/arXiv.hep-ph/0310241.

[279] A. Lenz, "Lifetimes and HQE", September 2019, doi:10.48550/arXiv.1405.3601.

[280] LHCb Collaboration, "Search for the rare decay $B^+ \to \mu^+\mu^-\mu^+\nu_\mu$", *Eur. Phys. J. C*, **79** (2019)„ no. 8, 675, doi:10.1140/epjc/s10052-019-7112-x, arXiv:1812.06004.

[281] H. Qu and L. Gouskos, "ParticleNet: Jet Tagging via Particle Clouds", *Phys. Rev. D*, **101** (March 2020) 056019, doi:10.1103/PhysRevD.101.056019, arXiv:1902.08570.

[282] CMS Collaboration, "Jet energy scale and resolution of jets with ParticleNet p_{T} regression using Run3 data collected by the CMS experiment in 2022 and 2023 at 13.6 TeV", technical report, CERN, 2024, cds:2904704.

[283] CMS Collaboration, "Identification of b-quark jets with the CMS experiment", *J. Inst.*, **8** (April 2013) P04013–P04013, doi:10.1088/1748-0221/8/04/P04013, arXiv:1211.4462.

[284] V. Khachatryan et al., "Jet energy scale and resolution in the CMS experiment in pp collisions at 8 TeV", *J. Inst.*, **12** (February 2017) P02014, doi:10.1088/1748-0221/12/02/P02014.

[285] CMS Collaboration, "Mitigation of anomalous missing transverse momentum measurements in data collected by CMS at sqrt(s) = 13 TeV during the LHC Run 2", technical report, CERN, 2020, cds:2714938.

[286] CMS Collaboration et al., "Electron and photon reconstruction and identification with the CMS experiment at the CERN LHC", *J. Inst.*, **16** (May 2021) P05014, doi:10.1088/1748-0221/16/05/P05014.

[287] A. Bodek et al., "Extracting Muon Momentum Scale Corrections for Hadron Collider Experiments", *Eur. Phys. J. C*, **72** (October 2012) 2194, doi:10.1140/epjc/s10052-012-2194-8, arXiv:1208.3710.

[288] CMS Collaboration, "CutBasedElectronIdentificationRun2 CMS TWiki", online, accessed sep 2024, https://twiki.cern.ch/twiki/bin/view/CMS/CutBasedElectronIdentificationRun2.

[289] CMS Collaboration, "Measurements of Inclusive W and Z Cross Sections in pp Collisions at $\sqrt{s} = 7$ TeV", *JHEP*, **01** (2011), 080, doi:10.1007/JHEP01(2011)080, arXiv:1012.2466.

[290] N. Adam, "Generic Tag and Probe Tool for Measuring Efficiency at CMS with Early Dat", Technical Report CMS AN-2009/111, "CMS experiment", 2009.

[291] J. Gallicchio and M. D. Schwartz, "Quark and gluon jet substructure", *J. High Energ. Phys.*, **2013** (April 2013) 90, doi:10.1007/JHEP04(2013)090.

[292] CMS Collaboration, "Measurement of multidifferential cross sections for dijet production in proton-proton collisions at $\sqrt{s} = 13$ TeV", arXiv:2312.16669.

[293] CMS Collaboration, "Measurement and QCD analysis of double-differential inclusive jet cross sections in proton-proton collisions at $\sqrt{s} = 13$ TeV", *JHEP*, **02** (2022), 142, doi:10.1007/JHEP02(2022)142, arXiv:2111.10431. [Addendum: JHEP 12, 035 (2022)].

[294] CMS Collaboration, "Measurement of Energy Correlators inside Jets and Determination of the Strong Coupling αS(mZ)", *Phys. Rev. Lett.*, **133** (2024),, no. 7, 071903, doi:10.1103/PhysRevLett.133.071903, arXiv:2402.13864.

[295] CMS Collaboration, "Measurement of the Ratio of the Inclusive 3-Jet Cross Section to the Inclusive 2-Jet Cross Section in pp Collisions at $\sqrt{s} = 7$ TeV and First Determination of the Strong Coupling Constant in the TeV Range", *Eur. Phys. J. C*, **73** (2013),, no. 10, 2604, doi:10.1140/epjc/s10052-013-2604-6, arXiv:1304.7498.

[296] CMS Collaboration, "Measurement of the cross section for $\mathrm{t\bar{t}}$ production with additional jets and b jets in pp collisions at $\sqrt{s} = 13$ TeV", *JHEP*, **07** (2020), 125, doi:10.1007/JHEP07(2020)125, arXiv:2003.06467.

[297] CMS Collaboration, "Calculation of Residual Energy Correction for b Jets Using Z+b Events in 8 TeV pp Collisions", technical report, CERN, Geneva, 2014, cds:1951028.

[298] Viola Sordini, Hugues Lattaud, and Viola Sordini, "Energy scale studies for b-jets with γ + jet events in Run2016 data.", Technical Report CMS AN-2017/174, CERN.

[299] K. Kallonen, "Quantitative Comparison of Deep Neural Networks for Quark/Gluon Jet Discrimination". Master's thesis, Helsinki U., 2019.

[300] N. T. Toikka, "Relative response measurement between light quark and gluon jets at the CMS experiment". Master's thesis, Helsinki U., 2023.

[301] Robin Cameron Aggleton, Anastasia Karavdina, and Andreas Hinzmann, "Flavour-dependent jet energy corrections for 2016 Monte Carlo", Technical Report AN-2018/109, CERN, May 2018.

[302] CMS Collaboration, "Development and validation of HERWIG 7 tunes from CMS underlying-event measurements", April 2021, doi:10.1140/epjc/s10052-021-08949-5.

[303] ATLAS Collaboration, "Jet Energy Scale uncertainties (R=0.4 PFlow) with updated flavour treatment", August 2022, https://atlas.web.cern.ch/Atlas/GROUPS/PHYSICS/PLOTS/JETM-2022-005/.

[304] Ilias Zisopoulos, Magda Diamantopoulou, Niki Saoulidou, and Eirini Tziaferi, "MC truth jet energy corrections using the Legacy 2016 simulations", Technical Report CMS AN-2021/148, CERN, 2021.

[305] J. Alwall, S. de Visscher, and F. Maltoni, "QCD radiation in the production of heavy colored particles at the LHC", *J. High Energy Phys.*, **2009** (February 2009) 017–017, doi:10.1088/1126-6708/2009/02/017, arXiv:0810.5350.

[306] R. Aggleton, "2018 Flavour JECs + High-pT b-jet response", 2018, https://indico.cern.ch/event/813625/#6-updates-on-flavor-jec-virtua.

[307] ATLAS Collaboration, "Measurement of b-quark fragmentation properties in jets using the decay $B^{\pm} \to J/\psi K^{\pm}$ in pp collisions at $\sqrt{s} = 13$ TeV with the ATLAS detector", *JHEP*, **12** (2021), 131, doi:10.1007/JHEP12(2021)131, arXiv:2108.11650.

[308] CMS HCAL/ECAL Collaborations et al., "The CMS barrel calorimeter response to particle beams from 2 to 350 GeV/c", *Eur. Phys. J. C*, **60** (April 2009) 359–373, doi:10.1140/epjc/s10052-009-0959-5.

[309] S. Banerjee and V. Ivanchenko, "Validation of Physics Models of Geant4 Versions 10.4.p03, 10.6.p02 and 10.7.p01 using Data from the CMS Experiment", *EPJ Web Conf.*, **251** (2021), 03010, doi:10.1051/epjconf/202125103010.

[310] CMS Collaboration, "StripsOfflinePlots2016 CMSPublic TWiki", online, accessed sep 2024, https://twiki.cern.ch/twiki/bin/view/CMSPublic/StripsOfflinePlots2016#Effect_of_APV_Saturation_on_S_N.

[311] CMS Collaboration, "Precision luminosity measurement in proton-proton collisions at $\sqrt{s} = 13$ TeV in 2015 and 2016 at CMS", *Eur. Phys. J. C*, **81** (2021),, no. 9, 800, doi:10.1140/epjc/s10052-021-09538-2, arXiv:2104.01927.

[312] CMS Collaboration, "CMS luminosity measurement for the 2017 data-taking period at $\sqrt{s} = 13$ TeV", technical report, CERN, 2018, cds:2621960.

[313] CMS Collaboration, "CMS luminosity measurement for the 2018 data-taking period at $\sqrt{s} = 13$ TeV", technical report, CERN, 2019, cds:2676164.

[314] P. Artoisenet, R. Frederix, O. Mattelaer, and R. Rietkerk, "Automatic spin-entangled decays of heavy resonances in Monte Carlo simulations", March 2013, doi:10.48550/arXiv.1212.3460.

[315] CMS Collaboration, "SWGuideMuonIdRun2 CMS TWiki", online, accessed sep 2024, https://twiki.cern.ch/twiki/bin/view/CMS/SWGuideMuonIdRun2.

[316] CMS Collaboration, "Measurement of the differential cross section for top quark pair production in pp collisions at $\sqrt{s} = 8\,\text{TeV}$", *Eur. Phys. J. C*, **75** (2015)„ no. 11, 542, doi:10.1140/epjc/s10052-015-3709-x, arXiv:1505.04480.

[317] CMS Collaboration, "Measurement of the $\mathrm{t\bar{t}}$ production cross section in the all-jets final state in pp collisions at $\sqrt{s} = 8$ TeV", *Eur. Phys. J. C*, **76** (2016)„ no. 3, 128, doi:10.1140/epjc/s10052-016-3956-5, arXiv:1509.06076.

[318] CMS Collaboration, "Measurement of the differential cross section for $\mathrm{t\bar{t}}$ production in the dilepton final state at $\sqrt{s} = 13$ TeV", technical report, CERN, 2016, cds:2140061.

[319] CMS Collaboration, "Measurement of differential cross sections for top quark pair production using the lepton+jets final state in proton-proton collisions at 13 TeV", *Phys. Rev. D*, **95** (2017)„ no. 9, 092001, doi:10.1103/PhysRevD.95.092001, arXiv:1610.04191.

[320] H. Siikonen, "Measurement of the Top Quark Mass with the CMS Experiment". PhD thesis, Helsinki U., 2022.

[321] CMS Collaboration, "JetID13TeVUL TWiki", online, accessed sep 2024, https://twiki.cern.ch/twiki/bin/view/CMS/JetID13TeVUL#Recommendations_for_the_13_T_AN1.

[322] CMS Collaboration, "Measurement of the inelastic proton-proton cross section at $\sqrt{s} = 13$ TeV", *JHEP*, **07** (2018), 161, doi:10.1007/JHEP07(2018)161, arXiv:1802.02613.

[323] ATLAS Collaboration, "Measurement of the Inelastic Proton-Proton Cross Section at $\sqrt{s} = 13$ TeV with the ATLAS Detector at the LHC", *Phys. Rev. Lett.*, **117** (2016)„ no. 18, 182002, doi:10.1103/PhysRevLett.117.182002, arXiv:1606.02625.

[324] W. Ford, G. Karathanasis, M. MacKenzie, and M. Pelliccioni, "Search for the charged lepton flavor violating decays of the Z boson with the Run II dataset", technical report, CERN, 2024.

[325] D. Kovalskyi and J.-F. Schulte, "Measurement of prefiring in the L1 muon trigger in Run 2", Technical Report CMS AN-2021/086, CERN, 2021.

[326] CMS Collaboration, "L1PrefiringWeightRecipe", online, accessed sep 2024, https://twiki.cern.ch/twiki/bin/viewauth/CMS/L1PrefiringWeightRecipe.

[327] S. S. Snyder, "Measurement of the Top Quark Mass at D0". PhD thesis, SUNY, Stony Brook, 1995. doi:10.2172/1422822.

[328] CMS Collaboration, "Measurement of the Top-Quark Mass in $t\bar{t}$ Events with Lepton+Jets Final States in pp Collisions at $\sqrt{s} = 7$ TeV", *JHEP*, **12** (2012), 105, doi:10.1007/JHEP12(2012)105, arXiv:1209.2319.

[329] CMS Collaboration, "The CMS statistical analysis and combination tool: COMBINE", April 2024, doi:10.48550/arXiv.2404.06614.

[330] CMS Collaboration, "Measurement of the top quark mass with lepton+jets final states using p p collisions at $\sqrt{s} = 13$ TeV", *Eur. Phys. J. C*, **78** (2018),, no. 11, 891, doi:10.1140/epjc/s10052-018-6332-9, arXiv:1805.01428. [Erratum: Eur.Phys.J.C 82, 323 (2022)].

[331] CMS Collaboration, "Measurement of the top quark mass using proton-proton data at $\sqrt{(s)} = 7$ and 8 TeV", *Phys. Rev. D*, **93** (2016),, no. 7, 072004, doi:10.1103/PhysRevD.93.072004, arXiv:1509.04044.

[332] R. Barlow and C. Beeston, "Fitting using finite Monte Carlo samples", *Computer Physics Communications*, **77** (October 1993) 219–228, doi:10.1016/0010-4655(93)90005-W.

[333] J. Conway, "Incorporating Nuisance Parameters in Likelihoods for Multisource Spectra", doi:10.5170/CERN-2011-006.115.

[334] CMS Collaboration, "Measurements of differential production cross sections for a Z boson in association with jets in pp collisions at $\sqrt{s} = 8$ TeV", *JHEP*, **04** (2017), 022, doi:10.1007/JHEP04(2017)022, arXiv:1611.03844.

[335] CMS Collaboration, "Measurements of the associated production of a Z boson and b jets in pp collisions at $\sqrt{s} = 8$ TeV", *Eur. Phys. J. C*, **77** (2017),, no. 11, 751, doi:10.1140/epjc/s10052-017-5140-y, arXiv:1611.06507.

[336] M. Czakon and A. Mitov, "Top++: A program for the calculation of the top-pair cross-section at hadron colliders", March 2013, doi:10.48550/arXiv.1112.5675.

[337] CMS Collaboration, "NNLO+NNLL top-quark-pair cross sections", online, accessed sep 2024, https://twiki.cern.ch/twiki/bin/view/LHCPhysics/TtbarNNLO.

[338] N. Kidonakis, "Two-loop soft anomalous dimensions for single top quark associated production with a W- or H-", May 2010, doi:10.48550/arXiv.1005.4451.

[339] CMS Collaboration, "NLO single-top channel cross sections", online, accessed sep 2024, https://twiki.cern.ch/twiki/bin/view/LHCPhysics/SingleTopRefXsec.

[340] CMS Collaboration, "Searches for physics beyond the standard model with the M_{T2} variable in hadronic final states with and without disappearing tracks in proton-proton collisions at $\sqrt{s} = 13$ TeV", *Eur. Phys. J. C*, **80** (2020),, no. 1, 3, doi:10.1140/epjc/s10052-019-7493-x, arXiv:1909.03460.

[341] CMS Collaboration, "Measurement of the WZ production cross section in pp collisions at $\sqrt{s} = 13$ TeV", *Phys. Lett. B*, **766** (2017), 268–290, doi:10.1016/j.physletb.2017.01.011, arXiv:1607.06943.

[342] CMS Collaboration, "Measurements of the pp $\to$ ZZ production cross section and the $Z \to 4\ell$ branching fraction, and constraints on anomalous triple gauge couplings at $\sqrt{s} = 13\,\text{TeV}$", *Eur. Phys. J. C*, **78** (2018), 165, doi:10.1140/epjc/s10052-018-5567-9, arXiv:1709.08601. [Erratum: Eur.Phys.J.C 78, 515 (2018)].

[343] A. Collaboration, "Study of the fragmentation of b quarks into B mesons at the Z peak", *Physics Letters B*, **512** (July 2001) 30–48, doi:10.1016/S0370-2693(01)00690-6, arXiv:hep-ex/0106051.

[344] D. Collaboration and J. Abdallah, "A study of the b-quark fragmentation function with the DELPHI detector at LEP I and an averaged distribution obtained at the Z Pole", *Eur. Phys. J. C*, **71** (February 2011) 1557, doi:10.1140/epjc/s10052-011-1557-x, arXiv:1102.4748.

[345] CMS Collaboration, "Investigations of the impact of the parton shower tuning in Pythia 8 in the modelling of $t\bar{t}$ at $\sqrt{s} = 8$ and 13 TeV", technical report, CERN, Geneva, 2016, cds:2235192.

[346] S. Argyropoulos and T. Sjöstrand, "Effects of color reconnection on $t\bar{t}$ final states at the LHC", *JHEP*, **11** (2014), 043, doi:10.1007/JHEP11(2014)043, arXiv:1407.6653.

[347] CMS Collaboration, "CMS PYTHIA 8 colour reconnection tunes based on underlying-event data", *Eur. Phys. J. C*, **83** (July 2023) 587, doi:10.1140/epjc/s10052-023-11630-8, arXiv:2205.02905.

[348] J. H. Friedman, "Data Analysis Techniques for High Energy Particle Physics". Springfield, 1974. https://www.slac.stanford.edu/pubs/slacreports/reports16/slac-r-176.pdf.

Andris Potrebko was born in 1996 in Riga. He obtained a Bachelor's degree in Physics (2018) from the University of Latvia and a Master's degree in Physics (2020) from Lund University, Sweden.
His interest in particle physics was sparked when he participated in the CERN summer student programme in 2018. In 2020, he was a scientific intern at Mainz University in Germany, where he worked on lattice quantum chromodynamics. Presently, he is a scientific assistant at the Institute of Particle Physics and Accelerator Technologies of RTU. From December 2025, he will take a researcher position at Université libre de Bruxelles (ULB) in Belgium.
His research interests include top quark, jet and standard model physics as well as computational physics. He is also passionate about machine learning. Since 2020, he has been a member of the CMS collaboration at CERN. During his PhD studies, he was an active guide of the CMS experiment and took detector control shifts during the experiment operations. In addition, he was teaching a physics course for high school students at RTU and at the University for Future Engineers (UNI). Andris is passionate about mountain climbing and hiking in his free time.